Cranfield University

Stephen Carnduff

System Identification of Unmanned Aerial Vehicles

Dynamics, Simulation and Control Group
Department of Aerospace Sciences
School of Engineering

Submitted for the Degree of Ph.D.

Cranfield University

Dynamics, Simulation and Control Group
Department of Aerospace Sciences
School of Engineering

Submitted for the Degree of Ph.D.
Academic Year: 2007-2008

Stephen Carnduff

System Identification of Unmanned Aerial Vehicles

Supervisor: Dr Alastair Cooke

14th August 2008

Abstract

The aim of this research is to examine aspects of system identification for unmanned aerial vehicles (UAVs). The process for aircraft in general can be broken down into a number of steps, including manoeuvre design, instrumentation requirements, parameter estimation, model structure determination and data compatibility analysis. Each of these steps is reviewed and potential issues that could be encountered when analysing UAV data are identified. Problems which may be of concern include lack of space within the airframe to mount sensors and a greater susceptibility to the effects of turbulence in comparison to manned aircraft. These issues are investigated using measurements from two experimental sources. Firstly, Cranfield University's dynamic wind tunnel facility is utilised, in which scale models are flown in semi-free flight. The control surfaces are actuated so that inputs, similar to those used when flight testing full-sized aircraft, can be applied and the resultant response of the model is recorded. Measurements from a 1/12 scale model of the BAe Hawk and a 1/3 scale model of the FLAVIIR project demonstrator UAV are used. An added benefit of the facility to this work is that the wind tunnel models are comparable in size to the miniature class of UAVs. Therefore, practical issues, similar to those faced for these aircraft, are encountered with the wind tunnel experiments. The second source of experimental data is UAV flight test data supplied by BAE Systems.

Acknowledgements

Firstly, I wish to thank my supervisor Dr Alastair Cooke, whose invaluable guidance and support has helped steer my work in the right direction over the last three years. I also wish to acknowledge the former Head of the Dynamics, Simulation and Control group Mike Cook for his encouragement and advice on all aspects of flight dynamics. Thanks must also go to other members of the Dynamics, Simulation and Control group, including Dr James Whidborne, Dr Ali Savvaris and Dr Sascha Erbsloeh. In particular, I am grateful to Sascha for lending me his expertise when preparing for and carrying out the wind tunnel experiments. Thanks also to Peter Thomas, who provided a valuable pair of hands for the tests of the DEMON model.

From BAE Systems, I am indebted to the project's industrial mentor Chris Fielding for his indispensable advice and support. I must also thank Chris for his help in arranging for me to have access to a valuable source of flight test data and putting me in contact with the system identification experts within the company. In this respect, I am grateful to Andy Perkins and Chris Forrest for providing an aircraft manufacturer's perspective on the subject and constructive feedback about the research I was conducting.

While trying to strike the work-life balance during my time at Cranfield, I have had the pleasure of meeting a wonderful group of people. For all the games of football, tennis, golf, barbeques and trips to the Lake District, I wish to thank Jason Bennett, Ross Chaplin, Ian Cowling, Simon Croucher, Marco Hahn, Marco Kalweit, Sunil Mistry, John Murphy, Sanjay Patel, Michael Porton, Adam Ruggles, Yosuke Shimada, Peter Thomas and Ben Thornber. A special mention goes to Ben, Sanj, and the two Marcos, from whom I like to think I have a learned a little about computational fluid dynamics during our many coffee breaks together.

Finally, I wish to express my gratitude to my family and friends for all their love and support over the last three years. I am especially thankful to my parents David and Evelyn, without whom I would never have reached this point.

Contents

List of Figures

List of Tables

Notation

$\mathbf{A}$	State matrix
a_x	Acceleration along the x-axis system
a_y	Acceleration along the y-axis system
a_z	Acceleration along the z-axis system
$\mathbf{B}$	Input matrix
$\mathbf{b}$	Vector of bias terms
b	bias term/error, aircraft wingspan
$\mathbf{C}$	Output matrix, direction cosine matrix
C	Condition index
C_l	Rolling moment coefficient
C_m	Pitching moment coefficient
C_n	Yawing moment coefficient
$\bar{c}$	Mean aerodynamic chord
$\mathbf{D}$	Direct matrix
E	Expected value of a variable
$\mathbf{F}$	Atmospheric turbulence distribution matrix
F_0	Partial F-statistic
f	Frequency in Hz, nonlinear state function
$\mathbf{G}$	Matrix of first order gradients of the cost function with respect to the unknown parameters
$\mathbf{G}_v$	Measurement noise distribution matrix
g	Acceleration due to gravity, nonlinear output function
h	Altitude
$\mathbf{I}$	Identity matrix, vector of insensitivities
I_{xx}	Moment of inertia in roll
I_{yy}	Moment of inertia in pitch
I_{zz}	Moment of inertia in yaw
I_{xy}	Product of inertia about x and y axes
I_{xz}	Product of inertia about x and z axes
I_{yz}	Product of inertia about y and z axes
J	Cost function
j	The complex variable ($\sqrt{-1}$)
$\mathbf{K}$	Kalman filter gain
k	Scale factor error
$\mathbf{M}$	Fisher information matrix
N	Number of discrete data points
$\mathbb{N}$	Normally distributed random variable
n_u	Number of input variables

n_x	Number of state variables
n_y	Number of measurement variables
n_θ	Number of unknown parameters to be determined
P	Parameter error covariance matrix, state prediction error covariance matrix
R	Residual covariance matrix
p	Roll rate
q	Quaternion variable
q	Pitch rate
$\bar{q}$	Dynamic pressure
r	Yaw rate
S	Matrix of singular values
$\mathbf{S}_{\epsilon\epsilon}$	Matrix of power spectral densities of ϵ
S	Aircraft wing area, singular value
s	Standard error, Laplace operator
T	Matrix of eigenvectors
T	Length of time of manoeuvres or data segment, engine thrust
t	Time
t_{comp}	Computational time
tr	Trace of a matrix
U	Theil's inequality coefficient
U_B	Theil's inequality bias portion
U_C	Theil's inequality covariance portion
U_V	Theil's inequality variance portion
u	Input vector
u	Axial velocity component
v	Sideslip velocity component, measurement noise
V	True airspeed
V_T	Wind tunnel velocity vector
v	Measurement noise vector
v	Sideslip velocity perturbation variable
w	Process noise vector
w	Normal velocity component
X	Matrix of regressors
X	Element of regressor matrix, discrete Fourier transform
x	State vector
x	Longitudinal coordinate in axis system
y	Output vector
y	Lateral coordinate in axis system
z	Measurement vector
z	Normal coordinate in axis system

Greek Letters

α	Angle of attack, t-distribution/F-distribution confidence level parameter
β	Angle of sideslip
ϵ	Vector of equation errors, vector of output errors
ζ	Rudder input, damping ratio

η	Elevator input
$\boldsymbol{\theta}$	Vector of unknown parameters
$\bar{\Theta}$	Confidence ellipsoid
θ	Pitch attitude, element of unknown parameter vector
$\boldsymbol{\lambda}$	Matrix of eigenvalues
λ	Geometric scaling factor, eigenvalue
ξ	Aileron input
ρ	Atmospheric density, correlation coefficient
σ^2	Variance
$\boldsymbol{\tau}$	Vector of time delays
τ	Time delay
$\boldsymbol{\upsilon}$	Vector of residuals
$\boldsymbol{\Phi}$	State transition matrix
ϕ	Roll attitude
$\boldsymbol{\Psi}$	Integral of state transition matrix
ψ	Yaw attitude
ω	Frequency in rad/s
ω_n	Natural frequency

Subscripts

0	Initial condition, offset term
E	Earth-referenced variable
g	Gust variable
m	Measured variable
p	Perturbation variable

Other Notation

Cov	Covariance
CG	Centre of gravity
EKF	Extended Kalman filter
MSE	Mean square error
MTOW	Maximum take-off weight
Re	Real part of a complex variable
Var	Variance
$\bar{}$	Mean of a variable
$\hat{}$	Estimated variable, nondimensional state variable, corrected Kalman filter variable
$\tilde{}$	Fourier transform, predicted Kalman filter variable
$\dot{}$	Time derivative
$\dagger$	Complex conjugate transpose
$*$	Standardised variable
Δt	Input pulse width, data sampling time
$\Delta \theta$	Parameter update vector

Chapter 1

Introduction

1.1 Background

A major trend within the aerospace industry in recent decades has been a growing interest in unmanned aerial vehicles (UAVs). While their application for military purposes has long been established, there are an increasing number of roles in the civil sector for which UAVs are being used, including surveillance for law enforcement, pipeline inspection and crop spraying. The size and performance metrics of UAVs can vary greatly depending on what the vehicle is designed to do. Table 1.1 contains a list of suggested categories for different types of unmanned aircraft [1].

Substantial research effort is currently being focused on developing UAVs that can operate autonomously. This goal of autonomous flight relies heavily on the use of control system technology. However, before these control systems can be designed, an accurate mathematical model of the vehicle's dynamics is required. Knowledge of the flight dynamics of an aircraft is also implemented, for example, when developing ground-based simulators for training purposes and when assessing aircraft handling qualities.

Mathematical models of aircraft dynamics can be obtained theoretically or from experiment. Theoretical methods tend to be based on semi-empirical rules of thumb, such as those published by the Engineering Science Data Unit (ESDU) [2] or DATCOM [3]. These methods have evolved from decades of experience with manned aircraft. However, without the need to accommodate a pilot, the designs of UAVs can be very different from those of manned aircraft making these techniques unreliable. One class of aircraft for which this is a concern is unmanned combat aerial vehicles (UCAVs). These aircraft are designed primarily to have a low radar signature and consequently have a blended wing-body configuration without a fin [4]. This makes certain dynamic properties of the aircraft difficult to predict theoretically. For example, the aircraft's directional stability would normally be predicted using knowledge of the fin geometry and from the destabilising effect of the forebody, which is usually approximated as an axi-symmetric shape [4, 5]. Clearly, this cannot be done for UCAV configurations. Another category, for which deriving models from first principles is problematic, is unmanned rotorcraft (RUAVs). Difficulties are caused by factors including the basic airframes of these aircraft being lightly damped or unstable, high cross-coupling existing between the dynamics in each axes and coupling between the fuselage and rotor dynamics [6]. In recent years, attempts have been made to determine stability and control characteristics of aircraft using techniques

based on Computational Fluid Dynamics (CFD) [7, 8]. The main drawback of these methods at present, though, is the computational power required to calculate the forces and moments acting on an entire aircraft.

UAV Category	Range(km)	Altitude(m)	Endurance(hrs)	MTOW(kg)
Tactical				
Micro	<10	250	1	<5
Miniature	<10	150-300	<2	<30
Close range	10-30	3000	2-4	150
Short range	30-70	3000	3-6	200
Medium range	70-200	5000	6-10	1250
Medium range endurance	>500	800	10-18	1250
Low altitude deep penetration	>250	50-9000	0.5-1	350
Low altitude long endurance	>500	3000	>24	<30
Medium altitude long endurance	>500	14000	24-48	1500
Strategic				
High altitude long endurance	>2000	20000	24-48	12000
Special Purpose				
Combat	≈1500	10000	≈2	10000
Lethal	300	4000	3-4	250
Decoy	<500	5000	<4	250
Stratospheric	>2000	20000-30000	>48	TBD
Exo-stratospheric	TBD	>30000	TBD	TBD

Table 1.1: Suggested categories of UAVs

Of the experimental procedures, tests of scale models in the wind tunnel environment are usually carried out first in the aircraft's development. These experiments can be performed either statically or dynamically [5]. The main advantage of wind tunnel testing is that it allows a representative model of the aircraft to be tested in characteristic aerodynamic conditions. However, the veracity of the results obtained can be limited by scaling effects and interference from the test rig. Ultimately, a prototype of the aircraft will be flight tested and a model of the vehicle flight dynamics obtained. Of the methods described, both analytical and experimental, the flight test process will provide a mathematical model with the highest degree of fidelity, as the aircraft is tested under conditions for which it was designed to operate. In light of the drawbacks, highlighted above, in using theoretical techniques to establish UAV flight dynamics properties, there is an increased importance in using experimental methods for this purpose.

System Identification, also sometimes referred to as parameter identification, is a method which has been utilised extensively to investigate aircraft flight dynamics based on flight test and dynamic wind tunnel data. It is the process of finding an appropriate mathematical model to describe the behaviour of a dynamic system, based on observations of the system inputs and outputs. In theory, system identification can be used to analyse any dynamic system and its principles find applications in a wide range of fields including biology [9], chemical engineering [10] and economics [11]. When applied to aircraft, the process provides a means of determining an appropriate form for the equations of motion and estimating the numerical values for the aerodynamic (or stability and control) derivatives within these equations of motion.

1.2 Survey of Aircraft System Identification

After the classical description of aircraft stability was proposed by Bryan in 1911 [12], attempts to determine stability and control derivatives from flight test were made as early as 1919, when Glauert analysed the phugoid mode based on airspeed recordings [13]. This was followed by the work of Norton, who studied roll damping [14] and longitudinal dynamic stability [15] from flight measurements in the early 1920s. During the period from the 1940s to the early 1960s, a number of frequency response approaches were employed to estimate the dynamic characteristics of aircraft [16, 17]. Milliken used sinusoidal inputs to the elevator in order to excite small amplitude pitching oscillations and used the resulting data to determine frequency response characteristics of the aircraft [18]. Later, a pulse method incorporating Fourier analysis was put forward by Seamans et al [19], while Shinbrot introduced analysis methods based on weighted least-squares curve fitting which resemble techniques used in system identification today [20]. Two more commonly used approaches which were developed during the 1950s and early 1960s were the time-vector method [21, 22, 23] and analogue matching [24, 25]. For the time-vector method, a pulse input was applied to excite a controls-fixed, free oscillation and then time-vector decomposition was used to analyse the amplitude and phase of the resultant response. Analogue matching involved programming a mathematical model of the aircraft, usually based on theoretical or wind tunnel analysis, onto an analogue computer. The control inputs used during the flight tests would then be applied to this computer model and the analyst would manually tune the stability and control parameters to obtained, qualitatively, a good match with the measured response from flight test.

The routine use of these early approaches for estimating stability and control derivatives from flight test data were hampered by a number of factors. The methods were usually time-consuming and could only provide estimates of a small subset of the derivatives [17]. Mainly, these techniques were inhibited by a lack of computational power. However, this changed in the 1960s with the advent of digital computers and it was at this time that the development of modern day aircraft system identification began.

Over the last four decades, a number of aerospace research institutes have been actively involved in the development of the subject. Major contributions have been made by the NASA research centres at Dryden [26, 27, 28, 29] and Langley [30, 31], the U.S. Army Aeroflightdynamics Directorate at Ames [6, 32], DLR [33, 34] in Germany, NLR and the Technical University of Delft [35, 36] in the Netherlands, the Royal Aircraft Establishment/DERA [37, 38] and Cranfield College of Aeronautics [39] in the UK and NRC [40] in Canada. Many different methods for estimating the aerodynamic derivatives have been developed. To establish which techniques are most commonly used, a survey of the methods reported in the literature over the last two decades was conducted. The results are summarised in Table 1.2 which, for each class of aircraft, details the methods applied to particular aircraft by various organisations. References to the source material are also provided. By far, the most commonly used techniques for fixed-wing aircraft are the equation error formulation, solved using methods of regression, and the output error approach, based on maximum likelihood estimation. These method have been formulated in both the time and frequency domain. However, the main application of frequency domain estimation has been rotorcraft identification. In particular, the frequency response method has been widely used. Two related issues to the estimation of the stability and control derivatives are the design of flight test manoeuvres and the selection of a suitable instrumentation system to record the resultant data. The accuracy of the parameter estimates are obviously heavily dependent on the quality of the measurements, therefore the subjects

of optimal control surface inputs [35, 41, 42] and characteristics of flight test instrumentation [25, 43, 44, 45] have also received much attention. Today, aircraft system identification has matured to a point where many aircraft manufacturers routinely use the process in the development of new aircraft [46, 47].

While a significant amount of material has been published on system identification for aircraft in general, there is a limited amount of information on what must be considered when applying the technique to UAVs. Many papers have been published which report system identification being carried out on unmanned aircraft. These are also summarised in Table 1.2. However, the focus of the research tends to have been on the application of the results obtained through system identification, rather than on the process itself. In these papers, the purpose of system identification was, generally, to obtain either a mathematical model of the vehicle dynamics to facilitate a control system design or to validate a simulation model. As may be expected, for security or commercial reasons, this published research has been almost exclusively carried out by universities rather than aircraft manufacturers. Therefore the vehicles being analysed are generally commercial off-the-shelf platforms falling into the category of small or miniature UAVs (see Table 1.1). Small UAV helicopters have been studied extensively, with many institutes using the frequency response method. The likely reason for this is that the technique is encapsulated in the commercially available software tool CIFER (Comprehensive Identification from Frequency Responses) [6], which was originally developed specifically for rotorcraft system identification problems.

Some aspects of applying system identification to unmanned aircraft are discussed by Theodore et al [48], with the focus of the paper again on the frequency response method employed in CIFER. The obvious physical difference between unmanned and piloted aircraft is that UAVs tend to be much smaller in size, and it is this fact that chiefly affects the process for unmanned aircraft. For example, for the class of miniature UAVs, there will be limited payload and space available for flight control systems, sensors and control surface actuators. This results in a compromise between the performance of these subsystems and their size and weight. In comparison to those systems typically employed on manned aircraft, flight control computers will have limited power and speed, sensors will be noisier and have a lower performance, while actuators will be slower and less precise. Thus, the dynamics introduced by the subsystems will have to be accounted for in order to obtain an accurate model of the vehicle's basic airframe. It is also worth noting that, again due to limited space, it may not be practical to measure control surface deflections directly, which is usually achieved on manned aircraft using bulky potentiometers or linear variable differential transducers [34]. In this case, the control surface positions can be inferred through knowledge of the commands being sent to the actuators and knowledge of the actuator and control linkage dynamics. As well as this, the way in which UAVs are flight tested is very different from that used for manned aircraft. A choice has to be made as to whether the inputs used for system identification are applied manually by a pilot on the ground or generated automatically by a computer. The disadvantage of having a pilot command inputs remotely is that the visual and motion cues that would typically be available to the pilot when testing manned aircraft do not exist for UAVs. In some cases, where the UAV of interest was a modification of an existing manned aircraft, the system identification tests were performed manually by a pilot on board. However, it was necessary to ensure that the mass, inertia and location of the centre of gravity during the flight tests were the same as those for the proposed UAV configuration.

Organisation	Aircraft	Method	Reference
Fighter/high performance aircraft			
NASA Langley	F-18 High Alpha Research Vehicle	Equation error, regression method	[49]
	X-29A	Equation error, regression method	[31, 50]
	X-31A	Equation error, regression method	[50]
NASA Dryden	F-18 High Alpha Research Vehicle	Maximum likelihood, output error method	[29]
	X-29A	Maximum likelihood, output error method	[29]
	SR-71	Maximum likelihood, output error method	[29]
DLR	X-31	Maximum likelihood, output error method	[34, 51]
Defence Science and Technology Organisation (Australia)	F-111C	Maximum likelihood, output error method	[52]
Science Applications International/Naval Air Systems Command	F/A-18E	Equation error, regression method	[53]
Science Application International	S-3B Viking	Equation error, regression method	[54]
Systems Control Technology Inc./Naval Air Warfare Centre	F-14	Equation error, regression method	[55]
Alenia, British Aerospace, CASA and Daimler-Benz Aerospace	Eurofighter Typhoon	Equation error and output error methods	[47]
Boeing	F-18 C/D/E, F-15E, AV-8B and X-36	Equation error, output error and filter error methods	[46]
Civil Transport Aircraft			
NASA Langley	Tu-144LL	Frequency domain equation error and output error methods	[56, 31, 30]
Boeing	B717, B737, B747, B757, B767 and B777	Equation error, output error and filter error methods	[46]

Table 1.2: Survey of aircraft parameter estimation methods - continued on next page

Continued from previous page

Organisation	Aircraft	Method	Reference
General Aviation Turboprops			
NASA Dryden / West Virginia University	Cessna U-206	Maximum likelihood, output error method	[57]
NASA Langley	Twin Otter	Time and frequency domain equation error and output error methods	[30, 31]
DLR	Dornier 328	Maximum likelihood, output error	[34, 33, 17]
Korean Aerospace Research Institute	Firefly	Maximum likelihood, filter error method	[58]
General Aviation Turbojets			
Delft University	Cessna Citation II	Maximum likelihood, output error method and estimation-before-modelling	[59]
Delft University/ University of Stellenbosch	Cessna Citation II	Maximum likelihood, output error method	[60]
Delft University	Eclipse 500	Equation error, regression method	[61]
DLR	VFW-614 ATTAS research aircraft	Maximum likelihood, output error method	[34, 33, 17]
National Research Council, Canada	Falcon 20	Maximum likelihood, output error method	[40]
	Raytheon Beech Jet 400A	Maximum likelihood, output error method	[62]
Rotorcraft			
U.S. Army Aeroflightdynamics Directorate	UH-60A	Frequency response method	[6]
	OH-58B	Frequency response method	[6, 63]
	S-92	Frequency response method	[6, 64]
U.S. Army Aeroflightdynamics Directorate / Kaman Aerospace	SH-2G	Frequency response method	[6, 65]
Glasgow University	VPM M-16 and Montgomerie-Parsons autogyros	Frequency domain, equation error regression	[66]

Table 1.2: Survey of aircraft parameter estimation methods - continued on next page

Continued from previous page

Organisation	Aircraft	Method	Reference
Military Training Aircraft			
Defence Science and Technology Organisation (Australia)	P/C-9A	Equation error and output Error methods	[52]
Military Transport Aircraft			
DLR	C-160	Maximum likelihood, output error method	[34, 33, 17]
Unmanned Aircraft			
NASA Langley/Dryden	X-43A (Hyper-X)	Frequency domain, equation error regression method	[67]
DLR	ARTIS UAV demonstrator	Extended Kalman filter	[68, 69]
U.S. Army Aeroflightdynamics Directorate	Pathfinder Solar-powered aircraft	Frequency response method	[70]
	Northrop Grumman Fire Scout RUAV	Frequency response method	[48]
	Kaman K-MAX RUAV	Frequency response method	[48]
	Yamaha R50 RUAV	Frequency response method	[48]
	Micro Craft ducted fan UAV	Frequency response method	[48]
	Honeywell ducted fan UAV	Frequency response method	[48]
Dynetics Inc./U.S. Army	Shadow 200	Frequency response method	[71, 6]
	Shadow 200	Frequency response method	[71, 6]
Stanford University	DragonFly	Frequency domain, equation error regression	[72]
Kansas University	Raptor 50 V2	Frequency response method	[73, 74, 75, 76]
National Cheng Kung University, Taiwan	SWAN UAV	Observer Kalman Identification Method	[77]
Carnegie Mellon University/NASA Ames	1/4 Scale Cessna 182	Frequency domain, equation error regression	[78]
University of California at Davis	Ducted fan UAV	Frequency response method	[79]

Table 1.2: Survey of aircraft parameter estimation methods

1.3   Objectives of the Research

Some aspects of the system identification process will vary slightly depending on the type of aircraft being investigated, as well as the practitioner carrying out the analysis. However, the critical stages of the procedure are shown in the simplified block diagram in Figure 1.1. The first stage is the design of the experiments which will be used to excite the aircraft dynamics of interest. In some cases, this requires prior estimates of the vehicle's dynamic characteristics and also includes the selection of appropriate instrumentation to measure the motion variables. Once the data has been recorded, the first stage in the analysis is to verify the consistency of the measurements before they are utilised in later stages of the system identification process. This check on the data, usually termed data compatibility check or flight path reconstruction, is performed by analytically generating the time history of a given variable using well-defined kinematic relationships and measurements of other variables. For example, the attitude angles can be reconstructed by integrating the angular rate data obtained from rate gyros. If the measured and reconstructed responses match then the data is said to be kinematically consistent. On the other hand, if the measured and reconstructed responses do not match, error models for each of the sensors can be postulated and the kinematic equations provide a means for estimating these error parameters. Having accounted for errors in the data, the core stage of the analysis is to determine the most appropriate form of the equations to describe the measured response and to estimate the numerical values of the stability and control derivatives appearing in the equations. This is known as model structure determination and parameter estimation respectively. The final step in the analysis is to validate the identified dynamics and this is usually done by comparing the response with a separate set of data not used in the preceding analysis. If the validation process is successful then the analysis is halted and the final model of the aircraft dynamics has been obtained. Otherwise, the analysis may have to be repeated using a different equation structure or parameter estimation technique. In severe cases, the experiments may have to be performed again.
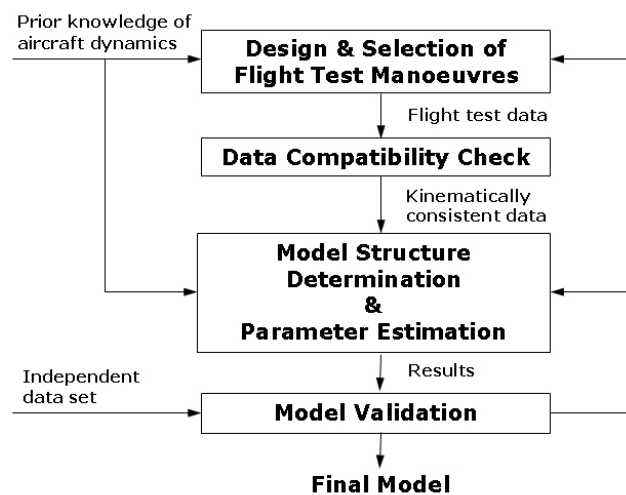
Figure 1.1: Block diagram of system identification process

Taking the above description of aircraft system identification into account, the objectives of the research were as follows:

- Review each of the steps defined in Figure 1.1.

- Identify potential issues that are likely to be encountered when applying system identification for UAVs.

- Investigate whether there are any methods that are particularly well suited to UAVs.

- Analyse experimental data to examine whether the potential issues are encountered in practice.

1.4   Sources of Experimental Data

The first source of data was Cranfield University's dynamic wind tunnel facility, which was originally developed in the early 1980s [80, 81] and has been used to investigate a number of aircraft configurations [82, 83]. A major part of this project was to update the instrumentation, sensors and hardware used in this facility. A benefit of this, with the current research in mind, was that the wind tunnel models were of comparable size to miniature UAVs and, as a result, much of the technology utilised was typical of that employed in this class of aircraft. Hence, similar issues concerning the gathering and analysis of data from miniature UAVs were encountered with the wind tunnel facility.

Figure 1.2 shows the test rig with a 1/12 scale model of the BAe Hawk, which has been used as a platform for testing the facility's instrumentation and hardware. The design of the rig is relatively simple, with the aircraft model suspended on a stiff vertical rod, which is itself attached to a Dexion framework. The vertical rod passes through a gimbal mechanism within the model, shown in Figure 1.3, that allows the aircraft to rotate in roll, pitch and yaw and to translate vertically along the axis of the rod. The rig therefore allows investigation of 4 degrees of freedom (DoF) of motion (see Figure 1.5). The range of motion that the rig permits is ± 30 degrees rotation in roll and pitch, 360 degrees in yaw and a translation of approximately 0.75m in the vertical axis. The gimbal and rod assembly was made as small and as light as possible to minimise their influence on the aircraft model and the gimbal incorporates precision ballraces and linear ball bearings to minimise frictional effects. The test rig is designed to be placed in an open section wind tunnel. The facility currently being used has a working section of 1.5m by 1.1m and a maximum speed of 40m/s inside the working section. The maximum wing span of the model is limited to around 0.9m.

In practice, the wind tunnel models tend to be very responsive in heave and quickly hit the end stops on the vertical rod. Therefore, the models cannot be tested in all 4 degrees of freedom safely without some form of closed-loop height control system. Although such a system had been successfully implemented in previous work [84], it has yet to be reproduced with the updated sensors and instrumentation due to difficulties in obtaining an accurate value of height. Therefore, the experiments carried out during the course of this research were performed with the model restricted from moving in the z-axis i.e. 3 DoF. A description of the equations of motion for a model on the rig is given in Appendix A.

Two wind tunnel models were tested as part of the research: the 1/12 scale BAe Hawk shown in Figure 1.2 and a 1/3 scale model of the FLAVIIR programme demonstrator UAV, known as DEMON and shown in Figure 1.4. The Hawk model had been analysed previously in a number of research exercises with the wind tunnel [80, 83]. Therefore, it represented a conventional

airframe design, the dynamic characteristics of which were well known. The DEMON model, on the other hand, was constructed during the course of this project, hence it provided an opportunity to test a model of a more unusual shape for which little prior knowledge existed. Note that the goal of the wind tunnel experiments was simply to gather data on which system identification algorithms could be tested, rather than to obtain information relevant to the full-sized aircraft. Hence, the model masses and inertias were not scaled appropriately prior to the tests.

Figure 1.2: 4 DoF rig with 1/12 scale BAe Hawk

An established method for determining stability and control derivatives from dynamic wind tunnel experiments is to mount a scaled model of the aircraft onto a test rig and observe the model's free or forced oscillatory response [85]. By connecting the rig to a suitable force and moment balance, the derivatives of the forces and moments with respect to the motion variables can be obtained. The 4 DoF rig utilises a different approach, in which the aim is to emulate flight test-like experiments in the wind tunnel environment [80, 82, 83, 86, 87, 88, 89, 90]. A scaled model with representative control surfaces is mounted on the test rig and flown in semi-free flight. Inputs can be applied to the control surfaces, which are deflected using miniature servo-actuators, and the resultant response of the model is measured using motion sensors. The stability and control derivatives can then be extracted from the input/output data using system identification techniques similar to those used in the flight test environment. A number of examples of the analysis carried out on the wind tunnel data are presented throughout the thesis. It should be noted that each example is based on measurements recorded at the same trim conditions, namely a tunnel speed of 30 m/s and an angle of attack of zero degrees.

The second source of experimental data was from UAV flight tests. This was provided by BAE Systems, who supplied two separate sets of data from the same aircraft. During the course of this research, system identification was performed on the data using algorithms which had
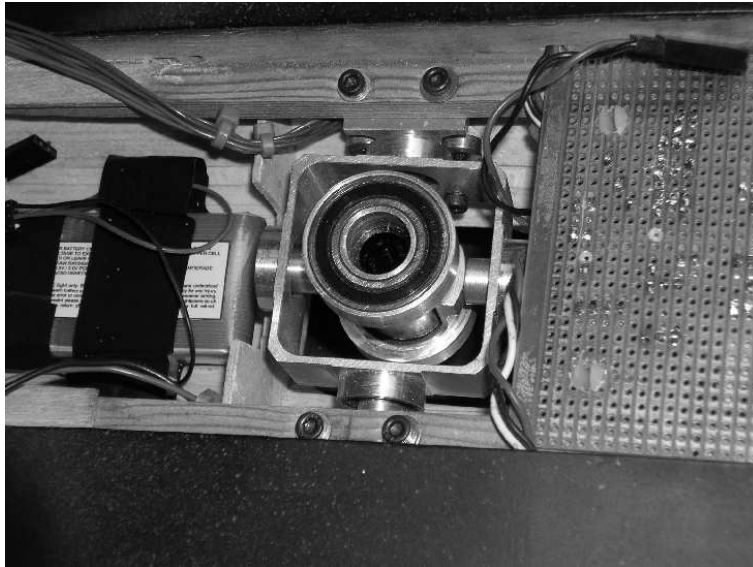
Figure 1.3: Gimbal mechanism
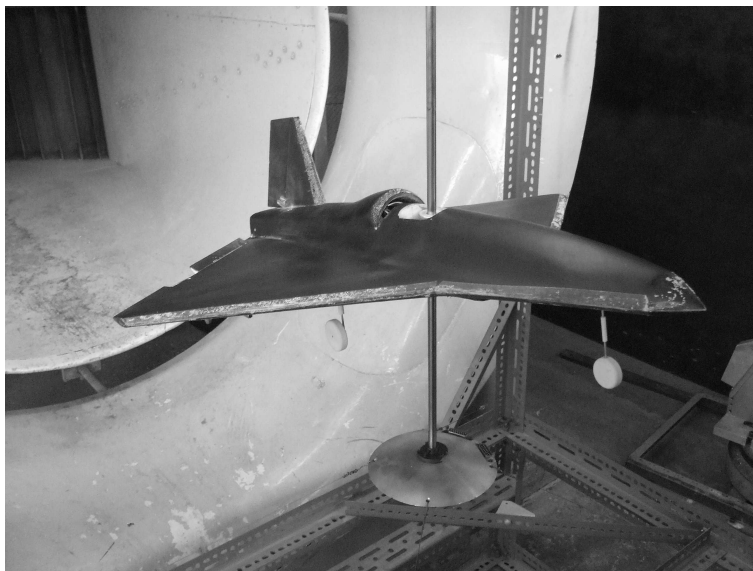
Figure 1.4: 1/3 Scale model of the DEMON UAV
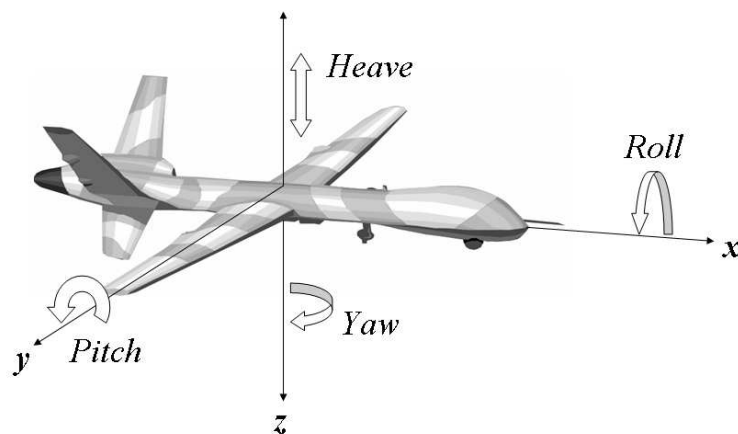
Figure 1.5: Degrees of freedom on 4 DoF rig

not been previously used to analyse this particular aircraft. For security and commercial reasons, the aerodynamic derivatives presented in this thesis have been normalised using empirical estimates and numerical values have been removed from the associated plots.

1.5   Layout of Thesis

The next chapter focuses on the design and selection of manoeuvres to excite the aircraft dynamics and is followed by a chapter outlining sensor and instrumentation requirements. From this point forward, rather than follow the order that each step is performed according to the block diagram in Figure 1.1, it is felt that it is logical to deal with parameter estimation first. This is because parameter estimation is often regarded as the key step in the procedure and, as a result, the other stages of the analysis can be influenced by which estimation methods are used. Also, the mathematical techniques used in the model structure determination and data compatibility check are very similar to those employed in parameter estimation. The first methods to be described are equation error methods (Chapter 4) and the output error methods (Chapter 5), which were identified in aircraft system identification survey as being the two most widely used approaches. The application of the two techniques in the frequency domain is then presented in Chapter 6 and parameter estimation issues of importance to UAVs are detailed in Chapter 7. Attention is turned to model structure determination in Chapter 8, while Chapter 9 deals with the data compatibility checks. Finally, the conclusions of the research, contributions to knowledge and recommendations for future work are outlined in Chapter 10.

1.6   Software Tools

To facilitate the analysis of experimental data, appropriate software tools were required and the MATLAB environment was utilised for this purpose. During the course of this work, two sets of MATLAB programs designed for aircraft system identification became available. These were published by Jategaonkar at DLR [34] and Morelli at NASA Langley [31] and both contained a number of parameter estimation algorithms. Rather than just providing executable code, the authors allow the user to study the implementations and thus provide a platform for the user to write additional routines to solve problems of interest. Therefore, these programs formed the basis of a collection of software tools designed to analyse the data being utilised during this project. The software was given a graphical user interface (GUI) to help make the programs easy to use. The philosophy behind the software tools was to provide a capability to rapidly analyse the data in situ and provide a "quick first look" at system identification results to determine whether the experiments were successful. A more detailed analysis could then be performed at a later stage. For access to the software toolset, please contact Dr Alastair Cooke at the Department of Aerospace Sciences, School of Engineering, Cranfield University.

Chapter 2

Manoeuvre Design

2.1 Introduction

As highlighted in Section 1.3, the first task in the system identification process is to design and conduct experiments from which data can be gathered and analysed to establish the stability and control derivatives of interest. A considerable amount of planning is required if these experiments are to be carried out efficiently and successfully. Ultimately, the quality of the parameter estimates will be dependent on how the tests were performed and if there is little information about a crucial derivative within the data then the identified value for that derivative will be unreliable or inaccurate. On top of this, the act of carrying out flight tests or wind tunnel experiments is a costly one, so having to repeat the process is highly undesirable.

To start with, the goal of the tests must be defined. This is usually related to the application of the results obtained from the system identification process. Typical examples, some of which were mentioned in Section 1.1, are to help in the design of flight control and stability augmentation systems, developing flight simulators for crew training, assessing the aircraft handling qualities, supporting flight envelope expansion, investigate the effects of configuration changes and simply to verify analytical or wind tunnel estimates [31, 34]. Decisions must then be made regarding which aircraft configurations to test and at which points within the flight envelope the experiments will be performed.

Depending on the application of the flight test results, requirements defined by the appropriate regulatory bodies may influence how the experiments are performed. For example, in the assessment of training simulators, organisations such as the Federal Aviation Administration (FAA) and the Joint Aviation Authorities (JAA) define over 100 test cases in which the simulator response must match that of the aircraft to within specified tolerances - a process termed proof-of-match [91, 92]. These test cases cover the entire operational envelope of the aircraft. Therefore, in order to assemble a comprehensive aerodynamic database for the simulator, manoeuvres must be performed at various Mach numbers, altitudes, flap settings and centre of gravity locations. As well as this, a second set of data, separate from the manoeuvres used to build the aerodynamic database, is required to cover the proof-of-match test points and provides the comparison against which the simulator is assessed. Another example is the assessment of an aircraft's handling qualities [93]. For military aircraft, the flight test procedure is influenced by the guidelines laid out in documents such as MIL-HDBK-1797A [94]. The equivalent for civil aircraft are defined in FAA Regulations FAR parts 23 [95] and 25 [96].

Having defined the purpose of the experiments, a set of manoeuvres or control inputs must be chosen and carried out at each of the selected test points. This chapter describes the process of designing these inputs. Another critical issue is the choice of a suitable instrumentation system to record the motion variables from the aircraft or wind tunnel model. This is dealt with in Chapter 3. The objective of the manoeuvre design is to select a control surface input which will adequately excite the aircraft dynamics of interest. This, in turn, should result in there being enough information content in the measured data from which the aerodynamic derivatives can be reliably identified. A number of approaches have been proposed and used in practice. The most commonly used are described in the following sections.

2.2   Frequency Sweeps

Frequency sweeps are continuous sinusoidal signals whose frequencies vary to cover the frequency range of interest. This variation in frequency can be linear or logarithmic. An example of a linear frequency sweep is shown in Figure 2.1, with the input beginning at a frequency of 0.1 rad/s and increasing to 10 rad/s. The signal is described mathematically by the expression [6, 31],

$$u(i) = \sin(\varphi(i)), \quad i = 1, 2, \ldots, N \tag{2.2.1}$$

where,

$$\varphi(i) = \omega_s t(i) + \frac{1}{2}(\omega_e - \omega_s)\frac{t(i)^2}{T} \tag{2.2.2}$$

and N is the number of data points. The variables ω_s and ω_e denote the start and end frequencies respectively (0.1 and 10 rad/s for the example signal), $t(i)$ is the discrete point in time and T is the length of time of the manoeuvre (90s for the example signal). The drawback of linear frequency sweeps is that the energy of the input tends to be concentrated at the higher frequencies, leading to less information in the data for lower frequency components. This is illustrated using the power spectral density plot in Figure 2.1.

(a) Linear frequency sweep   (b) Power spectral density
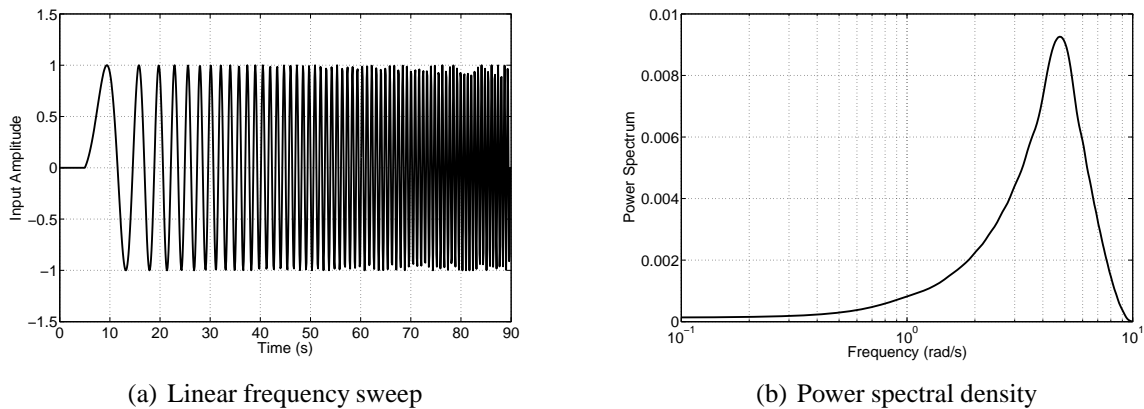
Figure 2.1: Linear frequency sweep and associated power
spectral density plot

A logarithmic frequency sweep, with the same frequency band as the linear frequency sweep, is shown in Figure 2.2. Its phase function is given by the equation,

$$\varphi(i) = \omega_s t(i) + C_2(\omega_e - \omega_s)\left[\frac{T}{C_1}e^{C_1 t(i)/T} - t(i)\right] \tag{2.2.3}$$

where C_1 and C_2 are scalars, with values typically of $C_1 = 4$ and $C_2 = 0.0187$ [6]. The power spectral density of the logarithmic signal is also illustrated in Figure 2.2. It can be seen that, in comparison to the linear sweep, the energy of the logarithmic input is much more evenly spread over the frequency range. This is due to a larger portion of the logarithmic sweep being concentrated at lower frequencies. For this reason, logarithmic frequency sweeps are preferred in practice to linear ones [6, 31]. Figures 2.1 and 2.2 depict sweeps of constant amplitude. However, it is usually necessary to reduce the amplitudes at low frequencies to avoid the aircraft deviating too far from the trim condition.

(a) Logarithmic frequency sweep   (b) Power spectral density
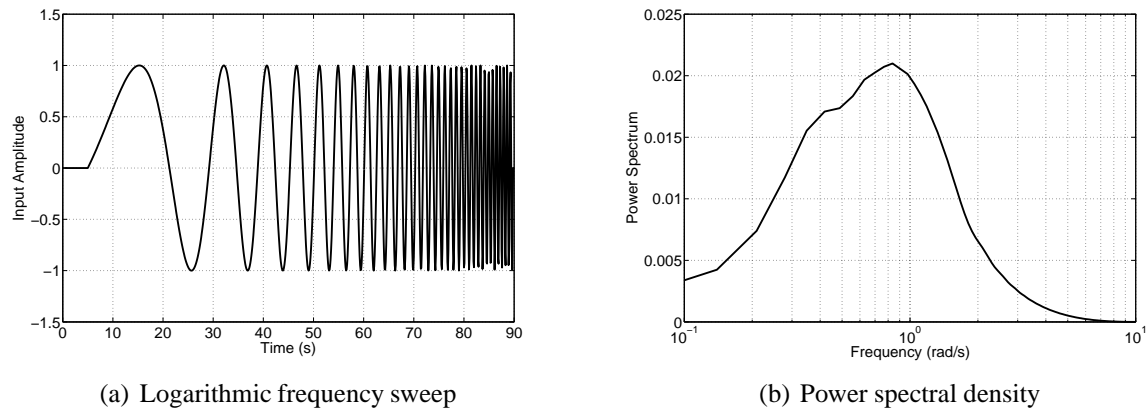
Figure 2.2: Logarithmic frequency sweep and associated power spectral density plot

Despite the complexity of the signal, pilots can be trained to apply frequency sweeps manually. In fact, the irregularities introduced by a human pilot enhance the information content of the data [6, 31]. Alternatively, the sweep can be computer-generated, based on Equations (2.2.1) to (2.2.3). To increase the variation in each input and, thus, the spectral richness of the data, band-limited white noise can be added to the computer generated sweeps. The computer-generated approach was reported by Lisoski and Tischler for flight tests on the AeroVironment Pathfinder solar-powered UAV [70].

The main advantages of frequency sweeps is that they excite a wide band of frequencies and their application requires little *a priori* knowledge of the aircraft dynamics. However, each sweep takes a relatively long time to implement - up to 90 seconds [6, 31]. They could also cause the inadvertent excitation of a structural resonance frequency, which would be a safety concern. Frequency sweeps are chiefly used for rotorcraft identification and structural mode identification, as the dynamics of interest in these applications cover a relatively wide frequency range. They are used less often for fixed-wing, rigid-body dynamics. Further, for miniature UAVs it has been found that, because the vehicle response is rapid (as a result of low mass and inertias), it is often difficult to perform frequency sweeps satisfactorily as the aircraft will quickly depart from trim [48].

2.3 Design by Statistical Analysis

A second approach to the input design problem is to find an input which maximises the information content of the data. Consider a dynamic system characterised by the following state

space model,

$$\dot{\mathbf{x}}(t) = \mathbf{A}\mathbf{x}(t) + \mathbf{B}\mathbf{u}(t), \ \mathbf{x}(0) = \mathbf{x}_0 \tag{2.3.1}$$

$$\mathbf{y}(t) = \mathbf{C}\mathbf{x}(t) + \mathbf{D}\mathbf{u}(t) \tag{2.3.2}$$

In the above expressions, $\mathbf{x}$ is a vector containing the aircraft states, $\mathbf{x}_0$ are their initial values, $\mathbf{y}$ is a vector of aircraft output variables and $\mathbf{u}$ is a vector of input variables. The system matrices $\mathbf{A}$, $\mathbf{B}$, $\mathbf{C}$ and $\mathbf{D}$ contain the stability and control derivatives, which are grouped together in a parameter vector denoted by $\boldsymbol{\theta}$. The elements of $\mathbf{y}$ are measured at N discrete points in time,

$$\mathbf{z}(i) = \mathbf{y}(i) + \mathbf{v}(i) \quad i = 1, 2, \dots, N \tag{2.3.3}$$

where $\mathbf{z}$ is the measurement vector containing measured values of the elements of $\mathbf{y}$ and $\mathbf{v}$ is a vector of noise corrupting the measurements of $\mathbf{y}$. The elements of $\mathbf{v}$ are assumed to be independent and have a Gaussian distribution with zero mean and covariance $\mathbf{R}$.

A measure of data information content is the Fisher information matrix, which for maximum likelihood estimation problems is defined as the second gradient of the cost function J with respect to the unknown parameters in $\boldsymbol{\theta}$. The maximum likelihood cost function can be expressed as,

$$J(\boldsymbol{\theta}) = \frac{1}{2} \sum_{i=1}^{N} [\mathbf{z}(i) - \hat{\mathbf{y}}(i)]^T \hat{\mathbf{R}}^{-1} [\mathbf{z}(i) - \hat{\mathbf{y}}(i)] \tag{2.3.4}$$

where $\hat{\mathbf{y}}$ is a prediction of $\mathbf{y}$ based on current estimates of the elements of $\boldsymbol{\theta}$ and $\hat{\mathbf{R}}$ is an estimate of the noise covariance calculated from,

$$\hat{\mathbf{R}} = \frac{1}{N} \sum_{i=1}^{N} [\mathbf{z}(i) - \hat{\mathbf{y}}(i)][\mathbf{z}(i) - \hat{\mathbf{y}}(i)]^T \tag{2.3.5}$$

By differentiating Equation (2.3.4) twice with respect to $\boldsymbol{\theta}$ the Fisher information matrix can therefore be found from,

$$\mathbf{M} = \frac{\partial^2 J}{\partial \boldsymbol{\theta} \partial \boldsymbol{\theta}^T} = \sum_{i=1}^{N} \left[\frac{\partial \hat{\mathbf{y}}(i)}{\partial \boldsymbol{\theta}} \right]^T \hat{\mathbf{R}}^{-1} \left[\frac{\partial \hat{\mathbf{y}}(i)}{\partial \boldsymbol{\theta}} \right] - \sum_{i=1}^{N} \left[\frac{\partial^2 \hat{\mathbf{y}}(i)}{\partial \boldsymbol{\theta} \partial \boldsymbol{\theta}^T} \right]^T \hat{\mathbf{R}}^{-1} [\mathbf{z}(i) - \hat{\mathbf{y}}(i)] \tag{2.3.6}$$

The determination of the second gradient of $\hat{\mathbf{y}}$ with respect to $\boldsymbol{\theta}$ is a complex process. However, it is observed that the term $\mathbf{z}(i) - \hat{\mathbf{y}}(i)$, known as the residual, will become smaller the closer the parameter estimates are to their true values. Therefore, the information matrix can be approximated as,

$$\mathbf{M} \approx \sum_{i=1}^{N} \left[\frac{\partial \hat{\mathbf{y}}(i)}{\partial \boldsymbol{\theta}} \right]^T \hat{\mathbf{R}}^{-1} \left[\frac{\partial \hat{\mathbf{y}}(i)}{\partial \boldsymbol{\theta}} \right] \tag{2.3.7}$$

The information matrix is an important factor in determining the statistical accuracy of maximum likelihood parameter estimates and is discussed in more detail in Chapter 5.

The partial derivatives of the output vector $\mathbf{y}$ with respect to the parameter vector $\boldsymbol{\theta}$ are termed the output sensitivities. For the system given by Equations (2.3.1) to (2.3.3), the sensitivities with respect to the jth element of $\boldsymbol{\theta}$ can be found from,

$$\frac{d}{dt} \left(\frac{\partial \mathbf{x}}{\partial \theta_j} \right) = \mathbf{A} \frac{\partial \mathbf{x}}{\partial \theta_j} + \frac{\partial \mathbf{A}}{\partial \theta_j} \mathbf{x} + \frac{\partial \mathbf{B}}{\partial \theta_j} \mathbf{u}, \ \frac{\partial \mathbf{x}(0)}{\partial \theta_j} = 0 \tag{2.3.8}$$

$$\frac{\partial \mathbf{y}}{\partial \theta_j} = \mathbf{C} \frac{\partial \mathbf{x}}{\partial \theta_j} + \frac{\partial \mathbf{C}}{\partial \theta_j} \mathbf{x} + \frac{\partial \mathbf{D}}{\partial \theta_j} \mathbf{u}, \ j = 1, 2, \dots, n_\theta \tag{2.3.9}$$

where n_θ denotes the number of parameters in $\boldsymbol{\theta}$. The goal of the parameter estimation process is to determine values for the elements in $\boldsymbol{\theta}$ which minimise the cost function J. However, if *a priori* estimates of the stability and control derivatives are available from, for example, theoretical analysis, wind tunnel experiments or previous flight tests, then these values can be inserted into Equations (2.3.8) and (2.3.9). The aim is then to find the input $\mathbf{u}$ which maximises the information content of the data, based on the information matrix $\mathbf{M}$.

A number of criteria can be used to optimise the input $\mathbf{u}$, with some expressed in terms of the parameter error covariance matrix, denoted $\mathbf{P}$. The parameter covariance matrix is also used as a statistical measure of the suitability of parameter estimates. For maximum likelihood estimation, the parameter covariance matrix converges on the inverse of the information matrix as the number of data points N increases i.e.,

$$\mathbf{P} \to \mathbf{M}^{-1} \text{ as } N \to \infty$$

As data tends to be recorded from flight tests at high rates, N is generally large for aircraft estimation problems. Therefore, the inverse of the Fisher information matrix is often used as an approximation of the parameter covariance,

$$\mathbf{P} \approx \mathbf{M}^{-1} \approx \left\{ \sum_{i=1}^{N} \left[\frac{\partial \mathbf{y}(i)}{\partial \boldsymbol{\theta}} \right]^{T} \mathbf{R}^{-1} \left[\frac{\partial \mathbf{y}(i)}{\partial \boldsymbol{\theta}} \right] \right\}^{-1} \tag{2.3.10}$$

The criteria used to optimise $\mathbf{u}$ include minimisation of the determinant of $\mathbf{P}$, equivalent to the maximisation of the determinant of $\mathbf{M}$,

$$\min_{\mathbf{u}(t)} \left\{ \det(\mathbf{P}) \right\} \Rightarrow \mathbf{u}_{\text{opt}}(t) \tag{2.3.11}$$

or

$$\max_{\mathbf{u}(t)} \left\{ \det(\mathbf{M}) \right\} \Rightarrow \mathbf{u}_{\text{opt}}(t) \tag{2.3.12}$$

Other approaches used are minimisation of the sum of the diagonal elements of $\mathbf{P}$ or, equivalently, maximisation of the trace of $\mathbf{M}$,

$$\min_{\mathbf{u}(t)} \left\{ \text{tr}(\mathbf{P}) \right\} \Rightarrow \mathbf{u}_{\text{opt}}(t) \tag{2.3.13}$$

or

$$\max_{\mathbf{u}(t)} \left\{ \text{tr}(\mathbf{M}) \right\} \Rightarrow \mathbf{u}_{\text{opt}}(t) \tag{2.3.14}$$

where "tr" denotes the trace of the matrix. Alternatively, the product of the diagonal elements of $\mathbf{P}$ can be minimised,

$$\min_{\mathbf{u}(t)} \left\{ \prod_{i} P_{ii} \right\} \Rightarrow \mathbf{u}_{\text{opt}}(t) \tag{2.3.15}$$

Whatever optimisation criterion is selected, the procedure leads to continuous, smoothly varying harmonic signals for the inputs. If the dynamics of interest are linear, constraints may have to be incorporated into the optimisation process so that the resulting input does not cause

the aircraft to diverge rapidly from the trim condition [97, 31]. This can be implemented by constraining the energy of the input signal,

$$\int_0^T \mathbf{u}(t)^T \mathbf{u}(t) dt \leq E \tag{2.3.16}$$

where E is the selected input energy. To ensure that the characteristics of the signal meet the design requirements, these inputs have to be implemented by a computer, rather than the pilot.

The advantage of designing control surface inputs using the statistical analysis outlined above is that it is rigorous and produces signals with a sound theoretical basis. However, the procedure is complex and involved. It is also dependent on good *a priori* knowledge of the aircraft dynamics. While this information is likely to be available for aircraft with conventional airframes, as mentioned in Section 1.1, *a priori* knowledge may be limited for UAVs and models of the aircraft dynamics which have been generated through theoretical methods can be unreliable for certain categories of unmanned aircraft.

2.4 Multistep Inputs

An engineering-based approach to input design is the use of multistep inputs. As the name suggests, these signals comprise a series of step inputs. There are two stages to the procedure. The first is to determine the frequency range in which the dynamics of interested are located. The second is to tailor the signal so that the identified frequency range is excited.

For the first stage of the design, frequency domain analysis, in the form of Bode plots, is used to provide an insight into which frequencies must be contained in the input signal to allow each of the derivatives to be identified. Again, it is assumed that *a priori* values of the aerodynamic derivatives are available. To illustrate the process, the Jetstream 31 aircraft shown in Figure 2.3, is utilised. At an airspeed of 160kts and an altitude of 8000ft, the aircraft's longitudinal dynamics predicted using semi-empirical analysis [98] are,

$$\begin{bmatrix} \dot{u} \\ \dot{w} \\ \dot{q} \\ \dot{\theta} \end{bmatrix} = \begin{bmatrix} -0.045 & 0.059 & 0.041 & -9.801 \\ -0.209 & -0.836 & 80.891 & -0.425 \\ 0.006 & -0.083 & -1.344 & 0.038 \\ 0 & 0 & 1 & 0 \end{bmatrix} \begin{bmatrix} u \\ w \\ q \\ \theta \end{bmatrix} + \begin{bmatrix} 0.006 \\ -0.156 \\ -0.141 \\ 0 \end{bmatrix} \eta \tag{2.4.1}$$

Focusing on the pitching moment equation,

$$\begin{aligned} \dot{q} &= m_u u + m_w w + m_q q + m_\theta \theta + m_\eta \eta \\ &= 0.006u - 0.083w - 1.344q + 0.038\theta - 0.141\eta \end{aligned} \tag{2.4.2}$$

the frequency response magnitudes of each term in the equation are plotted as functions of the input signal frequency. These are written as,

$$\left| \frac{\tilde{\dot{q}}(\omega)}{\tilde{\eta}(\omega)} \right|, \quad \left| \frac{m_u \tilde{u}(\omega)}{\tilde{\eta}(\omega)} \right|, \quad \left| \frac{m_w \tilde{w}(\omega)}{\tilde{\eta}(\omega)} \right|, \quad \left| \frac{m_q \tilde{q}(\omega)}{\tilde{\eta}(\omega)} \right|, \quad \left| \frac{m_\theta \tilde{\theta}(\omega)}{\tilde{\eta}(\omega)} \right|, \quad \left| \frac{m_\eta \tilde{\eta}(\omega)}{\tilde{\eta}(\omega)} \right|$$

where ˜ denotes the Fourier transform of a variable. The $\dot{q}$ component is called the inertial term, while the η component is known as the control term.

Figure 2.3: Cranfield University's Jetstream 31 aircraft

For a given frequency, if the magnitude of a term is high in comparison to the other components then it is an influential term in the equations of motion and is easily identifiable at that particular frequency. Conversely, if the magnitude of the component is small in comparison to the other terms, it is of little significance in the equations of motion and will be hard to identify at the chosen frequency. As a rule of thumb, a derivative is considered to be identifiable if its magnitude is at least 10% of that of the most influential term [97]. If the inertial term is small then only ratios of derivatives can be identified.

Figure 2.4 shows the Bode magnitude plot for the pitching moment terms in the frequency range of 0.01 to 100 rad/s. At frequencies below around 0.75 rad/s, the inertial term is less than 10% of the most influential component - the control term. Therefore, below this frequency, the derivatives can only be identified as ratios of each other. The least influential term is clearly m_θ, which has a peak magnitude at approximately 0.17 rad/s. The m_u term, while significant at low frequencies, is less influential at frequencies above 0.75 rad/s. Therefore, the values of m_θ and m_u can not be directly estimated. However, from flight dynamics theory, it is known that pitching moment is very nearly independent of velocity for subsonic flight and changes of pitching moment with respect to pitch attitude will only be significant when the aircraft is trimmed at high angles of attack [5], so for the Jetstream 31, accurate knowledge of m_u and m_θ is not considered to be crucial. For the remaining terms, the magnitudes are all greater than the 10% threshold in frequency regions above 0.75 rad/s so can be directly identified. The derivatives m_w, m_q and m_η are most identifiable in the frequency band around 3 rad/s. The natural frequency of the aircraft's short period mode is also located in this frequency region. Again, from theory, it is known that m_w, m_q and m_η are dominant in the short period mode dynamics, hence it is not surprising that these derivatives are most identifiable in this frequency band.

Having located the frequencies of interest, the shape and duration of the input is chosen. As the important frequency regions were determined based on *a priori* information, which may not be quite accurate, it is desirable to select an input which excites as wide a range of frequencies as possible. The simplest of the multistep inputs is a single pulse, depicted in Figure 2.5(a). The control surface is deflected and held at the desired position. After a given time Δt, the control is released and the aircraft is allowed to oscillate freely. There is a trade-off between the range of frequencies that can be excited and the amount of input energy concentrated at any particular frequency. This is illustrated in Figure 2.5(b) [34], which compares the energy spectra for three pulses of the same amplitude but varying duration. When Δt is selected as 0.4s, the energy is spread relatively evenly across the frequencies. However, the magnitude of the energy
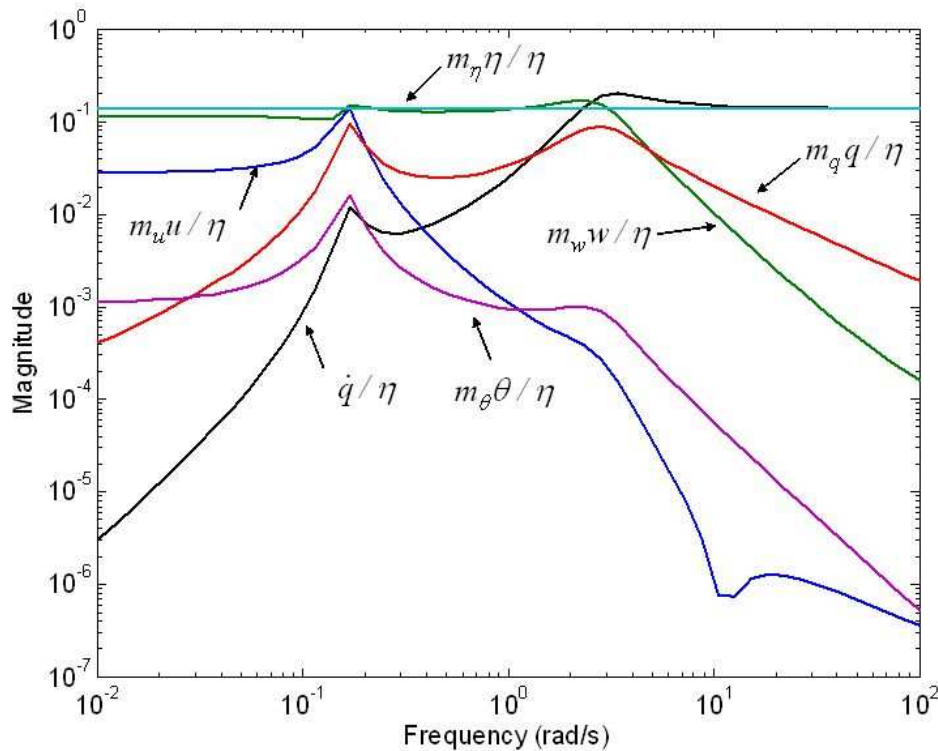
Figure 2.4: Bode plot of pitching moment frequency response magnitudes

is low and the input may not adequately excite the system dynamics to a level required for identification. As Δt is increased, the energy tends to be concentrated at lower frequencies and, while the magnitude of the energy increases, it decays more abruptly as the frequency rises. This inability to sufficiently excite high frequency dynamics, such as the short period or dutch roll mode, limits the use of pulses for system identification, as the high frequency modes are usually of primary interest. Instead, pulses are used to excite lower frequency dynamics, such as the phugoid or spiral modes [34, 5].

(a) Pulse input shape

(b) Energy spectra of pulses of varying duration
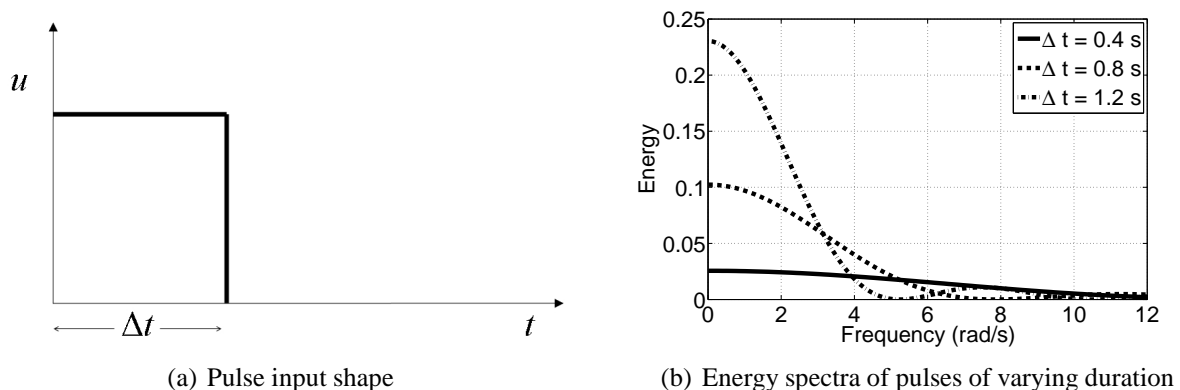
Figure 2.5: Pulse input and energy spectra

A wider range of frequencies can be excited by following a pulse input with a second pulse of the same amplitude and duration but in the opposite direction. This input is known as a doublet

and is depicted in Figure 2.6(a). As with the single pulse input, an increase in Δt will lead to the energy of the doublet being concentrated at lower frequencies (Figure 2.6(b)). Note that, as the doublet is symmetric about the starting position for the input, there is no energy at zero frequency.

(a) Doublet input shape

(b) Energy spectra of doublets of varying duration
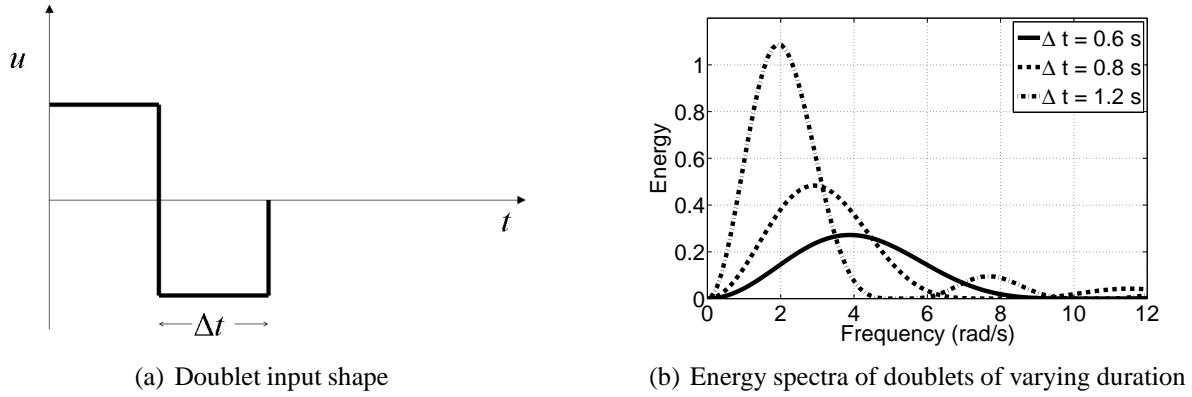
Figure 2.6: doublet input and energy spectra

Figure 2.7 shows the normalised energy spectrum for doublet inputs [34], which is the same regardless of the value of Δt. The frequencies ω_1 and ω_2 are the lower and upper limits respectively of the region in which the energy is at least half of the peak value. The values are $\omega_1 \approx 1.1$ and $\omega_2 \approx 3.6$, so the doublet has a bandwidth of approximately 1:3. The energy is at its maximum at a normalised frequency of around 2.3,

$$\omega \Delta t \approx 2.3 \qquad (2.4.3)$$

Therefore, (2.4.3) can be rearranged to provide a guideline for selecting the duration of a doublet,

$$\Delta t_{DBLT} \approx \frac{2.3}{\omega_n} \qquad (2.4.4)$$

where ω_n is the natural frequency of interest in rad/s. As the frequency band excited can be altered by simply varying Δt, the doublet is a commonly used input for system identification, particularly for the excitation of the lightly damped dutch roll mode [34]. However, a bandwidth of 1:3 may still not be sufficient, especially if there is low confidence in the accuracy of the *a priori* information, as may be the case for UAVs.

To solve this problem, a multistep input with a larger bandwidth, known as the 3-2-1-1, was developed by Koehler [97, 34]. The input shape is shown in Figure 2.8(a). As the name alludes to, a pulse is applied in one direction for three time units, a second pulse is then applied in the opposite direction for two time units, the control is reversed again for one time unit, and the input finishes with a second one time unit pulse in the opposite direction. Because of its shape, the 3-2-1-1 is also sometimes referred to as "the poor man's frequency sweep" [31].

The normalised energy spectrum for the 3-2-1-1 is plotted in Figure 2.8(b) [34]. As for the doublet, the frequency range $[\omega_1, \omega_2]$, in which the energy is at least half that of the peak value is shown. In comparison to the doublet, the bandwidth of the 3-2-1-1 is wider, being approximately 1:10. An appropriate Δt value for the 3-2-1-1 is chosen so that the natural frequency of the mode of interest lies at the centre or in the upper third of the spectrum [34]. If the centre point is chosen as the criterion then, from Figure 2.8(b), the time unit is calculated
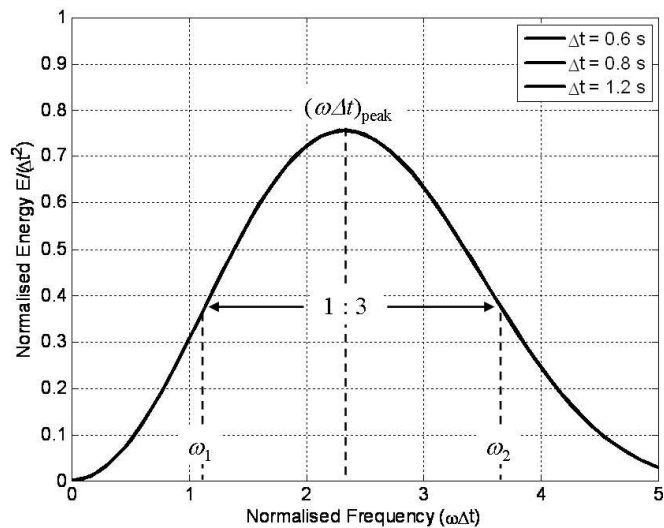
Figure 2.7: Doublet normalised energy spectra

(a) 3-2-1-1 input shape

(b) 3-2-1-1 normalised energy spectrum
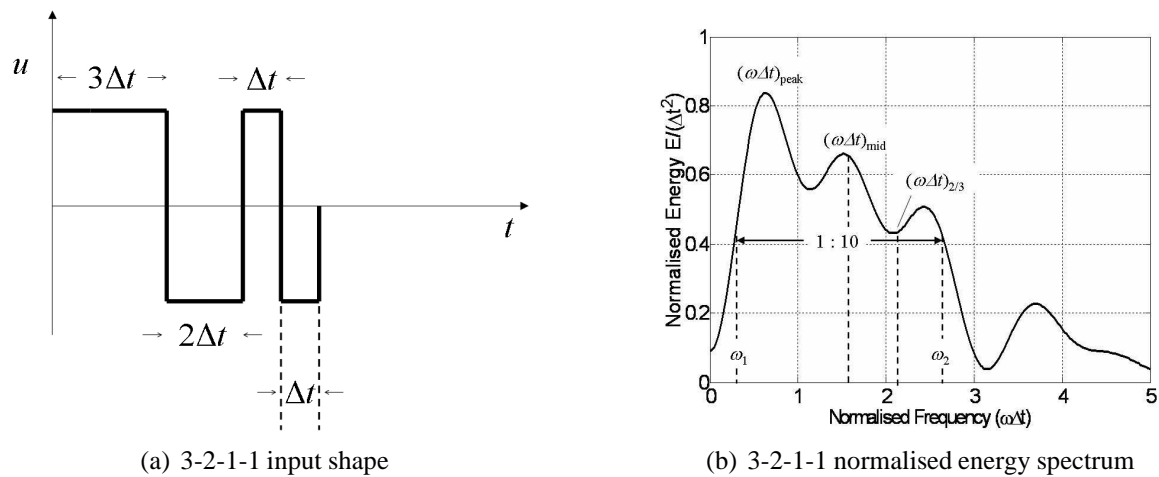
Figure 2.8: 3-2-1-1 input and energy spectra

as,

$$\Delta t_{3211} \approx \frac{1.6}{\omega_n} \tag{2.4.5}$$

Similarly, if it is decided that the natural frequency should lie in the upper third of the spectrum, then the input duration is found from,

$$\Delta t_{3211} \approx \frac{2.1}{\omega_n} \tag{2.4.6}$$

The 3-2-1-1 input is one of the most commonly used inputs for system identification due to the fact that it excites a wide range of frequencies. For the same reason, its performance is also less sensitive to inaccuracies in the *a priori* estimates of the natural frequencies used to select Δt_{3211}. A practical problem sometimes encountered with the 3-2-1-1, however, is that after the long duration "3" pulse at the start of the input, the aircraft may be far away from the initial trim condition. A solution is to use different amplitudes for each of the steps (smaller amplitude for the "3" pulse, larger amplitude for the "2" pulse etc.). Alternatively, the input can be reversed to become a 1-1-2-3. This leads to the higher frequency dynamics being excited first before the longer duration pulses are applied. Another approach is to remove the "3" step altogether, such as with a 1-1-2 input, although this leads to a reduction in the excited frequency range. Although slightly different numerical values appear in the numerators of Equations (2.4.4), (2.4.5) and (2.4.6), it has been found that, when designing multistep inputs of arbitrary shape, numerator coefficients of between 1.6 and 2.3 work well [34, 31].

Despite being somewhat heuristic in nature, the multistep approach to input design is more widely used than the design by statistical analysis, outlined in Section 2.3. This is mainly due to the simplicity of multistep inputs, which can be easily implemented manually by a pilot, and the short length of time required to apply them. As well as this, investigations have shown that parameter estimates obtained using 3-2-1-1s and doublets are comparable to, and in some cases better than, estimates achieved using statistically optimal inputs [97, 35].

2.5   Input Design for Dynamic Wind Tunnel Models

Based on the above discussion, it was decided that the multistep approach was the most appropriate for the dynamic wind tunnel experiments. Frequency sweeps were also attempted but it was difficult to keep the models close to the trim condition during the long duration input. When applying elevator sweeps for example, the models were prone to pitching up to high angles of attack, leading to a cross-coupling into rolling motion.

For the first stage of the multistep input design, *a priori* estimates of the Hawk and DEMON model derivatives were required. The 1/12 scale Hawk model has been analysed a number of times in the past at Cranfield University [80, 83] and, therefore, its dynamic properties have been well documented. In contrast, the 1/3 scale DEMON model was built specifically for the current research so information on its dynamics were limited. Initial guesses at the DEMON model derivatives were calculated based on a simulation model of the full-sized aircraft [99, 100].

The *a priori* state space representation of the 1/12 scale Hawk longitudinal dynamics at a wind

tunnel speed of 30 m/s and a trim angle of attack of zero degrees is,

$$\begin{bmatrix} \dot{w} \\ \dot{q} \end{bmatrix} = \begin{bmatrix} 0 & 30 \\ -1.64 & -4.01 \end{bmatrix} \begin{bmatrix} w \\ q \end{bmatrix} + \begin{bmatrix} 0 \\ -2.61 \end{bmatrix} \eta \qquad (2.5.1)$$

The lateral-directional dynamics of the Hawk model for the same conditions were predicted to be,

$$\begin{bmatrix} \dot{v} \\ \dot{p} \\ \dot{r} \end{bmatrix} = \begin{bmatrix} 0 & 0 & -30 \\ -5.08 & -5.32 & 2.75 \\ 1.28 & -0.40 & -1.53 \end{bmatrix} \begin{bmatrix} v \\ p \\ r \end{bmatrix} + \begin{bmatrix} 0 & 0 \\ -3.43 & 0.63 \\ 0.14 & -0.67 \end{bmatrix} \begin{bmatrix} \xi \\ \zeta \end{bmatrix} \qquad (2.5.2)$$

The numerical values in Equations (2.5.1) and (2.5.2) were obtained from semi-empirical analysis by Malik [80].

For the same trim conditions, the *a priori* estimates of the DEMON dynamics were calculated as,

$$\begin{bmatrix} \dot{w} \\ \dot{q} \end{bmatrix} = \begin{bmatrix} 0 & 30 \\ -9.022 & -8.186 \end{bmatrix} \begin{bmatrix} w \\ q \end{bmatrix} + \begin{bmatrix} 0 \\ -5.029 \end{bmatrix} \eta \qquad (2.5.3)$$

$$\begin{bmatrix} \dot{v} \\ \dot{p} \\ \dot{r} \end{bmatrix} = \begin{bmatrix} 0 & 0 & -30 \\ -27.436 & -56.590 & 8.487 \\ 6.156 & -0.669 & -6.326 \end{bmatrix} \begin{bmatrix} v \\ p \\ r \end{bmatrix} + \begin{bmatrix} 0 & 0 \\ -9.582 & 1.546 \\ -0.303 & -2.283 \end{bmatrix} \begin{bmatrix} \xi \\ \zeta \end{bmatrix} \qquad (2.5.4)$$

Using Equations (2.5.1) and (2.5.2), Bode magnitude plots for the pitch, roll and yawing moment derivatives were constructed. These are shown in Figures 2.9, 2.10 and 2.11 respectively. For the rolling and yawing moment plots, Figure (a) indicates the identifiability of the derivatives from an aileron input, while Figure (b) shows a similar plot for rudder inputs. It is obvious that, in general, the rolling moment derivatives will be more easily identified by applying an aileron input and the yawing moment dynamics are best excited with a rudder input. However, Figures 2.10 and 2.11 give an indication of which control surface input is better at exciting the cross-coupling dynamics.

From Figure 2.9, it can be seen that the pitching moment derivatives are most identifiable in the frequency region around 6-10 rad/s. For the rolling moment derivatives, the frequency region of interest is approximately 5-9 rad/s. However, in Figure 2.10(a), the magnitude of l_r is lower than that of the other derivatives and close to the 10% threshold introduced in Section 2.4, therefore it may be difficult to identify l_r from an aileron input. In Figure 2.10(b) the magnitude of l_r in comparison to the more significant terms is higher so a more reliable estimate of this derivative is likely to be obtained by applying a rudder excitation. Figure 2.10(b) also indicates that the control derivative l_ζ is likely to be unidentifiable in the 5-9 rad/s range, but the term becomes more significant at higher frequencies. However, in Equation (2.5.2), the estimate of l_ζ (0.63) is around an order of magnitude less than the values of the other rolling moment derivatives. Hence, the *a priori* information indicates l_ζ to be a relatively insignificant parameter. As with the rolling moment derivatives, the yawing moment terms peak in the frequency band of 5-9 rad/s. Figure 2.11 also indicates that both a rudder and an aileron input could be used to obtain a reliable estimate of the cross-coupling derivative n_p.

Similar analysis was carried out for the DEMON using Equations (2.5.3) and (2.5.4). The Bode magnitude plots for the pitching, rolling and yawing moment derivatives are shown in Figures 2.12, 2.13 and 2.14 respectively. The frequency band of interest in which the pitching moment derivatives are most identifiable, as determined from Figure 2.12, is around 12-20
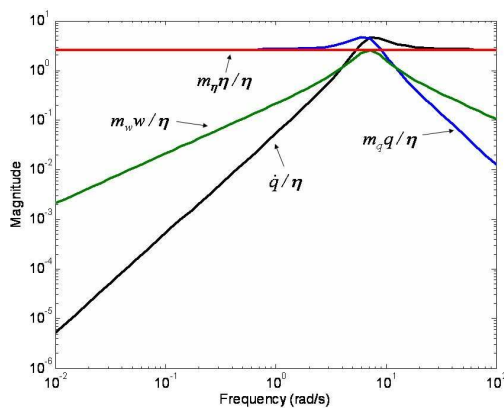
Figure 2.9: Bode plots of Hawk pitching moment
frequency response magnitudes
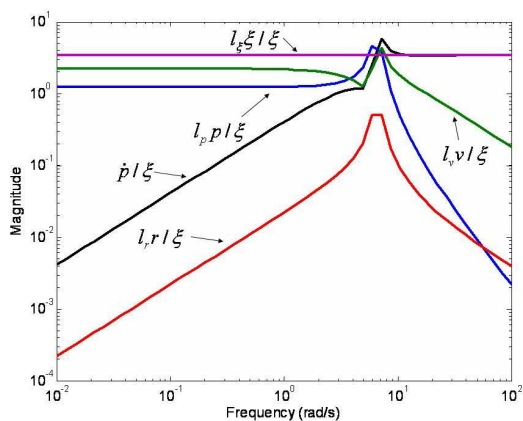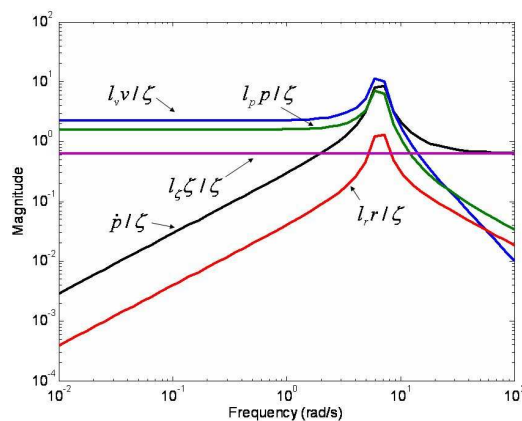
(a) Aileron input

(b) Rudder input

Figure 2.10: Bode plots of Hawk rolling moment
frequency response magnitudes
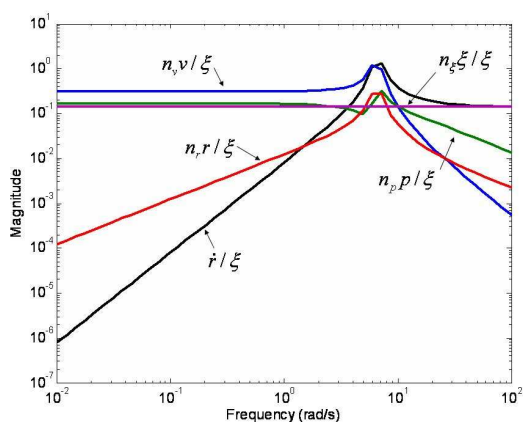
(a) Aileron input
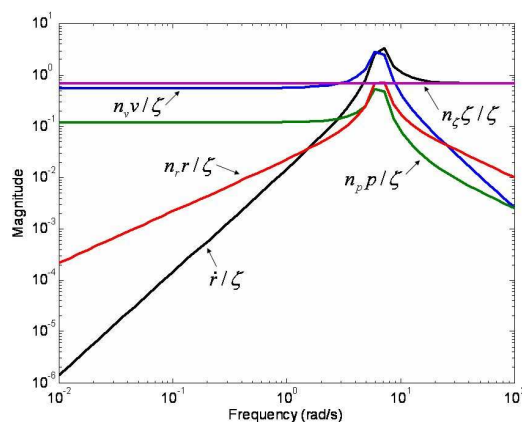
(b) Rudder input

Figure 2.11: Bode plots of Hawk yawing moment
frequency response magnitudes

rad/s. For the rolling moment parameters, Figure 2.13(a) shows that l_p and l_ξ are dominant across the whole frequency spectrum and only at a frequencies greater than 5 rad/s does the inertial term $\dot{p}$ exceed the 10% guideline for identifiability. As mentioned in section 2.4, if the inertial component is less than 10% of the most influential term, then only ratios of derivatives can be determined. The derivative l_r does not pass the 10% threshold at any frequency and so cannot be estimated directly from an aileron input. The lateral stability parameter l_v would also appear to be unidentifiable across much of the frequency spectrum, although its magnitude is greater than the 10% rule of thumb in the region around 8-16 rad/s. Figure 2.13(b) shows that a rudder input is more suitable for identifying l_v. The cross-coupling term l_r is also likely to be identifiable in the range of 10-18 rad/s using a rudder excitation. However, in this same frequency band, it is unlikely that the control derivative l_ζ can be accurately estimated and a rudder input of a higher frequency (≥ 20 rad/s) is required. Figure 2.14(b) also indicates that, in general, the yawing moment derivatives are identifiable in the range 10-18 rad/s. However, the cross-coupling term n_p is insignificant in this frequency band and Figure 2.14(a) suggests that an aileron input is better suited than a rudder excitation for identifying this term.
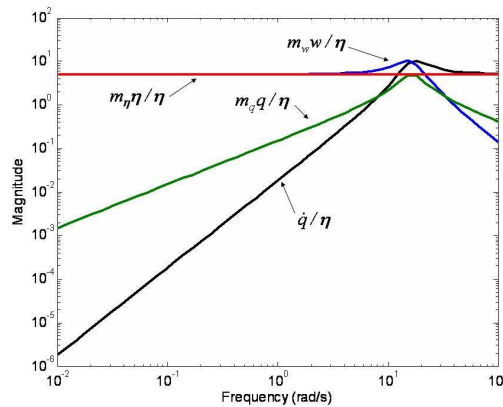
Figure 2.12: Bode plots of DEMON pitching moment
frequency response magnitudes

(a) Aileron input

(b) Rudder input
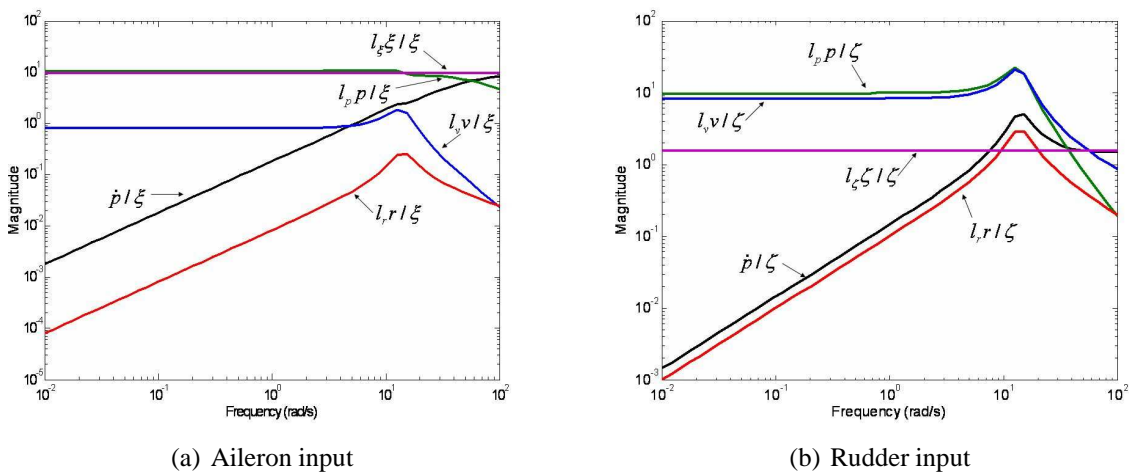
Figure 2.13: Bode plots of DEMON rolling moment
frequency response magnitudes

Using knowledge of the frequency regions identified from the Bode analysis, the pulse width

(a) Aileron input

(b) Rudder input
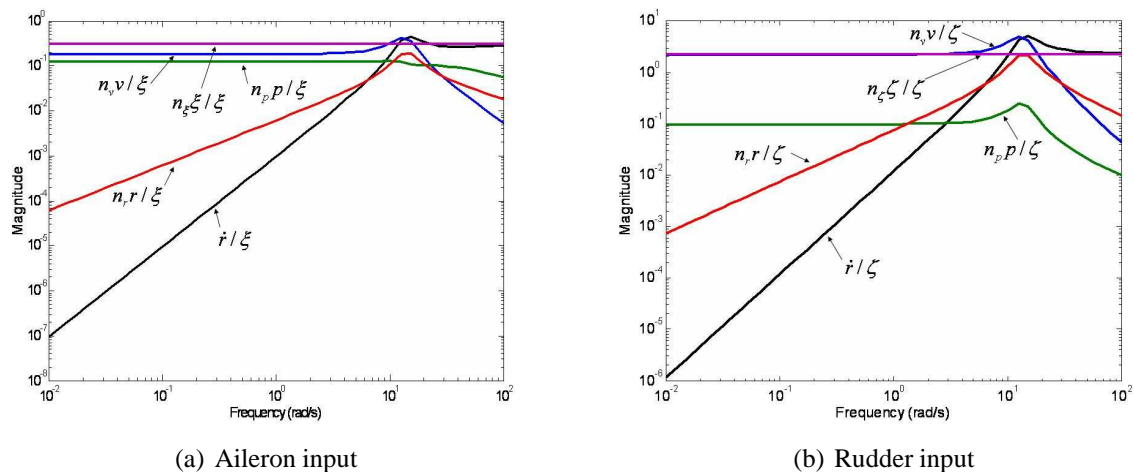
Figure 2.14: Bode plots of DEMON yawing moment
frequency response magnitudes

of the inputs were then selected. From Section 2.4, the rule of thumb used for the design of an input of arbitrary shape was,

$$\Delta t \approx \frac{2.3}{\omega} \qquad (2.5.5)$$

where ω is the frequency of interest in rad/s. For the Hawk model, the pulse width for the elevator and rudder inputs was chosen as 0.3s, which corresponds to $\omega \approx 8$ rad/s. For practical reasons, the Δt value for the ailerons was chosen as 0.15s. The Hawk model was observed as having a rapid roll response in previous experiments due to its low roll inertia [80, 83], so the aileron pulse width was reduced to ensure that the model did not reach the ± 30 degree limits permitted by the rig. For the DEMON model, the Δt value for all three control surfaces was selected as 0.2s, corresponding to $\omega \approx 12$ rad/s. The amplitude of the inputs were chosen so that the model dynamics were sufficiently excited, while at the same time making certain that the models motion could be described by small perturbations about the initial trim condition.

A number of input shapes were tested: doublet, 3-2-1-1, 1-1-2-3 and 1-1-2. An observation from the experiments with the Hawk was that when applying 3-2-1-1 inputs to the elevator, the "3" step was initially causing the model to pitch up to high angles of attack, leading to a cross-coupling into rolling motion similar to that encountered when trying frequency sweep inputs. To successfully apply the 3-2-1-1 so that only longitudinal motion was excited, the amplitude of the pulses had to be reduced. A similar scenario was encountered when applying 1-1-2-3 inputs. Not surprisingly, when using the 1-1-2 input instead, it was found that relatively larger amplitude inputs could be applied without the model undergoing undesirable lateral-directional motion.

It is clear that the required values of Δt were very small and it would have been difficult to accurately apply the required inputs manually. The frequency range in which a human pilot operates is generally around 0.1-10 rad/s [31]. Therefore, to excite higher frequency dynamics, computer generated inputs are required. This approach was used when testing both the Hawk and DEMON models. When computer generated inputs are employed, the upper limit on the frequencies that can be excited is determined by the dynamics of the control surface actuator. When performing the Bode analysis for the DEMON model, the frequency regions of interest were converging on the model's actuator natural frequency (see Chapter 3). In situations for

which the vehicle and actuator dynamics are located at similar frequencies, it will be difficult to properly excite the aircraft dynamics without the actuator reaching its rate limits. Hence, for miniature UAVs, there is a potential for the system identification process to be hampered by the performance of the actuators, leading to less reliable estimates of the stability and control derivatives.

Chapter 3

Sensors and Instrumentation

3.1 Introduction

The decision of which sensors to equip the aircraft with is obviously dependent on the motion variables that have to be measured. The minimum set of variables typically required for system identification is as follows:

- Linear accelerations along x, y and z body axes, denoted a_x, a_y and a_z respectively.

- Roll, pitch and yaw angular rates, denoted p, q and r respectively.

- Roll, pitch and yaw attitude angles, denoted ϕ, θ and ψ respectively.

- Air data: angle of attack α, angle of sideslip β and airspeed V.

- Deflection of aerodynamic control surfaces.

Engine parameters, such as thrust and RPM, may be of interest as knowledge of these properties allows the forces and moments due to propulsion to be separated from aerodynamic effects. Usually engine parameters are determined from manufacturer specifications.

For some parameter estimation methods, the aerodynamic moment coefficients will have to be derived from the measurements and, in this case, angular accelerations $\dot{p}$, $\dot{q}$ and $\dot{r}$ are needed. However, due to a lack of reliable angular acceleration sensors, $\dot{p}$, $\dot{q}$ and $\dot{r}$ are usually obtained through numerical differentiation. This process is discussed in detail in Chapter 4.

Other variables which could be required for the analysis include altitude, Mach number, dynamic pressure, ground speed, geodetic positions and pilot commands. The measurement of the most crucial motion variables listed above is discussed in the following sections.

3.2 Inertial Sensors

Measurements of linear accelerations are provided by accelerometers, while angular rates are sensed by rate gyroscopes. Strictly speaking, accelerometers measure specific force rather than acceleration [101, 102]. For example, if an accelerometer is housed in an aircraft that is sitting stationary on the ground and the sensor's measurement axis is pointing vertically down, it will

provide a reading of approximately -9.81 m/s^2 or -1g (i.e. acting in the upwards direction). This is a measure of specific force of the ground acting on the aircraft. Also, if the same aircraft were in free fall, the vehicle would be accelerating at approximately 9.81 m/s^2 but the sensor would give a reading of zero. In other words, accelerometers provide a measure of the total specific force acting on the aircraft minus that due to gravity [6]. As body axes acceleration and angular rates are normally required along/about three axes, a cluster of accelerometers and gyros are usually packaged together orthogonally, along with the associated electronics, in a system known as an inertial measurement unit (IMU), illustrated in Figure 3.1.
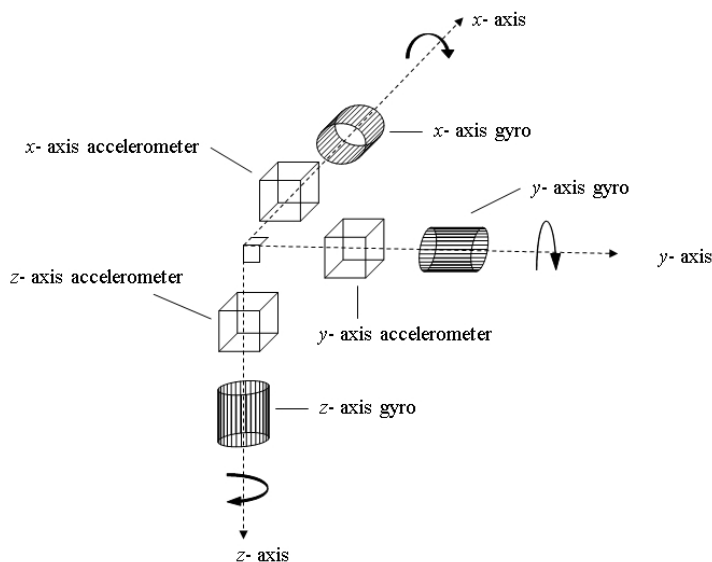
Figure 3.1: Illustration of an orthogonal cluster of sensors
contained in an IMU

The evolution of inertial sensors for aircraft applications has mainly been driven by their use for guidance, navigation and control purposes and various types of accelerometers and gyros have been developed [101, 102, 103]. For accelerometers, the principle on which the sensor operates is, in general, the same for each type of device. The accelerometer contains a proof mass which is tethered to the case of the sensor using springs, for the example of a mechanical accelerometer. When the accelerometer experiences an external force, the inertia of the proof mass will resist any movement of the mass relative to inertial space. However, the mass will be displaced relative to the sensor casing. This displacement will be proportional to the specific force experienced by the accelerometer and therefore, by measuring the displacement, a means of measuring the specific force exists. This is an example of an open-loop accelerometer. An alternative way of sensing specific force is to replace the springs with electromagnetic coils, which produce a force to return the proof mass to its null position whenever an acceleration is sensed. The magnitude of the electric current required to return the proof mass to its zero position is proportional to the applied specific force and thus provides the mechanism for measuring the specific force. This type of sensors is termed a closed-loop accelerometer. For rate gyros, a number of different approaches for sensing angular rate have been proposed. The most common are mechanical, spinning wheel gyros which are based on the principle of precession, and optical gyros, such as ring laser gyros (RLGs) or fibre optic gyros (FOGs), which measure angular rates using the Sagnac effect [101, 102, 103].

In the field of inertial sensor technology, the main aim in the past has been to drive forward the accuracy and performance of the devices. However, over the last two decades, there has been a

shift in focus to meeting current levels of performance but at a reduced cost and size [104, 105], and a major advancement has been the rapid growth of inertial sensors based on micro electromechanical systems (MEMS) technology. This has been motivated mainly by their use in automotive applications [106, 101], where bulk production has driven down cost. Their use for inertial navigation purposes has also been widely reported [101, 107, 108]. The main advantages of MEMS sensors are their small size, light weight, low cost and low power consumption. On the down side, they are, at present, not as accurate as more mature sensor technologies and exhibit noisier outputs, as well as more significant bias and drift characteristics. However, it has been reported that between 1991 and 1998 the performance of MEMS sensors (based on angle random walk) improved by a factor of 10 every two years [106]. While this progress has slowed in recent years, it is predicted that their performance will continue to improve in the future [104].

With the current application of UAV system identification in mind, inertial sensors based on MEMS technology are an attractive option and, in fact, for miniature UAVs or scale wind tunnel models they are the only sensor technology small and light enough to be housed within the airframe. However, their relatively noisy outputs means that obtaining reliable parameter estimates is likely to be more mathematically involved and care must be taken during the data compatibility check to ensure that bias and scale factor errors are removed from the data prior to the parameter estimation process. These issues are investigated in Chapters 4 and 9 respectively.

3.3 Attitude Determination

While dedicated attitude sensors have been used in the past, it has become common practice to determine the attitude angles through a process based on the integration of rate gyro data. The attitude angles are related to the angular rates by the following set of differential equations, known as the Euler equations,

$$\dot{\phi} = p + (q \sin \phi + r \cos \phi) \tan \theta \tag{3.3.1}$$

$$\dot{\theta} = q \cos \phi - r \sin \phi \tag{3.3.2}$$

$$\dot{\psi} = (q \sin \phi + r \cos \phi) \sec \theta \tag{3.3.3}$$

In theory, given initial values for the attitude angles, equations (3.3.1) to (3.3.3) could be integrated in time to generate time histories for ϕ, θ and ψ. However, if, for example, even one of the gyros contains a small constant error, the integration of this error will lead to an attitude error that will grow in time, an error known as drift. Also, because equations (3.3.1) to (3.3.3) are coupled, an error within the gyro measurements for one axis will translated into drift errors in all three attitude angles. The problem is further complicated in practice, as the errors tend to be stochastic rather than constant.

A standard technique to overcome the drift problem is to generate a second estimate of the aircraft attitude independently from the gyro data which does not drift with time. This second evaluation of the attitudes can then be combined with that derived from the gyro measurements to produce a more reliable estimate of ϕ, θ and ψ. This is often termed sensor fusion and is usually performed using some form of Kalman filter, which produces a weighted mean of attitudes based on knowledge of the noise corrupting the two sources. When the system of equations under consideration are linear the Kalman filter is optimal in the least squares mean sense, yielding a minimum variance estimator [34, 101]. However, for a nonlinear system of

equations this is not the case and an optimal filter for nonlinear cases is often unrealisable. Hence, it is customary to adapt the Kalman filter for the linear case for use with nonlinear systems and accept that the performance of the filter will not be optimal. This is known as the extended Kalman filter (EKF).

The method for generating attitude independently of the gyro data is usually termed the aiding system and is most commonly realised using a combination of accelerometer and magnetometer measurements. The principle of this technique is that the accelerometers will provide information on the aircraft's roll and pitch angles from the expressions,

$$\phi = \tan^{-1} \frac{a_y}{a_z} \tag{3.3.4}$$

$$\theta = -\sin^{-1} \frac{a_x}{g} \tag{3.3.5}$$

Then magnetometer data can be used to determine the yaw angle, based on knowledge of the earth's magnetic field vector [109],

$$\psi = \tan^{-1} \left(\frac{H_y \cos\theta + H_z \sin\theta}{H_x \cos\phi + H_y \sin\theta \sin\phi - H_z \cos\theta \sin\phi} \right) \tag{3.3.6}$$

where H_x, H_y and H_z are the components of the earth's magnetic field measured along the x, y and z aircraft body axes respectively.

It should be noted that during the manoeuvres in which the aircraft is accelerating, an error will exist in the aiding system estimates of ϕ and θ, as the accelerometers are unable to distinguish between tilt and vehicle acceleration [103, 107].

Another approach to the aiding system, which has seen recent application, is the use of multiple GPS antennas placed at various locations on the airframe [108]. Differential GPS measurements can supply information on the orientation of each of the antennas relative to each other, hence allowing the attitude of the aircraft to be determined.

In order to resolve the attitudes, the Kalman filter requires a model of the bias error within the gyros. Two laboratory calibration techniques which are commonly used to construct gyro bias models are the Allan variance method and power spectral density (PSD) analysis [110, 111, 112]. These methods involve, respectively, plotting the square root of the variance and PSD of the gyro output when the sensor is stationary. Under such conditions, it can be assumed that the gyro output is purely due to noise. The various components of the noise are then distinguished by analysing the slopes of the plot. For example, angle random walk error, which is caused by the integration of white noise, is indicated to be present if the slope of the Allan variance plot is $-1/2$, or if the PSD has a gradient of 0 [110, 111, 112].

For most gyro types angle random walk is the dominant error source, in which case the bias can be accurately modelled as a band-limited white noise process with variance σ_b^2. However, MEMS gyros often exhibit a long-term bias instability which typically becomes dominant after a few hundred seconds [107]. This is best modelled as an exponentially correlated Gaussian random process,

$$\dot{b}(t) = -\frac{1}{\tau}b(t) + w(t) \tag{3.3.7}$$

where b is the bias, τ is the correlation time which dictates the growth of b and w is the driving process noise, with variance σ_w^2. In fact, the bias of high-precision gyros can be modelled using

equation (3.3.7) as well. However, the correlation time for these sensors tends to be of the order of 1-10 hours [35], rather than a few hundred seconds, which is the case for MEMS gyros.

Having defined the model for the gyro bias, the equations for the Kalman filter can then be formulated. Many different forms of the Kalman filter have been proposed for attitude determination [113, 114]. These have been used mainly in spacecraft applications where large attitude changes can occur in very short spaces of time, requiring very accurate, computationally efficient algorithms. However, for aircraft attitude determination, it is often reasonable to assume that the vehicle motion can be modelled as small deviations from an equilibrium or trim condition. This greatly simplifies the problem.

The simplest formulation that is used in practice is sometimes termed the minimal representation Kalman filter [108, 113]. The state vector for this method is defined as,

$$\mathbf{x} = \begin{bmatrix} \phi & \theta & \psi & b_p & b_q & b_r \end{bmatrix}^T \tag{3.3.8}$$

where b_p, b_q and b_r are the biases in the roll, pitch and yaw gyros respectively. A prediction of how these states vary with time is given by equation,

$$\dot{\tilde{\mathbf{x}}} = \mathbf{A}\hat{\mathbf{x}} + \mathbf{B}\mathbf{u} \tag{3.3.9}$$

where $\tilde{\ }$ denotes the prediction of $\mathbf{x}$ and $\hat{\ }$ indicates the state vector having been corrected using information from the aiding system. An expression for $\hat{\mathbf{x}}$ is given below in equation (3.3.13). The input vector $\mathbf{u}$ contains the gyro outputs i.e.

$$\mathbf{u} = \begin{bmatrix} p & q & r \end{bmatrix}^T \tag{3.3.10}$$

The state matrix $\mathbf{A}$ is given by

$$\mathbf{A} = \begin{bmatrix} 0 & 0 & 0 & 1 & \sin\phi\tan\theta & \cos\phi\tan\theta \\ 0 & 0 & 0 & 0 & \cos\phi & -\sin\phi \\ 0 & 0 & 0 & 0 & \sin\phi\sec\theta & \cos\phi\sec\theta \\ 0 & 0 & 0 & 0 & 0 & 0 \\ 0 & 0 & 0 & 0 & 0 & 0 \\ 0 & 0 & 0 & 0 & 0 & 0 \end{bmatrix} \tag{3.3.11}$$

while the input matrix $\mathbf{B}$ is,

$$\mathbf{B} = \begin{bmatrix} 1 & \sin\phi\tan\theta & \cos\phi\tan\theta \\ 0 & \cos\phi & -\sin\phi \\ 0 & \sin\phi\sec\theta & \cos\phi\sec\theta \\ 0 & 0 & 0 \\ 0 & 0 & 0 \\ 0 & 0 & 0 \end{bmatrix} \tag{3.3.12}$$

When a measurement of the attitude from the aiding system becomes available, the corrected state vector $\hat{x}$ can be found from,

$$\hat{\mathbf{x}} = \tilde{\mathbf{x}} + \mathbf{K}[\mathbf{z} - \tilde{\mathbf{y}}] \tag{3.3.13}$$

where $\mathbf{z}$ is the aiding system measurement vector, $\tilde{\mathbf{y}}$ is the predicted observation and $\mathbf{K}$ is the Kalman gain matrix. The aiding system measurement vector is given by,

$$\mathbf{z} = \begin{bmatrix} \phi_{as} & \theta_{as} & \psi_{as} \end{bmatrix} \tag{3.3.14}$$

where ϕ_{as}, θ_{as} and ψ_{as} are the attitude estimates from the aiding system, while the vector $\tilde{\mathbf{y}}$ is obtained from

$$\tilde{\mathbf{y}} = \mathbf{C}\tilde{\mathbf{x}} \tag{3.3.15}$$

where the matrix $\mathbf{C}$ is defined as

$$\mathbf{C} = \begin{bmatrix} 1 & 0 & 0 & 0 & 0 & 0 \\ 0 & 1 & 0 & 0 & 0 & 0 \\ 0 & 0 & 1 & 0 & 0 & 0 \end{bmatrix} \tag{3.3.16}$$

The values within the Kalman gain matrix are chosen based on knowledge of the noise present within the gyro measurements and those from the aiding system. If it can be assumed that the aircraft is not performing manoeuvres that involve large deviations from trim, then a steady-state gain can be used for $\mathbf{K}$. If, however, the aircraft attitude is varying rapidly and through large angles, then the time-varying $\mathbf{K}$, calculated at each time point, may be required. For the minimal representation Kalman filter formulation, it is assumed that a steady-state gain is sufficient. As well as for sensor fusion, the Kalman filter is used widely in aircraft parameter estimation. Therefore, the process of calculating an appropriate Kalman gain matrix (both steady-state and time varying) is presented in detail in Chapter 7.

The above formulation utilises the Euler representation of attitude defined by equations (3.3.1) to (3.3.3). The use of the Euler equations, though, has two drawbacks. Firstly, the presence of $\tan\theta$ in (3.3.1) and $\sec\theta$ in (3.3.3) leads to a singularity when the aircraft pitches to an angle of 90 degrees. However, this is only a disadvantage when the aircraft in question is highly manoeuvrable. The second drawback is that solving a set of differential equations is computationally intensive, especially if the attitude is required in real-time and at a high sampling rate. The solution to this it to instead use the quaternion representation of the attitude, which avoids the singularity at $\theta = 90$ deg and is computationally faster than the Euler angle formulation [101, 114, 102]. The quaternion is a 4-element parameter, which defines the attitude as a single rotation about a single axis whose orientation in space is define by a unit vector. It can be expressed as,

$$\mathbf{q} = \begin{bmatrix} q_0 \\ \mathbf{q}_v \end{bmatrix} \tag{3.3.17}$$

The scalar part of the quaternion, q_0, defines the magnitude of the rotation about the unit vector and is given by,

$$q_0 = \cos\frac{\Phi}{2} \tag{3.3.18}$$

where Φ is the angle of rotation. The vector part of the quaternion, $\mathbf{q}_v$ describes the orientation of the unit vector in space and can be expressed as,

$$\mathbf{q}_v = \mathbf{e}\sin\Phi = \begin{bmatrix} q_1 \\ q_2 \\ q_3 \end{bmatrix} \tag{3.3.19}$$

where $\mathbf{e}$ is the unit vector. The propagation of the quaternion in time is described by the equation,

$$\dot{\mathbf{q}} = \frac{1}{2}\Omega\mathbf{q} \tag{3.3.20}$$

where Ω contains the gyro outputs and is given by

$$\Omega = \begin{bmatrix} 0 & -p & -q & -r \\ p & 0 & r & -q \\ q & -r & 0 & p \\ r & q & -p & 0 \end{bmatrix} \tag{3.3.21}$$

The attitude angles ϕ, θ and ψ are related to the quaternion elements by,

$$\phi = \tan^{-1} \frac{2(q_2 q_3 + q_0 q_1)}{(q_0^2 - q_1^2 - q_2^2 + q_3^2)} \tag{3.3.22}$$

$$\theta = -\sin^{-1}[2(q_1 q_3 - q_0 q_2)] \tag{3.3.23}$$

$$\psi = \tan^{-1} \frac{2(q_1 q_2 + q_0 q_3)}{(q_0^2 + q_1^2 - q_2^2 - q_3^2)} \tag{3.3.24}$$

3.4   Air Data Measurements

Air data measurement is primarily concerned with gathering accurate information on airspeed, angle of attack and angle of sideslip but is also used to gather data on dynamic pressure and altitude. A traditional method of obtaining air data is through the use of a noseboom, which contains a pitot tube to measure total or stagnation pressure and static pressure tappings to measure static pressure. The pressures are recorded by transducers connected to the tappings. From these pressures, the dynamic pressure and airspeed can be calculated, while the altitude can be determined from knowledge of the static pressure. The flow angles can be measured using mechanical vanes, attached to the noseboom, that pivot with changes in the flow direction. The angles of attack and sideslip are then determined by measuring the rotation of the vanes with, for example, a potentiometer [115]. An alternative approach to measuring α and β is the use of five-hole probes, illustrated in Figure 3.2 [34]. From the differential pressure measurements, the flow angles are obtained as follows,

$$\alpha = \frac{P_{\alpha 1} - P_{\alpha 2}}{K_\alpha P_{dyn}} \tag{3.4.1}$$

$$\beta = \frac{P_{\beta 1} - P_{\beta 2}}{K_\beta P_{dyn}} \tag{3.4.2}$$

where K_α and K_β are sensitivity factors and P_{dyn} is the dynamic pressure (total pressure minus static pressure).

The use of a noseboom may be impractical if, for example, the aircraft has a nose-mounted propeller or if radar equipment is located in the nosecone [31, 34]. In this case, a non-intrusive approach to measuring air data is to use a flush air data system . This is similar in principle to the five-hole probe method but the pressure tapping are located on the aircraft's nosecone. There are also usually more than five pressure orifices - possibly up to 25 [116].

Gathering of air data is difficult in practice as the measurements are affected by local flow characteristics of the aircraft. For this reason, nosebooms tend to have lengths of 2.5 to 3 times the fuselage diameter in order to assume that the probe is in freestream flow [34]. Precise calibration of air data systems is also an involved process [115, 117], which can only be performed in
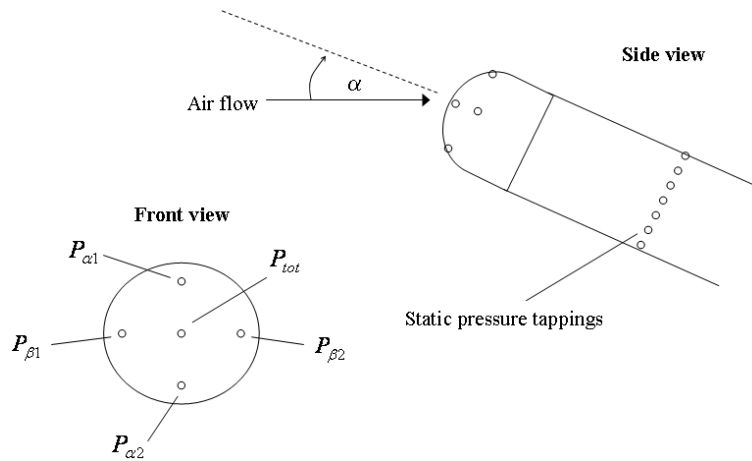
Figure 3.2: Illustration of a five-hole probe

the wind tunnel or flight test environment and is specific to each aircraft. One problem commonly encountered is that the pressure transducer, being too large to fit in the boom or probe, has to be located in the airframe away from the pressure tapping. Therefore, tubing is required to connect the pressure tapping to the associated transducer and the distance between the two introduces a time delay in the recording of the pressures [34].

The measurement of air data for UAVs is carried out in much the same manner as that for manned aircraft. The primary difference is the possible need for the air data system to be reduced in size, particularly for miniature UAVs. For this purpose, air data probes with diameters of the order of 1-2 mm have been developed [118]. Pressure transducers utilising MEMS technology have also been manufactured [119, 120] which are small enough to fit into the probes, although the performance of these sensors is not yet as high as that obtained with conventional pressure transducers. However, as the air data probes required for UAVs are generally much shorter in length, any tubing connecting tapping to transducers in the airframe will in turn be much shorter in length. Hence, the time delays in recording air data parameters, introduced by the distance between tappings and transducers, is likely to be smaller for UAVs.

3.5   Analogue-to-Digital Conversion Requirements

Before the analysis of the recorded data is carried out, the continuous-time, analogue signals from the sensors must be discretised using an analogue-to-digital (A/D) converter. Some guidelines for this process, when the final application of the measurements is aircraft system identification, are outlined here. Ideally, the raw analogue data should be available to the analyst performing the system identification process, allowing the analyst to discretise the data according to their own particular needs. However, in many practical cases, especially with off-the-shelf instrumentation units, the raw data is not available and the A/D conversion is done automatically by the sensor system. Whether the signals are digitised manually or automatically, some important characteristics to consider are the data sampling rate, anti-aliasing, sensor range and resolution.

Data is usually sampled at equally spaced time intervals Δt. The minimum theoretical data sampling rate is governed by the Nyquist-Shannon sampling theorem, which states that for

a continuous signal sampled at a rate of f_s, the maximum frequency that can be captured in the discrete signal is $f_s/2$ [121]. This is known as the Nyquist frequency f_N. Therefore, theoretically, the minimum sampling rate required is twice the maximum frequency of interest, denoted f_{max}. In reality, data must be sampled at a much higher rate in order to capture the significant aircraft dynamics and obtain reliable parameter estimates. A commonly used rule of thumb [31, 6] is,

$$f_s = 25f_{max} \tag{3.5.1}$$

As UAVs tend to have smaller masses and inertias than manned aircraft, their natural frequencies are higher. Therefore, it is clear from Equation (3.5.1) that UAVs will, in general, require higher sampling rates. This statement holds true for scale wind tunnel models as well, whose natural frequency is related to that of the full-sized aircraft by Froude scaling,

$$f_m = \frac{1}{\sqrt{\lambda}}f_a \tag{3.5.2}$$

where λ is the geometric scale factor. Therefore, for the 1/12 scale model of the Hawk, the required sampling frequency is approximately 3.5 times that needed for the full-sized aircraft. If there is doubt over the value of f_{max}, it is best to use a higher sampling frequency. Ideally, f_s should be the same for all measurements. If this is not the case then interpolation or data reduction can be performed once the digitised data becomes available.

Aliasing occurs when the analogue signal has frequency components higher than the Nyquist frequency. During the sampling process, these high frequencies are incorrectly associated with frequency components below f_N. To solve the problem, the continuous signal is low-pass filtered before it is discretised. The antialias filter removes the high frequency content, which could cause aliasing, from the signal. The low frequency components of interest will be only slightly modified by the filter. The resulting phase change is nearly linear with frequency, which leads to a small, constant time delay for all frequencies [31]. Identical antialias filters should be used on each signal so that the small time delay introduced on each measurement is the same. The break or cut-off frequency for the filters must be chosen so that the frequencies of interest are allowed to pass through unmodified while, at the same time, high frequency components which could cause aliasing are removed. A guideline for the choice of break frequency is [31, 6],

$$f_b = 5f_{max} = \frac{1}{5}f_s \tag{3.5.3}$$

As with sampling frequency, the relatively high natural frequencies of UAVs means that the break frequency of the antialias filters will need to be higher that those typically used for manned aircraft.

It should be noted that situations may arise in practice where the sensors used to measure data for system identification are designed for other purposes - installing a dedicated suite of instrumentation for system identification may be impractical for reasons of cost or because of limited space within the airframe. An example is obtaining inertial sensor data from an inertial navigation system (INS). These systems are designed to provide accurate navigation information over a long period of time and, therefore, the short term dynamics of the aircraft are not of primary concern. As a result, the sampling rate and break frequencies of the accelerometers and gyros may be set at levels lower than those described above and care must be taken to ensure that the instrumentation is able to meet the system identification requirements.

When the A/D conversion is performed, the resolution is the lower limit on the accuracy that can be achieved and is calculated from,

$$\text{resolution} = \frac{\text{range}}{2^N} \qquad (3.5.4)$$

where N is the bit binary word number used in the A/D conversion. To ensure adequate resolution in the digital signal, it is recommended that the A/D conversion use a 14-bit binary word [43, 31]. From Equation (3.5.4), it can be seen that for a given value of N, there is a trade-off between sensor range and resolution. The range should be chosen so that the dynamics of the aircraft can be recorded without the sensor saturating.

3.6   Instrumentation for Dynamic Wind Tunnel Facility

In the past, a drawback of emulating flight test-like experiments in the wind tunnel had been the lack of accurate inertial sensors that were small enough to fit within the aircraft model. To overcome this, potentiometers were used in previous work to measure the model's attitude about its pivot point and data for other motion variables was generated analytically using the attitude measurements and kinematic relationships. However, this lack of redundancy in the sensors meant that any errors in the output of the potentiometers would directly affect the values of other motion variables and, ultimately, the stability and control derivative estimates. The use of accelerometers and gyros for wind tunnel experiments was reported by Rajamurthy [90] but, because of their weight, they were only used to check the accuracy of potentiometer data and were removed from the model when the actual experiments were conducted. However, with the advances in MEMS accelerometers and gyros highlighted above, it was decided that an off-the-shelf IMU, small enough to be housed within the airframes of both the 1/12 scale Hawk and 1/3 scale DEMON models, would be used to record the motion of the models on the test rig. This allowed the suitability of such units for the dynamic wind tunnel experiments to be assessed.

The IMU is shown in Figure 3.3 and comprised a set of three MEMS accelerometers, three MEMS rate gyros and three solid state magnetometers, which were used to provide information on the linear accelerations, angular rates and attitude angles. The range of these sensors were ± 2 g, ± 150 deg/s and ± 2 Gauss respectively. The unit was physically very compact, with dimensions of $5.7 \times 4.5 \times 1.1$cm and a weight of 33 grams. Due to restricted space within the models, no other sensor systems, such as air data probes, were utilised. However, this was not considered a great disadvantage because, as pointed out in Appendix A, for the conditions at which the models were tested, it could be assumed that the angle of attack was equal to the pitch attitude and the angle of sideslip was the negative of the yaw attitude.

The highest frequencies of interest for the two models were not known precisely before the experiments but semi-empirical analysis predicted that the short period and dutch roll natural frequencies of the Hawk model were in the region of 1 Hz, while the corresponding natural frequencies of the DEMON model were closer to 2 Hz (note that some components of the rigid-body dynamics will actually be located above the natural frequencies of the modes). The IMU sampled data at a rate of 100 Hz, while the break frequency of the unit's antialiasing filters were set at 25 Hz. Considering the rules of thumb given in Equations (3.5.1) and (3.5.3), this meant that the system was suitable for recording data for f_{max} values up to around 4 to 5

Hz. As well as this, a 16 bit binary word was used in the A/D conversion. Hence, based on the discussion in Section 3.5, the chosen IMU was considered appropriate for the given application.

Control surface deflections were achieved using miniature electric servo-actuators (also shown in Figure 3.3), based on radio controlled aircraft technology. These were physically connected to the relevant control surfaces using standard model control linkages. Commands to the servo-actuators were transmitted from a computer "ground station" through a 2.4 GHz wireless network. The resultant motion recorded by the sensors was then sent back via the wireless network to the ground station. The use of the wireless network avoided the need to physically connect wires and cabling to the model or test rig, which could have been a source of aerodynamic interference.
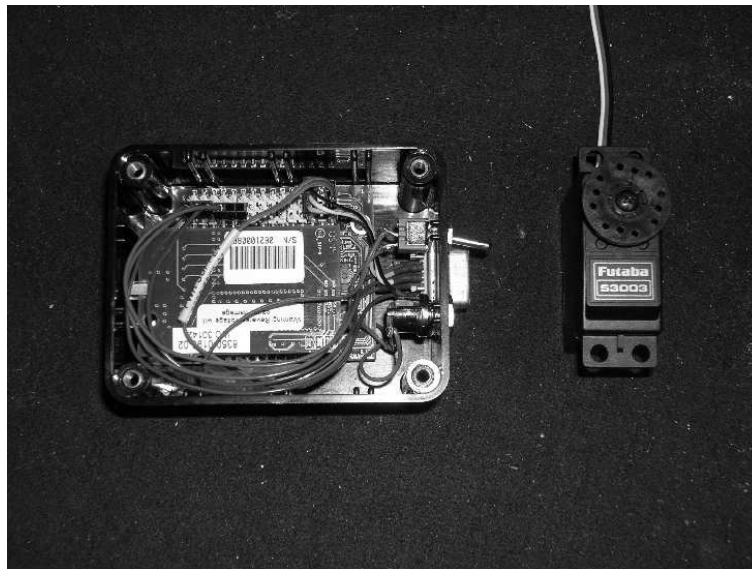
Figure 3.3: MEMS inertial measurement unit and
miniature servo-actuator

3.7   Determination of Control Surface Positions

When testing either of the scale models, it was impractical to measure the control surface deflections directly - it was mentioned in Section 1.2 that a similar problem has been found when performing system identification on miniature UAVs [48]. Therefore, the control surface deflections were inferred using knowledge of the commands transmitted from the ground station, a model of the actuator dynamics and a model of the dynamics of the linkages between the actuators and the control surfaces.

The control linkage between the actuators and each surface were represented by simple gains, while a mathematical model of the actuators was developed by carrying out bench tests on one of the actuators in isolation. A position command frequency sweep was applied to the actuator and its actual position was recorded. This is shown in Figure 3.4. The frequency sweep command begins at a frequency of 10 Hz and decreases to finish at 1 Hz. It can be seen that at the high initial frequencies, the actuator struggles to follow the changes in commanded position but, as the input frequency decreases, the match between commanded position and actual position improves. Ideally, such bench tests on actuators should be carried out under

representative loading conditions but, due to practical constraints, this was not possible during this research.

Using the actuator input and output information, parameter estimation was used to derive a second-order transfer to describe the actuator's response. The parameter estimation was performed in the frequency domain using the maximum likelihood, output error method. The mathematical details of this algorithm are given in Chapter 6. The identified transfer function for the actuator was,

$$\frac{y(s)}{\delta(s)} = \frac{482.657}{s^2 + 29.432s + 482.657} \tag{3.7.1}$$

where δ and y are the actuator command and output respectively. The same command input was then applied to this identified transfer function, and the resulting time history was compared to the measured actuator response (Figure 3.5). To generate the identified response, the transfer function in Equation (3.7.1) was incorporated into a SIMULINK model, which included position and rate limits specified by the manufacturer. Figure 3.5 shows that at the high starting frequencies there is a slight discrepancy between the measured and identified responses. However, as the command frequency reduced, the agreement between the two improves. Another method of comparing the response of the identified model to the measured data is through frequency response plots. Figure 3.6 shows comparisons of the gain and phase for the actuator data and the transfer function given in Equation (3.7.1) and, again, the identified response fits closely to the measured response. It is noted that some oscillations appear in the measured gain and phase plots at around 8 to 10 Hz. This indicates inadequate excitation of the system dynamics at these frequencies resulting in a reduced signal-to-noise ratio [6]. Frequency response characteristics are discussed further in Chapter 6.

To validate the mathematical model of the actuator, a second command for which the response had been measured was utilised. This was a step input, with the commanded position and measured position shown in Figure 3.7. Comparisons between the measured responses and the identified responses are displayed in Figure 3.8. Again, there is again good agreement between the measured data and the response obtained from the identified actuator model.

The accuracy of the control surface deflections determined using the above approach are dependent on the fidelity of the actuator and control linkage models. There can be significant nonlinearities in the actuator behaviour, particularly for small low-cost devices, and their performance will vary under different loading conditions. The control linkages can also introduce nonlinear effects due to hysteresis and dead bands. While the above approach worked well for this research, direct measurement of the control surface positions, if possible, is preferred.

The results of the bench tests on the actuator illustrates that, in general, the penalty for using small, low cost subsystems is a degradation in performance. From the transfer function in Equation (3.7.1), the electric actuator's natural frequency is calculated to be approximately 22 rad/s, which is less than the bandwidth of hydraulic actuators commonly used on manned aircraft which may be of the order of 60 rad/s [122]. It is also of the same order of magnitude as the rigid-body frequencies of the aircraft models. Therefore, to obtain an accurate mathematical description of the airframe, it is important to isolate the aircraft dynamics from the actuator dynamics. Other subsystems which could potentially introduced dynamics, which would need to be accounted for in the analysis, include the MEMS sensors and the associated filters. No facilities were available during the research to determine the dynamic characteristics of the sensors.
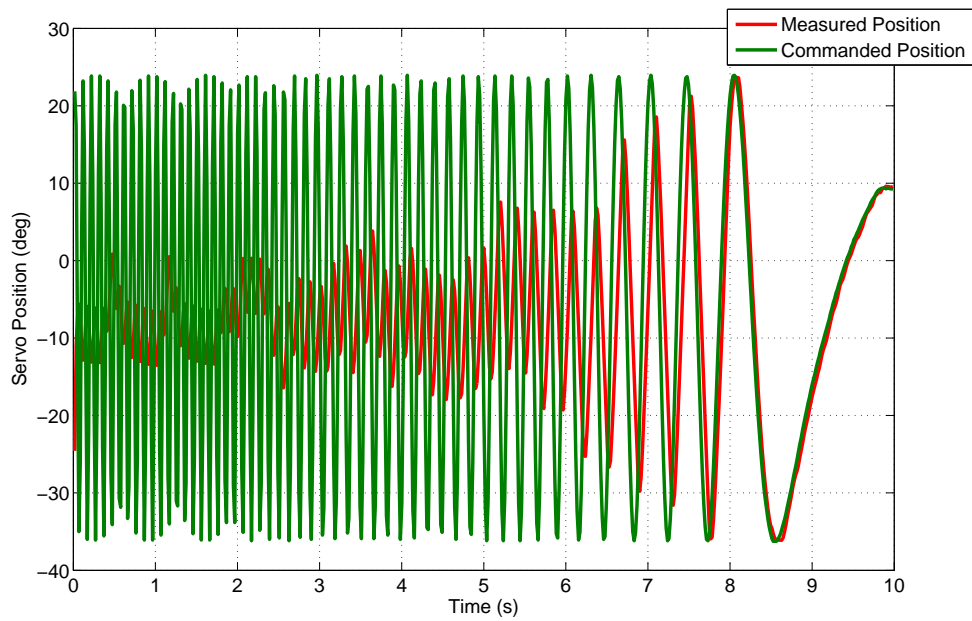
Figure 3.4: Time histories of the commanded position
frequency sweep and measured actuator response
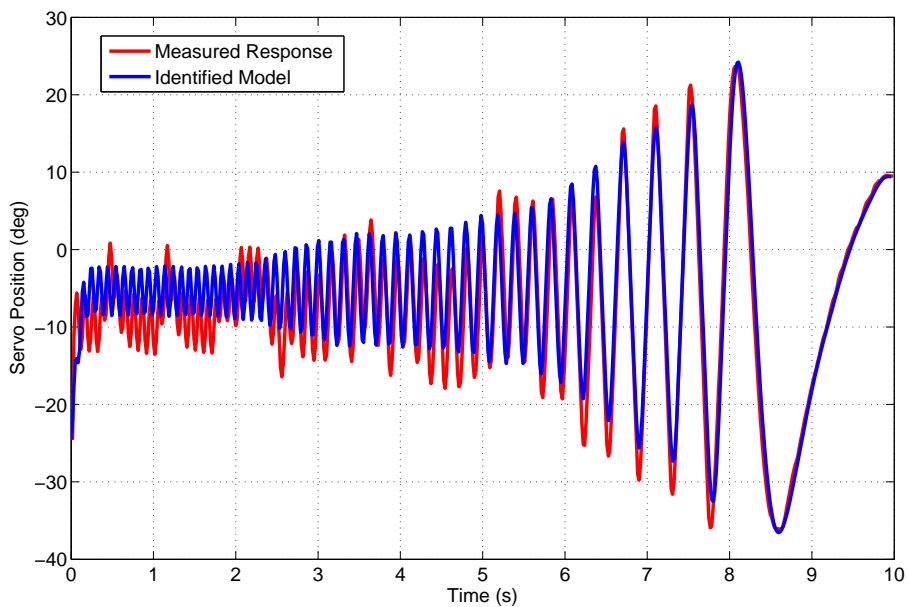
Figure 3.5: Comparison of the measured and identified
actuator response to the frequency sweep input
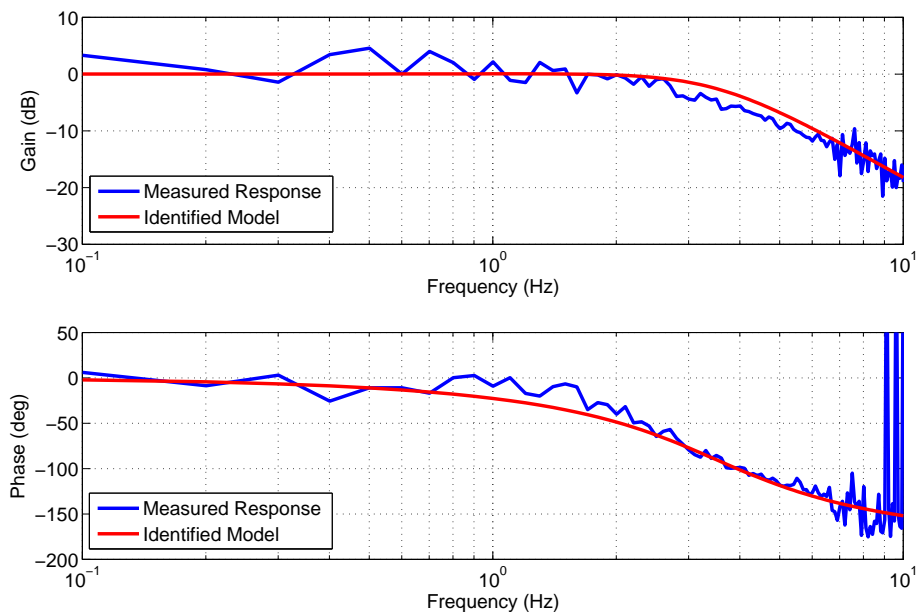
Figure 3.6: Comparison of the measured and identified
actuator frequency response characteristics
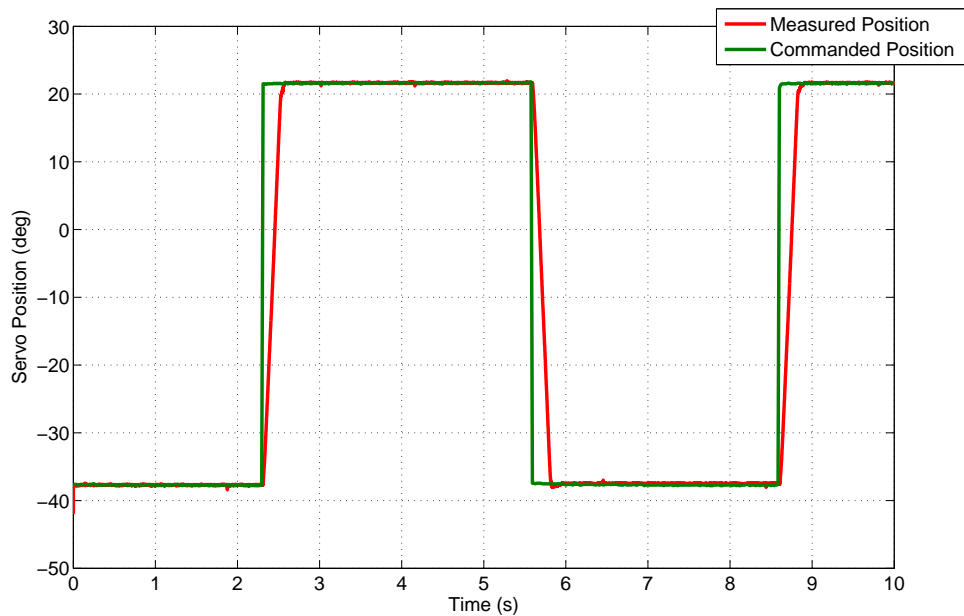
Figure 3.7: Time histories of the commanded position and
measured actuator response for a step input
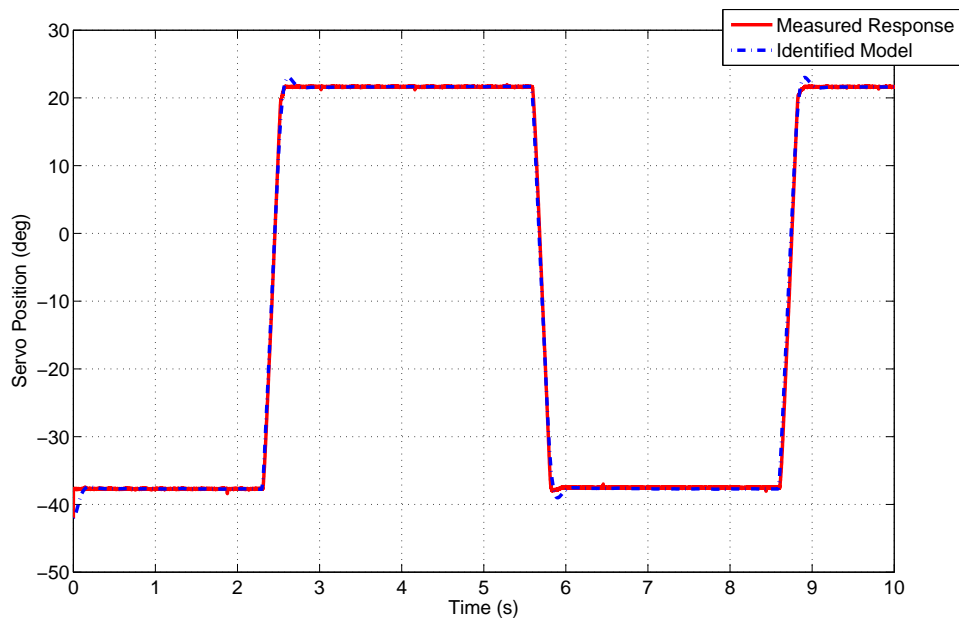
Figure 3.8: Comparison of the measured and identified
actuator response to a step input

Chapter 4

Equation Error Method

4.1   Introduction

The first parameter estimation method to be outlined is the equation error formulation. The equations of motion for the aircraft are postulated and the aim is to find estimates of the stability and control derivatives which lead to the dependent variables in the equations of motion matching data measured from the aircraft. In general, the equation error method utilises ordinary least squares regression, which is perhaps the simplest technique used for practical aircraft parameter estimation. The ordinary least squares algorithm is developed and discussed in the following sections.

4.2   Ordinary Least Squares Regression Algorithm

For the formulation of the algorithm, it is assumed that the aircraft equations of motion can be characterised by the form,

$$y(t) = \theta_0 + \theta_1 X_1(t) + \theta_2 X_2(t) + \ldots + \theta_n X_n(t) \tag{4.2.1}$$

where y is the dependent variable, X_1, X_2, ..., X_n are the n independent variables or regressors and θ_0, θ_1, θ_2, ..., θ_n are the $n_\theta = n+1$ unknown parameters to be determined.

It is assumed that both the dependent variable and the regressors are available from measurements from the aircraft. The measured value of y at the ith data point, denoted $z(i)$ is related to the true value by the expression,

$$\begin{aligned} z(i) &= y(i) + \epsilon(i) \\ &= \theta_0 + \sum_{j=1}^{n} \theta_j X_j(i) + \epsilon(i) \quad i = 1, 2, \ldots, N \end{aligned} \tag{4.2.2}$$

where N is the number of discrete measurement points. The variable ϵ is the so-called equation error and is assumed to account for random noise corrupting the measurement of the dependent variable in Equation (4.2.1). The regressors are assumed to be known without error.

Equation (4.2.2) can be written in matrix form as,

$$\mathbf{z} = \mathbf{X}\boldsymbol{\theta} + \boldsymbol{\epsilon} \tag{4.2.3}$$

where,

$$
\begin{aligned}
\mathbf{z} &= \begin{bmatrix} z(1) & z(2) & \dots & z(N) \end{bmatrix}^T \\
\mathbf{X} &= \begin{bmatrix}
1 & X_1(1) & \dots & X_n(1) \\
1 & X_1(2) & \dots & X_n(2) \\
\vdots & \vdots & & \vdots \\
1 & X_1(N) & \dots & X_n(N)
\end{bmatrix} \\
\boldsymbol{\theta} &= \begin{bmatrix} \theta_0 & \theta_1 & \dots & \theta_n \end{bmatrix}^T \\
\boldsymbol{\epsilon} &= \begin{bmatrix} \epsilon(1) & \epsilon(2) & \dots & \epsilon(N) \end{bmatrix}^T
\end{aligned}
$$

The elements of $\boldsymbol{\epsilon}$ are assumed to be uncorrelated with the regressors and have constant scatter across the values of the regressors i.e. their standard deviation is constant. The equation errors are treated as a white noise process with zero mean and variance σ^2,

$$\mathrm{E}\left[\boldsymbol{\epsilon}\right] = \mathbf{0} \text{ and } \mathrm{E}\left[\boldsymbol{\epsilon}\boldsymbol{\epsilon}^T\right] = \sigma^2\mathbf{I}$$

where E denotes the mean, or expected value, of a random variable and $\mathbf{I}$ is the identity matrix.

The least squares estimates of the unknown parameters in $\boldsymbol{\theta}$ are determined by minimising the sum of the squares of the equation error, so from Equation (4.2.3) the least squares cost function is defined as,

$$
\begin{aligned}
J(\boldsymbol{\theta}) &= \frac{1}{2}\sum_{i=1}^{N}\epsilon^2(i) = \frac{1}{2}\boldsymbol{\epsilon}^T\boldsymbol{\epsilon} \\
&= \frac{1}{2}(\mathbf{z} - \mathbf{X}\boldsymbol{\theta})^T(\mathbf{z} - \mathbf{X}\boldsymbol{\theta})
\end{aligned} \tag{4.2.4}
$$

Differentiating Equation (4.2.4) with respect to $\boldsymbol{\theta}$ gives,

$$\frac{\partial J(\boldsymbol{\theta})}{\partial \boldsymbol{\theta}} = -\mathbf{z}^T\mathbf{X} + \boldsymbol{\theta}^T\mathbf{X}^T\mathbf{X} \tag{4.2.5}$$

The minimum is found by setting Equation (4.2.5) equal to zero. Hence, taking the transpose of the above equation and rearranging,

$$\mathbf{X}^T\mathbf{X}\hat{\boldsymbol{\theta}} = \mathbf{X}^T\mathbf{z} \tag{4.2.6}$$

This is known as the normal equation and the term $\mathbf{X}^T\mathbf{X}$ is known as the information matrix as it provides a measure of the information content in the data. Provided the information matrix can be inverted, the normal equation can be rearranged to give,

$$\hat{\boldsymbol{\theta}} = \left(\mathbf{X}^T\mathbf{X}\right)^{-1}\mathbf{X}^T\mathbf{z} \tag{4.2.7}$$

where $\hat{\boldsymbol{\theta}}$ denotes the least squares estimate of the true unknown parameter vector $\boldsymbol{\theta}$.

Under the assumption that the equation errors are uncorrelated with the regressors, are characterised by white noise with zero mean and variance σ^2 and that the regressors are known without error, the least squares estimates have the following properties:

- They are unbiased i.e. $E[\hat{\boldsymbol{\theta}}] = \boldsymbol{\theta}$.

- They are a minimum variance, or efficient, estimate of $\boldsymbol{\theta}$. The parameter covariance matrix is given by,

$$\mathbf{P} = \sigma^2(\mathbf{X}^T\mathbf{X})^{-1} \tag{4.2.8}$$

- They are consistent, meaning that, as the number of data points N increases, the least squares estimates converge on the true parameter values.

Proofs of these properties are given in Appendix B.

In practice, however, measured variables will always contain errors, hence the assumption that the regressors are known without error is likely to be invalid. Another source of error is the effects of atmospheric turbulence, which is modelled as process noise. In Appendix B, it is shown that errors in the regressors lead to the least squares estimates becoming biased. It is also demonstrated that the covariance of the estimates is increased by the presence of measurement errors, in both the regressors and the dependent variable, and the presence of process noise. However, if the process noise can be assumed to be white with zero mean, its presence does not lead to biased estimates. This property implies that the least squares estimates account for process noise [34].

The above observations suggest that estimates of stability and control derivatives obtained using ordinary least squares regression are likely to be inaccurate and unreliable in any practical case. This may be particularly true for UAVs. As described in Section 3.2, MEMS sensors have traditionally exhibited noisier outputs and more significant bias and scale factor errors in comparison to conventional instrumentation. If MEMS sensors are employed on the aircraft, then this will lead to the bias and covariance of the least squares estimates being greater than they would have been if more precise instrumentation had been used. Another consideration is that, due to their relatively small masses and inertias in comparison to manned aircraft, UAVs will be more susceptible to the effects of atmospheric turbulence, leading to an increase in the covariance of the estimates.

Some extensions of the ordinary least squares method have been proposed, which account for the practical issues highlighted above. These include weighted least squares [123, 124], total least squares [34, 125] and the instrumental variable method [126]. However, their use for aircraft parameter estimation has not been widely reported. Instead, many practitioners prefer to carry out rigorous pre-processing of the data before applying ordinary least squares estimation [34, 31]. Systematic errors in the measurements, such as bias and scale factor errors, can be estimated and removed during the data compatibility check described in Chapter 9. As well as this, the effects of atmospheric turbulence can be minimised by carrying out flight tests early in the morning [34]. At this time of day, the thermal activity in the atmosphere which causes these disturbances is at a minimum. If atmospheric turbulence is encountered, gust components can also be estimated during the data compatibility check and removed from the measurements. This just leaves the effects of random measurement noise, which can be dealt with by smoothing the signals before using them for estimation. This process is discussed in the following section.

4.3 Smoothing Noisy Data

The aim of the smoothing process is to separate the deterministic component of the signal from the component due to unwanted measurement noise. The process is an important one for system identification and is required at a number of stages in the analysis. The following distinction is made between filtering and smoothing [31]. For a given point in time, a filter will only use the information at the current data point and past data points to remove noise components from the signal. A smoother, on the other hand, utilises future data points as well as current and past information. Therefore, smoothing can only be applied once the experiments have been carried out. If the analysis has to be performed in real-time then a filter is used. However, filtering can distort the amplitude and phase of the data, which smoothing avoids. Filter/smoother design is a vast field hence it would be impractical to review the subject in detail here. Instead, this section focuses on two smoothing techniques studied and applied throughout the research. The first is a local smoothing technique implemented in the time domain, while the second is a global method applied in the frequency domain.

The time domain smoothing method aims to fit a local polynomial to the data points around the point to be smoothed. In designing the smoother, choices must be made regarding the number of data points to use in the analysis and the order of the polynomial to fit to the data. Klein and Morelli [31] present an example of fitting a second-order polynomial to five data points (including the point to be smoothed). The second-order polynomial is given by the equation,

$$y = a + bt + ct^2 \tag{4.3.1}$$

which corresponds to the assumption that the second derivative of the measured variable is constant over the five data points. Denoting the measured variable at the ith data point $z(i)$, then the equations for the local fit to the five data points are,

$$\begin{aligned}
z(i-2) &= a + b(-2\Delta t) + c(-2\Delta t)^2 \\
z(i-1) &= a + b(-\Delta t) + c(-\Delta t)^2 \\
z(i) &= a \\
z(i+1) &= a + b(\Delta t) + c(\Delta t)^2 \\
z(i+2) &= a + b(2\Delta t) + c(2\Delta t)^2
\end{aligned} \tag{4.3.2}$$

where Δt is the data sampling time. The polynomial coefficients a, b and c are then estimated using least squares regression and, from Equation (4.3.2), the smoothed value for $z(i)$ is simply the estimate of a.

So, from Equation (4.3.2), the unknown parameter vector is,

$$\boldsymbol{\theta} = \begin{bmatrix} a \\ b \\ c \end{bmatrix} \tag{4.3.3}$$

the regressor matrix is,

$$\mathbf{X} = \begin{bmatrix} 1 & -2\Delta t & 4(\Delta t)^2 \\ 1 & -\Delta t & (\Delta t)^2 \\ 1 & 0 & 0 \\ 1 & \Delta t & (\Delta t)^2 \\ 1 & 2\Delta t & 4(\Delta t)^2 \end{bmatrix} \tag{4.3.4}$$

and the measurement vector is,

$$\mathbf{z} = \begin{bmatrix} z(i-2) \\ z(i-1) \\ z(i) \\ z(i+1) \\ z(i+2) \end{bmatrix} \tag{4.3.5}$$

Using Equation (4.2.6), the normal equations for this problem can be written as,

$$5a + 10(\Delta t)^2 c = \sum_{k=i-2}^{i+2} z(k)$$

$$10\Delta t b = \sum_{k=i-2}^{i+2} kz(k) \tag{4.3.6}$$

$$10a + 34(\Delta t)^2 c = \sum_{k=i-2}^{i+2} k^2 z(k)$$

The least squares estimate of a and, therefore, the smoothed value for $z(i)$ is then,

$$\hat{a} = z_s(i) = \frac{34}{70} \sum_{k=i-2}^{i+2} z(k) + \frac{1}{7} \sum_{k=i-2}^{i+2} k^2 z(k)$$

$$= \frac{1}{70}[-6z(i-2) + 24z(i-1) + 34z(i) + 24z(i+1) - 6z(i+2)] \tag{4.3.7}$$

At the beginning and end of the data segment, the smoothed values for the data points are obtained from the local model estimated at a point away from the start or end of the segment. For example, in the case of a second-order polynomial fitted to five data points, the smoothed values of the first two points in the segment, denoted $z_s(1)$ and $z_s(2)$, can be determined from the local model identified at the third data point i.e.,

$$z(1) = \hat{a} + \hat{b}(-2\Delta t) + \hat{c}(-2\Delta t)^2$$
$$z(2) = \hat{a} + \hat{b}(-\Delta t) + \hat{c}(-\Delta t)^2 \tag{4.3.8}$$

where $\hat{a}$, $\hat{b}$ and $\hat{c}$ are the estimates of the polynomial coefficients at $z(3)$.

By varying the order of the polynomial n and the number of neighbouring data points k used in the analysis, the cutoff frequency for the smoother can be altered. In general, a larger value of k for constant n lowers the cutoff frequency, while an increase in n for a given k increases the cutoff frequency. However, it is difficult to determine what the exact cutoff frequency is for the complete data segment, as the process involves repeated local smoothing [31].

The second smoothing technique used during the research is a global method in which all the data points in the time series are analysed at once. The method is performed in the frequency domain using Fourier analysis. To start with, a Fourier sine series is found to describe the measured data. For Fourier series expansions, it is assumed that the time history is periodic, which implies discontinuities in the amplitude and first time derivative at the end points of the time history [127, 31]. The amplitudes at the end points are set equal to zero by subtracting a linear trend from the measured data, then the resulting signal is reflected about the origin to

remove the first time derivative discontinuities. For a measured variable z, this process can be expressed mathematically as,

$$g(i) = z(i) - z(1) - (i-1) \left[\frac{z(N) - z(1)}{N-1} \right] \quad i = 1, 2, \ldots, N$$

$$g(-i) = -g(i) \quad i = 2, 3, \ldots, N$$

(4.3.9)

where g is the time history with the discontinuities removed, with $g(-N)=g(1)=g(N)=0$. Figure 4.1 shows a segment of pitch rate data measured from the 1/12 scale Hawk model and Figure 4.2 shows the pitch rate with the linear trend removed and reflected about the origin.
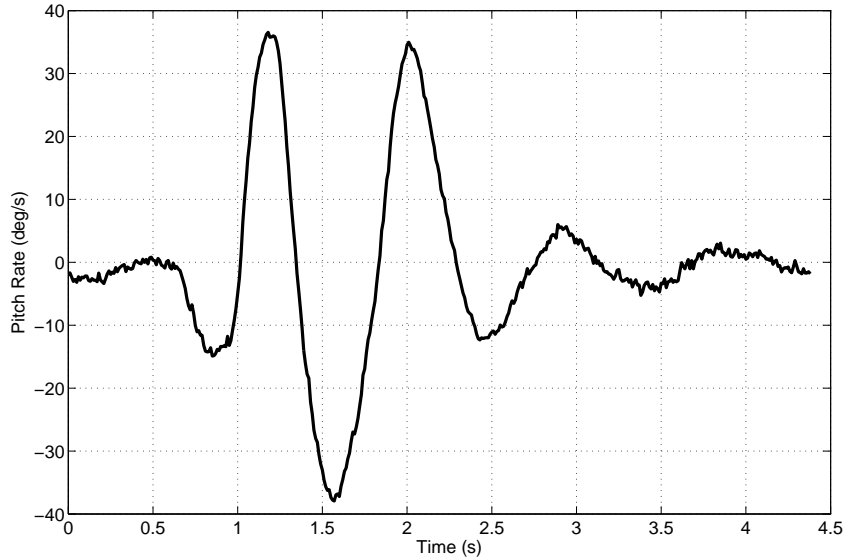
Figure 4.1: Pitch rate data from 1/12 scale Hawk model

The vector of data points with the discontinuities removed,

$$\mathbf{g} = \begin{bmatrix} g(-N) & g(-N+1) & \cdots & g(-2) & g(1) & g(2) & \cdots & g(N) \end{bmatrix}^T$$

(4.3.10)

is an odd function of time and can be approximated using a Fourier sine series,

$$\hat{g}(i) = \sum_{k=1}^{N-1} b(k) \sin \left[k\pi \left(\frac{i-1}{N-1} \right) \right]$$

(4.3.11)

where $b(k)$ are the Fourier sine series coefficients. The summation over frequency index k omits $k = 0$, the zero frequency, as this is a pure sine wave for an odd function and only the positive values of i, corresponding to the original time history, are included in (4.3.11).

The Fourier sine series coefficients are calculated from,

$$b(k) = \frac{2}{N-1} \sum_{i=2}^{N-1} g(i) \sin \left[k\pi \left(\frac{i-1}{N-1} \right) \right]$$

(4.3.12)

where it is again noted that $g(1)$ and $g(N)$ are zero. The kth frequency is found from,

$$f_k = \frac{k}{2(N-1)\Delta t}$$

(4.3.13)
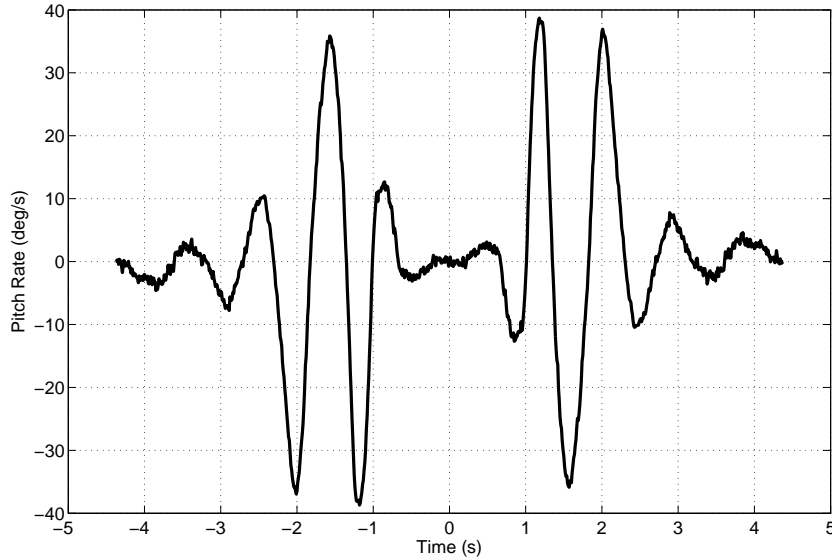
Figure 4.2: Pitch rate data with endpoint discontinuities removed

where Δt is again the data sampling time.

The Fourier sine series will contain all spectral components that can be computed from the discrete time signal but the series for a deterministic signal differs from that of random noise. For a deterministic signal, the amplitude of the sine series coefficients increase to a maximum before decreasing asymptotically to zero with increasing k. For a signal with discontinuities in the amplitude and first time derivative at the end points removed, this decrease in $|b(k)|$ is proportional to k^{-3} [127, 31]. Noise, on the other hand, theoretically has constant power over the entire frequency range so its Fourier sine series coefficients have a small, relatively constant amplitudes for all values of k. Figure 4.3 shows the Fourier sine series coefficients for the 1/12 scale Hawk pitch rate data. The amplitude of the coefficients increases to reach a maximum at around 1 Hz. It then rapidly decays to a small value and stays relatively constant for all frequencies above around 5 Hz. Therefore, the Fourier sine series coefficients below 5 Hz correspond to the rigid-body dynamics of the Hawk model, while the coefficients above this frequency belong to random measurement noise. Because of its relatively constant power over all frequencies, some noise will still be present in the frequency region below 5 Hz. However, the amplitudes of the coefficients corresponding to the aircraft dynamics are significantly greater than the constant value associated with the noise.

To smooth the signal, Equation (4.3.11) is used but the sine series coefficients above the cutoff frequency (5 Hz for pitch rate example) are set to zero,

$$\hat{g}_s(i) = \sum_{k=1}^{k_{max}} b(k) \sin \left[k\pi \left(\frac{i-1}{N-1} \right) \right] \tag{4.3.14}$$

where k_{max} is the frequency index corresponding to the cutoff frequency determined from the plot of the Fourier sine series coefficients.

The final smoothed time history is then obtained by adding the linear trend, removed in Equa-
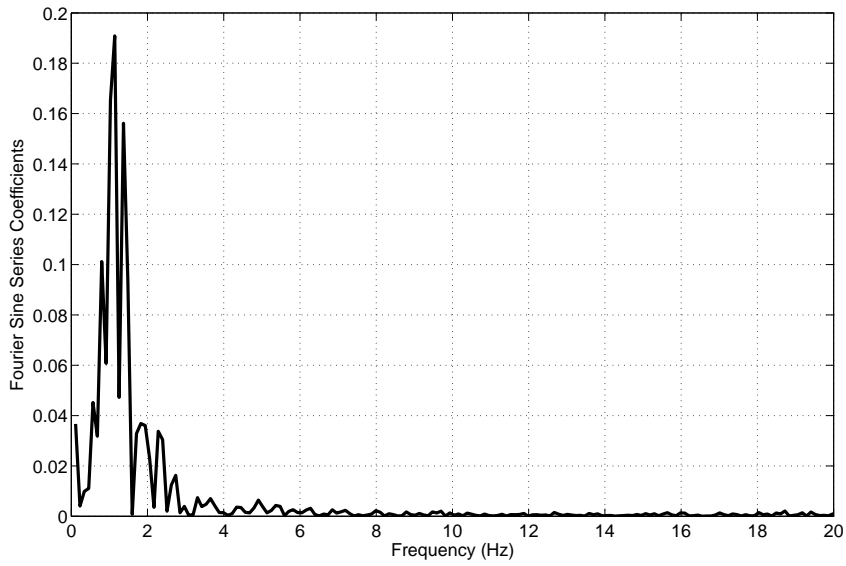
Figure 4.3: Fourier sine series coefficients for the 1/12
scale Hawk pitch rate data

tion (4.3.9), back to the smoothed values,

$$z_s(i) = \hat{g}_s(i) + z(0) + (i - 1) \left[\frac{z(N - 1) - z(0)}{N - 1} \right] \tag{4.3.15}$$

Due to the nature of the Fourier analysis, the end points $z(1)$ and $z(N)$ are excluded from the global smoothing process. Hence, they are smoothed separately using a local technique, such as the one described previously. Figure 4.4 shows a comparison between the original pitch rate time history and the smoothed signal.

The two smoothing techniques described above also provide a means for estimating the characteristics of the noise, which is useful when implementing the extended Kalman filter described in Section 7.2.4. The noise sequence is determined simply from,

$$v(i) = z(i) - z_s(i) \tag{4.3.16}$$

and assuming the noise to be stationary and having a Gaussian distribution, the mean and variance are calculated from,

$$\bar{v} = \frac{1}{N} \sum_{i=1}^{N} v(i) \tag{4.3.17}$$

$$\sigma_v^2 = \frac{1}{N - 1} \sum_{i=1}^{N} [v(i) - \bar{v}]^2 \tag{4.3.18}$$

4.4 Numerical Differentiation

For the equation error method, the calculation of the dependent variable from experimental data often requires that measurements be differentiated numerically. For example, consider the
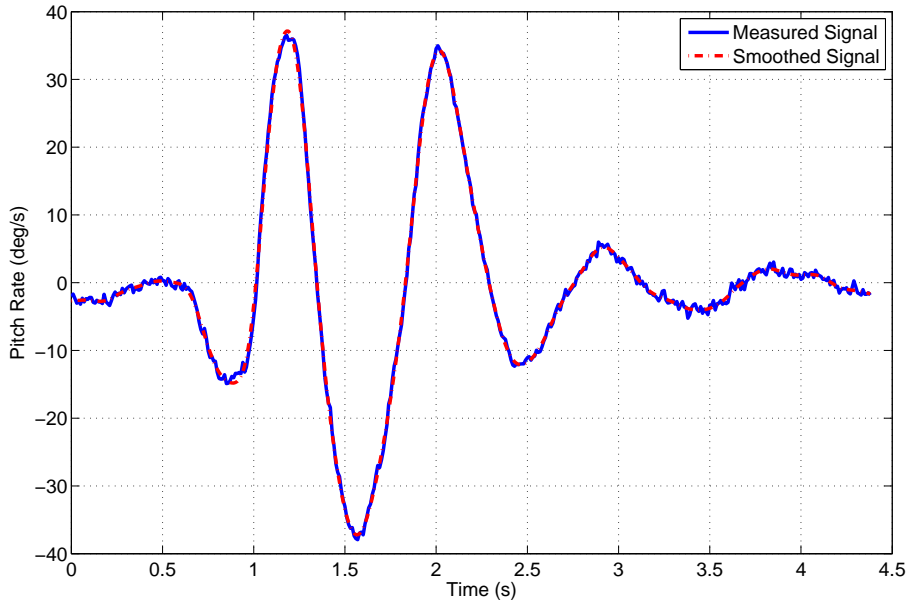
Figure 4.4: Comparison of measured and smoothed pitch
rate time histories

pitching moment equation,

$$\dot{q} = m_w w + m_q q + m_\eta \eta \tag{4.4.1}$$

The dependent variable is $\dot{q}$ and the regressors are w, q and η but angular accelerations are rarely measured directly due to a lack of reliable sensors, hence $\dot{q}$ is obtained by numerically differentiating pitch gyro data. The angular accelerations are also required when the equations of motion are expressed in non-dimensional form. Again, using the pitching moment equation to illustrate, the non-dimensional[1] pitching moment equation can be written as,

$$C_m = C_{m_0} + C_{m_\alpha}\alpha + C_{m_q}\hat{q} + C_{m_\eta}\eta \tag{4.4.2}$$

where the dependent variable is now the pitching moment coefficient C_m and the regressors are α, $\hat{q}$ and η. The non-dimensional pitch rate $\hat{q}$ is defined as,

$$\hat{q} = \frac{q\bar{c}}{V} \tag{4.4.3}$$

where $\bar{c}$ is the mean aerodynamic chord and V is the true airspeed.

The pitching moment coefficient is calculated from,

$$C_m = \frac{1}{\bar{q}S\bar{c}}[I_{yy}\dot{q} + I_{xz}(p^2 - r^2) + (I_{xx} - I_{zz})pr - z_{eng}T] \tag{4.4.4}$$

where $\bar{q}$ is the dynamic pressure, S is the wing area, I_{xx}, I_{yy}, I_{zz} and I_{xz} are the moments and products of inertia, T is engine thrust and z_{eng} is the offset along the z-axis between the engine thrust line and the moment reference point.

---

[1]The method used for non-dimensionalising the aerodynamic forces and moments throughout this thesis is a convention employed by BAE Systems closely related to the NACA non-dimensional system

The simplest method for numerically differentiating a signal is to use a central difference formula. For example, the pitch acceleration at the ith data point is calculated approximately from,

$$\dot{q}(i) \approx \frac{q(i+1) - q(i-1)}{2\Delta t} \tag{4.4.5}$$

However, the use of central difference formulas to differentiate a variable tends to amplify the noise in the signal. Figure 4.5 shows a time history of $\dot{q}$ for the 1/12 scale Hawk, which has been obtained by applying Equation (4.4.5) to pitch rate data. The resulting pitch acceleration signal is clearly very noisy.
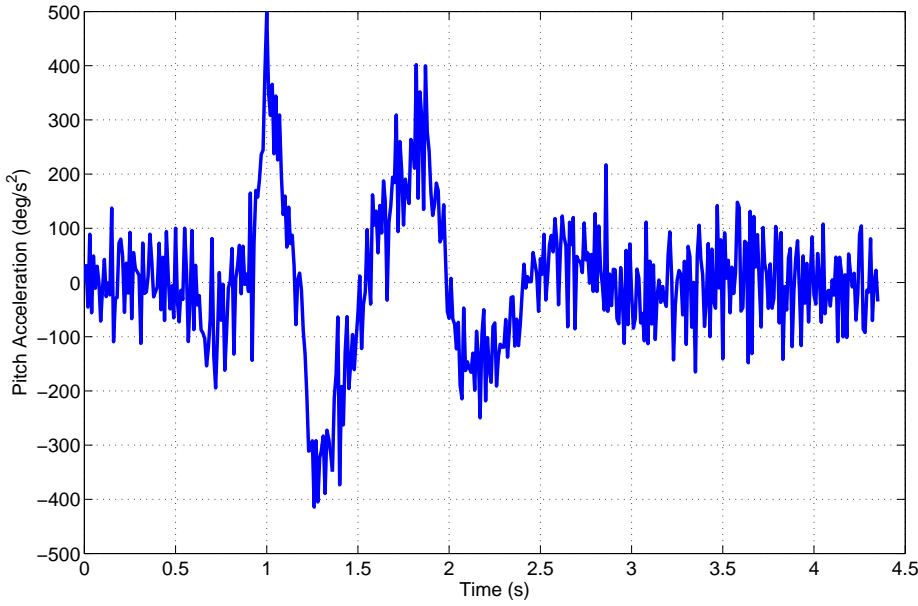
Figure 4.5: Pitch acceleration for the 1/12 scale Hawk
obtained using central difference formula

To overcome this issue, the data must be smoothed prior to the differentiation process and this can be achieved with either of the smoothing techniques described previously in Section 4.3. For the time domain method, the time derivative at each data point is obtained by differentiating the local smoothing polynomial fitted to that point. Hence, continuing the illustrative example of using a second-order polynomial fitted to five neighbouring data points to smooth the noisy signal, then from Equation (4.3.1),

$$\dot{y} = b + ct \tag{4.4.6}$$

So by setting $t = 0$, the time derivative at the current datapoint is simply the estimate of the local polynomial coefficient b. From Equation (4.3.6), the estimate of b and, therefore, the derivative of the measured variable with respect to time is calculated as,

$$\hat{b} = \dot{z}_s(i) = \frac{1}{10\Delta t}[-2z(i-2) - z(i-1) + z(i+1) + 2z(i+2)] \tag{4.4.7}$$

Next, recalling from Section 4.3 that the smoothing solution obtained using the global Fourier analysis is,

$$z_s(i) = \hat{g}_s(i) + z(1) + (i-1)\left[\frac{z(N) - z(1)}{N - 1}\right] \quad i = 1, 2, \ldots, N \tag{4.4.8}$$

where,

$$\hat{g}_s(i) = \sum_{k=1}^{k_{max}} \Phi(k)b(k)\sin\left[k\pi\left(\frac{i-1}{N-1}\right)\right] \qquad (4.4.9)$$

Then the derivative of the smoothed signal with respect to time is found to be,

$$\dot{z}_s(i) = \left[\frac{z(N) - z(1)}{N-1}\right] + \sum_{k=1}^{k_{max}} \Phi(k)b(k)\left(\frac{k\pi}{N-1}\right)\cos\left[k\pi\left(\frac{i-1}{N-1}\right)\right] \qquad (4.4.10)$$

Figure 4.6 again shows the time history of $\dot{q}$ for the 1/12 scale Hawk obtained by differentiating the pitch rate signal using the central difference formula, but this time also shows the estimates of $\dot{q}$ calculated using the local polynomial fitting technique and $\dot{q}$ determined using the global Fourier smoothing method. Having used the local polynomial fitting approach to smooth the data prior to differentiation, the noise level of the resulting signal is much reduced. However, some noise components are still clearly present in the data. A much smoother signal is obtained when using the global method based on Fourier analysis.
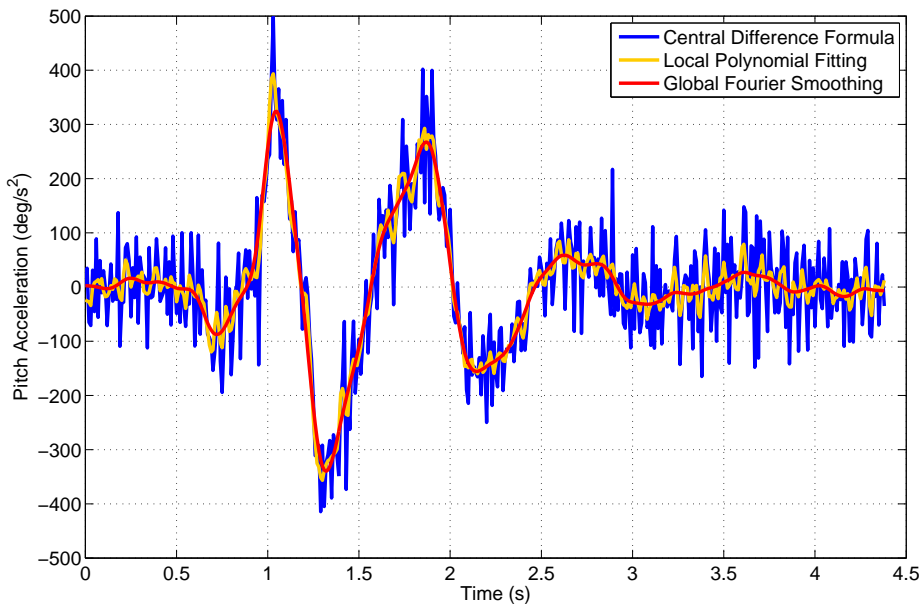
Figure 4.6: Pitch acceleration for the 1/12 scale Hawk
obtained using three numerical differentiation methods

A study by Morelli [128] has also found that the degree of smoothing from the local polynomial fitting method is often insufficient. To overcome this, he suggests that, prior to performing differentiation with the local polynomial approach, additional smoothing be done on the data using Fourier smoothing (Equation (4.4.8)), or alternatively that the Fourier analysis technique in Equation (4.4.10) be used on its own. The respective time histories of the pitch rate signal differentiated using Equations (4.4.7) and (4.4.10) are shown again in Figure 4.7 but, this time, Equation (4.4.8) was applied to the data before obtaining the derivative with local polynomial fitting. It can be seen that the noise present in Figure 4.6 has been removed and that the two differentiated signals shown in Figure 4.7 are indistinguishable.
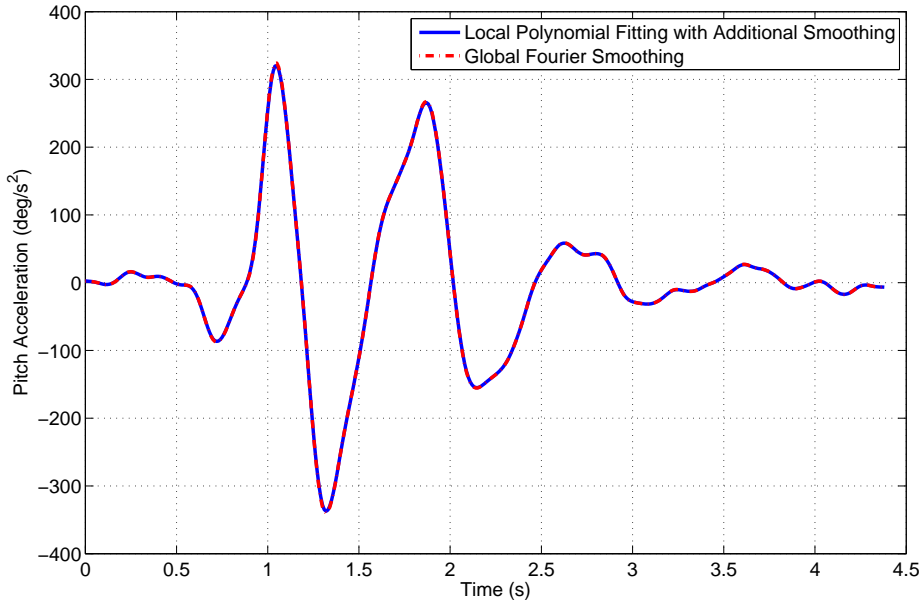
Figure 4.7: Pitch acceleration for the 1/12 scale Hawk:
additional smoothing performed prior to local polynomial
differentiation

4.5   Accuracy of Parameter Estimates and Identified Model

Having obtained a set of parameter estimates, an obvious question to ask is how accurate are the estimated values? A number of statistical metrics exist to help answer this question, depending on which estimation technique has been utilised. Those metrics typically used for aircraft parameter estimates determined using least squares regression are introduced in this section.

The parameter covariance matrix $\mathbf{P}$ was given earlier in Equation (4.2.8) and forms the basis of a number of the metrics,

$$\mathbf{P} = \sigma^2 \left(\mathbf{X}^T\mathbf{X}\right)^{-1} \tag{4.5.1}$$

Using the following notation for the inverse of the information matrix,

$$\mathbf{D} = \left(\mathbf{X}^T\mathbf{X}\right)^{-1} = [d_{jk}] \quad j, k = 1, 2, \ldots, n_\theta \tag{4.5.2}$$

the diagonal elements of the estimated parameter covariance matrix $\mathbf{P}$ are the variances of the estimated parameters,

$$\mathrm{Var}(\hat{\theta}_j) = \sigma^2 d_{jj} \quad j = 1, 2, \ldots, n_\theta \tag{4.5.3}$$

The square root of the variance for the jth parameter estimate is often termed the standard error and denoted,

$$s(\hat{\theta}_j) = \sigma \sqrt{d_{jj}} \tag{4.5.4}$$

The standard error approximates the standard deviation of the parameter. In other words, if the parameter value was to be estimated repeatedly from a number of manoeuvres carried out at the same flight condition, then the standard error calculated for each individual manoeuvre should approximate the scatter in the parameter estimates when the values from all manoeuvres are compared.

Confidence intervals can also be used to examine the quality of parameter estimates. For their development, it is assumed that the estimates $\hat{\boldsymbol{\theta}}$ from repeated manoeuvres have a normal, or Gaussian, distribution about the true values of the parameters $\boldsymbol{\theta}$. A normally distributed random variable is usually expressed in terms of its mean and variance using the notation $\mathbb{N}(\eta, \sigma^2)$, where η is the mean and σ^2 is the variance. Therefore, the properties of $\hat{\boldsymbol{\theta}}$ are,

$$\hat{\boldsymbol{\theta}} \sim \mathbb{N}\left[\boldsymbol{\theta}, \sigma^2\left(\mathbf{X}^T\mathbf{X}\right)^{-1}\right]$$

Because $\hat{\boldsymbol{\theta}}$ is normally distributed, it follows that each of its n_θ elements are also Gaussian with properties,

$$\hat{\theta}_j \sim \mathbb{N}(\theta_j, \sigma^2 d_{jj}) \quad j = 1, 2, \ldots, n_\theta \tag{4.5.5}$$

Calculation of the confidence interval requires knowledge of t-distributions, which for $\hat{\theta}_j$ is defined as,

$$t(\alpha/2, N - n_\theta) = \frac{\hat{\theta}_j - \theta_j}{\sqrt{\sigma^2 d_{jj}}} = \frac{\hat{\theta}_j - \theta_j}{s(\hat{\theta}_j)} \tag{4.5.6}$$

The t-distribution is defined in terms of the confidence level parameter α, and the number of degrees of freedom $N - n_\theta$, where N is again the number of data points. A typical confidence level chosen is 95%, which corresponds to $\alpha = 0.05$. The number of degrees of freedom refers to the number of independent pieces of information necessary to compute a given statistic [129]. By rearranging Equation (4.5.6), the confidence interval is found to be,

$$\hat{\theta}_j - t(\alpha/2, N - n_\theta)s(\hat{\theta}_j) \leq \theta_j \leq \hat{\theta}_j + t(\alpha/2, N - n_\theta)s(\hat{\theta}_j) \quad j = 1, 2, \ldots, n_\theta \tag{4.5.7}$$

From a table of t-distribution values, which can found for example in Reference [130], for $\alpha = 0.05$ and $(N - n_\theta) \rightarrow \infty$,

$$t(\alpha/2, N - n_\theta)s(\hat{\theta}_j) = 1.96$$

so Equation (4.5.7) becomes,

$$\theta_j = \hat{\theta}_j \pm 1.96 s(\hat{\theta}_j) \tag{4.5.8}$$

When the number of data points is much larger than the number of unknown parameters, the t-distribution approaches the normal distribution [31]. Thus, the confidence interval corresponding to two standard deviations is often used,

$$\theta_j = \hat{\theta}_j \pm 2s(\hat{\theta}_j) \tag{4.5.9}$$

In other words, there is a 95% probability that the true value θ_j falls within the interval,

$$[\hat{\theta}_j - 2s(\hat{\theta}_j), \hat{\theta}_j + 2s(\hat{\theta}_j)]$$

It is difficult to define an acceptable value for $s(\hat{\theta}_j)$. What is considered acceptable will be influenced by the accuracy required by the application of the final system identification results. Tischler [6] suggests that a parameter can be considered reliable if the estimate of its standard deviation is less than 20% of the estimated derivative value. Note that this suggested guideline was based on the frequency response method for system identification and not least squares regression.

The off-diagonal elements of $\mathbf{P}$ are the covariances between the estimated parameters,

$$\mathrm{Cov}(\hat{\theta}_j, \hat{\theta}_k) = \sigma^2 d_{jk} \quad j, k = 1, 2, \ldots, n_\theta \tag{4.5.10}$$

From Equations (4.5.2) and (4.5.10), the correlation coefficient between two estimated parameters is defined as,

$$\rho_{jk} = \frac{\text{Cov}(\hat{\theta}_j, \hat{\theta}_k)}{\sqrt{\text{Var}(\hat{\theta}_j)\text{Var}(\hat{\theta}_k)}} = \frac{d_{jk}}{\sqrt{d_{jj}d_{kk}}} \tag{4.5.11}$$

The correlation coefficient is a measure of the pair-wise correlation between the two parameters, or equivalently their corresponding regressors. The absolute value of ρ_{jk} falls between 0 and 1. A correlation coefficient of 0 indicates that the parameters, and the associated regressors, are completely independent from each other. On the other hand, a value of $\rho_{jk} = 1$ means that the two regressors X_j and X_k are linearly dependent and are in some way related to each other. In turn, this indicates that there is no unique solution for parameters $\hat{\theta}_j$ and $\hat{\theta}_k$ and any number of combinations of the two parameters could be used to describe the aircraft response. A simple method of dealing with correlation is to repeat the parameter estimation process but hold the value of the jth or kth parameter fixed at some *a priori* estimate. When analysing experimental data, it is rare to encounter correlation coefficients that are exactly 0 or 1. However, if the value of $\rho_{jk} \geq 0.9$, then some action must be taken [34, 31, 6].

For Equations (4.5.1) to (4.5.11) above, it should be noted that the variance σ^2 is usually unknown. Instead, it can be estimated using the expression,

$$\hat{\sigma}^2 = \frac{1}{N - n_\theta}\boldsymbol{v}^T\boldsymbol{v}\frac{1}{N - n_\theta}(\mathbf{z} - \hat{\mathbf{y}})^T(\mathbf{z} - \hat{\mathbf{y}}) = \frac{1}{N - n_\theta}(\mathbf{z} - \mathbf{X}\hat{\boldsymbol{\theta}})^T(\mathbf{z} - \mathbf{X}\hat{\boldsymbol{\theta}}) \tag{4.5.12}$$

where the elements of $\boldsymbol{v}$ are known as the residuals and $\hat{\mathbf{y}} = \mathbf{X}\hat{\boldsymbol{\theta}}$ is the estimated dependent variable vector. The residuals can be considered as samples of the equation errors $\boldsymbol{\epsilon}$.

Analysis of the residuals in $\boldsymbol{v}$ provides another method of assessing the identified model of the aircraft dynamics and, therefore, the veracity of the parameter estimates. The validation process involves using the identified model to predict the aircraft's response to a different set of data to that used for parameter estimation. The model can be considered suitable if the residuals from the validation step are of a similar magnitude and character to those from parameter estimation [31]. One technique of assessing the residuals is Theil's inequality, which was originally developed for econometrics but later found use in aircraft applications [33, 53, 6]. Theil's inequality coefficient is defined as,

$$U = \frac{\sqrt{(1/N)\sum_{i=1}^{N}[z(i) - \hat{y}(i)]^2}}{\sqrt{(1/N)\sum_{i=1}^{N}[z(i)]^2} + \sqrt{(1/N)\sum_{i=1}^{N}[\hat{y}(i)]^2}} \quad i = 1, 2, \ldots, N \tag{4.5.13}$$

where $\hat{y}(i)$ is the estimated dependent variable at the ith data point. The value of U falls between 0 and 1, with $U = 0$ indicating that the identified model matches perfectly to the measured data and $U = 1$ corresponding to no match between $\mathbf{z}$ and $\hat{\mathbf{y}}$ at all.

The fit error between $\mathbf{z}$ and $\hat{\mathbf{y}}$ can also be decomposed in terms of bias, variance and covariance. The bias portion is a measure of the systematic error in the identified model and is given by,

$$U_B = \frac{(\bar{z} - \bar{y})^2}{(1/N)\sum_{i=1}^{N}[z(i) - \hat{y}(i)]^2} \tag{4.5.14}$$

where $\bar{z}$ and $\bar{y}$ are the mean values found from,

$$\bar{z} = \frac{1}{N} \sum_{i=1}^{N} [z(i)]^2 \tag{4.5.15}$$

$$\bar{y} = \frac{1}{N} \sum_{i=1}^{N} [y(i)]^2 \tag{4.5.16}$$

The variance portion provides a measure of the identified model's ability to duplicate the variability of the true system and is expressed as,

$$U_V = \frac{(\sigma_z - \sigma_y)^2}{(1/N) \sum_{i=1}^{N} [z(i) - \hat{y}(i)]^2} \tag{4.5.17}$$

where σ_z and σ_y are standard deviations calculated from,

$$\sigma_z = \sqrt{\frac{1}{N} \sum_{i=1}^{N} [z(i) - \bar{z}]^2} \tag{4.5.18}$$

$$\sigma_y = \sqrt{\frac{1}{N} \sum_{i=1}^{N} [y(i) - \bar{y}]^2} \tag{4.5.19}$$

The covariance portion is a measurement of the nonsystematic error in the identified model, such as unmodelled measurement or process noise. It is given by the equation,

$$U_C = \frac{2(1 - \rho)\sigma_z \sigma_y}{(1/N) \sum_{i=1}^{N} [z(i) - \hat{y}(i)]^2} \tag{4.5.20}$$

where the correlation coefficient is found from,

$$\frac{1}{\sigma_z \sigma_y N} \sum_{i=1}^{N} [z(i) - \bar{z}][y(i) - \bar{y}] \tag{4.5.21}$$

As with the standard error $s(\hat{\theta}_j)$, an acceptable figure for U depends on the application of the identified model but, as a rule of thumb, a value of 0.25-0.3 indicates a good agreement between the measured and identified aircraft responses [33]. For a good model fit, U_B and U_V should be close to 0, while U_C should be close to 1. If the values of U_B and U_V exceed 0.1 then some investigation into the parameter estimates and model structure should be carried out [34]. The process of determining the most appropriate model for a given problem is dealt with in Chapter 8.

4.6   Coloured Residuals

As mentioned in the previous section, the residuals v can be considered as samples of the equation errors ϵ, which are assumed to be due to measurement noise corrupting knowledge of the dependent variable. However, when performing parameter estimation, the equations of motion chosen to represent the aircraft dynamics are a simplification of the actual vehicle

dynamics. Hence, ϵ will account for errors in the model structure, as well as noise corrupting the measurement of $\mathbf{y}$. The equation errors were assumed, in Section 4.2, to be characterised as a white noise process, meaning that the equation error at the ith data point, $\epsilon(i)$, is uncorrelated with the equation error at any other data point. Modelling errors, however, will lead to the equation error having a deterministic component, in which case the assumption that $\epsilon(i)$ is independent from the equation error at its neighbouring data points is invalid. The equation errors will resemble a coloured noise process, leading the residuals to also be coloured.

The importance of the above observation is that the covariance of the parameter estimates $\mathbf{P}$ and, in turn the standard errors and confidence intervals, are altered by coloured equation errors. The parameter covariance can be written as (see Appendix B),

$$
\begin{aligned}
\mathbf{P} &= \mathrm{E}[(\hat{\boldsymbol{\theta}} - \boldsymbol{\theta})(\hat{\boldsymbol{\theta}} - \boldsymbol{\theta})^T] = \mathrm{E}[\left(\mathbf{X}^T\mathbf{X}\right)^{-1}\mathbf{X}^T(\mathbf{z} - \mathbf{y})(\mathbf{z} - \mathbf{y})^T\mathbf{X}\left(\mathbf{X}^T\mathbf{X}\right)^{-1}] \\
&= \left(\mathbf{X}^T\mathbf{X}\right)^{-1}\mathbf{X}^T\mathrm{E}[\boldsymbol{\epsilon}\boldsymbol{\epsilon}^T]\mathbf{X}\left(\mathbf{X}^T\mathbf{X}\right)^{-1}
\end{aligned}
\tag{4.6.1}
$$

where again the regressor matrix $\mathbf{X}$ is assumed to be known without error. When the equation errors are assumed to be characterised by white noise with zero mean and variance σ^2, the equation error covariance is given by,

$$
\mathrm{E}[\boldsymbol{\epsilon}\boldsymbol{\epsilon}^T] = \sigma^2\mathbf{I}
\tag{4.6.2}
$$

which leads to Equation (4.6.1) reducing to the expression given earlier in Equation (4.2.8). However, Equation (4.6.2) will not hold when the residuals are coloured and, if the covariance is calculated based on the assumption of white residuals, then the standard errors will not be consistent with the scatter in parameter estimates obtained from repeated manoeuvres at the same flight condition. In fact, the standard errors calculated under the assumption of white residuals can be around five to ten times smaller than the scatter from repeated manoeuvres [28, 131, 132], falsely indicating that the parameter estimates are more reliable than they actually are. Similar problems are encountered with other parameter estimation techniques.

To resolve this issue, some analysts simply multiply the standard errors by a "fudge factor" of between 5 and 10 [31, 34]. A more scientific approach is to modify the calculation of the covariance matrix once the parameters have estimated [133, 31]. For the case of the equation errors being coloured,

$$
\mathrm{E}[\boldsymbol{\epsilon}\boldsymbol{\epsilon}^T] = \mathrm{E}[\epsilon(i)\epsilon(j)] = \mathcal{R}_{\epsilon\epsilon}(i - j) = \mathcal{R}_{\epsilon\epsilon}(j - i) \quad i, j = 1, 2, \ldots, N
\tag{4.6.3}
$$

where $\mathcal{R}_{\epsilon\epsilon}$ is the autocorrelation matrix for the equation errors, which is estimated from the residuals as follows,

$$
\hat{\mathcal{R}}_{\epsilon\epsilon}(k) = \frac{1}{N}\sum_{i=1}^{N-k} \upsilon(i)\upsilon(i + k) = \hat{\mathcal{R}}_{\epsilon\epsilon}(-k) \quad k = 0, 1, 2, \ldots, l
\tag{4.6.4}
$$

The index k is the time separation of the residuals, with l denoting the maximum time difference. If it is assumed that residual at the ith data point is only significantly correlated with residuals in close proximity then the value of l can be small, typically $l = N/5$ [31].

Substituting Equation (4.6.3) into Equation (4.6.1), the parameter covariance corrected for coloured residuals becomes,

$$
\mathbf{P} = \left(\mathbf{X}^T\mathbf{X}\right)^{-1}\left[\sum_{i=1}^{N}\mathbf{x}(i)\sum_{j=1}^{N}\hat{\mathcal{R}}_{\epsilon\epsilon}(i - j)\mathbf{x}^T(j)\right]\left(\mathbf{X}^T\mathbf{X}\right)^{-1}
\tag{4.6.5}
$$

where $\mathbf{x}(i)$ denotes the ith row of the regressor matrix $\mathbf{X}$ and $\hat{\mathcal{R}}_{\epsilon\epsilon}(i-j)$ is the estimate of the autocorrelation matrix calculated from Equation (4.6.4).

In practice, it has been suggested that a factor of 2 is still often needed to match the scatter in parameter estimates from repeated manoeuvres [132] once the above correction has been made. Hence, some practitioners apply a "fudge factor" of 2 to achieve this and, in fact, the 20% guideline for acceptable standard errors, introduced in Section 4.5, assumes this factor of 2 has been applied [6]. Therefore, the standard errors presented in the examples throughout this thesis have been calculated with the additional "fudge factor" of 2.

4.7   UAV Yawing Moment Example

An example of the application of least squares estimation is presented in this section utilising UAV flight test data supplied by BAE Systems. The goal of the analysis was to find estimates of the aerodynamic derivatives in the non-dimensional yawing moment equation,

$$C_n = C_{n_0} + C_{n_\beta}\beta + C_{n_p}\hat{p} + C_{n_r}\hat{r} + C_{n_\xi}\xi + C_{n_\zeta}\zeta \tag{4.7.1}$$

where β is the sideslip angle, ξ is the aileron input and ζ is the rudder input. The variables $\hat{p}$ and $\hat{r}$ are the non-dimensional roll rate and yaw rate respectively, defined as,

$$\hat{p} = \frac{pb}{2V}, \quad \hat{r} = \frac{rb}{2V} \tag{4.7.2}$$

where b is the wingspan and V is the airspeed. For the estimation problem,

$$\mathbf{z} = \begin{bmatrix} C_n(1) & C_n(2) & \dots & C_n(N) \end{bmatrix}^T$$

$$\mathbf{X} = \begin{bmatrix} 1 & \beta(1) & \hat{p}(1) & \hat{r}(1) & \xi(1) & \zeta(1) \\ 1 & \beta(2) & \hat{p}(2) & \hat{r}(2) & \xi(2) & \zeta(2) \\ \vdots & \vdots & \vdots & \vdots & \vdots & \vdots \\ 1 & \beta(N) & \hat{p}(N) & \hat{r}(N) & \xi(N) & \zeta(N) \end{bmatrix}$$

$$\boldsymbol{\theta} = \begin{bmatrix} C_{n_0} & C_{n_\beta} & C_{n_p} & C_{n_r} & C_{n_\xi} & C_{n_\zeta} \end{bmatrix}^T$$

The analysis was performed on four data segments measured at the same flight condition. Least squares regression allows measured data from multiple manoeuvres to be stacked, or concatenated, together into the matrices $\mathbf{z}$ and $\mathbf{X}$. Analysing segments of data simultaneously increases the information content for the estimation process, which in turns increases the chance of obtaining reliable parameter estimates. The measurements contained two rudder doublets and two aileron doublets as shown in Figure 4.8. The excitation of rolling motion, as well as yawing motion, meant that there was increased information in the data regarding the cross-coupling derivatives C_{n_p} and C_{n_ξ}.

The yawing moment coefficient C_n was derived from the measurements using the equation,

$$C_n = \frac{1}{\bar{q}S\frac{b}{2}}[I_{zz}\dot{r} - I_{xz}(\dot{p} - qr) + (I_{yy} - I_{xx})pq] \tag{4.7.3}$$

The time histories of $\dot{p}$ and $\dot{r}$ were calculated using the global Fourier smoothing technique given in Equation (4.4.10). The noise levels in the regressor variables were very low, due to the
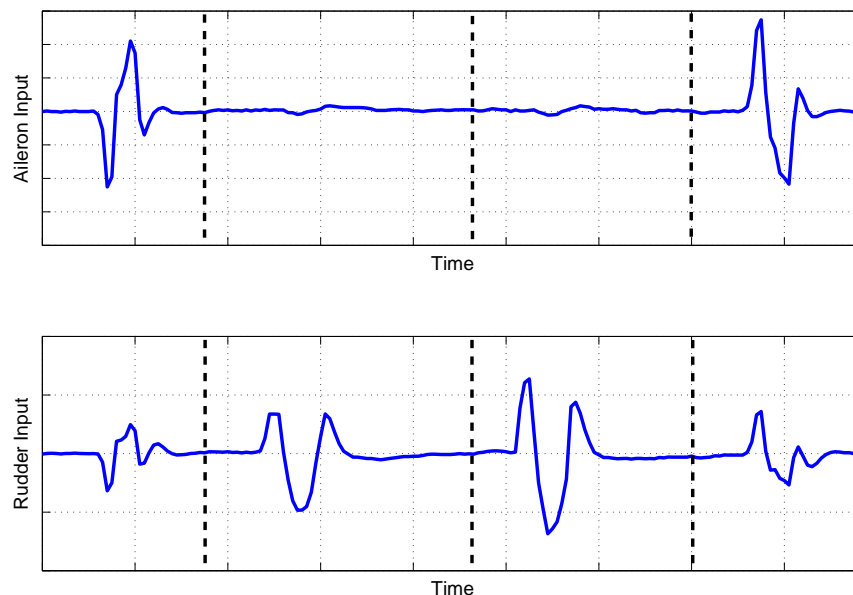
Figure 4.8: Aileron and rudder inputs for parameter
estimation

high precision of the instrumentation system and sensors, so estimation was attempted initially
without smoothing **X**. The parameter estimates are given in the first column of Table 4.1. Note
that the estimate of C_{n_0} was found to be very small so this parameter was removed from the
identified model. The second column of Table 4.1 contains the standard errors of the estimates
when the covariance matrix **P** was calculated using the correction for coloured residuals (Equation (4.6.5)). The standard errors are expressed as a percentage of the estimated parameter
value. Based on the discussion in Section 4.5, the standard errors for each parameter can be
considered acceptable, as their magnitudes are all around 20% of the corresponding parameter
estimate or under. The derivative with the highest uncertainty is the cross-coupling term C_{n_p},
which has a standard error of around 18%. The parameter estimate with the highest degree of
confidence is that for the rudder control power C_{n_ζ}, whose standard error is approximately 3%
of the estimated value.

	Unsmoothed Regressors		Smoothed Regressors	
	$\hat{\theta}$	$100[s/|\hat{\theta}|]$	$\hat{\theta}$	$100[s/|\hat{\theta}|]$
C_{n_β}	0.698	16.39	0.656	17.02
C_{n_p}	1.623	17.94	1.770	16.89
C_{n_r}	1.015	16.12	0.938	15.77
C_{n_ξ}	0.890	13.44	0.850	14.05
C_{n_ζ}	1.008	2.99	1.013	2.88

Table 4.1: Estimates of yawing moment derivatives

Inspection of the aileron and rudder inputs used for parameter estimation reveals that, while the
aileron doublets were being applied, the rudder was also being deflected by a small amount.
This automatic rudder input is used to counteract an uncommanded yawing motion experienced

by the aircraft when it rolls. Because some relationship exists between the aileron input and the rudder input, there is potential for the estimates of C_{n_ξ} and C_{n_ζ} to be highly correlated. Ideally, for system identification purposes, this function should be disengaged during the flight tests. However, analysis of the correlation coefficients, shown in Table 4.2, indicated that the two derivatives were sufficiently independent, with $\rho = 0.4102$. In fact, Table 4.2 shows that all the derivatives and the corresponding regressors could be considered independent of each other, as none of the correlation coefficients exceeded the 0.9 guideline.

	C_{n_β}	C_{n_p}	C_{n_r}	C_{n_ξ}	C_{n_ζ}
C_{n_β}	1	0.4534	0.0776	0.2758	0.1649
C_{n_p}	-	1	0.2793	0.7555	0.2182
C_{n_r}	-	-	1	0.2658	0.2810
C_{n_ξ}	-	-	-	1	0.4102
C_{n_ζ}	-	-	-	-	1

Table 4.2: Correlation coefficients for yawing moment
estimates - unsmoothed regressors

Theil's inequality analysis was also applied to the residuals. The values obtained were,

$$U = 0.1406, \ U_B = 0.0211, \ U_V = 0.0210, \ U_C = 0.9579$$

Recall from Section 4.5 that a good agreement between the measured response and the identified model is indicated by U being in the range 0.25-0.3 or under, the bias and variance portions, U_B and U_V, being close to zero and the covariance portion approaching a value of 1. Therefore, Theil's inequality analysis suggests that the parameter estimates and the identified model provide a satisfactory fit to the response recorded from the aircraft. Figure 4.9 shows the yawing moment coefficient derived from the measured data against the response of the identified model, calculated using the equation,

$$\hat{\mathbf{y}} = \mathbf{X}\hat{\boldsymbol{\theta}} \tag{4.7.4}$$

and also shows an accurate visual match between the measured and identified responses.

The analysis presented above was then repeated but with the regressors smoothed using the Fourier smoothing algorithm outlined in Section 4.3. The resulting parameter estimates are also shown in Table 4.1 along with their standard errors. As can be seen, the derivative values were very close to those obtained with the unsmoothed regressors. There was also little difference between the standard error values obtained from the two cases. In Appendix B, it is shown that the presence of noise in the regressors leads to an increase in the parameter variance. Therefore, the close match between the standard errors can be taken as an indicator of the low noise levels in the sensors. The correlation coefficients found from the smoothed regressors, displayed in Table 4.3, were close to those in Table 4.2 and Theil's analysis yielded very similar results to those for the unsmoothed case,

$$U = 0.1389, \ U_B = 0.0214, \ U_V = 0.0205, \ U_C = 0.9581$$

Figure 4.10 shows the identified time history of C_n achieved with the smoothed regressors plotted against the measured response.

To validate the parameter estimates and assess the predictive capability of the identified model, a comparison was made to a set of "unseen" flight test data not used for the preceding parameter
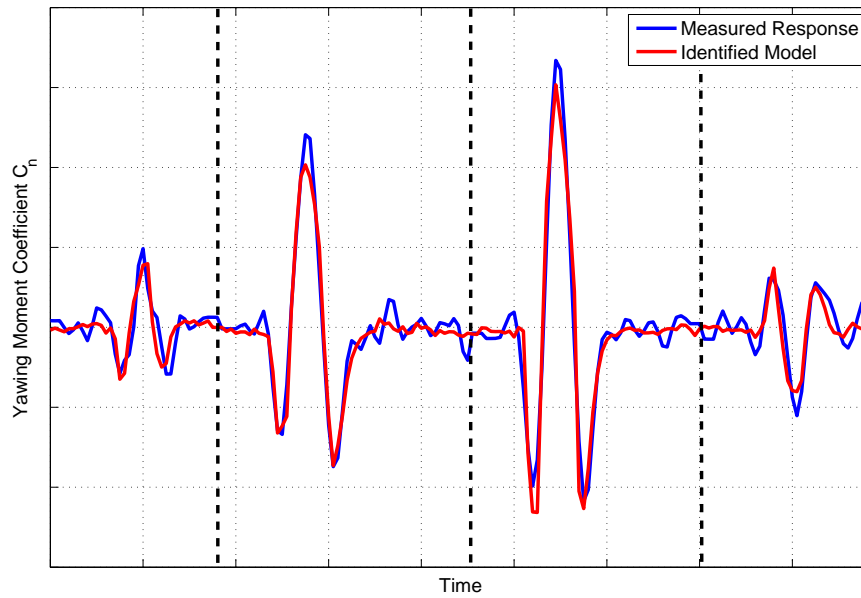
Figure 4.9: Measured and identified yawing moment
responses - unsmoothed regressors

	C_{n_β}	C_{n_p}	C_{n_r}	C_{n_ξ}	C_{n_ζ}
C_{n_β}	1	0.4405	0.0972	0.2803	0.1616
C_{n_p}	-	1	0.3144	0.7844	0.2561
C_{n_r}	-	-	1	0.2872	0.2950
C_{n_ξ}	-	-	-	1	0.4168
C_{n_ζ}	-	-	-	-	1

Table 4.3: Correlation coefficients for yawing moment
estimates - smoothed regressors
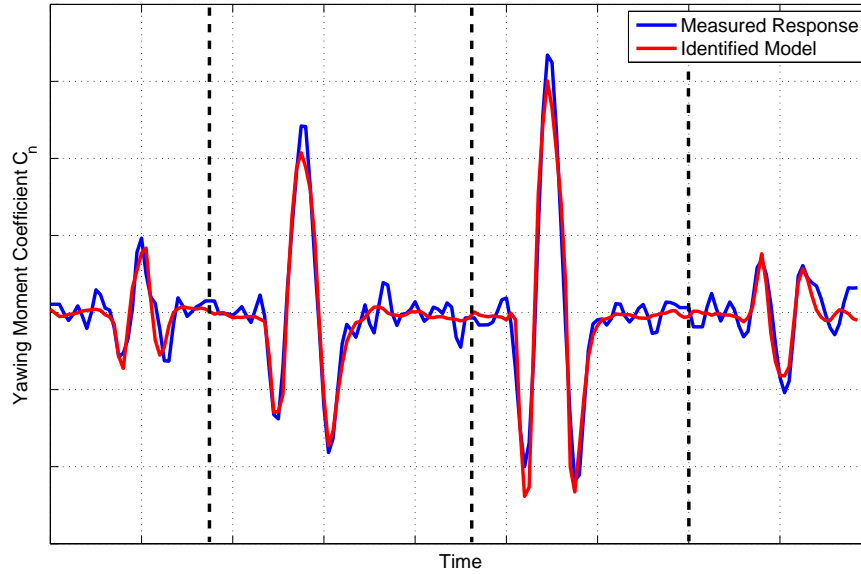
Figure 4.10: Measured and identified yawing moment
responses - smoothed regressors

estimation process. This data contained another aileron doublet and a rudder doublet, as shown in Figure 4.11. A predicted response was generated using Equation (4.7.4), with measurements of the dependent variable **z** and the regressors **X** coming from the unseen set of data but the parameter values in $\hat{\boldsymbol{\theta}}$ being those from the analysis on the first set of flight test data given in Table 4.1. Theil's inequality was then used to assess the match between the measured and predicted responses. The results were,

$$U = 0.1165, \ U_B = 0.0063, \ U_V = 0.0419, \ U_C = 0.9517$$

Again, Theil's inequality analysis indicated an excellent fit between the measured and predicted responses, further confirming the veracity of the parameter estimates and the identified model. Figure 4.12 contains time histories of the measured and predicted responses. This process of validation illustrated above is the basis for the proof-of-match assessment performed when developing training simulators, described earlier in Chapter 2.

4.8 UAV Nonlinear Yawing Moment Example

In Equation (4.2.1), it was assumed that the relationship between the dependent variable y and the n regressors X_1, X_2,…,X_n was linear. However, linear models tend to be valid for only a very small portion of the flight envelope and it is often desirable to have a model which can adequately describe the aircraft's behaviour over a range of flight conditions. This will undoubtedly require a model which is nonlinear. Least squares estimation can still be used to estimate the parameters for a nonlinear model provided that the equations of motion are linear in terms of the parameters to be estimated. A simple example is to modify the non-dimensional pitching moment equation in (4.4.2) to the following,

$$C_m = C_{m_0} + C_{m_\alpha}\alpha + C_{m_{\alpha^2}}\alpha^2 + C_{m_q}\hat{q} + C_{m_\eta}\eta \tag{4.8.1}$$
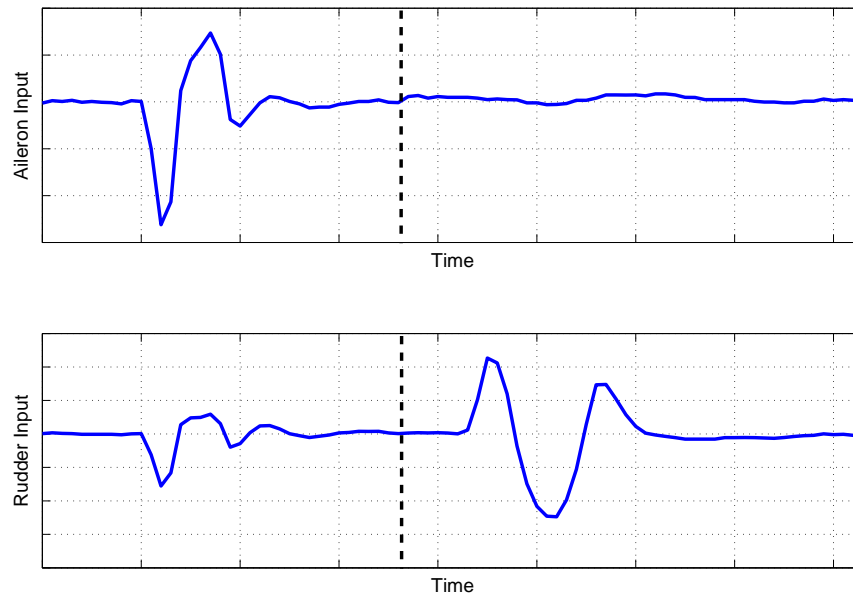
Figure 4.11: Aileron and rudder inputs for validation
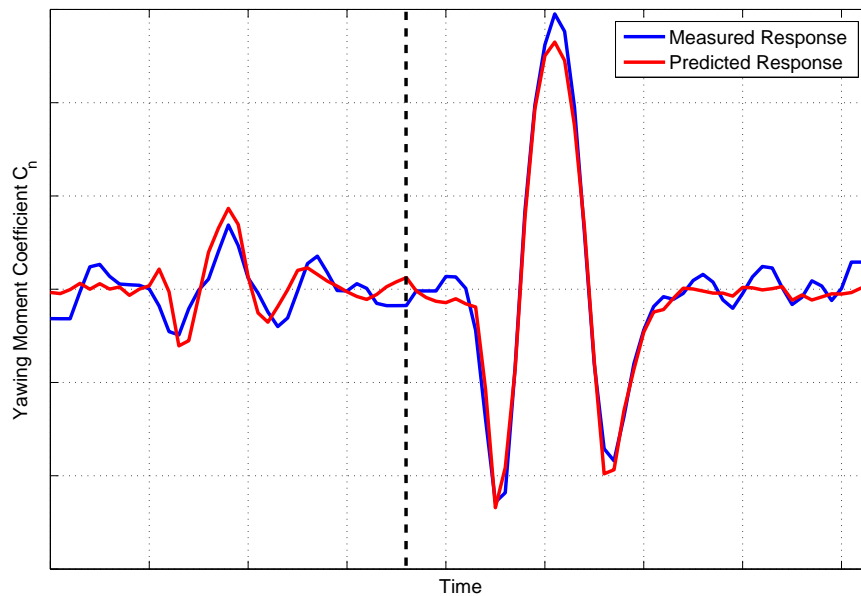
Figure 4.12: Measured and predicted yawing moment
responses for validation process

where the derivative $C_{m_{\alpha 2}}$ has been included to account for the nonlinear effect of changes in the pitching moment with respect to the square of the angle of attack. Equation (4.8.1) is now nonlinear in the regressors, because of the appearance of α^2, but remains linear in the parameters. Therefore, least squares regression can still be used for the estimation problem.

The change in the stability and control derivatives over the flight condition can be described efficiently using spline functions [134, 31]. Spline functions are defined as piecewise polynomials [130], where piecewise implies that the polynomials are different for specific ranges of the variables that define the flight conditions, such as angle of attack or Mach number. At the locations where the piecewise polynomials join, known as knots, the function values and derivatives must agree.

Second degree spline functions were used to model the directional stability C_{n_β} and rudder control power C_{n_ζ} as functions of sideslip angle. The range of sideslip angles analysed was -15 to 15 deg and allowed asymmetric effects to be investigated. The remaining yawing moment derivatives C_{n_0}, C_{n_p}, C_{n_r} and C_{n_ξ} were assumed to be independent of β. Hence, the yawing moment equation can be written as,

$$C_n(\beta) = C_{n_0} + C_{n_\beta}(\beta)\beta + C_{n_p}\hat{p} + C_{n_r}\hat{r} + C_{n_\xi}\xi + C_{n_\zeta}(\beta)\zeta \tag{4.8.2}$$

Using rudder control power as an example, $C_{n_\beta}(\beta)$ and $C_{n_\zeta}(\beta)$ were modelled in the following manner,

$$C_{n_\zeta}(\beta) = C_{n_\zeta}(0) + C_{n_{\zeta\beta}}\beta + C_{n_{\zeta\beta 2}}\beta^2 + \sum_{i=1}^{k} D_{\beta_i}(\beta - \beta_i)^2_+ \tag{4.8.3}$$

where,

$$(\beta - \beta_i)^2_+ = \begin{cases} (\beta - \beta_i)^2 & \beta \geq \beta_i \\ 0 & \beta < \beta_i \end{cases} \tag{4.8.4}$$

and β_i is the ith of the k knot locations. The associated parameters D_{β_i} are constants that quantify the contribution of each spline and are estimated along with the aerodynamic derivatives.

The knots were located at nine angles of sideslip between -15 and 15 degrees, with the number of unknown parameters to be determined being 28. Data from 27 manoeuvres, covering the angle of sideslip range, was used for the estimation process. Figures 4.13 and 4.14 show the variations of C_{n_β} and C_{n_ζ} with sideslip identified from the data. The results suggested that the values of both derivatives vary significantly with changes in β and that the variations were asymmetric about the origin. Also shown on the plots are the parameter estimates from the linear analysis outlined in Section 4.7, which was carried out on data recorded at $\beta = 0$ deg. For both derivatives, there was a satisfactory agreement between the values obtained from the linear analysis and those for the nonlinear estimation. The estimate from Section 4.7 for C_{n_β} was 0.698 and the nonlinear estimate, at $\beta = 0$ deg, was 0.764, while for C_{n_ζ} the linear and nonlinear estimates were 1.008 and 0.876 respectively. Estimates for the remaining yawing moment derivatives are given in Table 4.4, with the values from Section 4.7 repeated in the second column. There is a close match between the linear and nonlinear values of C_{n_ξ}. However, a greater discrepancy exists in the estimates for the damping derivatives C_{n_p} and C_{n_r}, with the magnitudes of the nonlinear estimates being smaller in size compared to the values from Section 4.7. The final column of Table 4.4 shows the standard errors of the nonlinear estimates (corrected for coloured residuals). The standard errors are all around 10% or under, indicating a strong confidence in all of the estimates values.
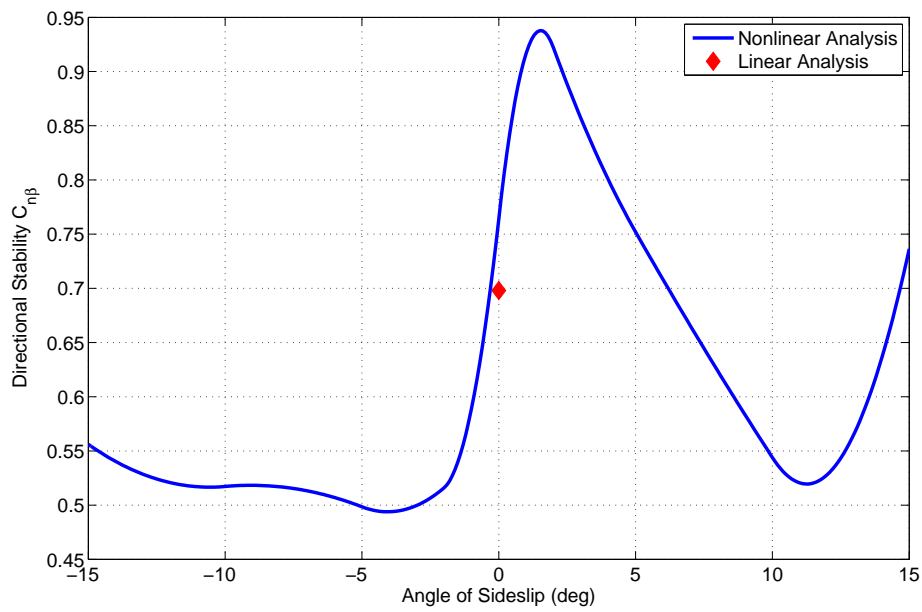
Figure 4.13: Variation of directional stability C_{n_β} with sideslip
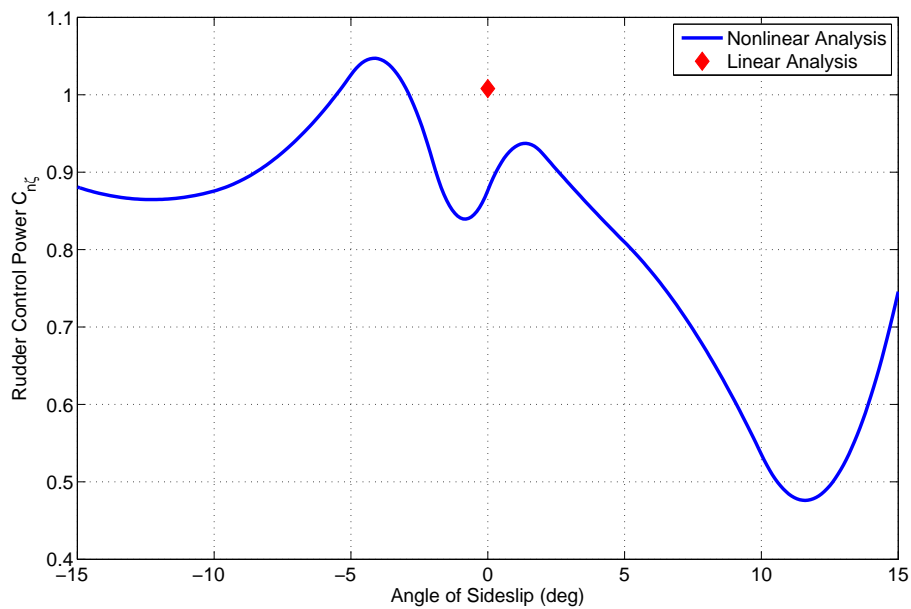
Figure 4.14: Variation of directional stability C_{n_ζ} with sideslip

	$\hat{\theta}_{NL}$	$\hat{\theta}_L$	$100[s/|\hat{\theta}|]$
C_{n_p}	0.813	1.623	9.03
C_{n_r}	0.558	1.015	10.74
C_{n_ξ}	0.982	0.890	4.83
C_{n_0}	0.500	-	8.11

Table 4.4: Comparison of yawing moment derivatives from linear and nonlinear analysis

The results of Theil's inequality analysis for the residuals were,

$$U = 0.3922, \ U_B = 0.0000, \ U_V = 0.1538, \ U_C = 0.8462$$

The value of the inequality coefficient U was relatively high, based on the 0.25-0.3 guideline stated in Section 4.5. The variance portion was also significant, suggesting that the identified model might be poor in duplicating the variability of the true system. However, the bias portion was negligibly small, indicating that there was no systematic error in the identified model, and the covariance portion was also relatively close to 1. Figure 4.15 shows the time histories of the measured and identified responses from the nonlinear analysis for the four data segments used for parameter estimation in Section 4.7. Again, visually, a relatively good fit was achieved, although the identified model tended to under-predict the values of C_n at the peaks.
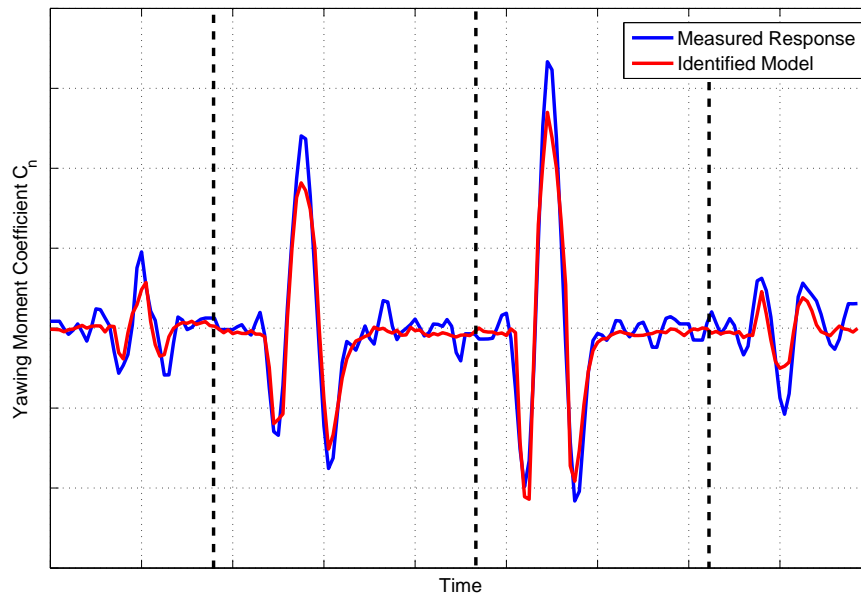
Figure 4.15: Measured and identified yawing moment responses

For validation, the nonlinear model was used to predict the aircraft's response to two rudder inputs not used in the parameter estimation process and the predicted response was then compared to the unseen measured response. These two rudder inputs are shown in Figure 4.16 and the measured and predicted yawing moment responses are shown in Figure 4.17. Qualitatively, there was a good fit between the measured and predicted responses although, as with

Figure 4.15, the model tended to under-predict the values of C_n at the peaks. Theil's inequality analysis was also applied to the predicted residuals with the results as follows,

$$U = 0.2242, \; U_B = 0.0376, \; U_V = 0.1507, \; U_C = 0.8116$$

The inequality coefficient fell below the 0.25-0.3 region, indicating a satisfactory fit between the measured and predicted responses. The bias portion was also small. However, the variance portion could be considered relatively high.
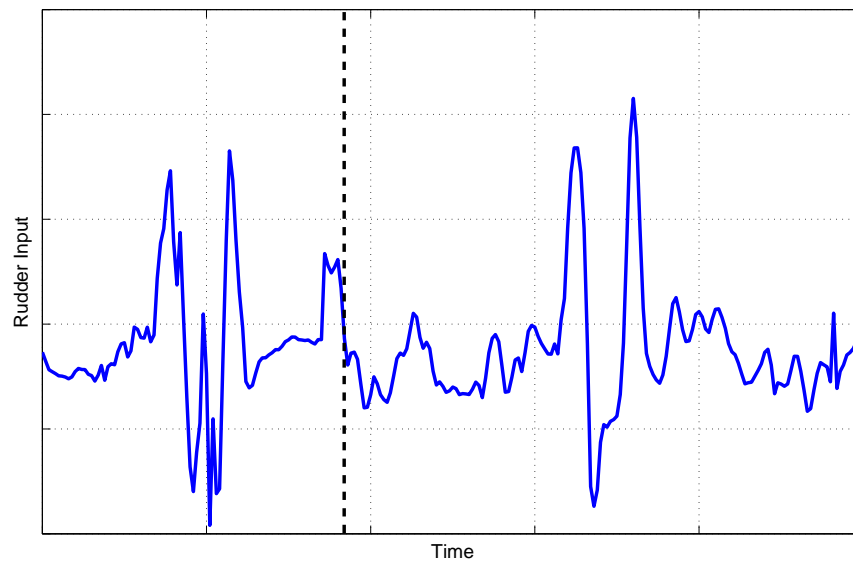
Figure 4.16: Rudder inputs for validation process

The above analysis illustrated that ordinary least squares regression can be used for estimating parameters in a nonlinear model, provided that the model is linear in the parameters. However, the method cannot be implemented if the equations of motion are nonlinear in terms of the parameters to be estimated. This is the case when estimating aerodynamic derivatives from nonlinear regions of the flight envelope, such as near or post-stall. A simpler example of the equations being nonlinear in the parameters, often encountered in practice, is if the measured variables contain time delays relative to each other. Accurate knowledge of time delays is important as it has been shown that time shifts in the data lead to degraded estimates of the stability and control derivatives, particularly if the time shift is in the control input [135]. There are a number of way of dealing with time shifts, with two approaches investigated during this research. The simplest method is to inspect the data and manually shift any delayed variable to synchronise it with the others. This generally means that the time shift has to be approximated as a multiple of the data sampling time Δt. Interpolation could be used to overcome this constraint but introduces another, potentially time-consuming, pre-processing step prior to estimation. A more rigorous approach is to include the time delays in the vector of unknown parameters to be determined. However, as mentioned above, this leads to the estimation problem becoming nonlinear and ordinary least squares regression cannot be used in this situation. Instead, manual time shifting of variables must be applied. An example of this process is presented next.
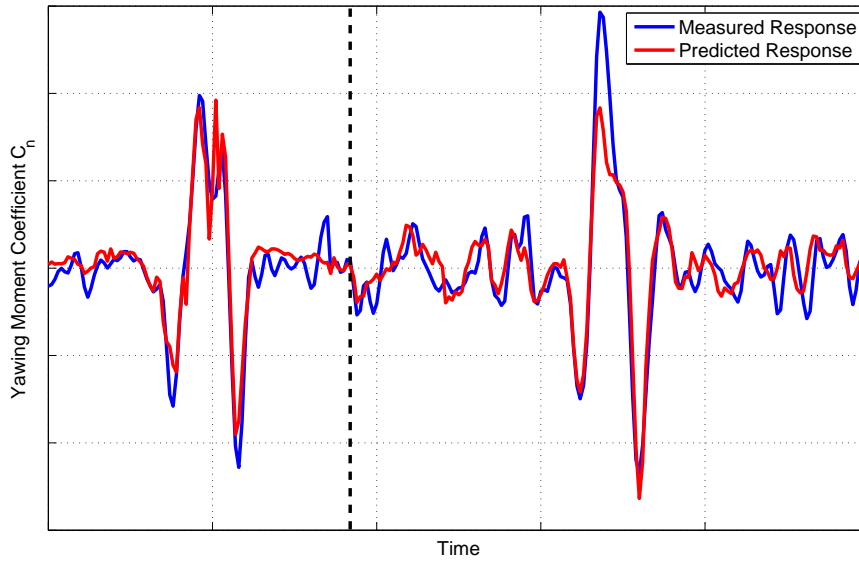
Figure 4.17: Measured and predicted yawing moment
responses for validation process

4.9 DEMON Dutch Roll Example

When performing parameter estimation on data from the dynamic wind tunnel models, it was necessary to account for a time delay caused principally by the need to transmit and receive data through the wireless network. The block diagram in Figure 4.18 illustrates the process of transmitting and logging the data. The control inputs were time-logged when the user command was applied at the ground station and the resultant response was time-logged when the data was received from the sensors. Ideally, all input and output data should have been time-logged by a processor onboard the wind tunnel models, thus removing the time delay. However, because the instrumentation used was large purchased off-the-shelf, this option was viewed as being impractical.

The state-space equations of motion incorporating a time delay can be written in the general form,

$$\dot{\mathbf{x}}(t) = \mathbf{A}\mathbf{x}(t) + \mathbf{B}\mathbf{u}(t - \boldsymbol{\tau}) \tag{4.9.1}$$

$$\mathbf{y}(t) = \mathbf{C}\mathbf{x}(t) + \mathbf{D}\mathbf{u}(t - \boldsymbol{\tau}) \tag{4.9.2}$$

Hence, although the wind tunnel model dynamics were linear, attempting to estimate the elements of $\boldsymbol{\tau}$ makes the parameter estimation process nonlinear. Another difficulty was that the time delay was not constant for every manoeuvre but was found to vary approximately between 0.23 and 0.35 seconds.

For the example presented here, inspection of a segment of data, containing a 1-1-2 input to the rudder of the 1/3 scale DEMON model, revealed a delay of around 0.26 seconds between the command being sent to the model and the resultant response being received. Hence, the rudder input data, shown in Figure 4.19, was time shifted forward by 0.26 sec to match the sensor measurements, before least squares estimation was carried out to find estimates of the
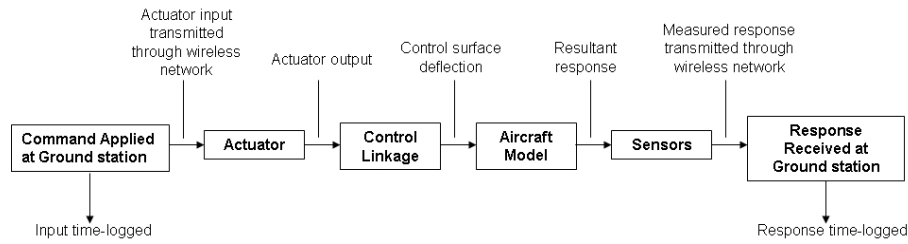
Figure 4.18: Transmission and logging of data

derivatives in following equation,

$$\begin{bmatrix} \dot{v} \\ \dot{r} \end{bmatrix} = \begin{bmatrix} 0 & -V_T \\ n_v & n_r \end{bmatrix} \begin{bmatrix} v \\ r \end{bmatrix} + \begin{bmatrix} 0 \\ n_\zeta \end{bmatrix} \zeta + \begin{bmatrix} b_{\dot{v}} \\ b_{\dot{r}} \end{bmatrix} \tag{4.9.3}$$

The additional terms, $b_{\dot{v}}$ and $b_{\dot{r}}$, are lumped bias parameters which account for uncertainty in the control inputs and the initial conditions of the states [34]. These are unknowns so had to be estimated along with the stability and control derivatives. Although the wind tunnel speed was known (30 m/s), the V_T term in the equations of motion was also treated as an unknown to be determined.
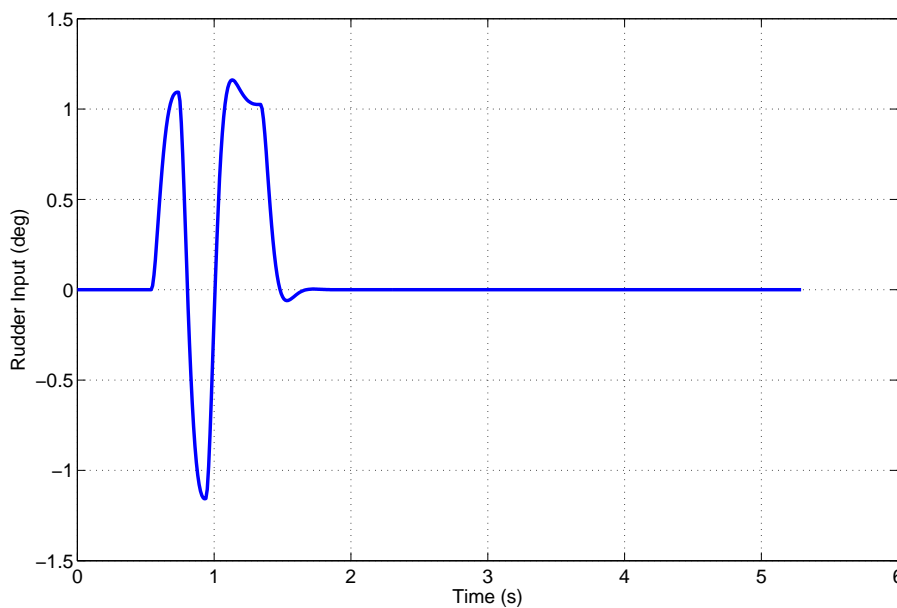
Figure 4.19: 1-1-2 input applied to the rudder

The equation error approach deals with each of the equations of motion separately, hence estimation was carried out twice - once for $\dot{v}$ as the dependent variable and once with $\dot{r}$ as dependent variable. For the lateral velocity equation, the regressors were simply r and a vector of 1s to account for the bias term. For the yaw equation, v and ζ were also included as regressors.

In the example outlined in Section 4.7, it was shown that for the UAV data, recorded using conventional instrumentation, the results of least squares estimation obtained with unsmoothed regressors matched closely to those determined using smoothed regressors. It could therefore be concluded that the noise in these high accuracy sensors was low enough that it did not

adversely affect the least squares estimates. To investigate the effects of noise in the measurements from the MEMS IMU, the results of a similar analysis will be presented here. Initially no smoothing was performed on the regressors (although smoothing was still performed before differentiating v and r to obtain the dependent variables). The resulting estimates are shown in the first column of Table 4.5 alongside the associated standard errors expressed as a percentage of the estimated parameter values. Again, the correction for coloured residuals was applied. Despite the regressors being unsmoothed, the standard errors of the least squares estimates are all acceptably low. Figure 4.20 shows the time histories of lateral acceleration $\dot{v}$ and yaw acceleration $\dot{r}$ plotted against the responses obtained from the identified model and indicates a close fit between the two.

	Unsmoothed Regressors		Smoothed Regressors	
	$\hat{\theta}$	$100[s/|\hat{\theta}|]$	$\hat{\theta}$	$100[s/|\hat{\theta}|]$
V_T	29.4739	0.25	29.5486	0.25
n_v	3.3571	1.99	3.3691	1.97
n_r	-2.0834	11.37	-2.1140	11.16
n_ζ	-5.9186	7.42	-5.9894	7.32
$b_{\dot{v}}$	0.9621	4.05	0.9668	4.00
$b_{\dot{r}}$	0.8828	19.05	0.8910	18.72

Table 4.5: Estimates of DEMON dutch roll derivatives
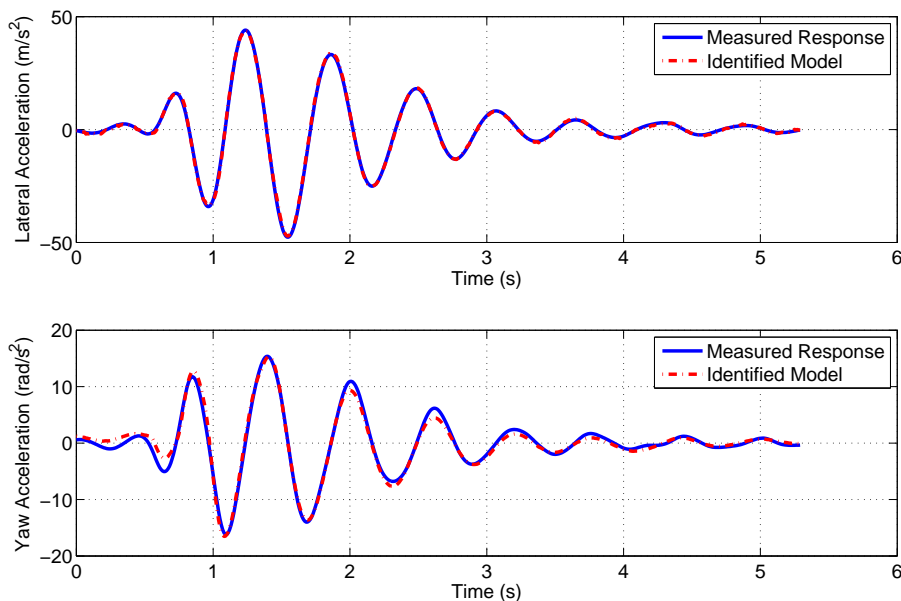
Figure 4.20: Measured and identified responses for DEMON lateral and yaw acceleration - unsmoothed regressors

The pair-wise correlation coefficients for the parameter estimates are given in Table 4.6. The values all fell below the 0.9 guideline, hence the estimated parameters and corresponding regressors can be considered to be sufficiently independent. Because the lateral velocity and yaw rate equations are treated separately, correlation between the lateral force derivatives and the

yawing moment derivatives cannot be calculated. Theil's inequality analysis was applied to the residuals of both $\dot{v}$ and $\dot{r}$ and the following results were found,

$$\dot{v} : \ U = 0.0175, \ U_B = 0.0000, \ U_V = 0.0003, \ U_C = 0.9997$$
$$\dot{r} : \ U = 0.0753, \ U_B = 0.0000, \ U_V = 0.0057, \ U_C = 0.9943$$

	V_T	$b_{\dot{v}}$	n_v	n_r	n_ζ	$b_{\dot{r}}$
V_T	1	0.1051	-	-	-	-
$b_{\dot{v}}$	-	1	-	-	-	-
n_v	-	-	1	0.1261	0.2017	0.0112
n_r	-	-	-	1	0.6670	0.1382
n_ζ	-	-	-	-	1	0.1543
$b_{\dot{r}}$	-	-	-	-	-	1

Table 4.6: Correlation coefficients for DEMON dutch roll derivatives - unsmoothed regressors

The above process was then repeated but with the Fourier smoothing technique applied to the regressors before estimation. The estimated values and standard errors are also shown in Table 4.5. In comparison to the case of the unsmoothed regressors, the parameter values were very similar. As expected, when the regressors were smoothed the standard errors decreased, however this increase in the confidence of the parameter values was marginal. The pair-wise correlation coefficients calculated for the smoothed regressors are displayed in Table 4.7. Again, the values were very similar between the two cases. The match between the dependent variables derived from measurement and those predicted by the model are shown in Figure 4.21. Theil's inequality analysis gave the following results for the match between the measured and identified responses,

$$\dot{v} : \ U = 0.0128, \ U_B = 0.0000, \ U_V = 0.0002, \ U_C = 0.9998$$
$$\dot{r} : \ U = 0.0753, \ U_B = 0.0000, \ U_V = 0.0057, \ U_C = 0.9943$$

	V_T	$b_{\dot{v}}$	n_v	n_r	n_ζ	$b_{\dot{r}}$
V_T	1	0.1082	-	-	-	-
$b_{\dot{v}}$	-	1	-	-	-	-
n_v	-	-	1	0.1240	0.1975	0.0124
n_r	-	-	-	1	0.6709	0.1405
n_ζ	-	-	-	-	1	0.1566
$b_{\dot{r}}$	-	-	-	-	-	1

Table 4.7: Correlation coefficients for DEMON dutch roll derivatives - smoothed regressors

From the above analysis, there were no significant differences between the results obtained with the unsmoothed regressors and those achieved when the regressors were smoothed. This suggests that the noise levels in the measurements provided by the MEMS IMU were not large enough to significantly degrade the least squares estimates and that the data provided by the unit was of good enough quality to obtain reliable parameter estimates.
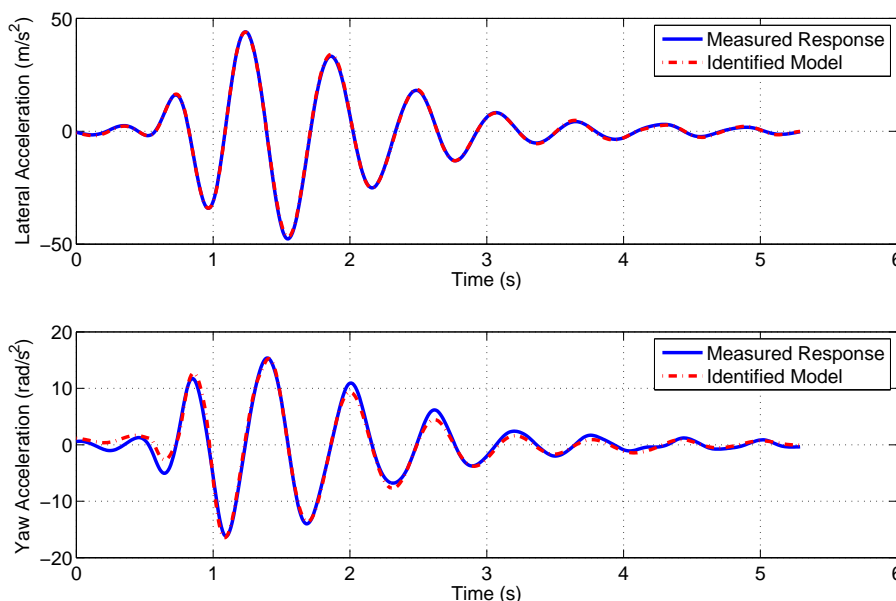
Figure 4.21: Measured and identified responses for
DEMON lateral and yaw acceleration - smoothed
regressors

For the validation step, a rudder doublet manoeuvre was applied to the identified model to generate a predicted response and was compared to the measured data for the same input. The measured and predicted time histories are shown in Figure 4.22 and the results of Theil's inequality analysis for the predicted dependent variables were,

$$\dot{v}: \; U = 0.0186, \; U_B = 0.0000, \; U_V = 0.0003, \; U_C = 0.9997$$
$$\dot{r}: \; U = 0.1321, \; U_B = 0.1002, \; U_V = 0.0280, \; U_C = 0.8712$$

Hence, there was good agreement between the measured and predicted responses, although the value of U_B for yaw acceleration could be considered to be on the high side.

Looking again at the derivative values in Table 4.5, it can be seen that there were significant differences between some of the equation error parameter estimates and the DEMON *a priori* values, given in Equation (2.5.4) in Chapter 2, which were used to design the multistep inputs. The directional stability n_v was around half the size of the empirical estimate, while there were factors of around 3 between the *a priori* and least squares estimates of the yaw damping term n_r and the rudder control power n_ζ. However, the standard errors, correlation coefficients and the analysis of the residuals all indicated that the parameter estimates were reliable and the identified model was validated against a second segment of data. Therefore, it can be concluded that, despite the *a priori* information being limited, the design of the 1-1-2 input was still adequate to excite the DEMON yaw dynamics. If this were not the case, the standard errors and correlation coefficients would have been higher. Most likely, this observation is due to the ability of the multistep inputs to excite a wide band of frequencies.
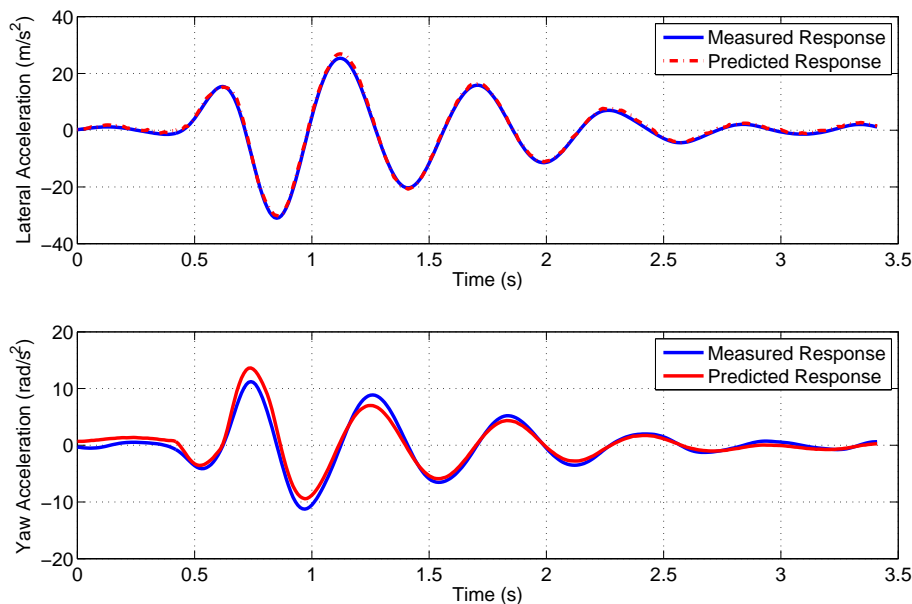
Figure 4.22: Measured and predicted DEMON dutch roll responses for rudder doublet validation manoeuvre

4.10 Hawk Short Period Example

To further investigate the effects of noise in the MEMS IMU data on least squares estimates, the process outline above was repeated on measurements recorded from the 1/12 scale Hawk. The manoeuvre used in this example was a 3-2-1-1 input to the elevator, shown in Figure 4.23, and the equations of interest were,

$$\begin{bmatrix} \dot{w} \\ \dot{q} \end{bmatrix} = \begin{bmatrix} 0 & V_T \\ m_w & m_q \end{bmatrix} \begin{bmatrix} w \\ q \end{bmatrix} + \begin{bmatrix} 0 \\ m_\eta \end{bmatrix} \eta + \begin{bmatrix} b_{\dot{w}} \\ b_{\dot{q}} \end{bmatrix} \tag{4.10.1}$$

where $b_{\dot{w}}$ and $b_{\dot{q}}$ are bias terms similar to those estimated in the previous example. The velocity term V_T was, again, also treated as an unknown. A time delay of 0.31 seconds in the elevator input was found from inspection of the data and removed prior to estimation.

The least squares estimates were, again, obtained first without any smoothing of the regressors. The parameter values and their standard errors are given in Table 4.8. As in the example presented in Section 4.9, despite no smoothing being performed on the regressors, the standard errors indicated a high level of confidence in the derivative values, with all parameters having standard errors below 10%. The pair-wise correlation coefficients of the estimates were also all below the 0.9 guideline, as shown in Table 4.9, and Theil's inequality analysis indicated an accurate match between the measured response and the identified model,

$$\dot{w}: \; U = 0.0448, \; U_B = 0.0000, \; U_V = 0.0020, \; U_C = 0.9980$$
$$\dot{q}: \; U = 0.1506, \; U_B = 0.0000, \; U_V = 0.0227, \; U_C = 0.9773$$

The time histories of $\dot{w}$ and $\dot{q}$ from both the measurements and identified model are plotted in Figure 4.24. It can be seen, particularly in the plot for pitch acceleration, that the responses obtained from the identified model contain a high frequency oscillatory component. This is due
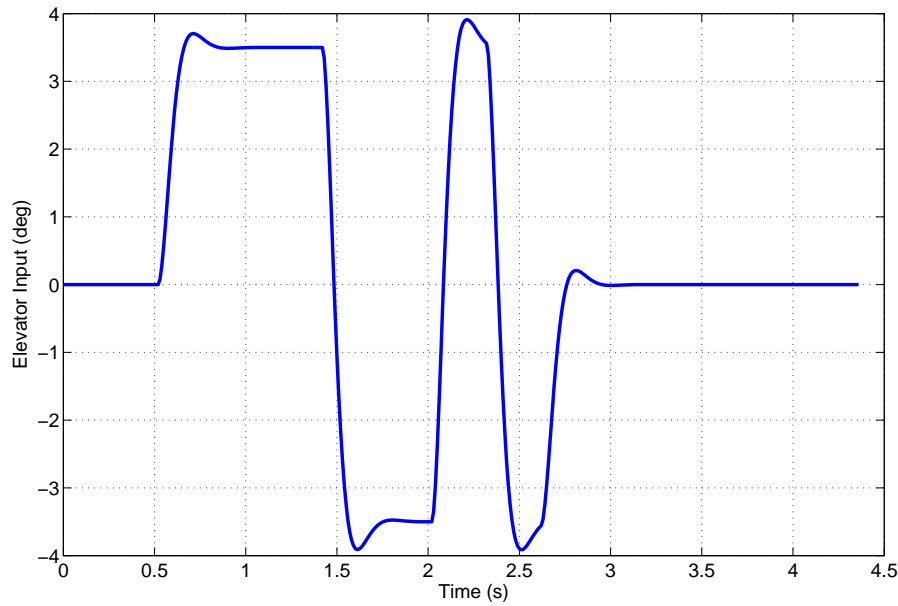
Figure 4.23: Plot of the 3-2-1-1 input applied to the
Hawk's elevator

	Unsmoothed Regressors		Smoothed Regressors	
	$\hat{\theta}$	$100[s/|\hat{\theta}|]$	$\hat{\theta}$	$100[s/|\hat{\theta}|]$
V_T	28.8759	1.14	28.9443	1.12
m_w	-1.3313	3.58	-1.3495	3.73
m_q	-3.7722	9.08	-3.8208	9.24
m_η	-2.2053	6.39	-2.2330	6.38
$b_{\dot{w}}$	0.5494	3.84	0.5508	3.79
$b_{\dot{q}}$	0.3509	7.02	0.3564	6.98

Table 4.8: Estimates of Hawk short period derivatives

	V_T	$b_{\dot{w}}$	m_w	m_q	m_η	$b_{\dot{q}}$
V_T	1	0.3983	-	-	-	-
$b_{\dot{w}}$	-	1	-	-	-	-
m_w	-	-	1	0.3178	0.4047	0.4288
m_q	-	-	-	1	0.7039	0.2198
m_η	-	-	-	-	1	0.3571
$b_{\dot{q}}$	-	-	-	-	-	1

Table 4.9: Correlation coefficients for Hawk short period
derivatives - unsmoothed regressors

to an undesirable structural vibration in the wind tunnel rig that was found to predominantly affect the longitudinal motion variables. Its presence can be seen in Figure 4.25, which shows a plot of the Fourier sine series coefficients of the angle of attack data against frequency. The Fourier sine series coefficients with large amplitudes located at frequencies below 3Hz belong to the model's rigid-body dynamics. Above 3Hz, the amplitudes reduce to a relatively small and constant value, corresponding to noise in the data. However, the amplitudes increase again at approximately 8-9Hz. This is caused by the structural vibration. Note that the time histories of $\dot{w}$ and $\dot{q}$ derived from the measurement do not contain the effects of the vibration as the data was smoothed prior to differentiation. Therefore, the results presented above indicated that statistically reliable parameter estimates were still achieved despite the data being corrupted by the vibration.
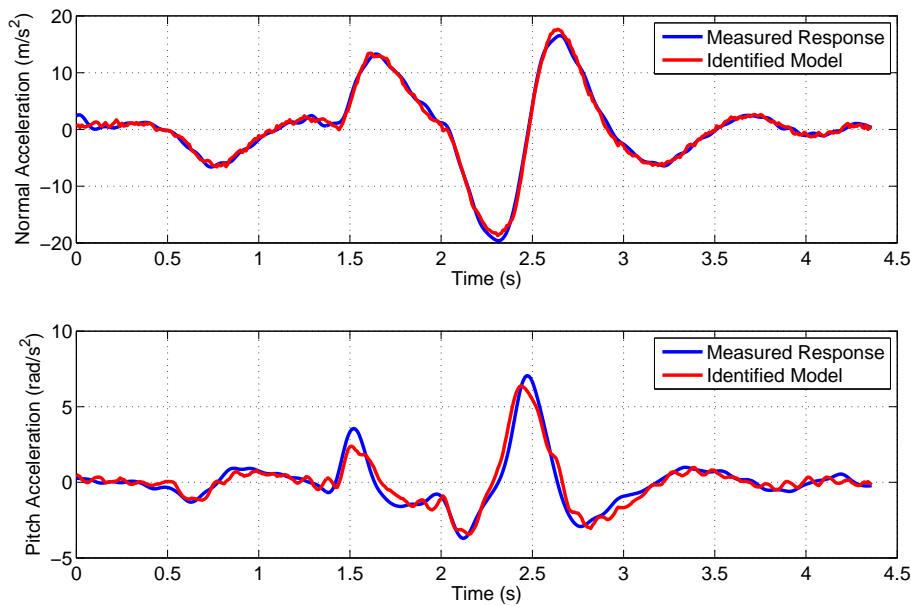
Figure 4.24: Measured and identified responses for Hawk normal and pitch acceleration - unsmoothed regressors

Again, the estimation process was repeated but with the regressors smoothed to remove the presence of the vibration and measurement noise. The least squares estimates and corresponding standard errors are given in the right hand side of Table 4.8. As with the example in Section 4.9, the parameter values found with smoothed regressors were very similar to those for the unsmoothed case. There was also little change in the standard errors of the estimates. The same was true for the correlation coefficients, which are displayed in Table 4.10 for the smoothed regressors. From Theil's analysis, the following match between the measured and identified responses was obtained,

$$\dot{w}: \quad U = 0.0379, \quad U_B = 0.0000, \quad U_V = 0.0014, \quad U_C = 0.9986$$
$$\dot{q}: \quad U = 0.1419, \quad U_B = 0.0000, \quad U_V = 0.0201, \quad U_C = 0.9799$$

The above figures indicate a slight improvement in the match in comparison to the unsmoothed case. Again, however, the improvement is not significant. Therefore, although MEMS sensors have a reputation for providing noisier outputs in comparison to more traditional instrumentation types, the analysis outlined here, as well as in Section 4.9, suggests that the noise corrupting
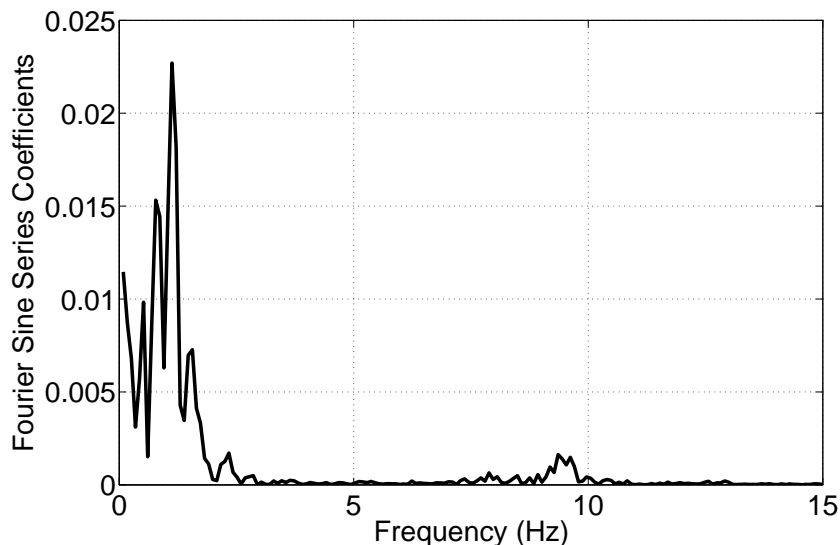
Figure 4.25: Fourier sine series coefficients for angle of
attack against frequency

the outputs from the MEMS IMU was not great enough to affect the least squares estimates. Figure 4.26 shows the measured and identified responses for $\dot{w}$ and $\dot{q}$ when the regressors were smoothed. This time, the effects of the structural vibration were not observed.

	V_T	$b_{\dot{w}}$	m_w	m_q	m_η	$b_{\dot{q}}$
V_T	1	0.3995	-	-	-	-
$b_{\dot{w}}$	-	1	-	-	-	-
m_w	-	-	1	0.3129	0.4148	0.4463
m_q	-	-	-	1	0.6871	0.2079
m_η	-	-	-	-	1	0.3674
$b_{\dot{q}}$	-	-	-	-	-	1

Table 4.10: Correlation coefficients for Hawk short period
derivatives - smoothed regressors

For the validation process, an elevator doublet was applied to the identified model to create the predicted response. The comparison to the measured data is illustrated in Figure 4.27 and shows that visually the predicted response fitted closely to the measured data. Theil's analysis also suggested the predicted response was an accurate match to the measured response,

$$\dot{w}: \quad U = 0.0529, \ U_B = 0.0032, \ U_V = 0.0019, \ U_C = 0.9949$$
$$\dot{q}: \quad U = 0.1796, \ U_B = 0.0150, \ U_V = 0.0473, \ U_C = 0.9377$$

In comparison to the analysis presented for the DEMON in the previous section, the least squares estimates in Table 4.8 match more closely to the *a priori* values given in Chapter 2, with the two sets of values agreeing with each other in within around 20%. This was to be expected, as the Hawk model was a more conventional configuration which had been extensively analysed in previous research projects.
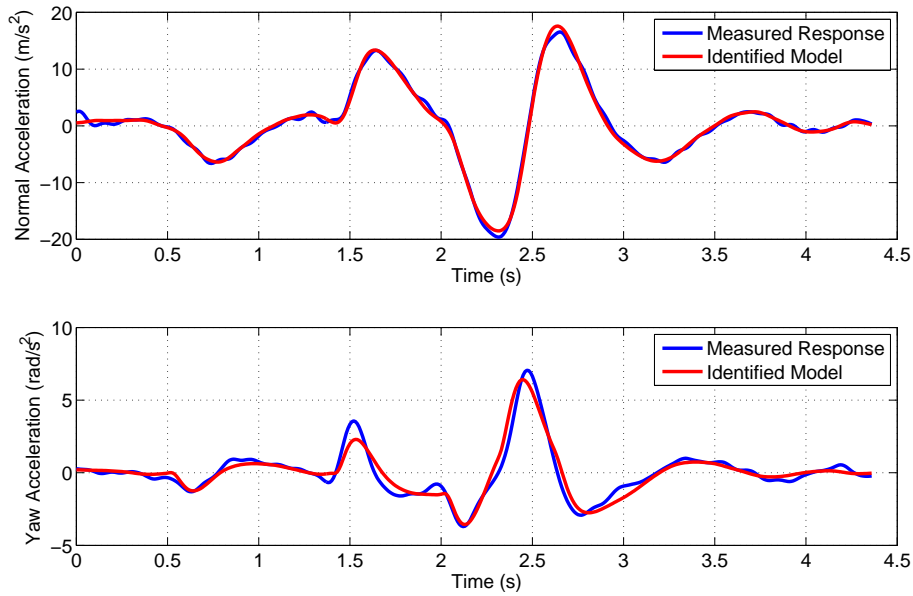
Figure 4.26: Measured and identified responses for Hawk
normal and pitch acceleration - smoothed regressors
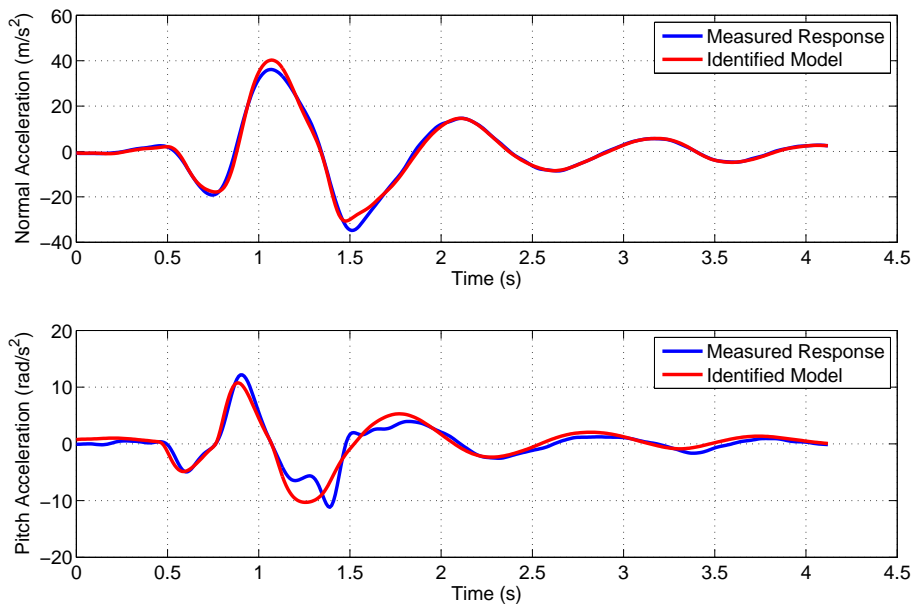
Figure 4.27: Measured and predicted Hawk short period
response for elevator doublet validation manoeuvre

Chapter 5

Output Error Method

5.1 Introduction

As described in the previous chapter, the aim of the equation error approach is to find a model for the aircraft dynamics which matches dependent variables derived from flight test data. A drawback of the method is that the regressors are assumed to be free of errors. In practice, the measured data is always corrupted by noise and systematic errors. If these errors are significant, this can lead to inaccurate parameter estimates. A different formulation for the estimation process is the output error method, in which the objective is to find a model which matches the measurements from the aircraft. Because a direct comparison is being made between the measured outputs $\mathbf{z}$ and estimated outputs $\hat{\mathbf{y}}$, measurement noise in the output variables is explicitly accounted for. However, the relationship between the unknown parameters to be determined $\boldsymbol{\theta}$ and the aircraft output variables $\mathbf{y}$ can be nonlinear. Thus the estimation problem itself is nonlinear, which requires a more computationally complex algorithm. For aircraft parameter estimation, the maximum likelihood principle is used to solve the output error formulation. Maximum likelihood estimation is a probabilistic approach, the idea being that the correct values of the unknown parameters are those that are most likely to have led to the observed aircraft response. Mathematically, a likelihood function is formed and the parameter estimates are the values that optimise this function.

5.2 Maximum Likelihood Estimation

Consider the following equation for the measurements from an aircraft,

$$\mathbf{z} = \mathbf{y} + \boldsymbol{\epsilon} = g[\mathbf{x}, \mathbf{u}, \boldsymbol{\theta}] + \boldsymbol{\epsilon} \tag{5.2.1}$$

The form of the function g, relating the output variables $\mathbf{y}$ to the unknown parameters in $\boldsymbol{\theta}$, is assumed to be known but is, in general, nonlinear in the parameters. The variable $\boldsymbol{\epsilon}$ is now the vector of output errors, which are assumed to be due to measurement noise. The output errors are specified by the probability density function denoted $p(\boldsymbol{\epsilon})$ and assumed to be a white, Gaussian random variable with zero mean and covariance $\mathbf{R}$,

$$\boldsymbol{\epsilon} \sim \mathbb{N}[\mathbf{0}, \mathbf{R}]$$

The above assumptions regarding the nature of the measurements are sometimes referred to as the Fisher model [31]. The likelihood function for the Fisher model is then defined as,

$$L(\mathbf{z}; \boldsymbol{\theta}) = p(\mathbf{z}|\boldsymbol{\theta}) \qquad (5.2.2)$$

where $p(\mathbf{z}|\boldsymbol{\theta})$ denotes the conditional probability of obtaining $\mathbf{z}$ given that the unknown parameters are $\boldsymbol{\theta}$. Note, however, that the unknown parameter vector $\boldsymbol{\theta}$ is not a random variable so the probability density function $p(\boldsymbol{\theta})$ is undefined. Therefore, assuming that the measurement errors ϵ are Gaussian, it follows that the measurement vector $\mathbf{z}$ is also Gaussian and the likelihood function becomes [31, 34],

$$L(\mathbf{z}; \boldsymbol{\theta}) = [(2\pi)^{n_y} |\mathbf{R}|]^{-\frac{1}{2}} \exp\left[-\frac{1}{2}\sum_{i=1}^{N}[\mathbf{z}(i) - \mathbf{y}(i)]^T \mathbf{R}^{-1}[\mathbf{z}(i) - \mathbf{y}(i)]\right] \quad i = 1, 2, \ldots, N$$

$$(5.2.3)$$

where n_y is the number of output variables measured from the aircraft and N is again the number of data points.

The properties of maximum likelihood estimation can be investigated in a similar way to that used to study least squares estimates in Appendix B. Derivations of the maximum likelihood characteristics are more involved than for least squares, hence will not be developed here but can be found, for example, in texts by Eykhoff [136] and Jategaonkar [34]. The properties of maximum likelihood estimates can be stated as follows,

- The estimates are asymptotically unbiased, with the expected value of $\hat{\boldsymbol{\theta}}$ approaching the true value $\boldsymbol{\theta}$ as the number of data points increases,

$$\lim_{N \to \infty} \mathrm{E}[\hat{\boldsymbol{\theta}}] = \boldsymbol{\theta}$$

- The estimates are consistent i.e. as the number of data points increases, $\hat{\boldsymbol{\theta}}$ approaches $\boldsymbol{\theta}$,

$$\hat{\boldsymbol{\theta}} \to \boldsymbol{\theta} \ \text{ as } \ N \to \infty$$

- The estimates are asymptotically efficient. For a parameter covariance $\mathbf{P}$,

$$\mathbf{P} \to \mathbf{M}^{-1} \ \text{ as } \ N \to \infty$$

where $\mathbf{M}$ is the Fisher's information matrix introduced earlier in Section 2.3. The information matrix can be written in terms of the likelihood function as follows,

$$\mathbf{M} \equiv \mathrm{E}\left[\left\{\frac{\partial \ln L(\mathbf{z}; \boldsymbol{\theta})}{\partial \boldsymbol{\theta}}\right\} \left\{\frac{\partial \ln L(\mathbf{z}; \boldsymbol{\theta})}{\partial \boldsymbol{\theta}}\right\}^T\right] = -\mathrm{E}\left[\frac{\partial^2 \ln L(\mathbf{z}; \boldsymbol{\theta})}{\partial \boldsymbol{\theta} \partial \boldsymbol{\theta}^T}\right] \qquad (5.2.4)$$

The main diagonal elements of $\mathbf{M}^{-1}$ are the lower bounds on the parameter variances and thus, represent the maximum achievable accuracy of the parameter estimates. These are known as the Cramer-Rao bounds and are specified by the Cramer-Rao inequality,

$$\mathbf{P} \geq \mathbf{M}^{-1} \qquad (5.2.5)$$

- The estimates are asymptotically normal. That is, as the number of data points increases, the distribution of $\hat{\boldsymbol{\theta}}$ tends towards a normal distribution with mean $\boldsymbol{\theta}$ and covariance $\mathbf{M}^{-1}$,

$$\hat{\boldsymbol{\theta}} \sim \mathbb{N}\left[\boldsymbol{\theta}, \mathbf{M}^{-1}\right] \ \text{ as } \ N \to \infty$$

5.3 Minimisation of Cost Function

The estimates of $\boldsymbol{\theta}$ are those that maximise the function in Equation (5.2.3). However, it is more convenient computationally to minimise the negative logarithm of the function. This is permissible because the logarithm is a monotonic function [31],

$$\hat{\boldsymbol{\theta}} = \min_{\boldsymbol{\theta}}[-\ln L(\mathbf{z}; \boldsymbol{\theta})] \tag{5.3.1}$$

so the cost function to be minimised for maximum likelihood estimation is,

$$J(\boldsymbol{\theta}, \mathbf{R}) = -\ln L(\mathbf{z}; \boldsymbol{\theta}) = \frac{1}{2}\sum_{i=1}^{N}[\mathbf{z}(i)-\mathbf{y}(i)]^{T}\mathbf{R}^{-1}[\mathbf{z}(i)-\mathbf{y}(i)]+\frac{N}{2}\ln|\mathbf{R}|+\frac{Nn_{y}}{2}\ln(2\pi) \tag{5.3.2}$$

From Equation (5.3.2), J is a function of both the unknown parameters $\boldsymbol{\theta}$ and the measurement noise covariance $\mathbf{R}$. For most cases, $\mathbf{R}$ is unknown and must be estimated. However, rather than include the elements of $\mathbf{R}$ in $\boldsymbol{\theta}$, the noise covariance is estimated separately by differentiating the right hand side of the cost function (5.3.2) with respect to $\mathbf{R}$, setting the resulting expression to zero and solving for $\mathbf{R}$,

$$\hat{\mathbf{R}} = \frac{1}{N}\sum_{i=1}^{N}[\mathbf{z}(i)-\hat{\mathbf{y}}(i)][\mathbf{z}(i)-\hat{\mathbf{y}}(i)]^{T} = \frac{1}{N}\sum_{i=1}^{N}\boldsymbol{\upsilon}(i)\boldsymbol{\upsilon}^{T}(i) \tag{5.3.3}$$

where $\hat{\mathbf{y}}$ is the vector of predicted outputs, calculated using an estimate of the unknown parameters $\hat{\boldsymbol{\theta}}$, and $\boldsymbol{\upsilon}$ is again used to denote the residuals. It is usually assumed that the measurement noise for the n_{y} outputs are uncorrelated with each other. Hence, only the diagonal elements of $\hat{\mathbf{R}}$ are determined.

The estimate $\hat{\mathbf{R}}$ is then substituted back into Equation (5.3.2) to obtain the cost function which must be minimised to find the estimates of the unknown parameters,

$$J(\boldsymbol{\theta}) = \frac{1}{2}\sum_{i=1}^{N}[\mathbf{z}(i)-\hat{\mathbf{y}}(i)]^{T}\hat{\mathbf{R}}^{-1}[\mathbf{z}(i)-\hat{\mathbf{y}}(i)] = \frac{1}{2}\sum_{i=1}^{N}\boldsymbol{\upsilon}^{T}(i)\hat{\mathbf{R}}^{-1}\boldsymbol{\upsilon}(i) \tag{5.3.4}$$

Again, the output vector $\mathbf{y}$ has been replaced with the estimate $\hat{\mathbf{y}}$ and the last two terms in Equation (5.3.2) have been ignored in Equation (5.3.4) as they are independent of $\boldsymbol{\theta}$. The cost function in Equation (5.3.4) can now be minimised to find the next estimate $\hat{\boldsymbol{\theta}}$.

The two step strategy outlined above leads to the estimation problem being solved iteratively. The procedure can be summarised as follows,

1. Choose initial estimates for the unknown parameters $\hat{\boldsymbol{\theta}}$.

2. Calculate the predicted outputs $\hat{\mathbf{y}}$, the residuals $\boldsymbol{\upsilon}$ and the estimate of the noise covariance matrix $\hat{\mathbf{R}}$.

3. Minimise $J(\boldsymbol{\theta})$ with respect to $\boldsymbol{\theta}$ to find the updated parameter estimates $\hat{\boldsymbol{\theta}}$.

4. Return to Step 2 and repeat until convergence is achieved.

Typically, the initial values for $\hat{\boldsymbol{\theta}}$ used to begin the iterative process come from *a priori* sources of information, such as semi-empirical analysis, or least squares regression.

A number of different optimisation techniques can be used to minimise the cost function in Equation (5.3.4) and find the parameter estimates. The most frequently used method for determining aircraft stability and control derivatives is the modified Newton-Raphson technique, which has been shown to have good convergence rates even when a large number of unknowns are to be determined [137]. The algorithm for the modified Newton-Raphson approach is outlined below.

To start with, assume that the parameter vector at the $(k+1)$th iteration $\boldsymbol{\theta}_{k+1}$ can be represented as a small perturbation $\Delta\boldsymbol{\theta}$ from the parameter vector at the previous iteration $\boldsymbol{\theta}_k$. Then a Taylor series expansion can be used to describe the cost function $J(\boldsymbol{\theta}_{k+1})$ as follows,

$$J(\boldsymbol{\theta}_{k+1}) = J(\boldsymbol{\theta}_k + \Delta\boldsymbol{\theta}) \approx J(\boldsymbol{\theta}_k) + \Delta\boldsymbol{\theta}^T \left.\frac{\partial J}{\partial \boldsymbol{\theta}}\right|_{\theta=\theta_k} + \Delta\boldsymbol{\theta}^T \left.\frac{\partial^2 J}{\partial \boldsymbol{\theta} \partial \boldsymbol{\theta}^T}\right|_{\theta=\theta_k} \Delta\boldsymbol{\theta} \qquad (5.3.5)$$

where terms higher than second-order are considered to be negligibly small. The minimum of the cost function is found from differentiating Equation (5.3.5) with respect to $\boldsymbol{\theta}$ and setting the resulting expression to zero,

$$\left.\frac{\partial J}{\partial \boldsymbol{\theta}}\right|_{\theta=\theta_{k+1}} \approx \left.\frac{\partial J}{\partial \boldsymbol{\theta}}\right|_{\theta=\theta_k} + \left.\frac{\partial^2 J}{\partial \boldsymbol{\theta} \partial \boldsymbol{\theta}^T}\right|_{\theta=\theta_k} \Delta\boldsymbol{\theta} = \mathbf{0} \qquad (5.3.6)$$

Rearranging Equation (5.3.6), the update in the parameter estimate from the kth iteration to the $(k+1)$th is found to be,

$$\Delta\boldsymbol{\theta} = -\left[\left.\frac{\partial^2 J}{\partial \boldsymbol{\theta} \partial \boldsymbol{\theta}^T}\right|_{\theta=\theta_k}\right]^{-1} \left.\frac{\partial J}{\partial \boldsymbol{\theta}}\right|_{\theta=\theta_k} \qquad (5.3.7)$$

and the new parameter estimation vector is,

$$\hat{\boldsymbol{\theta}}_{k+1} = \hat{\boldsymbol{\theta}}_k + \Delta\boldsymbol{\theta} \qquad (5.3.8)$$

where it is assumed that the inverse exists for the second gradient of the cost function with respect to the parameters, known as the Hessian matrix for optimisation problems. Equation (5.3.7) is the Newton-Raphson algorithm. Note that the second gradient of the cost function with respect to the parameters is also Fisher's information matrix $\mathbf{M}$ in a slightly different form to that given in Equation (5.2.4).

The next stage in the development of the method is to find expressions for the first and second gradients of J with respect to $\boldsymbol{\theta}$. The first gradient is found from Equation (5.3.4),

$$\mathbf{G} = \frac{\partial J}{\partial \boldsymbol{\theta}} = -\sum_{i=1}^{N} \left[\frac{\partial \hat{\mathbf{y}}(i)}{\partial \boldsymbol{\theta}}\right]^T \hat{\mathbf{R}}^{-1}[\mathbf{z}(i) - \hat{\mathbf{y}}(i)] \qquad (5.3.9)$$

An expression for the information matrix (given earlier in Equation (2.3.6)) is then obtained by differentiating Equation (5.3.9) with respect to $\boldsymbol{\theta}$,

$$\mathbf{M} = \frac{\partial^2 J}{\partial \boldsymbol{\theta} \partial \boldsymbol{\theta}^T} = \sum_{i=1}^{N} \left[\frac{\partial \hat{\mathbf{y}}(i)}{\partial \boldsymbol{\theta}}\right]^T \hat{\mathbf{R}}^{-1} \left[\frac{\partial \hat{\mathbf{y}}(i)}{\partial \boldsymbol{\theta}}\right] - \sum_{i=1}^{N} \left[\frac{\partial^2 \hat{\mathbf{y}}(i)}{\partial \boldsymbol{\theta} \partial \boldsymbol{\theta}^T}\right]^T \hat{\mathbf{R}}^{-1}[\mathbf{z}(i) - \hat{\mathbf{y}}(i)] \qquad (5.3.10)$$

The first gradient of the output variables $\mathbf{y}$ to the unknown parameters $\boldsymbol{\theta}$ are termed the output sensitivities, the calculation of which is dealt with in the Section 5.5. As mentioned in Section

2.3, the determination of the second gradient of **y** with respect to $\boldsymbol{\theta}$ is more complex. However, it is again observed that, because of the presence of the residual, the second term on the right hand side of Equation (5.3.10) will become less significant as the parameter estimates near their true value. Therefore, the information matrix can be approximated as,

$$\mathbf{M} = \frac{\partial^2 J}{\partial \boldsymbol{\theta} \partial \boldsymbol{\theta}^T} \approx \sum_{i=1}^{N} \left[\frac{\partial \hat{\mathbf{y}}(i)}{\partial \boldsymbol{\theta}} \right]^T \hat{\mathbf{R}}^{-1} \left[\frac{\partial \hat{\mathbf{y}}(i)}{\partial \boldsymbol{\theta}} \right] \tag{5.3.11}$$

When the above approximation is used in Equation (5.3.7), the algorithm is known as the modified Newton-Raphson, or Gauss-Newton, technique.

5.4   Calculation of the Estimated Output

The calculation of the estimated output vector for the ith data point $\hat{\mathbf{y}}(i)$ requires knowledge of the aircraft state vector $\mathbf{x}(i)$. As the aircraft state equation is usually a differential equation of some form, the propagation of $\mathbf{x}$ from the ith to the $(i+1)$th data point is achieved using a method of integration. Considering first a linear system described by the Equations (2.3.1) and (2.3.2), given earlier in Section 2.3,

$$\dot{\mathbf{x}}(t) = \mathbf{A}\mathbf{x}(t) + \mathbf{B}\mathbf{u}(t), \;\; \mathbf{x}(0) = \mathbf{x}_0 \tag{5.4.1}$$
$$\mathbf{y}(t) = \mathbf{C}\mathbf{x}(t) + \mathbf{D}\mathbf{u}(t) \tag{5.4.2}$$

The propagation of the aircraft state vector **x** can be performed by converting Equation (5.4.1) into its discrete-time form,

$$\mathbf{x}(i+1) = \boldsymbol{\Phi}\mathbf{x}(i) + \boldsymbol{\Psi}\mathbf{B}\bar{\mathbf{u}}(i) \tag{5.4.3}$$

where $\bar{\mathbf{u}}$ is the average of the control inputs at the two discrete time points i.e.,

$$\bar{\mathbf{u}}(i) = \frac{1}{2}[\mathbf{u}(i+1) - \mathbf{u}(i)] \tag{5.4.4}$$

The term $\boldsymbol{\Phi}$ is known as the state transition matrix and $\boldsymbol{\Psi}$ is its integral,

$$\boldsymbol{\Phi} = e^{\mathbf{A}\Delta t}, \;\; \boldsymbol{\Psi} = \int_0^{\Delta t} e^{\mathbf{A}\tau} d\tau \tag{5.4.5}$$

The matrix exponential in these two terms is usually approximated using a Taylor series expansion,

$$\boldsymbol{\Phi} = e^{\mathbf{A}\Delta t} \approx \mathbf{I} + \mathbf{A}\Delta t + \mathbf{A}^2 \frac{\Delta t^2}{2!} + \cdots \tag{5.4.6}$$

$$\boldsymbol{\Psi} = \int_0^{\Delta t} e^{\mathbf{A}\tau} d\tau \approx \mathbf{I}\Delta t + \mathbf{A}\frac{\Delta t^2}{2!} + \mathbf{A}^2 \frac{\Delta t^3}{3!} + \cdots \tag{5.4.7}$$

where Δt is again the data sampling time. The output is then found from,

$$\mathbf{y}(i+1) = \mathbf{C}\mathbf{x}(i+1) + \mathbf{D}\mathbf{u}(i+1) \tag{5.4.8}$$

However, a different approach is required if the aircraft dynamics are nonlinear. This time, consider a system described by the equations,

$$\dot{\mathbf{x}}(t) = f[\mathbf{x}(t), \mathbf{u}(t), \boldsymbol{\theta}], \;\; \mathbf{x}(0) = \mathbf{x}_0 \tag{5.4.9}$$
$$\mathbf{y}(t) = g[\mathbf{x}(t), \mathbf{u}(t), \boldsymbol{\theta}] \tag{5.4.10}$$

where, again, f and g are nonlinear functions of the states variables, input variables and the stability and control derivatives. The state variable vector is then propagated forward in time using the equation,

$$\mathbf{x}(t + \Delta t) = \mathbf{x}(t) + \int_t^{t+\Delta t} f[\mathbf{x}(t), \mathbf{u}(t), \boldsymbol{\theta}]dt \qquad (5.4.11)$$

Rather than trying to find an exact solution, it is more convenient to solve Equation (5.4.11) using numerical integration. The most commonly applied numerical integration techniques for aircraft applications are the Runge-Kutta methods, in particular the fourth-order technique [34, 31]. The development of this algorithm will not be presented here but can be found in a number of sources, including the text by Chapra and Canale [138]. The fourth-order Runge-Kutta method estimates the gradient of the function at four points between t and $t + \Delta t$,

$$\begin{aligned}
f_1 &= f[\mathbf{x}(t), \mathbf{u}(t), \boldsymbol{\theta}] \\
f_2 &= f[\mathbf{x} + f_1\Delta t/2, \bar{\mathbf{u}}, \boldsymbol{\theta}] \\
f_3 &= f[\mathbf{x} + f_2\Delta t/2, \bar{\mathbf{u}}, \boldsymbol{\theta}] \\
f_4 &= f[\mathbf{x} + f_3\Delta t, \bar{\mathbf{u}}, \boldsymbol{\theta}]
\end{aligned} \qquad (5.4.12)$$

In discrete form, the state vector at the $(i + 1)$th data point is then calculated from,

$$\mathbf{x}(i + 1) = \mathbf{x}(i) + \frac{(f_1 + 2f_2 + 2f_3 + f_4)\Delta t}{6} \qquad (5.4.13)$$

and the output vector is obtained from Equation (5.4.10). Note that the Runge-Kutta method could also be applied to a system of linear equations and the resulting output vector should match that generated using Equation (5.4.8).

5.5 Calculation of the Output Sensitivities

Having calculated the estimate of the output vector $\hat{\mathbf{y}}$ using one of the approaches discussed in the previous section, the sensitivities of the outputs to changes in the parameter estimates must be established. Again, considering first a linear system represented by Equations (5.4.1) and (5.4.2), the sensitivities with respect to the jth parameter can be found analytically from,

$$\frac{d}{dt}\left(\frac{\partial\mathbf{x}}{\partial\theta_j}\right) = \mathbf{A}\frac{\partial\mathbf{x}}{\partial\theta_j} + \frac{\partial\mathbf{A}}{\partial\theta_j}\mathbf{x} + \frac{\partial\mathbf{B}}{\partial\theta_j}\mathbf{u}, \quad \frac{\partial\mathbf{x}(0)}{\partial\theta_j} = 0 \qquad (5.5.1)$$

$$\frac{\partial\mathbf{y}}{\partial\theta_j} = \mathbf{C}\frac{\partial\mathbf{x}}{\partial\theta_j} + \frac{\partial\mathbf{C}}{\partial\theta_j}\mathbf{x} + \frac{\partial\mathbf{D}}{\partial\theta_j}\mathbf{u}, \quad j = 1, 2, \ldots, n_\theta \qquad (5.5.2)$$

These expressions were given earlier in Equations (2.3.8) and (2.3.9). Converting the above equations into discrete-time form gives,

$$\frac{\partial\mathbf{x}(i + 1)}{\partial\theta_j} = \boldsymbol{\Phi}\frac{\partial\mathbf{x}(i)}{\partial\theta_j} + \frac{\partial\boldsymbol{\Phi}}{\partial\theta_j}\mathbf{x}(i) + \boldsymbol{\Psi}\frac{\partial\mathbf{B}}{\partial\theta_j}\bar{\mathbf{u}}(i) + \frac{\partial\boldsymbol{\Psi}}{\partial\theta_j}\mathbf{B}\bar{\mathbf{u}}(i) \qquad (5.5.3)$$

$$\frac{\partial\mathbf{y}(i + 1)}{\partial\theta_j} = \mathbf{C}\frac{\partial\mathbf{x}(i + 1)}{\partial\theta_j} + \frac{\partial\mathbf{C}}{\partial\theta_j}\mathbf{x}(i + 1) + \frac{\partial\mathbf{D}}{\partial\theta_j}\mathbf{u}(i + 1) \qquad (5.5.4)$$

There is a large computation cost associated with calculating the partial derivatives of $\boldsymbol{\Phi}$ and $\boldsymbol{\Psi}$ with respect to θ_j. Therefore, the following approximation is suggested for Equation (5.5.3)

[139, 34],

$$\frac{\partial \mathbf{x}(i+1)}{\partial \theta_j} \approx \mathbf{\Phi} \frac{\partial \mathbf{x}(i)}{\partial \theta_j} + \mathbf{\Psi} \frac{\partial \mathbf{A}}{\partial \theta_j} \bar{\mathbf{x}}(i) + \mathbf{\Psi} \frac{\partial \mathbf{B}}{\partial \theta_j} \bar{\mathbf{u}}(i) \tag{5.5.5}$$

where,

$$\bar{\mathbf{x}}(i) = \frac{1}{2}[\mathbf{x}(i+1) - \mathbf{x}(i)] \tag{5.5.6}$$

For nonlinear equations of motion, the output sensitivities can be determined numerically, with the partial derivative of the output vector with respect to the jth parameter calculated approximately from,

$$\begin{aligned}\frac{\partial \mathbf{y}(i)}{\partial \theta_j} &\approx \frac{\mathbf{y}_p(i) - \mathbf{y}(i)}{\delta \theta_j} \\ &\approx \frac{g[\mathbf{x}_p(i), \mathbf{u}(i), \boldsymbol{\theta} + \delta \theta_j] - g[\mathbf{x}(i), \mathbf{u}(i), \boldsymbol{\theta}]}{\delta \theta_j}\end{aligned} \tag{5.5.7}$$

where $\delta \theta_j$ is a perturbation in the jth parameter, while $\mathbf{x}_p$ and $\mathbf{y}_p$ are the perturbed state and output vectors, respectively, resulting from $\delta \theta_j$. The perturbed state and output vectors are calculated in a similar manner to that outlined in Section 5.4, the exception being that θ is replaced with $\boldsymbol{\theta} + \delta \theta_j$. A perturbation is introduced to one parameter at a time.

The value chosen for $\delta \theta_j$ must be small enough to ensure that the approximation is valid for the true sensitivities but large enough to avoid problems due to round-off errors. It is best to choose a perturbation value relative to the magnitude of the current parameter estimates, however the relative perturbations recommended by analysts varies widely. Jategaonkar [34] suggests a value of $\delta \theta_j = 10^{-6}\hat{\theta}_j$, while Klein and Morelli [31] advocate a much larger value of $\delta \theta_j = 0.01\hat{\theta}_j$. Larger perturbations may be required for a parameter if a change in its value has little effect on the system response in comparison to other parameters. During the course of this research, relative perturbations of both $10^{-6}\hat{\theta}_j$ and $0.01\hat{\theta}_j$ were tried but it was found that the choice did not significantly affect the final parameter estimates. Note that if the starting or current estimate for θ_j is zero then the perturbed parameter estimate $(\hat{\theta}_j + \delta \theta_j)$ should be set to a small value, for example 0.01.

Equation (5.5.7) is a forward difference approximation. A more accurate way of determining the output sensitivities is with a central difference approximation,

$$\frac{\partial \mathbf{y}(i)}{\partial \theta_j} \approx \frac{g[\mathbf{x}_p(i), \mathbf{u}(i), \boldsymbol{\theta} + \delta \theta_j] - g[\mathbf{x}_{-p}(i), \mathbf{u}(i), \boldsymbol{\theta} - \delta \theta_j]}{2\delta \theta_j} \tag{5.5.8}$$

The drawback of using equation (5.5.8) instead of (5.5.7) is that twice as many perturbation states and outputs need to be calculated. However, the number of iterations that need to be carried out before convergence is achieved will reduce if more accurate approximations of the sensitivities are used [31].

5.6 Algorithmic Variations

In general, the modified Newton-Raphson algorithm works well. However, it has been found to have a tendency to perform poorly when close to the minimum of the cost function, experiencing intermediate local divergence or stalling [137, 34]. As well as this, if the initial estimate

of $\boldsymbol{\theta}$ is far away from the optimum values, then the method may struggle to find the minimum. These deficiencies happen for a number of reasons. Firstly, the calculation of the parameter update, given by Equation (5.3.7), assumes that the cost function is quadratic in terms of the unknown parameters [137, 31, 34]. In reality, the relationship between the cost function and $\boldsymbol{\theta}$ is more complex. Secondly, a number of approximations are used to calculate $\Delta\boldsymbol{\theta}$, such as for the information matrix in Equation (5.3.11) and the output sensitivities in Section 5.5, leading to numerical errors.

A number of modifications to the modified Newton-Raphson method have been proposed to overcome the above problems. To avoid poor performance when near to the cost function minimum, some form of step size control can be introduced once the direction of the update $\Delta\boldsymbol{\theta}$ has been determined. The simplest method for stepsize control is an engineering approach explained as follows,

1. Calculate $\Delta\boldsymbol{\theta}$ and determine $\hat{\boldsymbol{\theta}}_{k+1} = \hat{\boldsymbol{\theta}}_k + \Delta\boldsymbol{\theta}$.

2. Calculate new value of cost function $J(\hat{\boldsymbol{\theta}}_{k+1})$. If $J(\hat{\boldsymbol{\theta}}_{k+1}) > J(\hat{\boldsymbol{\theta}}_k)$, then the modified Newton-Raphson update has overshot the cost function minimum J_{min} and local divergence has occurred.

3. Recalculate new parameter estimates using $\hat{\boldsymbol{\theta}}_{k+1} = \hat{\boldsymbol{\theta}}_k + \Delta\boldsymbol{\theta}/2$.

4. Calculate new value of cost function $J(\hat{\boldsymbol{\theta}}_{k+1})$. If $J(\hat{\boldsymbol{\theta}}_{k+1}) > J(\hat{\boldsymbol{\theta}}_k)$, then return to Step 3 and half $\Delta\boldsymbol{\theta}$ again.

5. Iterate on Steps 3 and 4 until $J(\hat{\boldsymbol{\theta}}_{k+1}) < J(\hat{\boldsymbol{\theta}}_k)$. If $J(\hat{\boldsymbol{\theta}}_{k+1}) > J(\hat{\boldsymbol{\theta}}_k)$ after 10 halvings of $\Delta\boldsymbol{\theta}$ then $\hat{\boldsymbol{\theta}}_k$ are the final parameter estimates.

The choice of a maximum of 10 halvings of the original modified Newton-Raphson update means that $\Delta\boldsymbol{\theta}$ will have been reduced by a factor of $2^{10} = 1024$ after the tenth iteration [34]. If, at this point, the new cost function is still greater than the previous value, then it can be concluded that, essentially, convergence was achieved on the kth iteration. While this simple approach will improve the algorithm performance close to the minimum, it does not help the convergence if the initial parameter estimates are far away from the optimum.

A more suitable technique may be the use of a line search [140, 141, 28]. The equation for the update to the parameter estimates is modified to become,

$$\hat{\boldsymbol{\theta}}_{k+1} = \hat{\boldsymbol{\theta}}_k + \alpha_k \Delta\boldsymbol{\theta} \tag{5.6.1}$$

where α_k is a scalar. Once the basic modified Newton-Raphson update has been calculated, a one-dimensional search is used to find the value of α_k which leads to the maximum reduction in the cost function for the kth iteration. Because, α_k can take a value greater than 1, the convergence region is widened. Any line search algorithm can be used. A quadratic line search was shown to have good performance by Foster [140].

The Levenberg-Marquardt method is another variation of the basic modified Newton-Raphson algorithm. The calculation of the parameter update is modified to the following,

$$\Delta\boldsymbol{\theta} = -(\mathbf{M} + \lambda\mathbf{I})^{-1}\mathbf{G} \tag{5.6.2}$$

where λ is a scalar known as the Levenberg-Marquardt parameter. The value of λ is assessed at each iteration and, if necessary, varied to again achieve the maximum reduction in the cost function. The process of determining λ is outlined below [34],

1. Choose an initial value for λ, typically 0.001 or 0.01.

2. At the kth iteration, determine a value for λ_k based on the previous value λ_{k-1} from the expression $\lambda_k = \lambda_{k-1}/\nu$, where ν is termed the reduction factor. The value of ν is always greater than 1, with a typical value of 10.

3. For λ_k and λ_{k-1}, determine the two parameter update vector from Equation (5.6.2). These are denoted $\Delta\boldsymbol{\theta}$ when the previous value λ_{k-1} is used and $\Delta\boldsymbol{\theta}_\nu$ when the calculation utilises the reduced value λ_k.

4. Calculate the two resulting values of the cost function, denoted $J(\hat{\boldsymbol{\theta}}_k)$ and $J(\hat{\boldsymbol{\theta}}_k^\nu)$ and compare these values with the value from the previous iteration $J(\hat{\boldsymbol{\theta}}_{k-1})$.

5. (a) If $J(\hat{\boldsymbol{\theta}}_k^\nu) \leq J(\hat{\boldsymbol{\theta}}_{k-1})$ then set $\lambda_k = \lambda_{k-1}/\nu$ and use the reduced value of λ for the next iteration $k+1$.
   (b) If $J(\hat{\boldsymbol{\theta}}_k^\nu) > J(\hat{\boldsymbol{\theta}}_{k-1})$ but $J(\hat{\boldsymbol{\theta}}_k) < J(\hat{\boldsymbol{\theta}}_{k-1})$ then keep the value of λ at λ_{k-1} for the $(k+1)$th iteration.
   (c) Otherwise, if $J(\hat{\boldsymbol{\theta}}_k^\nu) > J(\hat{\boldsymbol{\theta}}_{k-1})$ and $J(\hat{\boldsymbol{\theta}}_k) > J(\hat{\boldsymbol{\theta}}_{k-1})$ then the cost function has not reduced from $(k-1)$th value. Increase λ_k using the expression $\lambda_k = \lambda_{k-1}\nu$ and repeat Steps 3 to 5 until conditions (a) or (b) are satisfied.

At first glance, a drawback with the Levenberg-Marquardt method may be the extra computational burden, as $\Delta\boldsymbol{\theta}$ has to be determined at least twice for each iteration. However, the majority of the computational cost associated with the output error method is the calculation of the information matrix **M**. As the information matrix only has to be determined once for each iteration of the Levenberg-Marquardt method, the extra computational burden is not as severe as it first appears. The Levenberg-Marquardt method has been found to perform well when close to the cost function minimum and for starting estimates far from the optimum [34].

Direct search methods of optimisation, as opposed to the gradient-based method such as the modified Newton-Raphson algorithm, are also available [34]. However, studies have shown that direct search methods are much slower than the gradient techniques for aircraft parameter estimation problems [142, 143]. Also direct search methods do not readily provide the information about the accuracy of the parameter estimates that gradient methods do.

5.7   Convergence Criteria

A number of different criteria can be used to determine if convergence has been achieved and the final parameter estimates have been obtained. One or more of the following checks are typically used [31, 34, 133],

- Small relative change in the cost function J for consecutive iterations

- Absolute values of the elements of $\Delta\boldsymbol{\theta}$ are small

- Absolute values of the elements of the cost function gradient $\partial J/\partial\boldsymbol{\theta}$ are small

- Small relative change in the elements of the covariance matrix $\hat{\mathbf{R}}$

For the cost function, a "small relative change" is typically considered to be,

$$\left| \frac{J(\hat{\boldsymbol{\theta}}_{k+1}) - J(\hat{\boldsymbol{\theta}}_k)}{J(\hat{\boldsymbol{\theta}}_k)} \right| < 0.001 \tag{5.7.1}$$

with the cost function value determined using Equation (5.3.4). Alternatively, the cost function value is defined as the determinant of the covariance matrix [34],

$$J(\boldsymbol{\theta}) = \left| \hat{\mathbf{R}} \right| \tag{5.7.2}$$

The other checks for convergence can be expressed as,

$$\frac{\left\| \hat{\boldsymbol{\theta}}_{k+1} - \hat{\boldsymbol{\theta}}_k \right\|}{\left\| \hat{\boldsymbol{\theta}}_k \right\|} < 0.001 \tag{5.7.3}$$

$$\left| \frac{\partial J}{\partial \theta_j} \right| < 0.05 \ \forall j, \ j = 1, 2, \ldots, n_\theta \tag{5.7.4}$$

$$\left| \frac{(\hat{r}_{jj})_{k+1} - (\hat{r}_{jj})_k}{(\hat{r}_{jj})_k} \right| < 0.05 \ \forall j, \ j = 1, 2, \ldots, n_y \tag{5.7.5}$$

where $\|\|$ denotes the norm of a vector i.e. the square root of the sum of squares of its elements and $\hat{r}_{jj}$ is the estimate of the jth diagonal element of $\hat{\mathbf{R}}$.

Based on the discussion in Sections 5.3 to 5.6, it is clear that the computational complexity of the modified Newton-Raphson method is significant in comparison to ordinary least square regression presented in Chapter 4. With the level of modern computing power available, however, convergence of the modified Newton-Raphson algorithm can be achieved rapidly. To help clarify the process, Figure 5.1 shows the steps involved in implementing the algorithm.

5.8   Accuracy of Parameter Estimates and Identified Model

The Fisher information matrix $\mathbf{M}$ is the basis for assessing the accuracy of maximum likelihood parameter estimates and was approximated in Equation (5.3.11) as,

$$\mathbf{M} \approx \sum_{i=1}^{N} \left[\frac{\partial \hat{\mathbf{y}}(i)}{\partial \boldsymbol{\theta}} \right]^T \hat{\mathbf{R}}^{-1} \left[\frac{\partial \hat{\mathbf{y}}(i)}{\partial \boldsymbol{\theta}} \right] \tag{5.8.1}$$

One of the properties of maximum likelihood estimation, introduced in Section 5.2, was that they are asymptotically efficient. The number of data points N typically used for aircraft parameter estimation is large, therefore the following approximation is used to estimate the parameter covariance matrix,

$$\mathbf{P} \approx \mathbf{M}^{-1} \approx \left\{ \sum_{i=1}^{N} \left[\frac{\partial \hat{\mathbf{y}}(i)}{\partial \boldsymbol{\theta}} \right]^T \hat{\mathbf{R}}^{-1} \left[\frac{\partial \hat{\mathbf{y}}(i)}{\partial \boldsymbol{\theta}} \right] \right\}^{-1} \tag{5.8.2}$$

In other word, the variance of each parameter is estimated as the Cramer-Rao lower bound. The square root of the jth diagonal elements of the matrix in Equation (5.8.2) is the standard error of the jth parameter estimate which, again, is assumed to approximate the scatter of parameter

Initial Estimates $\hat{\boldsymbol{\theta}}_{\boldsymbol{0}}$ Define state and output relationships:

$$\dot{\mathbf{x}} = f[\mathbf{x}, \mathbf{u}, \boldsymbol{\theta}] \quad \mathbf{y} = g[\mathbf{x}, \mathbf{u}, \boldsymbol{\theta}]$$

Integrate state equations and calculate estimated outputs $\hat{\mathbf{y}}$

Calculate parameter update $\boldsymbol{\Delta\theta}$ and new parameter estimates
$$\hat{\theta}_{k+1} = \hat{\theta}_k + \triangle\boldsymbol{\theta}$$

Measured outputs $\mathbf{z}$

Calculate residuals $\boldsymbol{\upsilon}$, estimate covariance matrix $\mathbf{R}$ and calculate cost function J

Calculate gradient of cost function and information matrix

Convergence achieved or maximum number of iterations performed?

no

Calculate output sensitivities $\dfrac{\partial\hat{\mathbf{y}}}{\partial\boldsymbol{\theta}}$

yes

Final Parameter Estimates
$\hat{\boldsymbol{\theta}}$

Figure 5.1: Computational steps for modified
Newton-Raphson algorithm

estimates calculated from repeated manoeuvres. The off-diagonal elements are the pair-wise correlation coefficients ρ between the parameter estimates.

Section 4.6 contained a discussion on the equation error residuals in practice being coloured, rather than white, due to errors in the model specification. This led to the standard errors being inconsistent with the scatter in estimates obtained from repeated manoeuvres and required that a correction be applied in the calculation of the parameter covariance matrix $\mathbf{P}$. A similar problem is encountered with maximum likelihood estimates as, in Section 5.2, the output errors $\boldsymbol{\epsilon}$ were also assumed to be white. To account for coloured residuals in maximum likelihood estimation, the calculation of the parameter covariance matrix in Equation (5.8.2) can be modified as follows [133, 31],

$$\mathbf{P} \approx \mathbf{M}^{-1} \left[\sum_{i=1}^{N} \left[\frac{\partial \hat{\mathbf{y}}(i)}{\partial \boldsymbol{\theta}} \right]^{T} \hat{\mathbf{R}}^{-1} \sum_{j=1}^{N} \hat{\mathcal{R}}_{\epsilon\epsilon}(i-j) \hat{\mathbf{R}}^{-1} \frac{\partial \hat{\mathbf{y}}(i)}{\partial \boldsymbol{\theta}} \right] \mathbf{M}^{-1} \tag{5.8.3}$$

where $\hat{\mathcal{R}}_{\epsilon\epsilon}$ is, again, the estimate of the autocorrelation matrix for the residuals, obtained from Equation (4.6.4),

$$\hat{\mathcal{R}}_{\epsilon\epsilon}(k) = \frac{1}{N} \sum_{i=1}^{N-k} \upsilon(i)\upsilon(i+k) = \hat{\mathcal{R}}_{\epsilon\epsilon}(-k) \quad k = 0, 1, 2, \ldots, l \tag{5.8.4}$$

The index k is the time separation of the residuals, with l denoting the maximum time difference. The value for l is, again, typically $N/5$.

5.9 UAV Short Period Example

To illustrate the use of the output error method, the technique was used to estimate the stability and control derivatives of a longitudinal, short period model from the BAE Systems UAV data. The short period can be described by the equation,

$$\begin{bmatrix} \dot{w} \\ \dot{q} \end{bmatrix} = \begin{bmatrix} z_w & z_q \\ m_w & m_q \end{bmatrix} \begin{bmatrix} w \\ q \end{bmatrix} + \begin{bmatrix} z_\eta \\ m_\eta \end{bmatrix} \eta + \begin{bmatrix} b_{\dot{w}} \\ b_{\dot{q}} \end{bmatrix} \tag{5.9.1}$$

The outputs used for the estimation process were angle of attack α and pitch rate q which, for the short period approximation, are assumed to be related to the state variables by the following expressions,

$$\begin{bmatrix} \alpha \\ q \end{bmatrix} = \begin{bmatrix} 1/U_e & 0 \\ 0 & 1 \end{bmatrix} \begin{bmatrix} w \\ q \end{bmatrix} + \begin{bmatrix} 0 \\ 0 \end{bmatrix} \eta + \begin{bmatrix} b_\alpha \\ b_q \end{bmatrix} \tag{5.9.2}$$

where U_e is the axial velocity component of the aircraft at trim. The output bias terms, b_α and b_q, are additional unknowns to be determined. Like those in the state equations, b_α and b_q account for uncertainty in the initial conditions and control inputs. They can also comprise of systematic errors in the measured outputs which have not been removed during the data compatibility check [34]. Because the bias terms in Equations (5.9.1) and (5.9.2) take into account some of the same phenomena, it is not always necessary to include both state and output bias terms in the equations of motion. For example, with the short period example presented here, the output biases were found to be negligible so b_α and b_q were removed from Equation (5.9.2). The analysis also indicated that the control derivative z_η was insignificant,
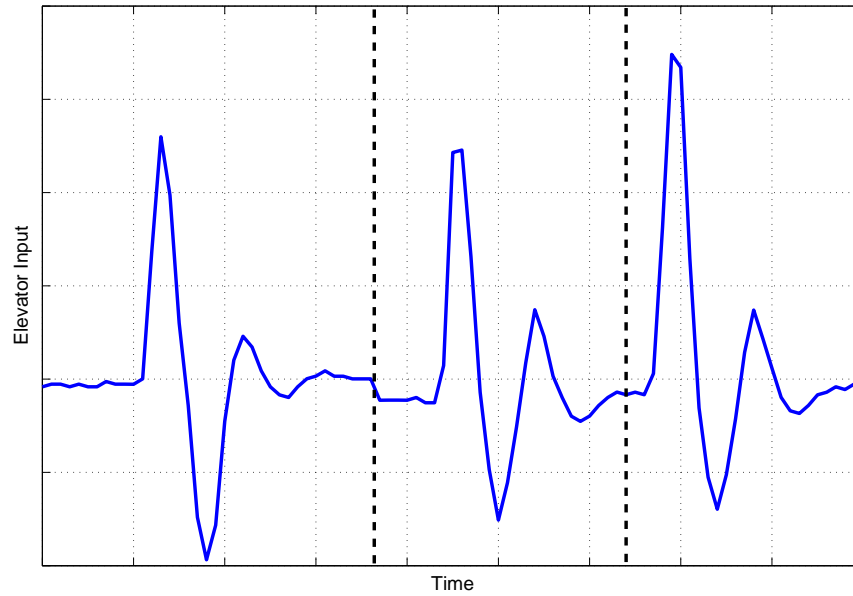
Figure 5.2: Elevator inputs for parameter estimation

hence this term was also removed from the equations of motion. The estimation process utilised three data segments, each containing an elevator doublet. These are shown in Figure 5.2.

Prior to performing estimation with the output error technique, the equation error method was used to estimate the derivatives. The equation error estimates were then used as the initial values for the modified Newton-Raphson algorithm, with the initial cost function value, calculated from Equation (5.7.2), being $J_1 = 0.0033$. The modified Newton-Raphson algorithm was then executed. The output sensitivities were calculated using the forward difference formula in Equation (5.5.7) and the simple parameter halving approach for dealing with intermediate local divergence was implemented, although no local divergence occurred. The algorithm converged in 10 iterations, with a final cost function value of $J_{10} = 4.0591 \times 10^{-9}$. The computational time required to achieve convergence was very short, $t_{comp} = 1.61$ sec. Table 5.1 displays the final parameter estimates obtained from the output error method, along with the results from the equation error method. The standard errors of the estimates obtained using both techniques and corrected for the effects of coloured residuals are also given. The measured time histories of angle of attack and pitch rate are plotted in Figure 5.3 along with the responses predicted using the identified model. In general, there is good agreement between the output error and the equation error estimates. The magnitudes of the standard errors obtained with the two algorithms also match closely, although the standard errors for z_w are somewhat large at around 21%.

The correlation coefficients for the parameter estimates are shown in Table 5.2. Because the output error method analyses each of the equations of motion simultaneously (unlike the equation error method which deals with each equation separately), the correlation between normal force and pitch moment derivatives can be determined. Table 5.2 indicates that all parameters

	Output Error		Equation Error	
	$\hat{\theta}$	$100[s/\|\hat{\theta}\|]$	$\hat{\theta}$	$100[s/\|\hat{\theta}\|]$
z_w	0.768	21.49	0.496	21.78
z_q	1.155	7.98	1.147	4.95
m_w	0.937	9.88	1.007	7.47
m_q	1.310	10.93	-2.3805	7.72
m_η	1.046	4.49	0.914	3.98
$b_{\dot{w}}$	0.8380	14.89	0.9639	18.85
$b_{\dot{q}}$	-0.0455	16.26	-0.0452	17.04

Table 5.1: Estimates of short period derivatives from output error and equation error methods
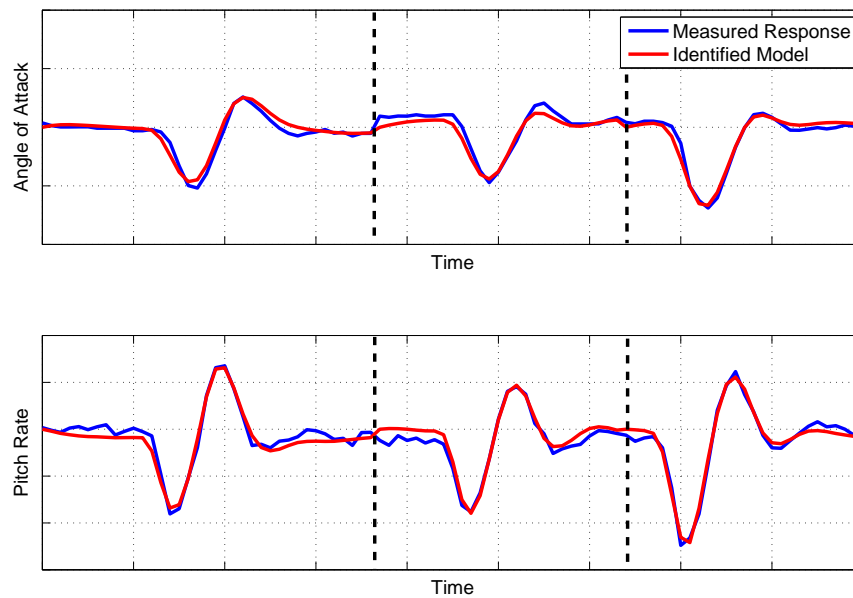
Figure 5.3: Measured and identified responses for output error method

were sufficiently independent. The results from Theil's inequality analysis were as follows:

$$\alpha: \quad U = 0.1161, \quad U_B = 0.0076, \quad U_V = 0.0203, \quad U_C = 0.9721$$
$$q: \quad U = 0.0983, \quad U_B = 0.0004, \quad U_V = 0.0093, \quad U_C = 0.9902$$

which again indicated a good match between the measured response and the identified model.

	z_w	z_q	$b_{\dot{w}}$	m_w	m_q	m_η	$b_{\dot{w}}$
z_w	1	0.4732	0.2160	0.5056	0.1390	0.1430	0.3550
z_q	-	1	0.5938	0.2086	0.4185	0.3035	0.2188
m_w	-	-	1	0.3320	0.0941	0.2123	0.1849
m_q	-	-	-	1	0.6996	0.1156	0.3010
m_η	-	-	-	-	1	0.1197	0.0900
$b_{\dot{w}}$	-	-	-	-	-	1	0.3229
$b_{\dot{q}}$	-	-	-	-	-	-	1

Table 5.2: Correlation coefficients for short period
parameter estimates

To test the robustness of the modified Newton-Raphson algorithm to starting values being far away from the optimum, the parameter estimation analysis was repeated again but with the initial values given in the second column of Table 5.3. Note that, as well as being far from the optimum values, the initial estimates for z_w, m_q and m_η also had incorrect signs. When the modified Newton-Raphson algorithm was run, the initial cost function value was $J_1 = 7.5596$, which was around three orders of magnitude greater than the initial cost function value from the first run. However, the algorithm still managed to converge, obtaining the same parameter estimates as those for the first run. This was achieved in 15 iterations, with the final cost function value again being $J_{15} = 4.0591 \times 10^{-9}$, and after a time of $t_{comp} = 2.08$ sec. Intermediate divergence was encountered on the eighth and tenth iteration but was dealt with successfully by the parameter halving routine.

Estimation was then repeated one more time, but with the initial values of all stability and control parameters set to 1 and the bias parameters set to 0 (third column of Table 5.3). This time the modified Newton-Raphson algorithm failed to converge. Estimation using the Levenberg-Marquardt method, which has been found to be more robust to poor starting values, was then tried and convergence was achieved in 35 iterations and $t_{comp} = 7.88$ sec. Again, the resulting parameter values were identical to those in Table 5.1. The convergence of the Levenberg-Marquardt algorithm is shown in Table 5.4, with the values of the Levenberg-Marquardt parameter λ given in the second column and the cost function value in the third. As can be seen, with the poor starting values for the parameters, the cost function was extremely large at $J = 7.3660 \times 10^{50}$. An initial value of 0.01 was used for λ and, after the first iteration first, the cost function had reduced to 1.9821×10^{-6}. On the third iteration, the value of λ had to be increased to 100 before a reduction of J was achieved. Over the next few iterations, λ was reduced gradually back to 0.01 and this value was retained until the 31st iteration. As the method converged on the cost function minimum, λ was successively reduced by an order of magnitude until it reached 1×10^{-6} on the 35th iteration, at which point convergence was achieved.

The results above indicate that while, in theory, the modified Newton-Raphson algorithm can perform poorly when the initial parameter values are inaccurate, the method is relatively robust (however, further investigation would be required to confirm this). Convergence was still

	2nd Run $\hat{\theta}_1$	3rd Run $\hat{\theta}_1$
z_w	1.000	1.000
z_q	20.000	1.000
m_w	-0.005	1.000
m_q	1.0000	1.000
m_η	1.0000	1.000
$b_{\dot{w}}$	0.000	0.000
$b_{\dot{q}}$	0.000	0.000

Table 5.3: Variations of starting estimates for output error methods

Iteration	λ	J
1	1×10^{-2}	7.3660×10^{50}
2	1×10^{-2}	1.9821×10^{-6}
3	1×10^{2}	1.7473×10^{-6}
4	1×10^{1}	1.1011×10^{-6}
5	1×10^{0}	6.3785×10^{-7}
6	1×10^{-1}	2.0751×10^{-7}
7	1×10^{-1}	6.6570×10^{-8}
$\vdots$	$\vdots$	$\vdots$
31	1×10^{-2}	1.4453×10^{-8}
32	1×10^{-3}	4.4356×10^{-9}
33	1×10^{-4}	4.0680×10^{-9}
34	1×10^{-5}	4.0593×10^{-9}
35	1×10^{-6}	4.0591×10^{-9}

Table 5.4: Convergence history of Levenberg-Marquardt method

reached on the second run despite the starting estimates being far from the optimum values and some of the derivative estimates having incorrect signs. It was only in the extreme case when the initial estimates were all set to 1 that the modified Newton-Raphson algorithm could not find a solution, in which case the Levenberg-Marquardt method was applied successfully to obtain the estimates. Therefore, in the majority of practical cases encountered, if it is not possible to obtain starting values using the equation error method, the *a priori* estimates from, for example, semi-empirical analysis should be accurate enough that the modified Newton-Raphson method converges. This should be true even for the case of unconventional UAVs for which the semi-empirical estimates may be unreliable. For rare cases where the algorithm fails, the Levenberg-Marquardt method should provide better performance.

For validation, the identified model was used to predict the response to an elevator input not used for the parameter estimation step. The input time history is shown in Figure 5.4 along with a comparison of the unseen measured data and the predicted response for angle of attack and pitch rate. As can be seen, a close visual match between the measured and predicted responses was obtained for both motion variables. Theil's inequality analysis also suggested a close match between the measured and predicted data, although the variance portions for both angle of attack and pitch rate could be considered large,

$$\alpha:\ U = 0.1391,\ U_B = 0.0000,\ U_V = 0.1923,\ U_C = 0.8067$$
$$q:\ U = 0.121,\ U_B = 0.0000,\ U_V = 0.2082,\ U_C = 0.7918$$

5.10 DEMON Dutch Roll Example

As described in Chapter 4, when estimating the derivatives of the wind tunnel models, it was necessary to account for a time delay between the input and the measured response. For least squares regression, the delay was dealt with simply by manually shifting the input variables to match the outputs. However, as the output error method is capable of handling nonlinear
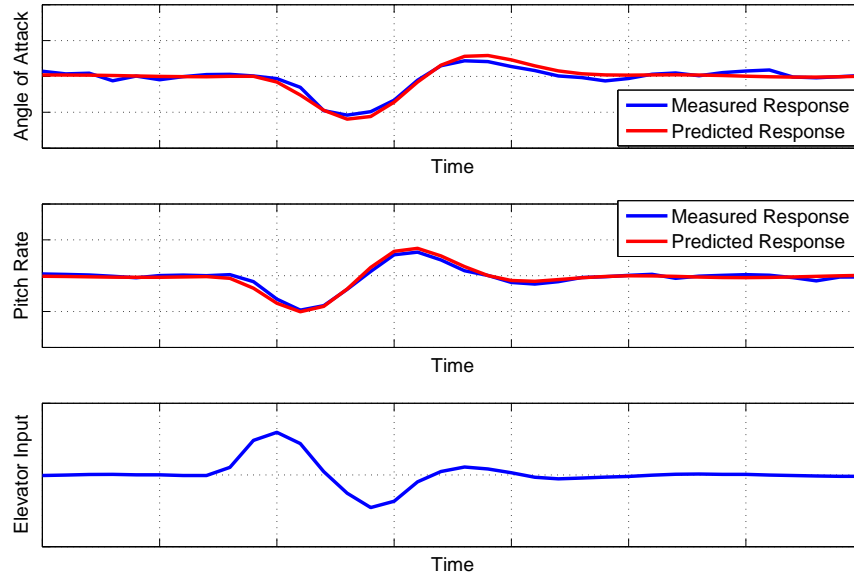
Figure 5.4: Measured and predicted responses due to an
elevator input for validation process

estimation problems, it provides a means for estimating the time delay [144]. Additional sub-routines are required, which permit the input variable to be shifted in time and ensure that the estimated time delay is a multiple of the sampling time Δt. When calculating the output sensitivities with respect to the time delay using the forward difference formula in Equation (5.5.7), Δt is also used as the perturbation value.

An example is presented here for a 1-1-2 input to the rudder of the 1/3 scale DEMON UAV. Note that a different data segment to that used earlier in Section 4.9 was analysed for this example. The state equations for this case were,

$$\begin{bmatrix} \dot{v}(t) \\ \dot{r}(t) \end{bmatrix} = \begin{bmatrix} 0 & -V_T \\ n_v & n_r \end{bmatrix} \begin{bmatrix} v(t) \\ r(t) \end{bmatrix} + \begin{bmatrix} 0 \\ n_\zeta \end{bmatrix} \zeta(t - \tau_\zeta) \tag{5.10.1}$$

where τ_ζ is the delay in the rudder input. The output variables used for the analysis were sideslip β and yaw rate r, assumed to be related to the state variables by the expressions,

$$\begin{bmatrix} \beta(t) \\ r(t) \end{bmatrix} = \begin{bmatrix} 1/V_T & 0 \\ 0 & 1 \end{bmatrix} \begin{bmatrix} v(t) \\ r(t) \end{bmatrix} + \begin{bmatrix} 0 \\ 0 \end{bmatrix} \zeta(t - \tau_\zeta) + \begin{bmatrix} b_\beta \\ 0 \end{bmatrix} \tag{5.10.2}$$

The starting parameter values for the modified Newton-Raphson algorithm were taken to be *a priori* estimates calculated from a simulation model of the full-sized aircraft and given earlier in Equations (2.5.4). These are given in the last column of Table 5.5. Note that, initially, it was assumed the time delay τ_ζ was zero. The converged output error parameter estimates are also shown in Table 5.5, along with their standard errors. For this example, the output error method was relatively slow to converge, requiring 67 iterations and a time of $t_{comp} = 24.27$ sec. The initial cost function value was $J_1 = 0.0017$ and the final value was $J_{67} = 8.9012 \times 10^{-7}$.

Table 5.5 shows that the standard errors of V_T, n_v, n_r and n_ζ were relatively high, with figures of around 20 % and over. There was less uncertainty in the estimated value of $\tau_\zeta = 0.33$ sec,

	$\hat{\theta}$	$100[s/|\hat{\theta}|]$	$\hat{\theta}_1$
V_T	30.6678	23.39	30
n_v	3.4638	23.34	6.156
n_r	-2.4524	22.98	-6.326
n_ζ	-6.2552	20.35	-2.283
τ_ζ	0.33	0.50	0
b_β	-0.0119	7.23	0

Table 5.5: Estimates of DEMON dutch roll derivatives
from output error method - Run 1

with the standard error being just 0.5 %. The possible cause of some of the standard errors being high was found when analysing the correlation coefficients, shown in Table 5.6, which suggested high correlation between V_T and n_v, with $\rho = 0.9717$.

	y_r	n_v	n_r	n_ζ	τ_ζ	b_β
y_r	1	0.9717	0.0115	0.3303	0.0914	0.0433
n_v	-	1	0.0684	0.4177	0.0871	0.1493
n_r	-	-	1	0.7524	0.0714	0.2483
n_ζ	-	-	-	1	0.0541	0.4302
τ_ζ	-	-	-	-	1	0.0232
b_β	-	-	-	-	-	1

Table 5.6: Correlation coefficients for DEMON dutch roll
parameter estimates - Run 1

Because of this high correlation, the modified Newton-Raphson algorithm was run again, with the same initial values, but with V_T held fixed at 30. Again, the algorithm took 67 iterations to converge, with $t_{comp} = 21.91$ sec. The final cost function value was slightly lower than that for the first run - $J_{67} = 8.7504 \times 10^{-7}$. The resulting estimates are shown in Table 5.7 and the new correlation coefficients are given in Table 5.8. There was little change in the estimated parameter values from the first run but the standard errors for n_v and n_ζ had reduced in size. The uncertainty in the estimate of n_r remained virtually unchanged. With V_T held fixed, Table 5.8 shows that the remaining parameters were all sufficiently independent. It was also noted that the output error estimates, given in Table 5.7, were in close agreement with the least squares estimates presented in Section 4.9.

Theil's inequality analysis for the second run gave the following results,

$$\beta : \ U = 0.1114, \ U_B = 0.0000, \ U_V = 0.0275, \ U_C = 0.9725$$
$$r : \ U = 0.0742, \ U_B = 0.0108, \ U_V = 0.0000, \ U_C = 0.9892$$

indicating a good fit between the measured response and the identified model. Figure 5.5 shows plots of the measured and identified responses, along with the rudder input.

For validation, a rudder doublet was applied to the identified model to produce a predicted response and compared with the unseen measured data for the same manoeuvre. This is shown in Figure 5.6. Note that for the doublet input, the time delay was 0.27 sec rather than 0.33 sec, therefore some additional shifting had to be done manually to synchronise the input and output

	$\hat{\theta}$	$100[s/|\hat{\theta}|]$	$\hat{\theta}_1$
V_T	30*	-	30
n_v	3.5406	3.83	6.156
n_r	-2.4519	22.89	-6.326
n_ζ	-6.2944	16.04	-2.283
τ_ζ	0.33	0.50	0
b_β	-0.0119	5.70	0

* - parameter held fixed

Table 5.7: Estimates of DEMON dutch roll derivatives from output error method - Run 2

	n_v	n_r	n_ζ	τ_ζ	b_β
n_v	1	0.2419	0.4321	0.0066	0.8106
n_r	-	1	0.7935	0.0767	0.2451
n_ζ	-	-	1	0.0914	0.4707
τ_ζ	-	-	-	1	0.0192
b_β	-	-	-	-	1

Table 5.8: Correlation coefficients for DEMON dutch roll parameter estimates - Run 2
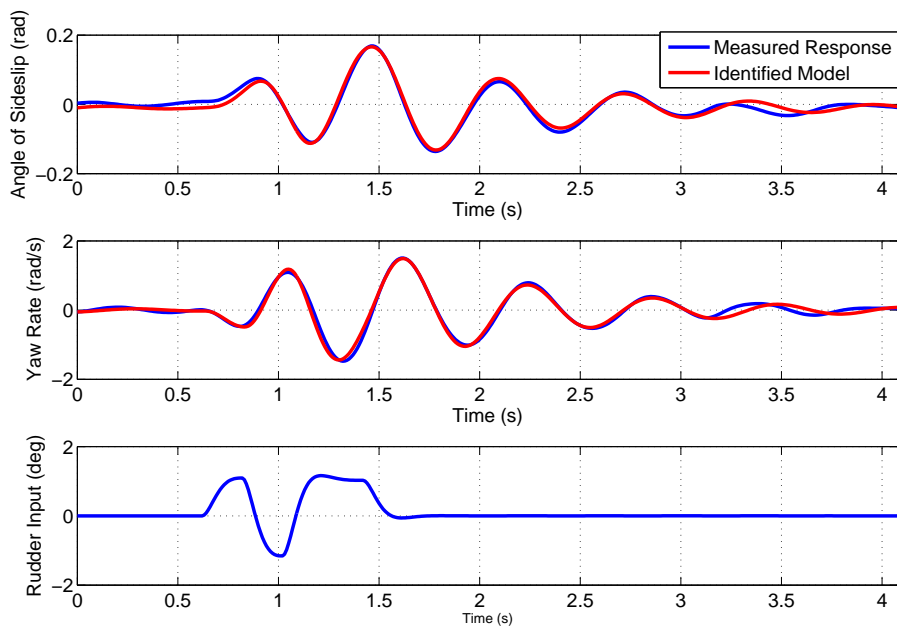
Figure 5.5: Measured and identified responses for a 1-1-2 input to the rudder

variables. Theil's inequality analysis was also used to assess the match between the measured and predicted responses. The results were,

$$\beta: \quad U = 0.1882, \quad U_B = 0.0000, \quad U_V = 0.1412, \quad U_C = 0.8588$$
$$r: \quad U = 0.1364, \quad U_B = 0.0000, \quad U_V = 0.1029, \quad U_C = 0.8971$$

Overall, the fit between the measured and simulated responses is satisfactory. The values of U, for both β and r are below 0.25 and the bias portions are negligible. The variance portions, however, are quite high, particularly for β.

From the analysis outlined above, it was shown that the modified Newton-Raphson algorithm can be used successfully to estimate time delays in the data. Due to the high sampling rate used when conducting the experiments, the restriction that the time delay had to be a multiple of Δt was not found to be a problem. However, some additional subroutines had to be added to the basic algorithm, which increased the complexity of the estimation process. It was also found that a relatively large number of iterations were required to reach convergence. Further, when validating the identified model, the time delay in the doublet data was different from that for the 1-1-2 input. Therefore, additional shifting of the input had to be done manually during the validation process. The estimation of time delays is also possible in the frequency domain and is, in some respects more straightforward, as will be discussed in Chapter 6.
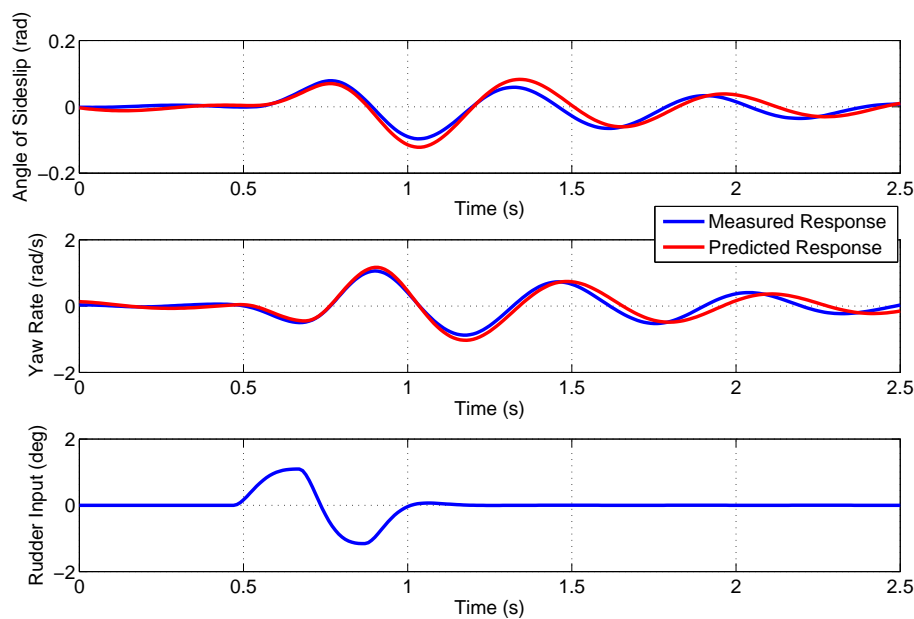
Figure 5.6: Measured and simulated responses for a validation process

Chapter 6

Frequency Domain Estimation

6.1 Introduction

The least squares regression and maximum likelihood methods, presented in Chapters 4 and 5 respectively, can also be applied in the frequency domain. As mentioned in Section 1.1, frequency domain estimation is widely used for rotorcraft identification. However, it finds a number of applications in fixed-wing estimation as well. The approach allows the analysis to be restricted to a given band of frequencies, which is useful, for example, if trying to separate the aircraft's rigid-body dynamics from higher frequency structural modes. Also, many methods of control system design and handling qualities assessment are performed in the frequency domain, in which case frequency domain estimation results may be directly applicable. Prior to performing estimation, the measured data must be transformed into the frequency domain, hence this issue will be dealt with next.

6.2 Transformation of Data

The basis for converting the measured data into the frequency domain is the finite Fourier transform. For a variable $x(t)$, this can be written as,

$$\tilde{x}(f) = \int_0^T x(t)e^{-j2\pi ft}dt \tag{6.2.1}$$

where $\tilde{\ }$ denotes the transformed variable, f the frequency in Hertz and T is the length of time of the data under analysis. When x is measured at N discrete, evenly spaced points in time Equation (6.2.1) can be approximated by,

$$\tilde{x}(f) \approx \Delta t \sum_{i=0}^{N-1} x(i)e^{-j2\pi fi\Delta t} \quad i = 0, 1, 2, \ldots, N-1 \tag{6.2.2}$$

Note that the time index i starts at 0. The frequencies for a conventional Fourier transform are chosen as,

$$f_k = \frac{k}{N\Delta t} \quad k = 0, 1, 2, \ldots, N-1 \tag{6.2.3}$$

which can be expressed in radians as,

$$\omega_k = 2\pi f_k = 2\pi \frac{k}{N\Delta t} \tag{6.2.4}$$

Then the approximation to the finite Fourier transform becomes,

$$\tilde{x}(k) \approx \Delta t \sum_{i=0}^{N-1} x(i) e^{-j(2\pi k/N)i} = \Delta t X(k) \quad k = 0, 1, 2, \ldots, N-1 \tag{6.2.5}$$

where the summation $X(k)$ is termed the discrete Fourier transform (DFT). The calculation of the DFT is not carried out directly due to its computational cost. Instead, the fast Fourier transform (FFT) algorithm is used.

The approximation presented above, however, is not suited to aircraft rigid-body estimation problems [31, 6]. The discrete frequencies used for transforming the data are fixed according to N and Δt. As aircraft rigid-body dynamics are generally located within a region at low frequencies, computational time will be wasted by calculating the DFT for frequencies that are not of interest. Further, the accuracy of the approximation of the finite Fourier transform using Equation (6.2.5) degrades with increased frequency ω and sampling time Δt. The resolution of the transformed data also becomes coarse as N decreases, which can lead to important components of the signal being omitted.

A better method is the use of the chirp z-transform, which decouples the frequency resolution from the length of the data, meaning that the user can choose the frequency band of interest. The accuracy of the transform is improved by combining the chirp z-transform with an interpolation scheme to obtain the values of x, based on the sampled data $x(i)$ and, because the interpolation approximates the continuous time function $x(t)$ rather than $x(t)e^{-j\omega t}$, the accuracy of the transform is not dependent on the chosen frequencies. A common method used for this purpose is cubic Lagrange polynomial interpolation [145]. When transforming the data, choices must be made regarding the upper and lower frequencies of interest and the resolution of the discrete frequencies within this band. The upper frequency limit can be determined by performing the Fourier analysis described earlier in Section 4.3, while a commonly chosen lower limit, in Hertz, is $2/T$ [31, 128], where T is the time length of data under analysis. This means that, for each discrete frequency, there are at least two full sinusoidal waveforms in the transformed data. For problems concerning aircraft rigid-body dynamics, the frequency resolution is typically selected to be around 0.02 or 0.04 Hz [31, 128].

6.3   Least Squares Regression

The formulation of the least squares regression algorithm in the frequency domain is carried out in a similar manner to that outlined in Section 4.2 for the time domain. The regression equation can be written in matrix form as,

$$\tilde{\mathbf{z}} = \tilde{\mathbf{X}}\boldsymbol{\theta} + \tilde{\boldsymbol{\epsilon}} \tag{6.3.1}$$

where the variables are the same as those defined in Equation (4.2.3), except that the measurements of the dependent variable $\mathbf{z}$, the regressors $\mathbf{X}$ and the equation errors $\boldsymbol{\epsilon}$ have been

transformed to the frequency domain. The equation errors are assumed to have the following properties,

$$\text{E}[\tilde{\boldsymbol{\epsilon}}] = \mathbf{0} \text{ and } \text{E}[\tilde{\boldsymbol{\epsilon}}\tilde{\boldsymbol{\epsilon}}^\dagger] = \sigma^2 \mathbf{I}$$

where the superscript $\dagger$ denotes the complex conjugate transpose. The cost function to be minimised is defined as,

$$J(\boldsymbol{\theta}) = \tilde{\boldsymbol{\epsilon}}^\dagger \tilde{\boldsymbol{\epsilon}} = (\tilde{\mathbf{z}} - \tilde{\mathbf{X}}\boldsymbol{\theta})^\dagger (\tilde{\mathbf{z}} - \tilde{\mathbf{X}}\boldsymbol{\theta}) \tag{6.3.2}$$

which leads to the least squares estimate of $\boldsymbol{\theta}$,

$$\hat{\boldsymbol{\theta}} = \left[\text{Re}\left(\tilde{\mathbf{X}}^\dagger \tilde{\mathbf{X}} \right) \right]^{-1} \text{Re}\left(\tilde{\mathbf{X}}^\dagger \tilde{\mathbf{z}} \right) \tag{6.3.3}$$

Note that, as the parameter vector is assumed to be real, only the real parts of $\tilde{\mathbf{X}}$ and $\tilde{\mathbf{z}}$ are required for the calculation. The covariance matrix of the parameter estimates is found from,

$$\mathbf{P} = \text{E}\left[(\hat{\boldsymbol{\theta}} - \boldsymbol{\theta})(\hat{\boldsymbol{\theta}} - \boldsymbol{\theta})^\dagger \right] = \sigma^2 \left[\text{Re}\left(\tilde{\mathbf{X}}^\dagger \tilde{\mathbf{X}} \right) \right]^{-1} \tag{6.3.4}$$

The predicted dependent variable is given by,

$$\hat{\tilde{\mathbf{y}}} = \tilde{\mathbf{X}}\hat{\boldsymbol{\theta}} \tag{6.3.5}$$

and the residuals are determined as,

$$\tilde{\boldsymbol{v}} = \tilde{\mathbf{z}} - \hat{\tilde{\mathbf{y}}} \tag{6.3.6}$$

6.4 Maximum Likelihood Estimation

The major difference between the time domain and frequency domain output error formulations, both solved using maximum likelihood estimation, is that the method is limited to linear systems in the frequency domain. This is because the finite Fourier transform is a linear operator [146]. Least squares regression in the frequency domain can still be used for problems which are nonlinear in the regressors, but linear in the parameters, as the nonlinear regressors are generated in the time domain prior to their transformation.

The linear system dynamics can be described in the frequency domain by the following set of equations,

$$j\omega_k \tilde{\mathbf{x}}(\omega_k) = \mathbf{A}\tilde{\mathbf{x}}(\omega_k) + \mathbf{B}\tilde{\mathbf{u}}(\omega_k) \tag{6.4.1}$$
$$\tilde{\mathbf{y}}(\omega_k) = \mathbf{C}\tilde{\mathbf{x}}(\omega_k) + \mathbf{D}\tilde{\mathbf{u}}(\omega_k) \tag{6.4.2}$$
$$\tilde{\mathbf{z}}(\omega_k) = \tilde{\mathbf{y}}(\omega_k) + \tilde{\boldsymbol{\epsilon}}(\omega_k) \quad k = 0, 1, 2, \ldots, N-1 \tag{6.4.3}$$

where $j = \sqrt{-1}$. Note that, in the frequency domain, the state equation (6.4.1) is no longer a differential equation and can be solved algebraically. The properties of the output errors $\tilde{\boldsymbol{\epsilon}}$ are,

$$\text{E}[\tilde{\boldsymbol{\epsilon}}] = \mathbf{0} \text{ and } \text{E}[\tilde{\boldsymbol{\epsilon}}\tilde{\boldsymbol{\epsilon}}^\dagger] = \frac{\mathbf{S}_{\boldsymbol{\epsilon}\boldsymbol{\epsilon}}}{N}$$

The term $\mathbf{S}_{\boldsymbol{\epsilon}\boldsymbol{\epsilon}}$ is a real diagonal matrix whose elements are the power spectral densities of the elements of $\boldsymbol{\epsilon}$. As with the time domain, the output error cost function is defined as the negative logarithm of the likelihood function, resulting in,

$$J(\boldsymbol{\theta}) = N \sum_{k=0}^{N-1} \tilde{\boldsymbol{\epsilon}}^\dagger(\omega_k, \boldsymbol{\theta}) \mathbf{S}_{\boldsymbol{\epsilon}\boldsymbol{\epsilon}}^{-1} \tilde{\boldsymbol{\epsilon}}(\omega_k, \boldsymbol{\theta}) + N \ln |\mathbf{S}_{\boldsymbol{\epsilon}\boldsymbol{\epsilon}}| \tag{6.4.4}$$

where the power spectral density matrix is estimated from the residuals,

$$\hat{\mathbf{S}}_{\boldsymbol{\epsilon\epsilon}} = \sum_{k=0}^{N-1} \tilde{\boldsymbol{v}}(\omega_k, \hat{\boldsymbol{\theta}}) \tilde{\boldsymbol{v}}^\dagger(\omega_k, \hat{\boldsymbol{\theta}}) = \sum_{k=0}^{N-1} \left[\tilde{\mathbf{z}} - \hat{\tilde{\mathbf{y}}}(\omega_k, \hat{\boldsymbol{\theta}}) \right] \left[\tilde{\mathbf{z}} - \hat{\tilde{\mathbf{y}}}(\omega_k, \hat{\boldsymbol{\theta}}) \right]^\dagger \tag{6.4.5}$$

The modified Newton-Raphson algorithm can again be used to iteratively update the vector of unknown parameters using Equation (5.3.7),

$$\Delta\boldsymbol{\theta} = -\left[\frac{\partial^2 J}{\partial\boldsymbol{\theta}\partial\boldsymbol{\theta}^T} \right]^{-1} \frac{\partial J}{\partial\boldsymbol{\theta}} \tag{6.4.6}$$

The gradient and information matrix are then obtained as,

$$\mathbf{G} = \frac{\partial J}{\partial\boldsymbol{\theta}} = -2N\mathrm{Re}\left\{ \sum_{k=0}^{N-1} \left[\frac{\partial\hat{\tilde{y}}(\omega_k)}{\partial\boldsymbol{\theta}} \right]^\dagger \hat{\mathbf{S}}_{\boldsymbol{\epsilon\epsilon}}^{-1} \tilde{\boldsymbol{v}}(\omega_k, \hat{\boldsymbol{\theta}}) \right\} \tag{6.4.7}$$

$$\mathbf{M} = \frac{\partial^2 J}{\partial\boldsymbol{\theta}\partial\boldsymbol{\theta}^T} \approx 2N\mathrm{Re}\left\{ \sum_{k=0}^{N-1} \left[\frac{\partial\hat{\tilde{y}}(\omega_k)}{\partial\boldsymbol{\theta}} \right]^\dagger \hat{\mathbf{S}}_{\boldsymbol{\epsilon\epsilon}}^{-1} \left[\frac{\partial\hat{\tilde{y}}(\omega_k)}{\partial\boldsymbol{\theta}} \right] \right\} \tag{6.4.8}$$

6.5 Frequency Response Method

The output error method can also be formulated in terms of frequency response data. A frequency response can be defined as the ratio of a system's output per unit of control input as a function of the control input frequency [6]. The output of a linear, time-invariant system can be related to the input by the following expression,

$$\tilde{\mathbf{y}}(t) = \int_0^t \mathbf{H}(t - \tau)\tilde{\mathbf{u}}(\tau)d\tau \tag{6.5.1}$$

where zero initial conditions were assumed. Taking the Laplace transform of Equation (6.5.1),

$$\tilde{\mathbf{y}}(s) = \mathbf{H}(s)\tilde{\mathbf{u}}(s) \tag{6.5.2}$$

where s is the Laplace operator and $\mathbf{H}$ is a matrix of transfer functions. For the system described by Equations (6.4.1) and (6.4.2), the transfer function matrix can be obtained from,

$$\mathbf{H}(s) = \mathbf{C}(s\mathbf{I} - \mathbf{A})^{-1}\mathbf{B} + \mathbf{D} \tag{6.5.3}$$

Replacing s with $j\omega$ and rearranging Equation (6.5.2), the frequency response matrix is,

$$\mathbf{H}(j\omega) = \frac{\tilde{\mathbf{y}}(j\omega)}{\tilde{\mathbf{u}}(j\omega)} \tag{6.5.4}$$

The frequency response matrix can also be expressed as,

$$\mathbf{H}(j\omega) = |\mathbf{H}(j\omega)|\, e^{j\phi(\omega)} \tag{6.5.5}$$

where,

$$|\mathbf{H}(j\omega)| = \sqrt{\{\mathrm{Re}[\mathbf{H}(j\omega)]\}^2 + \{\mathrm{Im}[\mathbf{H}(j\omega)]\}^2}$$

$$\phi(\omega) = \angle\mathbf{H}(j\omega) = \tan^{-1}\left\{ \frac{\mathrm{Im}[\mathbf{H}(j\omega)]}{\mathrm{Re}[\mathbf{H}(j\omega)]} \right\}$$

The term $|\mathbf{H}(j\omega)|$ is the amplitude and $\phi(\omega)$ is the phase.

Spectral densities are normally used for the determination of the frequency responses[6, 31]. Expressions for $\mathbf{H}(j\omega)$ in terms of spectral densities are developed as follows. Firstly, the input-output relationship defined in Equation (6.5.1) is written in terms of correlation functions,

$$\mathcal{R}_{yu}(\tau) = \int_0^\infty \mathbf{H}(t)\mathcal{R}_{uu}(t+\tau)dt = \mathcal{R}_{uy}(-\tau) \tag{6.5.6}$$

where $\mathcal{R}_{yu}$ is the cross-correlation function for the input and output and $\mathcal{R}_{uu}$ is the input auto-correlation function,

$$\mathcal{R}_{yu}(\tau) = \lim_{T\to\infty} \frac{1}{T}\int_0^T \mathbf{y}(t)\mathbf{u}(t+\tau)dt \tag{6.5.7}$$

$$\mathcal{R}_{uu}(\tau) = \lim_{T\to\infty} \frac{1}{T}\int_0^T \mathbf{u}(t)\mathbf{u}(t+\tau)dt \tag{6.5.8}$$

The power spectral density functions are then obtained by applying the Fourier transform to the correlation functions in Equations (6.5.7) and (6.5.8) giving,

$$\mathbf{S}_{yu}(j\omega) = \int_0^\infty \mathcal{R}_{yu}(\tau)e^{-j\omega\tau}d\tau \tag{6.5.9}$$

$$\mathbf{S}_{uu}(j\omega) = \int_0^\infty \mathcal{R}_{uu}(\tau)e^{-j\omega\tau}d\tau \tag{6.5.10}$$

Now, it can be shown that convolution in the time domain is equivalent to multiplication in the frequency domain [31] so the Fourier transform of Equation (6.5.6) becomes,

$$\mathbf{S}_{yu}(j\omega) = \mathbf{H}(j\omega)\mathbf{S}_{uu}(j\omega) \tag{6.5.11}$$

and the spectral densities can be written as,

$$\mathbf{S}_{yu}(j\omega) = \tilde{\mathbf{y}}(j\omega)\tilde{\mathbf{u}}^*(j\omega) \tag{6.5.12}$$

$$\mathbf{S}_{uu}(j\omega) = \tilde{\mathbf{u}}(j\omega)\tilde{\mathbf{u}}^*(j\omega) \tag{6.5.13}$$

where * denotes the complex conjugate of a transformed variable. Therefore, the frequency response matrix can be obtained from the spectral densities,

$$\hat{\mathbf{H}}(j\omega) = \frac{\mathbf{S}_{yu}(j\omega)}{\mathbf{S}_{uu}(j\omega)} = \frac{\tilde{\mathbf{y}}(j\omega)\tilde{\mathbf{u}}^*(j\omega)}{\tilde{\mathbf{u}}(j\omega)\tilde{\mathbf{u}}^*(j\omega)} \tag{6.5.14}$$

Because of inaccuracies, direct calculation of the spectral densities from the Fourier transforms in Equations (6.5.12) and (6.5.13) are not carried out. Practical approaches to calculating power spectral densities for measured data can be found, for example, in texts by Bendat and Piersol [147], Tischler [6] and Klein and Morelli [31].

The cost function to be minimised can be written in terms of frequency responses as follows,

$$J(\boldsymbol{\theta}) = N\sum_{k=0}^{N-1}\left[\mathbf{H}(k) - \hat{\mathbf{H}}(k,\boldsymbol{\theta})\right]^\dagger \hat{\mathbf{S}}_{\epsilon\epsilon}^{-1}\left[\mathbf{H}(k) - \hat{\mathbf{H}}(k,\boldsymbol{\theta})\right] \tag{6.5.15}$$

where $\mathbf{H}(k)$ is the frequency response matrix determined from the experimental data for the kth frequency and $\hat{\mathbf{H}}(k,\boldsymbol{\theta})$ is an estimate of the frequency response matrix calculated using

Equation (6.5.3) and estimates of the unknown parameters in the system matrices **A**, **B**, **C** and **D**. Alternatively, the frequency responses can be partitioned into their amplitude and phase components [6],

$$J(\boldsymbol{\theta}) = \frac{20}{N} \sum_{k=0}^{N-1} w_\gamma \left[w_g \left\{ |\mathbf{H}(k)| - |\hat{\mathbf{H}}(k, \boldsymbol{\theta})| \right\}^2 + w_p \left\{ \angle\mathbf{H}(k) - \angle\hat{\mathbf{H}}(k, \boldsymbol{\theta}) \right\}^2 \right] \quad (6.5.16)$$

where w_g and w_p are relative weightings for the amplitude and phase errors. Typically, $w_g = 1$ and $w_p = 0.01745$. The third weighting term, w_γ, is dependent on the coherence at each frequency, which is defined by the equation,

$$\gamma_{yu}^2(\omega) = \frac{|\mathbf{S}_{yu}(j\omega)|^2}{\mathbf{S}_{uu}(j\omega)\mathbf{S}_{yy}(j\omega)} \quad (6.5.17)$$

Coherence is a measure of the fraction of the output spectrum $\mathbf{S}_{yy}$ that is linearity attributed to the input spectrum $\mathbf{S}_{uu}$ at each of the discrete frequencies and indicates whether the system being modelled is well characterised as a linear process in the frequency range of interest. The coherence value falls between 0 and 1, with 1 indicating a perfectly linear relationship between **y** and **u**. The cost function given in Equation (6.5.16) is that used for the frequency response method encapsulated in the software program CIFER.

6.6   UAV Pitching Moment Example

The first example of frequency domain estimation presented here is analysis applied to the UAV data, used previously in Section 5.9, containing three elevator doublets. In the previous example, the modified Newton-Raphson algorithm in the time domain was used to estimate the short period derivatives. This time, the results of frequency domain least squares regression to find the non-dimensional pitching moment derivatives is outlined. The equation of motion for this example is,

$$C_m = C_{m_0} + C_{m_\alpha}\alpha + C_{m_V}\hat{V} + C_{m_q}\hat{q} + C_{m_\eta}\eta \quad (6.6.1)$$

Note the inclusion of the derivative C_{m_V} in Equation (6.6.1). This term was not used to account for any aircraft dynamics, as the airspeed is assumed to be constant for the short period approximation, but instead used to model slight drifts in the airspeed during the manoeuvres. This phenomenon has also been reported by Morelli [128].

When the data is transformed into the frequency domain, the Fourier transform removes all biases and linear trends from the signals. Hence, for the pitching moment example, it was not possible to estimate C_{m_0} and C_{m_V} (which models the pitching moment trend with airspeed) in the frequency domain. These two derivatives were estimated separately in the time domain using the output error method, which was carried out as normal but with the values of C_{m_α}, C_{m_q} and C_{m_η} held fixed at the estimates obtained from frequency domain least squares regression. Table 6.1 displays the resulting parameter estimates from this two step process, along with the standard errors for the estimates, which indicate a high level of confidence in the values. The estimates and standard errors obtained from time domain least squares regression are also shown for comparison. There is good agreement between the frequency domain and time domain estimates and the magnitudes of the two sets of standard errors are very similar.

With regards to the standard errors, it should be noted that for frequency domain estimation a correction for coloured residuals is generally not applied as is done for the time domain. The analysis is restricted to the frequencies in which the rigid-body dynamics are located and, while it is in this band that the largest spectral components of the residuals are located, the noise power over the rigid-body frequencies is relatively constant. This matches closely to the assumption of white residuals with constant power over the frequency spectrum, hence no correction needs to be applied. In practice, the additional factor of 2, introduction in Section 4.6, is still often needed to match the scatter in parameter estimates [132, 6], hence has still been applied to the standard errors presented in this chapter.

	Frequency Domain		Time Domain	
	$\hat{\theta}$	$100[s/|\hat{\theta}|]$	$\hat{\theta}$	$100[s/|\hat{\theta}|]$
C_{m_0}	0.947*	0.60	0.949	0.46
C_{m_α}	1.002	7.19	1.096	8.47
C_{m_V}	0.880*	7.06	0.930	6.53
C_{m_q}	1.367	6.14	1.218	7.43
C_{m_η}	1.084	3.24	1.012	3.40

* - estimated separately in time domain

Table 6.1: Estimates of pitching moment derivatives from frequency domain and time domain least squares regression

Figure 6.1 shows a plot of the magnitude of the transformed pitching moment coefficient $|\tilde{C}_m|$ against frequency for both the measured data and the identified model. Visually, an accurate match between the two was achieved. Next, once the estimates of C_{m_0} and C_{m_V} were obtained, it was possible to reconstruct the time history of the identified model and compare it against the measured data. This is illustrated in Figure 6.2, along with the elevator inputs applied during the three manoeuvres. Again, there is close agreement between the two responses and Theil's inequality analysis also indicated a satisfactory match,

$$U = 0.0220, \ U_B = 0.0118, \ U_V = 0.0008, \ U_C = 0.9874$$

Figure 6.3 shows the measured and predicted pitching moment responses obtained from the validation process, which used the elevator input displayed in the lower plot. Is can be seen that the predicted response fitted closely to the unseen measured data. The results of Theil's inequality analysis for the validation process were,

$$U = 0.0236, \ U_B = 0.0792, \ U_V = 0.0008, \ U_C = 0.9200$$

Again, this suggested that the predicted response provided an accurate match to the measured response.

6.7 DEMON Short Period Example

Next, the frequency domain parameter estimation process used to establish the short period derivatives of the DEMON model is illustrated. In this example, the data contained a 1-1-2
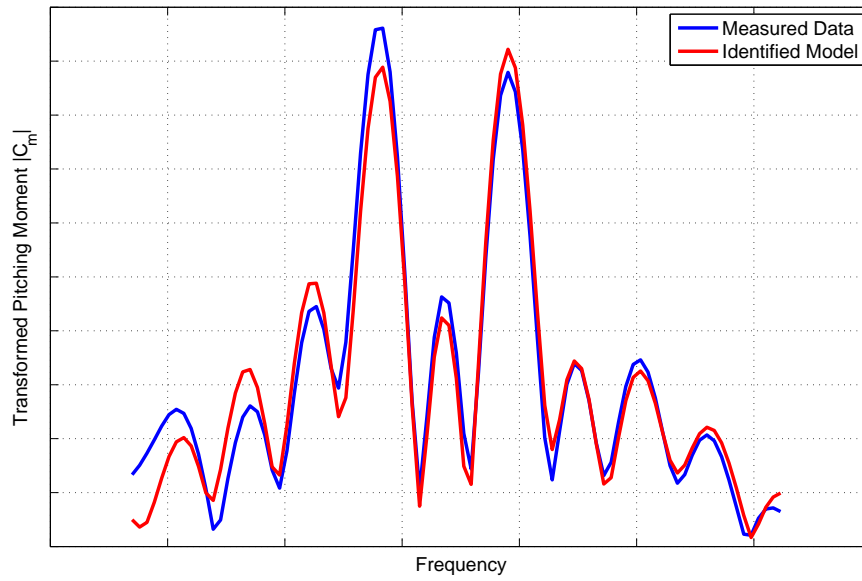
Figure 6.1: Frequency domain fit between measured data and the identified model
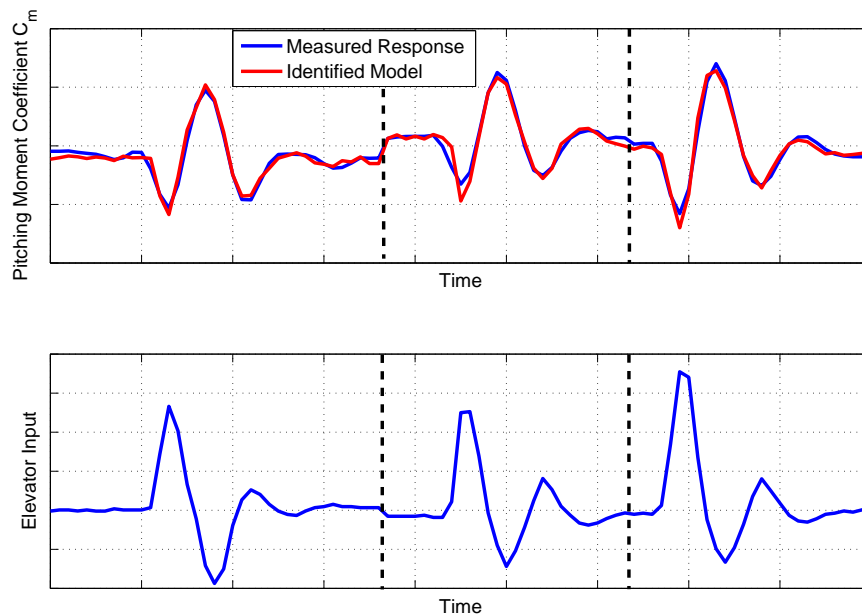
Figure 6.2: Measured and identified responses for elevator doublets
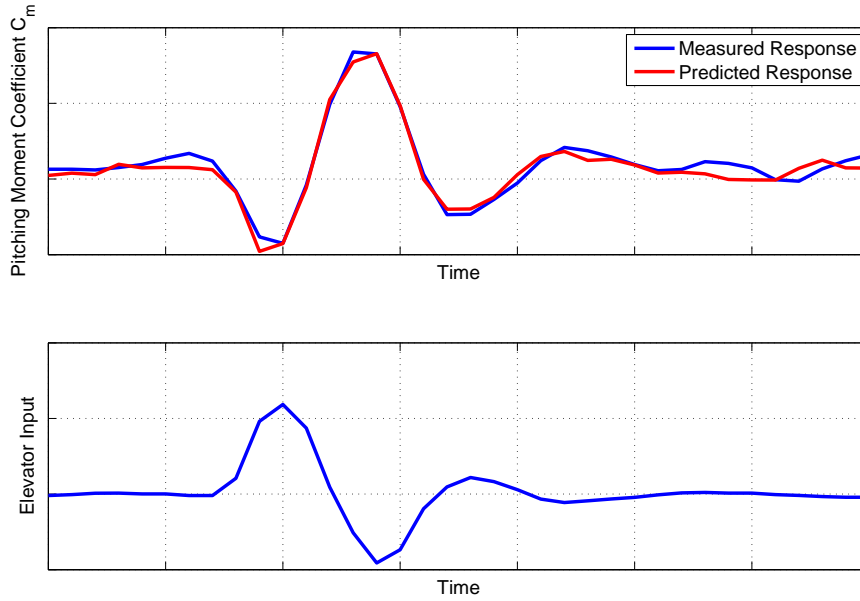
Figure 6.3: Measured and identified pitching moment
responses to an elevator input for validation process

input to the elevator. As well as the stability and control derivatives, the time delay between the
control input and measured response was treated as an unknown parameter to be determined.
Repeating Equations (4.9.1) and (4.9.2), the linear state-space equations of motion incorporat-
ing a time delay on the input can be written as.

$$\dot{\mathbf{x}}(t) = \mathbf{A}\mathbf{x}(t) + \mathbf{B}\mathbf{u}(t - \boldsymbol{\tau}) \tag{6.7.1}$$

$$\mathbf{y}(t) = \mathbf{C}\mathbf{x}(t) + \mathbf{D}\mathbf{u}(t - \boldsymbol{\tau}) \tag{6.7.2}$$

When transformed to the frequency domain, the above expressions become,

$$j\omega\tilde{\mathbf{x}}(\omega) = \mathbf{A}\tilde{\mathbf{x}}(\omega) + \mathbf{B}\tilde{\mathbf{u}}(\omega)e^{-j\omega\boldsymbol{\tau}} \tag{6.7.3}$$

$$\tilde{\mathbf{y}}(\omega) = \mathbf{C}\tilde{\mathbf{x}}(\omega) + \mathbf{D}\tilde{\mathbf{u}}(\omega)e^{-j\omega\boldsymbol{\tau}} \tag{6.7.4}$$

and the corresponding equations for the short period problem were,

$$\begin{bmatrix} j\omega\tilde{w}(\omega) \\ j\omega\tilde{q}(\omega) \end{bmatrix} = \begin{bmatrix} 0 & V_T \\ m_w & m_q \end{bmatrix} \begin{bmatrix} \tilde{w}(\omega) \\ \tilde{q}(\omega) \end{bmatrix} + \begin{bmatrix} 0 \\ m_\eta \end{bmatrix} \eta(\omega)e^{-j\omega\tau_\eta} \tag{6.7.5}$$

$$\begin{bmatrix} \tilde{\alpha}(\omega) \\ \tilde{q}(\omega) \end{bmatrix} = \begin{bmatrix} 1/V_T & 0 \\ 0 & 1 \end{bmatrix} \begin{bmatrix} \tilde{w}(\omega) \\ \tilde{q}(\omega) \end{bmatrix} + \begin{bmatrix} 0 \\ 0 \end{bmatrix} \eta(\omega)e^{-j\omega\tau_\eta} \tag{6.7.6}$$

Once again, the appearance of the time delay term τ_η makes the parameter estimation problem
a nonlinear one, hence it was not possible to use least squares regression. Instead, the modi-
fied Newton-Raphson algorithm was implemented to solve first an equation error formulation
followed by an output error problem. For the equation error method, the state derivatives were
treated as the measured values i.e.,

$$\tilde{\mathbf{z}}(\omega) = \begin{bmatrix} j\omega\tilde{w}(\omega) \\ j\omega\tilde{q}(\omega) \end{bmatrix} \tag{6.7.7}$$

and the aim of the process was to find the parameter values which lead to a match between the measured and predicted state derivatives. For the output error method, the goal was to seek a model to match the transformed angle of attack and pitch rate signals $\tilde{\alpha}$ and $\tilde{q}$ respectively. Because the modified Newton-Raphson method is iterative, starting parameter estimates were required for both methods. However, the equation error formulation is more robust to starting values of the parameters in comparison with the output error method [31] and it was found that the initial estimates for the equation error approach could all be set to zero without effecting convergence. The final equation error estimates were then used as starting values for the output error method.

The measured data was transformed with a lower frequency of around 0.67 Hz, an upper frequency of approximately 5 Hz and a resolution of 0.02 Hz. The structural vibration in the test rig, described in Section 4.10 and illustrated in Figure 4.25, of around 8-9 Hz was observed during the experiments but, as the analysis was restricted to frequencies under 5 Hz, was removed during the data transformation process.

The results obtained with the equation error and output error methods are displayed in Table 6.2. Convergence was achieved using the equation error formulation after $t_{comp} = 20.92$ sec and 92 iterations, while the output error method required $t_{comp} = 23.00$ sec and 44 iterations. The values in Table 6.2 show good agreement between the estimates from the two approaches, while the standard errors indicate high confidence in the estimates. Further, there was no excessive correlation between any of the parameters as shown in Table 6.3. Figure 6.4 displays plots of the magnitudes of the transformed angle of attack and pitch rate, $|\tilde{\alpha}|$ and $|\tilde{q}|$ respectively, against frequency for the measured data and the identified model.

	Equation Error Method		Output Error Method	
	$\hat{\theta}$	$100[s/|\hat{\theta}|]$	$\hat{\theta}$	$100[s/|\hat{\theta}|]$
V_T	28.6316	0.59	28.1490	3.71
m_w	-3.7858	2.36	-3.7803	3.56
m_q	-11.6458	3.32	-11.4113	2.39
m_η	-2.0256	3.07	-2.0972	2.54
τ_η	0.3248	0.53	0.3259	0.45

Table 6.2: Estimates of DEMON short period derivatives from frequency domain estimation

	V_T	m_w	m_q	m_η	τ_η
V_T	1	0.6215	0.1911	0.5803	0.2692
m_w	-	1	0.0821	0.7344	0.1103
m_q	-	-	1	0.6413	0.6654
m_η	-	-	-	1	0.3395
τ_η	-	-	-	-	1

Table 6.3: Correlation coefficients for DEMON short period parameter estimates - output error method

Once the frequency domain output error estimates were obtained, the time histories of the predicted α and q signals were reconstructed and compared with the measured responses (Figure
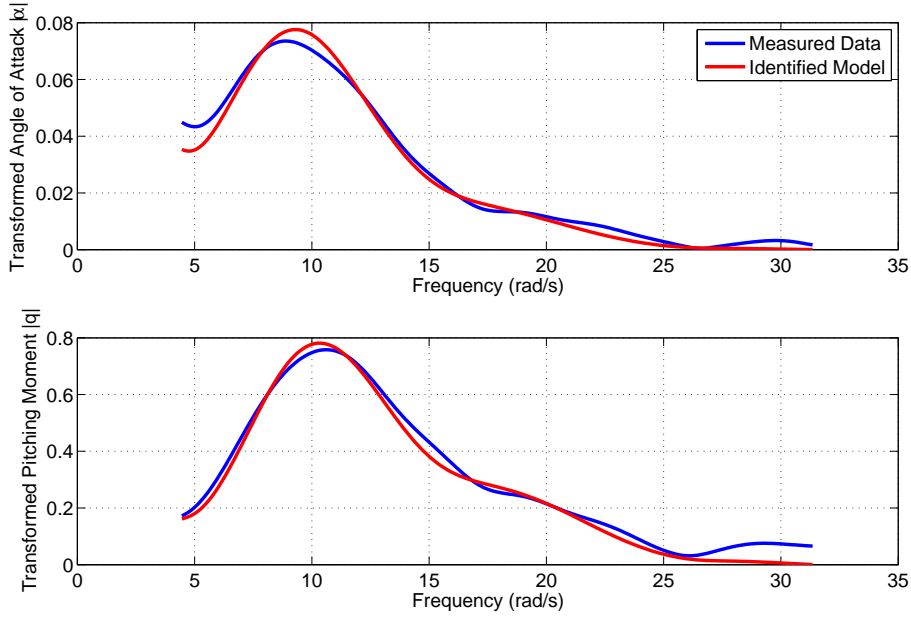
Figure 6.4: Frequency domain fit between measured and
identified angle of attack and pitch rate responses

6.5) . This required that two bias terms be determined - one for the normal velocity state equation, $b_{\dot{w}}$, and one for the angle of attack output equation, b_α. As with the previous example, these bias terms were estimated using the modified Newton-Raphson algorithm in the time domain, with the values for the derivatives and the time delay held fixed at those given in Table 6.2. The estimate of $b_{\dot{w}}$ was -1.0689 with a relative standard error of 13.62%, while b_α was found to be -0.0021 with a relative standard error of 15.46%. Theil's inequality analysis was then carried out, with the following results,

$$\alpha : U = 0.0757, \ U_B = 0.0000, \ U_V = 0.0016, \ U_C = 0.9984$$
$$q : U = 0.0946, \ U_B = 0.0010, \ U_V = 0.0404, \ U_C = 0.9585$$

Therefore, a very close match between the measured and identified responses was achieved.

Data for an elevator doublet manoeuvre was then used to validate the model identified from the 1-1-2 input. The measured and predicted responses for angle of attack and pitch rate are displayed in Figure 6.6 along with the elevator time history. Theil's inequality analysis on the predicted residuals produced the following results,

$$\alpha : U = 0.0943, \ U_B = 0.0000, \ U_V = 0.0092, \ U_C = 0.9908$$
$$q : U = 0.0959, \ U_B = 0.0957, \ U_V = 0.0076, \ U_C = 0.8967$$

Both the plots in Figure 6.6 and Theil's inequality analysis indicate that the predicted response provided a satisfactory match to the measured data.

As with the dutch roll estimates presented in Section 4.9, there are discrepancies between the estimated short period derivatives and the *a priori* values given in Chapter 2. The worst affected are m_w and m_q for which the experimental values are around 40% of empirical estimates. However, the analysis above indicates that the estimates were statistically reliable. Again,
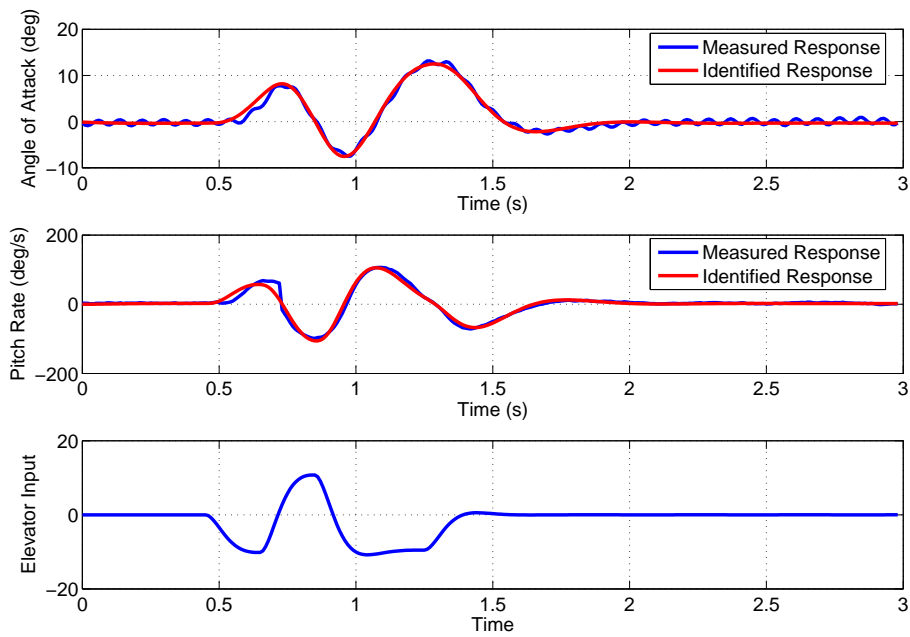
Figure 6.5: Measured and identified responses for 1-1-2 elevator input
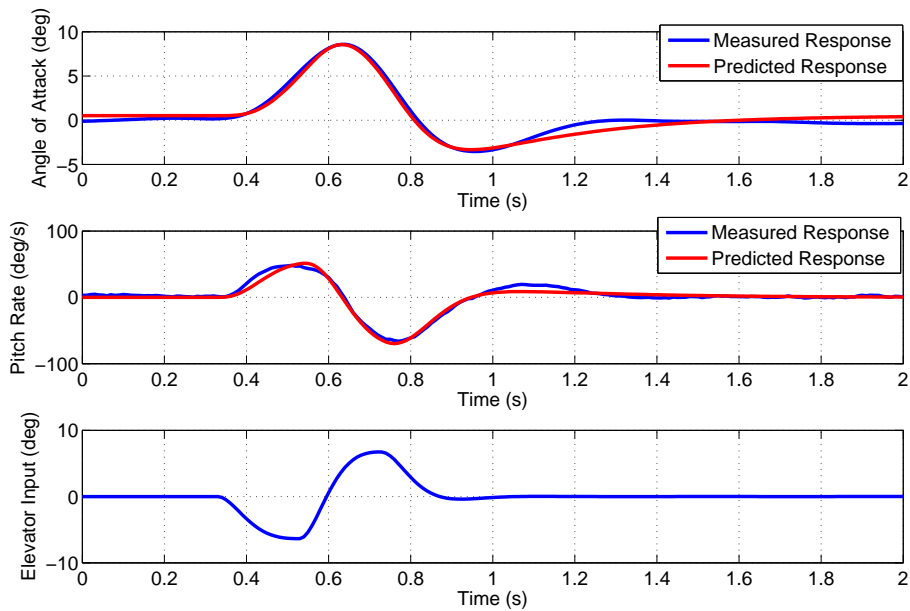
Figure 6.6: Measured and predicted responses to an elevator doublet for validation process

despite the inputs having been designed using limited *a priori* information, there was enough information content in the data to obtain satisfactory parameter estimates. This further confirms the suitability of the multistep input approach for the wind tunnel experiments.

Chapter 7

Estimation Issues for UAVs

7.1 Introduction

This next chapter of the thesis focuses on two issues that are of particular concern when performing estimation on UAVs. The first is estimation in the presence of atmospheric turbulence. It has already been mentioned that flight tests of aircraft are usually performed early in the morning when the thermal activity responsible for turbulence is at a minimum. However, because of their low mass and inertias in comparison to manned aircraft, UAVs will be more susceptible to the effects of turbulence, especially those classed as miniature UAVs. For these aircraft, it may not be practical to wait for the favourable conditions required to assume that the data is free of turbulence, therefore methods for parameter estimation which explicitly model turbulence effects are considered.

The second issue is estimation of the open-loop characteristics of the aircraft from data in which closed-loop feedback control was used. If an aircraft contains any form of feedback control system then, ideally, these should be disengaged during flight tests as they will tend to mask or augment the bare airframe properties. However, some aircraft configurations, such as UCAVs, have inherently unstable airframes and therefore cannot be flown safely without some form of stability augmentation system. Further, because of the drive towards autonomous operation, the level of control system architecture employed on UAVs is high, even for aircraft with stable airframes, and it may not always be practical to disengage the control systems prior to flight testing. Hence, this chapter also discusses some aspects of extracting the stability and control derivatives of the bare airframe from closed-loop flight test data.

7.2 Estimation in the Presence of Atmospheric Turbulence

The equation error and output error methods outlined in the previous two chapters are not suited to estimation when the measurements are corrupted by turbulence. In Chapter 4 and Appendix B, it was shown that process noise leads to an increased variance in the least squares parameter estimates, while the output error approach only accounts for measurement noise and may struggle to converge if the process noise is significant. Note that, as well as atmospheric turbulence, another source of process noise could be errors in the measurement of the control input variables, including motion variables fedback as part of a flight control system. Two

methods which can be used when data is corrupted by both measurement and process noise are presented below.

7.2.1 Maximum Likelihood Filter Error Method

The first method to be considered is an extension of the output error approach also based on maximum likelihood estimation. To start with, a general linear form of the aircraft equations of motion will be considered. This can be written as,

$$\dot{\mathbf{x}}(t) = \mathbf{A}\mathbf{x}(t) + \mathbf{B}\mathbf{u}(t) + \mathbf{F}\mathbf{w}(t) + \mathbf{b}_x, \quad \mathbf{x}(t_0) = \mathbf{x}_0 \qquad (7.2.1)$$

$$\mathbf{y}(t) = \mathbf{C}\mathbf{x}(t) + \mathbf{D}\mathbf{u}(t) + \mathbf{b}_y \qquad (7.2.2)$$

$$\mathbf{z}(i) = \mathbf{y}(i) + \mathbf{G}_v\mathbf{v}(i), \quad i = 1, 2, \dots, N \qquad (7.2.3)$$

The state equation (7.2.1) has an additional term $\mathbf{F}\mathbf{w}(t)$, where $\mathbf{w}(t)$ is process noise, characterised as zero-mean Gaussian noise with an identity spectral density, used to model the effects of atmospheric turbulence. The matrix $\mathbf{F}$ is the process noise distribution matrix, which is assumed to be diagonal. In the measurement equation, the N discrete observations of $\mathbf{y}$ are corrupted by measurement noise $\mathbf{v}(i)$, which is assumed to be a sequence of Gaussian random variables with zero mean and identity covariance. The matrix $\mathbf{G}_v$ is the measurement noise distribution matrix. For completeness, the vectors of lumped biases $\mathbf{b}_x$ and $\mathbf{b}_y$, which account for uncertainty in the initial conditions and biases in the measurements of the input and output variables, are also included in Equations (7.2.1) and (7.2.2). In general, the elements of $\mathbf{F}$ and $\mathbf{G}_v$ are unknowns.

The above model of turbulence as a white noise process is a very simple one and attempts have been made to incorporate more sophisticated turbulence models into the equations of motion. For example, Foster [140] used the Dryden spectrum [148] in which turbulence is modelled as a first order Gauss-Markov process,

$$\dot{x}_g = -ax_g + b\mu_g \qquad (7.2.4)$$

where x_g is the gust velocity component, μ_g is the driving process noise and a and b are the statistical parameters characterising the turbulence. These gust components are then added to the system as additional states. The drawback of this approach is that the increased number of states means the problem is computationally slower to solve. Also, it requires the specification of the turbulence noise statistics a and b, which are difficult to determine and vary from case to case. Further, it has been shown that the estimates of the stability and control derivatives are largely unaffected by the model chosen to represent turbulence [149]. As the primary interest of the parameter estimation process is to obtain reliable estimates of the stability and control derivatives, rather than estimate turbulence parameters, it can be seen as advantageous to retain the simpler white noise process model. However, if the gust components are estimated during the data compatibility check then a model of the form of Equation (7.2.4) is often utilised. This is discussed further in Chapter 9.

The appearance of the process noise term makes the equations of motion stochastic, meaning that a state estimator such as the Kalman filter is required to integrate the aircraft states. The Kalman filter was introduced in Section 3.3, where its use for sensor fusion and attitude determination was outlined. State estimation is a two stage process. Firstly, there is a prediction step in which the aircraft states for the next time point are calculated. This is then followed by

a correction step in which measured data is incorporated to improve the estimates of the states. Using the discrete-time form, the expressions for the predicted state vector and subsequent predicted output vector for the ith data point are,

$$\tilde{\mathbf{x}}(i) = \boldsymbol{\Phi}\hat{\mathbf{x}}(i-1) + \boldsymbol{\Psi}\mathbf{B}\bar{\mathbf{u}}(i-1) + \boldsymbol{\Psi}\mathbf{b}_x \quad (7.2.5)$$

$$\tilde{\mathbf{y}}(i) = \mathbf{C}\tilde{\mathbf{x}}(i) + \mathbf{D}\mathbf{u}(i) + \mathbf{b}_y \quad (7.2.6)$$

where $\tilde{\mathbf{x}}$ and $\tilde{\mathbf{y}}$ are the predicted state and output vector respectively. The matrix $\boldsymbol{\Phi}$ is the state transition matrix and $\boldsymbol{\Psi}$ is its integral, the definitions of which were given previously in Equation (5.4.5). The term $\bar{\mathbf{u}}(i-1)$ is again the average of the control inputs at the $(i-1)$th and ith data points. The vector $\hat{\mathbf{x}}$ contains the corrected state variables, which are determined from the following correction step,

$$\hat{\mathbf{x}}(i) = \tilde{\mathbf{x}}(i) + \mathbf{K}[\mathbf{z}(i) - \tilde{\mathbf{y}}(i)] \quad (7.2.7)$$

where $\mathbf{K}$ is the Kalman filter gain matrix.

In situations where the aircraft dynamics can be modelled as time-invariant and perturbations from trim are small, the steady-state form of the Kalman filter can be used. This significantly reduces the computational burden of the problem because the Kalman gain matrix only has to be computed once rather than at each point in time. The steady-state gain matrix is calculated using the expression,

$$\mathbf{K} = \mathbf{P}\mathbf{C}^T\mathbf{R}^{-1} \quad (7.2.8)$$

where $\mathbf{P}$ now denotes the covariance matrix of the state prediction error and $\mathbf{R}$ is the covariance matrix of the residuals $[\mathbf{z}(i) - \tilde{\mathbf{y}}(i)]$. Covariance $\mathbf{R}$ is related to $\mathbf{P}$ and the measurement noise covariance matrix $\mathbf{G}_v\mathbf{G}_v^T$ by,

$$\mathbf{R} = \mathbf{G}_v\mathbf{G}_v^T + \mathbf{C}\mathbf{P}\mathbf{C}^T \quad (7.2.9)$$

The cost function for the filter error method takes the same form as that given in Equation (5.3.2) for the output error method,

$$J(\boldsymbol{\theta}, \mathbf{R}) = \frac{1}{2}\sum_{i=1}^{N}[\mathbf{z}(i) - \tilde{\mathbf{y}}(i)]^T\mathbf{R}^{-1}[\mathbf{z}(i) - \tilde{\mathbf{y}}(i)] + \frac{N}{2}\ln|\mathbf{R}| + \frac{Nn_y}{2}\ln(2\pi) \quad (7.2.10)$$

and J can be minimised again using the modified Newton-Raphson algorithm outlined in Chapter 5.

Now, as well as the system matrices $\mathbf{A}$, $\mathbf{B}$, $\mathbf{C}$ and $\mathbf{D}$, along with the lumped bias terms $\mathbf{b}_x$ and $\mathbf{b}_y$, the elements of $\mathbf{F}$, $\mathbf{G}_v$, $\mathbf{K}$ and $\mathbf{R}$ are unknown parameters to be determined. However, including all of the above terms in the parameter vector $\boldsymbol{\theta}$ will lead to identifiability problems from trying to estimate a large number of parameters from a limited amount of data. To solve this problem, three formulations of the filter error method have been proposed [139, 34]. In general, all three approaches include $\mathbf{A}$, $\mathbf{B}$, $\mathbf{C}$, $\mathbf{D}$, $\mathbf{b}_x$ and $\mathbf{b}_y$ in the unknown parameter vector $\boldsymbol{\theta}$. A choice is then made regarding which of the remaining terms to estimate directly and which to calculate *a posteriori*. The first method is termed the natural formulation, in which the elements of $\mathbf{F}$ and $\mathbf{G}_v$ are added to $\boldsymbol{\theta}$. However, the maximum likelihood cost function must be minimised with respect to the residual covariance and the approach has been found to suffer from convergence problems, caused mainly by complex relationship between $\mathbf{F}$, $\mathbf{G}$ and $\mathbf{R}$. Also, estimation of $\mathbf{F}$ is by far the most complex part of the algorithm, hence, in the past, this formulation was limited by the computational burden. The second approach, termed the innovation formulation, seeks

to overcome the difficulties with the natural formulation by instead estimating $\mathbf{R}$ and $\mathbf{K}$. The residual covariance is determined in a similar manner to the output error method i.e. with the asymptotic approximation,

$$\hat{\mathbf{R}} = \frac{1}{N} \sum_{i=1}^{N} [\mathbf{z}(i) - \tilde{\mathbf{y}}(i)][\mathbf{z}(i) - \tilde{\mathbf{y}}(i)]^T \tag{7.2.11}$$

and $\mathbf{K}$ is included in $\boldsymbol{\theta}$. A drawback of this approach, however, is that it is difficult to interpret if the estimated elements of $\mathbf{K}$ are reasonable as they have no direct physical meaning. Also, $\mathbf{R}$ and $\mathbf{K}$ are estimated separately but are related by Equation (7.2.8) so the two estimates may be incompatible. The third approach is a combination of the natural and innovation formulations. The residual covariance $\mathbf{R}$ is estimated using Equation (7.2.11) and the process noise matrix $\mathbf{F}$ is included as an unknown parameter. As mentioned above, estimation of $\mathbf{F}$ is the most computationally intensive part of the algorithm. However, the elements of $\mathbf{F}$ are easier to interpret than those of $\mathbf{K}$ and the method has been found to perform well in practice. Therefore, only the third formulation is considered for the rest of this chapter.

7.2.2 Filter Error Method Algorithm for Linear Systems

The major steps in the filter error algorithm are as follows,

1. Specify initial estimate of $\boldsymbol{\theta}$ i.e. elements of $\mathbf{A}$, $\mathbf{B}$, $\mathbf{C}$, $\mathbf{D}$, $\mathbf{F}$, $\mathbf{b}_x$ and $\mathbf{b}_y$.

2. Determine an initial estimate of the residual covariance $\mathbf{R}$ from (7.2.11).

3. Calculate the Kalman gain matrix $\mathbf{K}$ and perform state estimation to determine predicted output $\tilde{\mathbf{y}}$.

4. Compute a new estimate of $\mathbf{R}$ from (7.2.11).

5. Execute the modified Newton-Raphson algorithm to update $\hat{\boldsymbol{\theta}}$.

6. Repeat steps 3-5 until convergence is achieved.

For step 2, the initial estimate of $\mathbf{R}$ is usually obtained by assuming that all noise within the data is measurement noise [34], in which case the Kalman gain matrix $\mathbf{K}$, the process noise distribution $\mathbf{F}$ and the state prediction error covariance $\mathbf{P}$ are all zero. Steps 3 to 5 of the process outlined above will now be described.

The Kalman gain matrix is calculated from Equation (7.2.8), which requires knowledge of $\mathbf{P}$. The state error covariance is found by solving the continuous-time Riccati equation,

$$\mathbf{AP} + \mathbf{PA}^T - \frac{1}{\Delta t}\mathbf{PC}^T\mathbf{R}^{-1}\mathbf{CP} + \mathbf{FF}^T = 0 \tag{7.2.12}$$

where $\mathbf{FF}^T$ is the process noise covariance matrix. The Riccati equation can be solved using Potter's method for eigenvector decomposition [139, 34]. Firstly, the following Hamiltonian matrix is constructed,

$$\mathbf{H} = \begin{bmatrix} \mathbf{A} & -\mathbf{FF}^T \\ -\frac{1}{\Delta t}\mathbf{C}^T\mathbf{R}^{-1}\mathbf{C} & -\mathbf{A}^T \end{bmatrix} \tag{7.2.13}$$

The matrix $\mathbf{H}$ is of size $(2n_x \times 2n_x)$, where n_x is the number of states. The eigenvalues and eigenvectors of $\mathbf{H}$ are then calculated and the matrix of eigenvectors is partitioned into two

equal parts such that the eigenvectors corresponding to the eigenvalues with positive real parts (unstable eigenvalues) are in the left half of the eigenvector matrix. Note controllability by the process noise and observability ensure that exactly half the eigenvalues will have positive real parts [139]. So, if the eigenvector matrix has been rearranged and further partitioned into 4 $n_x \times n_x$ matrices such that it can be written as

$$\mathbf{E} = \begin{bmatrix} \mathbf{E}_{11} & \mathbf{E}_{12} \\ \mathbf{E}_{21} & \mathbf{E}_{22} \end{bmatrix} \tag{7.2.14}$$

then the state-error covariance is found from

$$\mathbf{P} = -\mathbf{E}_{11}\mathbf{E}_{21}^{-1} \tag{7.2.15}$$

and Equation (7.2.8) can be used to find the steady-state gain $\mathbf{K}$ and the state estimation can be performed using Equations (7.2.5) to (7.2.7).

Now, having obtained the predicted output vector $\tilde{\mathbf{y}}$, the next stage in the procedure is to calculate the sensitivities $\partial\tilde{\mathbf{y}}/\partial\boldsymbol{\theta}$ required by the modified Newton-Raphson algorithm. Firstly, partial differentiation of the Kalman filter equations (7.2.5) to (7.2.7) with respect to $\boldsymbol{\theta}$ is performed,

$$\frac{\partial\tilde{\mathbf{x}}(i+1)}{\partial\boldsymbol{\theta}} \approx \boldsymbol{\Phi}\frac{\partial\hat{\mathbf{x}}(i)}{\partial\boldsymbol{\theta}} + \boldsymbol{\Psi}\frac{\partial\mathbf{A}}{\partial\boldsymbol{\theta}}\bar{\mathbf{x}}(i) + \boldsymbol{\Psi}\frac{\partial\mathbf{B}}{\partial\boldsymbol{\theta}}\bar{\mathbf{u}}(i) + \boldsymbol{\Psi}\frac{\partial\mathbf{b}_x}{\partial\boldsymbol{\theta}}, \quad \frac{\partial\tilde{\mathbf{x}}(1)}{\partial\boldsymbol{\theta}} = 0 \tag{7.2.16}$$

$$\frac{\partial\tilde{\mathbf{y}}(i)}{\partial\boldsymbol{\theta}} = \mathbf{C}\frac{\partial\tilde{\mathbf{x}}(i)}{\partial\boldsymbol{\theta}} + \frac{\partial\mathbf{C}}{\partial\boldsymbol{\theta}}\tilde{\mathbf{x}}(i) + \frac{\partial\mathbf{D}}{\partial\boldsymbol{\theta}}\mathbf{u}(i) + \frac{\partial\mathbf{b}_y}{\partial\boldsymbol{\theta}} \tag{7.2.17}$$

$$\frac{\partial\hat{\mathbf{x}}(i)}{\partial\boldsymbol{\theta}} = \frac{\partial\tilde{\mathbf{x}}(i)}{\partial\boldsymbol{\theta}} - \mathbf{K}\frac{\partial\tilde{\mathbf{y}}(i)}{\partial\boldsymbol{\theta}} + \frac{\partial\mathbf{K}}{\partial\boldsymbol{\theta}}\left[\mathbf{z}(i) - \tilde{\mathbf{y}}(i)\right] \tag{7.2.18}$$

Note that Equation (7.2.16) is only an approximation of the true partial derivative of $\tilde{\mathbf{x}}$ with respect to $\boldsymbol{\theta}$ as there is a large computational cost associated with determining the terms $\partial\boldsymbol{\Phi}/\partial\boldsymbol{\theta}$ and $\partial\boldsymbol{\Psi}/\partial\boldsymbol{\theta}$. However, this approximation is adequate for a small value of Δt [34] i.e. a high data sampling rate, which is usually the case in practice.

All terms within equations (7.2.16) to (7.2.18) are easily obtained with the exception of the partial derivative of $\mathbf{K}$ with respect to $\boldsymbol{\theta}$. Differentiation of Equation (7.2.8) with respect to $\boldsymbol{\theta}$ gives

$$\frac{\partial\mathbf{K}}{\partial\boldsymbol{\theta}} = \frac{\partial\mathbf{P}}{\partial\boldsymbol{\theta}}\mathbf{C}^T\mathbf{R}^{-1} + \mathbf{P}\frac{\partial\mathbf{C}^T}{\partial\boldsymbol{\theta}}\mathbf{R}^{-1} \tag{7.2.19}$$

Note that the residual covariance matrix $\mathbf{R}$ is fixed for each iteration so is not differentiated with respect to $\boldsymbol{\theta}$ in Equation (7.2.19). The partial derivative of $\mathbf{P}$ with respect to $\boldsymbol{\theta}$ is then calculated by differentiating the Riccati equation (7.2.12) with respect to $\boldsymbol{\theta}$,

$$\mathbf{A}\frac{\partial\mathbf{P}}{\partial\boldsymbol{\theta}} + \frac{\partial\mathbf{A}}{\partial\boldsymbol{\theta}}\mathbf{P} + \mathbf{P}\frac{\partial\mathbf{A}^T}{\partial\boldsymbol{\theta}} + \frac{\partial\mathbf{P}}{\partial\boldsymbol{\theta}}\mathbf{A}^T - \frac{1}{\Delta t}\frac{\partial\mathbf{P}}{\partial\boldsymbol{\theta}}\mathbf{C}^T\mathbf{R}^{-1}\mathbf{C}\mathbf{P} - \frac{1}{\Delta t}\mathbf{P}\frac{\partial\mathbf{C}^T}{\partial\boldsymbol{\theta}}\mathbf{R}^{-1}\mathbf{C}\mathbf{P}$$
$$- \frac{1}{\Delta t}\mathbf{P}\mathbf{C}^T\mathbf{R}^{-1}\frac{\partial\mathbf{C}}{\partial\boldsymbol{\theta}}\mathbf{P} - \frac{1}{\Delta t}\mathbf{P}\mathbf{C}^T\mathbf{R}^{-1}\mathbf{C}\frac{\partial\mathbf{P}}{\partial\boldsymbol{\theta}} + \mathbf{F}\frac{\partial\mathbf{F}^T}{\partial\boldsymbol{\theta}} + \frac{\partial\mathbf{F}}{\partial\boldsymbol{\theta}}\mathbf{F} = 0 \tag{7.2.20}$$

To make the above expression more manageable, a number of the terms can be grouped together and recognising that $\mathbf{P}$ and $\mathbf{R}$ are symmetric, therefore $\mathbf{P}^T = \mathbf{P}$ and $\mathbf{R}^T = \mathbf{R}$, then Equation (7.2.20) can be rewritten in the form,

$$\bar{\mathbf{A}}\frac{\partial\mathbf{P}}{\partial\boldsymbol{\theta}} + \frac{\partial\mathbf{P}}{\partial\boldsymbol{\theta}}\bar{\mathbf{A}}^T = \bar{\mathbf{C}} + \bar{\mathbf{C}}^T \tag{7.2.21}$$

where,

$$\bar{\mathbf{A}} = \mathbf{A} - \frac{1}{\Delta t}\mathbf{P}\mathbf{C}^T\mathbf{R}^{-1}\mathbf{C} = \mathbf{A} - \frac{1}{\Delta t}\mathbf{K}\mathbf{C} \tag{7.2.22}$$

$$\bar{\mathbf{C}} = -\frac{\partial \mathbf{A}}{\partial \boldsymbol{\theta}}\mathbf{P} + \frac{1}{\Delta t}\mathbf{P}\mathbf{C}^T\mathbf{R}^{-1}\frac{\partial \mathbf{C}}{\partial \boldsymbol{\theta}}\mathbf{P} - \frac{\partial \mathbf{F}}{\partial \boldsymbol{\theta}}\mathbf{F}^T \tag{7.2.23}$$

Equation (7.2.21) represents a set of n_K Lyapunov equations, where $n_K = n_x \times n_y$ and is the number of elements in the Kalman gain matrix $\mathbf{K}$. The Lyapunov equations have the general form $\mathbf{A}\mathbf{X} + \mathbf{X}\mathbf{A}^T = \mathbf{B}$. To solve Equation (7.2.21) for $\partial \mathbf{P}/\partial \boldsymbol{\theta}$, the following transformations are introduced,

$$\bar{\mathbf{A}}' = \mathbf{T}^{-1}\bar{\mathbf{A}}\mathbf{T} \tag{7.2.24}$$

$$(\bar{\mathbf{C}} + \bar{\mathbf{C}}^T)' = \mathbf{T}^{-1}(\bar{\mathbf{C}} + \bar{\mathbf{C}})\mathbf{T}^{-\dagger} \tag{7.2.25}$$

where $\mathbf{T}$ is the matrix of eigenvectors of $\bar{\mathbf{A}}$ and † again denotes the complex conjugate transpose. The transformation in Equation (7.2.24) makes the matrix $\bar{\mathbf{A}}'$ diagonal, in which case Equation (7.2.21) becomes,

$$\bar{\mathbf{A}}'\left(\frac{\partial \mathbf{P}}{\partial \boldsymbol{\theta}}\right)' + \left(\frac{\partial \mathbf{P}}{\partial \boldsymbol{\theta}}\right)'\bar{\mathbf{A}}^\dagger = (\bar{\mathbf{C}} + \bar{\mathbf{C}}^T)' \tag{7.2.26}$$

In general, the solution to $\mathbf{A}\mathbf{X} + \mathbf{X}\mathbf{A}^T = \mathbf{B}$ when $\mathbf{A}$ is diagonal is [34],

$$\mathbf{X}_{ij} = \frac{\mathbf{B}_{ij}}{\mathbf{A}_{ii} + \mathbf{A}_{jj}} \tag{7.2.27}$$

Therefore, for each of the n_K sets of Lyapunov equations,

$$\left(\frac{\partial \mathbf{P}}{\partial \boldsymbol{\theta}}\right)'_{ij} = \frac{(\bar{\mathbf{C}} + \bar{\mathbf{C}}^T)'_{ij}}{\bar{\mathbf{A}}'_{ii} + \bar{\mathbf{A}}'_{jj}} \quad i, j = 1, 2, \ldots, n_x \tag{7.2.28}$$

The partial derivative of $\mathbf{P}$ with respect to $\boldsymbol{\theta}$ is then obtained through back transformation,

$$\frac{\partial \mathbf{P}}{\partial \boldsymbol{\theta}} = \mathbf{T}\left(\frac{\partial \mathbf{P}}{\partial \boldsymbol{\theta}}\right)'\mathbf{T}^\dagger \tag{7.2.29}$$

Having calculated the output sensitivities for each of the N data points, the modified Newton-Raphson update is calculated in a similar manner to that for the output error method,

$$\Delta\boldsymbol{\theta} = \left\{\sum_{i=1}^{N}\left[\frac{\partial \tilde{\mathbf{y}}(i)}{\partial \boldsymbol{\theta}}\right]^T \hat{\mathbf{R}}^{-1}\left[\frac{\partial \tilde{\mathbf{y}}(i)}{\partial \boldsymbol{\theta}}\right]\right\}^{-1}\left\{\sum_{i=1}^{N}\left[\frac{\partial \tilde{\mathbf{y}}(i)}{\partial \boldsymbol{\theta}}\right]^T \hat{\mathbf{R}}^{-1}[\mathbf{z}(i) - \tilde{\mathbf{y}}(i)]\right\} \tag{7.2.30}$$

and the parameter estimates for the $(k+1)$th iteration are found from,

$$\hat{\boldsymbol{\theta}}_{k+1} = \hat{\boldsymbol{\theta}}_k + \Delta\boldsymbol{\theta} \tag{7.2.31}$$

The convergence criteria outlined for the output error method in Section 5.7 is also used for the filter error method. As well as the process described above, the method must also incorporate some computational checks to ensure that the results generated are physically meaningful and to ensure the algorithm does not suffer from convergence difficulties. These are discussed briefly below.

Firstly, it must be verified that the measurement noise covariance matrix $\mathbf{G}_v\mathbf{G}_v^T$, related to the residual covariance matrix $\mathbf{R}$ generated during the computational process, is realistic. This means that it must be positive semi-definite and corresponds to the constraint that the eigenvalues of $\mathbf{KC}$ must be less than or equal to 1 [139]. If this constraint is violated, a correction factor must be applied to the modified Newton-Raphson parameter update $\Delta\boldsymbol{\theta}$, resulting in a nonlinear programming problem. A linear approximation to the constraints can be expressed as,

$$(\mathbf{KC})_{ii} + \frac{\partial(\mathbf{KC})_{ii}}{\partial\boldsymbol{\theta}}\Delta\boldsymbol{\theta} \quad i = 1, 2, \ldots, n_x \tag{7.2.32}$$

where,

$$\frac{\partial(\mathbf{KC})}{\partial\boldsymbol{\theta}} = \frac{\partial\mathbf{K}}{\partial\boldsymbol{\theta}}\mathbf{C} + \mathbf{K}\frac{\partial\mathbf{C}}{\partial\boldsymbol{\theta}} \tag{7.2.33}$$

If after the parameters have been updated with the unconstrained modified Newton-Raphson algorithm, given by Equation (5.3.7), l of the n_x constraints have been violated then the constrained parameter update vector is used instead. This is given by,

$$\Delta\boldsymbol{\theta}_c = \Delta\boldsymbol{\theta} - \left(\frac{\partial^2 J}{\partial\boldsymbol{\theta}}\right)^{-1}\mathbf{L}^T\left\{\mathbf{L}\left(\frac{\partial^2 J}{\partial\boldsymbol{\theta}}\right)^{-1}\mathbf{L}^T\right\}^{-1}\mathbf{S} \tag{7.2.34}$$

where $\mathbf{L}$ and $\mathbf{S}$ are calculated from,

$$\mathbf{L}(i,j) = \frac{\partial(\mathbf{KC})_{ii}}{\partial\boldsymbol{\theta}} \tag{7.2.35}$$

$$\mathbf{S}_i = 1 - (\mathbf{KC})_{ii}, \quad i = 1, \ldots, l; j = 1, \ldots, n_\theta \tag{7.2.36}$$

Secondly, the cost function is minimised with respect to both $\boldsymbol{\theta}$ and $\mathbf{R}$, which are calculated separately. However, the basic modified Newton-Raphson algorithm does not account for how $\boldsymbol{\theta}$ and $\mathbf{R}$ influence each other. This can lead to strong correlation between the turbulence distribution matrix $\mathbf{F}$, which is included in $\boldsymbol{\theta}$, and $\mathbf{R}$ and, in turn, affect convergence of the algorithm. Hence, to compensate, another correction factor can be used to adjust the estimate of $\mathbf{F}$ each time $\mathbf{R}$ is updated. For the ith diagonal element of $\mathbf{F}$, Maine and Iliff [139] suggest the following correction,

$$F_{ii}^{\text{new}} = F_{ii}^{\text{old}}\left(\frac{\sum_{j=1}^{n_y} C_{ij}^2 r_j^{\text{old}}\sqrt{r_j^{\text{old}}/r_j^{\text{new}}}}{\sum_{j=1}^{n_y} C_{ij}^2 r_j^{\text{old}}}\right), \quad i = 1, 2, \ldots, n_x \tag{7.2.37}$$

where r_j denotes the jth diagonal element of $\mathbf{R}^{-1}$ and C_{ij} is the entry occupying the ith row and jth column of $\mathbf{C}$. The superscripts "old" and "new" refer to the previous and updated values of the residual covariance matrix $\mathbf{R}$. To ensure a smooth convergence, generally the estimate of $\mathbf{R}$ is held fixed for the first few iterations, while the estimates of the elements of $\mathbf{F}$ are updated.

Finally, it has already been observed in Chapter 5 that the modified Newton-Raphson algorithm can sometimes perform poorly when the cost function is nearing its minimum. Therefore, one of the routines to avoid this problem, such as parameter halving or a line search, must be incorporated into the filter error algorithm as well. Figure 7.1 illustrates the major computational steps of the filter error method for linear systems.
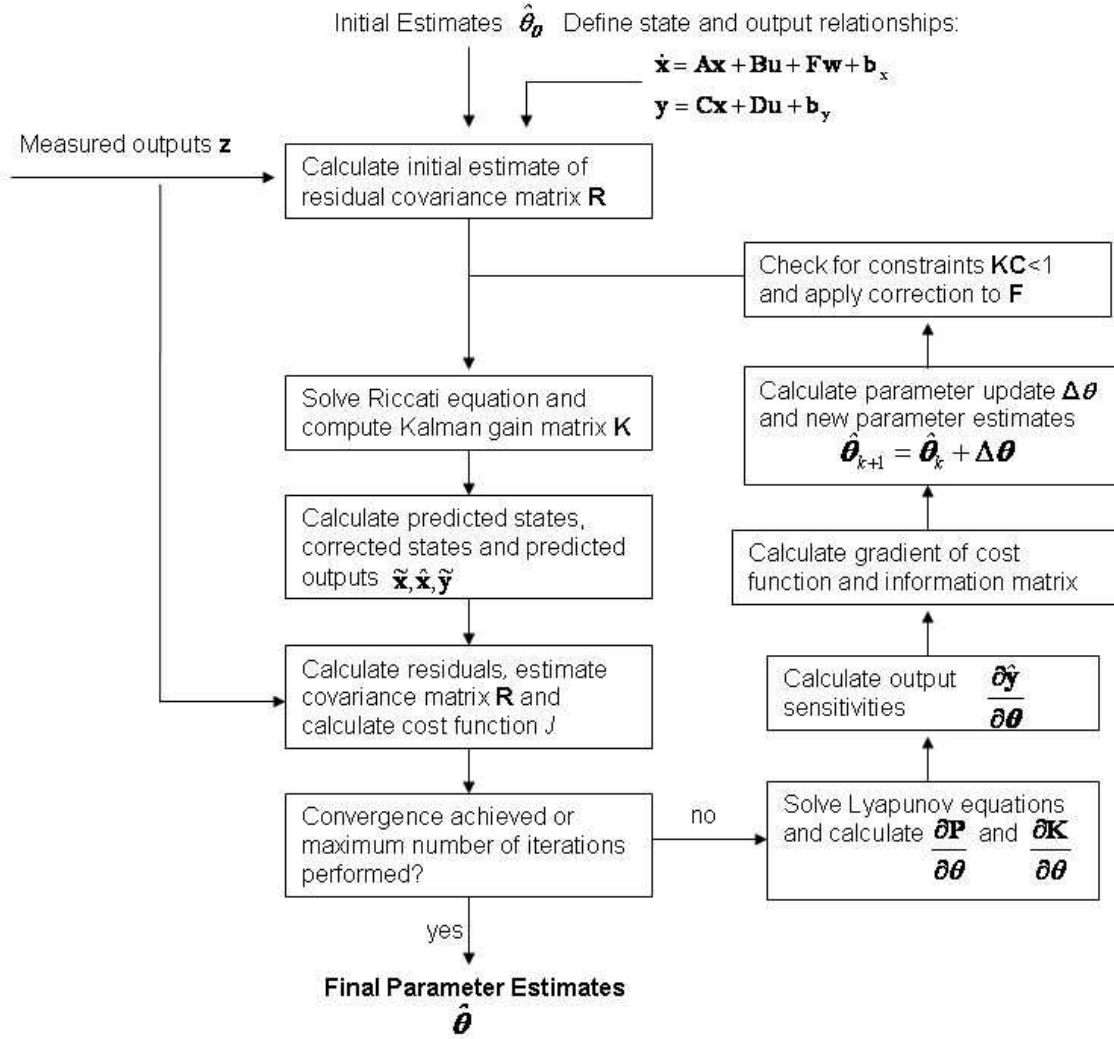
Figure 7.1: Computational steps of the filter error method for linear systems

7.2.3   Filter Error Method Algorithm for Nonlinear Systems

The filter error method for nonlinear systems is very similar to that for the linear case outlined above. The major differences between the two are the form of the Kalman filter used for state estimation and how the sensitivities are calculated. A general set of nonlinear equations describing the aircraft dynamics can be written as,

$$\dot{\mathbf{x}}(t) \quad = \quad f[\mathbf{x}(t), \mathbf{u}(t), \boldsymbol{\theta}] + \mathbf{F}\mathbf{w}(t), \quad \mathbf{x}(t_0) = \mathbf{x}_0 \qquad (7.2.38)$$

$$\mathbf{y}(t) \quad = \quad g[\mathbf{x}(t), \mathbf{u}(t), \boldsymbol{\theta}] \qquad (7.2.39)$$

$$\mathbf{z}(i) \quad = \quad \mathbf{y}(i) + \mathbf{G}_v \mathbf{v}(i), \quad i = 1, 2, \ldots, N \qquad (7.2.40)$$

where f and g denote the nonlinear system functions. When the equations under consideration are nonlinear an extended Kalman filter (EKF) is used for state estimation of stochastic systems. Like the linear case, a steady-state form of the EKF is again suitable for most applications, although, as mentioned previously, a time-varying filter may be necessary if the system parameters are time-varying or the aircraft manoeuvre under examination involves large deviations from trim. The steady-state filter discussed here consists of a prediction step with a

nonlinear model followed by a correction step based on a first-order approximation of the state and measurement equations. The equations for the prediction step are,

$$\tilde{\mathbf{x}}(i) = \hat{\mathbf{x}}(i-1) + \int_{t(i-1)}^{t(i)} f[\mathbf{x}(t), \bar{\mathbf{u}}(i-1), \boldsymbol{\theta}]dt, \quad \hat{\mathbf{x}}(t_0) = \mathbf{x}_0 \qquad (7.2.41)$$

$$\tilde{\mathbf{y}}(i) = g[\tilde{\mathbf{x}}(i), \mathbf{u}(i), \boldsymbol{\theta}] \qquad (7.2.42)$$

while the correction step is achieved using,

$$\hat{\mathbf{x}}(i) = \tilde{\mathbf{x}}(i) + \mathbf{K}[\mathbf{z}(i) - \tilde{\mathbf{y}}(i)] \qquad (7.2.43)$$

Integration of the function f from one time point to the next in Equation (7.2.41) is achieved using a suitable numerical scheme, such as the 4th-order Runge-Kutta method introduced in Chapter 5. The Kalman gain for Equation (7.2.43) is calculated in the same way as for the linear case,

$$\mathbf{K} = \mathbf{P}\mathbf{C}^T\mathbf{R}^{-1} \qquad (7.2.44)$$

with the state-error covariance $\mathbf{P}$ again calculated by solving the continuous-time Riccati equation,

$$\mathbf{A}\mathbf{P} + \mathbf{P}\mathbf{A}^T - \frac{1}{\Delta t}\mathbf{P}\mathbf{C}^T\mathbf{R}^{-1}\mathbf{C}\mathbf{P} + \mathbf{F}\mathbf{F}^T = 0 \qquad (7.2.45)$$

Estimates of the system matrices $\mathbf{A}$ and $\mathbf{C}$ for the nonlinear case are obtained using central-difference formulas, with the elements of $\mathbf{A}$ and $\mathbf{C}$ formed from,

$$A_{ij} \approx \left. \frac{f_i[\mathbf{x} + \delta\mathbf{x}_j, \mathbf{u}, \boldsymbol{\theta}] - f_i[\mathbf{x} - \delta\mathbf{x}_j, \mathbf{u}, \boldsymbol{\theta}]}{2\delta\mathbf{x}_j} \right|_{\mathbf{x}=\mathbf{x}_0}, \quad i, j = 1, 2, \ldots, n_x \qquad (7.2.46)$$

$$C_{ij} \approx \left. \frac{g_i[\mathbf{x} + \delta\mathbf{x}_j, \mathbf{u}, \boldsymbol{\theta}] - g_i[\mathbf{x} - \delta\mathbf{x}_j, \mathbf{u}, \boldsymbol{\theta}]}{2\delta\mathbf{x}_j} \right|_{\mathbf{x}=\mathbf{x}_0}, \quad i = 1, 2, \ldots, n_y; j = 1, 2, \ldots, n_x \qquad (7.2.47)$$

where $\delta\mathbf{x}_j$ represents a perturbation in the jth state variable. Note, linearisation of the system equations is performed about the initial conditions $\mathbf{x}_0$.

For the calculation of the sensitivities $\partial\tilde{\mathbf{y}}/\partial\boldsymbol{\theta}$, the finite-difference approximation described in Section 5.5 is used. For a small perturbation $\delta\theta_j$ in each of the n_θ unknown parameters, the resulting perturbed observations $\tilde{\mathbf{y}}_p$ are computed and the sensitivities are given by,

$$\frac{\partial\tilde{\mathbf{y}}(i)}{\partial\theta_j} \approx \frac{[\tilde{\mathbf{y}}_p(i) - \tilde{\mathbf{y}}(i)]}{\delta\theta_j} \qquad (7.2.48)$$

The perturbed observations are computed using equations (7.2.41) to (7.2.43)

$$\tilde{\mathbf{x}}_p(i) = \hat{\mathbf{x}}_p(i-1) + \int_{t_{i-1}}^{t_i} f[\mathbf{x}_p(t), \bar{\mathbf{u}}(i), \boldsymbol{\theta} + \delta\theta_j]dt \qquad (7.2.49)$$

$$\tilde{\mathbf{y}}_p(i) = g[\tilde{\mathbf{x}}_p(i), \mathbf{u}(i), \boldsymbol{\theta} + \delta\theta_j] \qquad (7.2.50)$$

$$\hat{\mathbf{x}}_p(i) = \tilde{\mathbf{x}}_p(i) + \mathbf{K}_p[\mathbf{z}(i) - \tilde{\mathbf{y}}_p(i)] \qquad (7.2.51)$$

with the perturbed gain matrix calculated using equation (7.2.8)

$$\mathbf{K}_p = \mathbf{P}_p\mathbf{C}_p^T\mathbf{R}^{-1} \qquad (7.2.52)$$

The perturbed state-error covariance matrix $\mathbf{P}_p$ is obtained by solving the Riccati equation with the perturbed system matrices $\mathbf{A}_p$ and $\mathbf{C}_p$ approximated using central-difference formulas (7.2.46) and (7.2.47). Note, that the residual covariance $\mathbf{R}$ remains fixed throughout. As with the output error method, a typical value for the perturbation falls in the region of $1\mathrm{e}^{-6}\theta_j$ to $0.01\theta_j$.

The calculation of the output sensitivities using the forward difference approximation is less computationally intensive than the process described in Section 7.2.2, as it does not require that a set of Lyapunov equations be solved to find $\partial\mathbf{P}/\partial\boldsymbol{\theta}$ which, in turn, are needed to find $\partial\mathbf{K}/\partial\boldsymbol{\theta}$. Note that the derivative of $\mathbf{K}$ with respect to $\boldsymbol{\theta}$ is still required when checking the constraint that the eigenvalues of $\mathbf{KC} < 1$ (see Equation (7.2.33)). For the nonlinear case, this is also obtained using a forward difference approximation,

$$\frac{\partial(\mathbf{KC})}{\partial\theta_j} \approx \frac{\mathbf{K}_p\mathbf{C}_p - \mathbf{KC}}{\partial\theta_j} \tag{7.2.53}$$

The filter error algorithm outlined in this and the previous sections is robust in the sense that it can be used to solve nonlinear estimation problems when the experimental data is corrupted by measurement noise and atmospheric turbulence effects. In the past, the amount of computational power required to run the algorithm has been cited as a drawback. However, with advances in digital computing power, this is less of an issue. On the downside, it is clear that the method is very mathematically-involved and it is by far the most complex algorithm that is used for aircraft parameter estimation. Care also has to be taken to ensure that the model structure used for the estimation process is correct because the filter error method will always yield a good match to the measured response, even if important terms in the mathematical model have been omitted [34]. In essence, the algorithm assumes that any unmodelled dynamics are due to turbulence and lumps these effects into the process noise term.

7.2.4 Extended Kalman Filter Method

For the filter error method described previously, state estimation and parameter estimation were performed separately, with the states determined using some form of Kalman filter and the parameter estimates subsequently updated using the modified Newton-Raphson algorithm. The second approach to be outlined in this chapter is one in which state and parameter estimation are performed simultaneously using an extended Kalman filter. The steady-state form of the EKF was been used in the previous section for state estimation of nonlinear equations for the filter error method. However, for simultaneous state and parameter estimation, the time-varying form of the EKF is required.

To start with, the unknown parameters are artificially defined as additional state variables that remain constant over time,

$$\dot{\boldsymbol{\theta}} = \mathbf{0} \tag{7.2.54}$$

and an augmented state vector is formed,

$$\mathbf{x}_a = \begin{bmatrix} \mathbf{x}^T & \boldsymbol{\theta}^T \end{bmatrix}^T \tag{7.2.55}$$

so, using the general nonlinear model defined in equations in the previous section,

$$\dot{\mathbf{x}}_a(t) = \begin{bmatrix} f[\mathbf{x}_a(t), \mathbf{u}(t)] \\ 0 \end{bmatrix} + \begin{bmatrix} \mathbf{F} & 0 \\ 0 & 0 \end{bmatrix} \begin{bmatrix} \mathbf{w}(t) \\ 0 \end{bmatrix}$$

$$= f_a[\mathbf{x}_a(t), \mathbf{u}(t)] + \mathbf{F}_a\mathbf{w}_a(t) \tag{7.2.56}$$

$$\mathbf{y}(t) = g_a[\mathbf{x}_a(t), \mathbf{u}(t)] \tag{7.2.57}$$

$$\mathbf{z}(i) = \mathbf{y}(i) + \mathbf{G}_v\mathbf{v}(i), \;\; i = 1, 2, \ldots, N \tag{7.2.58}$$

where f_a and g_a are the augmented system functions and $\mathbf{F}_a$ is the augmented process noise distribution matrix.

As in section 7.2.3, the EKF used to estimate the states consists of a prediction step with a nonlinear model followed by a correction step based on a first-order approximation of the state and measurement equations. However, as already mentioned, a time-varying filter is used in this instance, hence as well as propagating the states forward in time the filter must also update the state-error covariance $\mathbf{P}$. The equations for the prediction step are,

$$\tilde{\mathbf{x}}_a(i) = \hat{\mathbf{x}}_a(i-1) + \int_{t_{i-1}}^{t_i} f[\hat{\mathbf{x}}_a(t), \bar{\mathbf{u}}(i)]dt, \;\; \hat{\mathbf{x}}_a(1) = \mathbf{x}_{a0} \tag{7.2.59}$$

$$\tilde{\mathbf{P}}_a(i) \approx \mathbf{\Phi}_a(i)\hat{\mathbf{P}}_a(i)\mathbf{\Phi}_a^T(i) + \Delta t \mathbf{F}_a\mathbf{F}_a^T, \;\; \hat{\mathbf{P}}_a(1) = \mathbf{P}_{a0} \tag{7.2.60}$$

where Equation (7.2.60) is a valid approximation for a high data sampling rate. The state transition matrix is determined from the approximation,

$$\mathbf{\Phi}_a(i) = e^{\mathbf{A}_a(i)\Delta t} \approx \mathbf{I} + \mathbf{A}_a(i)\Delta t + \mathbf{A}_a(i)^2\frac{\Delta t^2}{2!} + \cdots \tag{7.2.61}$$

where the augmented state matrix $\mathbf{A}_a$ is defined as,

$$\mathbf{A}_a(i) = \left.\frac{\partial f_a[\mathbf{x}_a(t), \mathbf{u}(t)]}{\partial \mathbf{x}_a}\right|_{\mathbf{x}_a=\hat{\mathbf{x}}_a(i)} = \begin{bmatrix} \partial f/\partial\mathbf{x} & \partial f/\partial\boldsymbol{\theta} \\ 0 & 0 \end{bmatrix}_{\mathbf{x}_a=\hat{\mathbf{x}}_a(i)} \tag{7.2.62}$$

A numerical technique, such as the 4th-order Runge-Kutta method, is again used to integrate the states forward in time in equation (7.2.59).

The correction step of the EKF is carried out using the following equations,

$$\tilde{\mathbf{y}}(t) = g_a[\tilde{\mathbf{x}}_a(i), \mathbf{u}(i)] \tag{7.2.63}$$

$$\mathbf{K}_a(i) = \tilde{\mathbf{P}}_a(i)\mathbf{C}_a^T(i)[\mathbf{C}_a(i)\tilde{\mathbf{P}}_a(i)\mathbf{C}_a^T(i) + \mathbf{G}_v\mathbf{G}_v^T]^{-1} \tag{7.2.64}$$

$$\hat{\mathbf{x}}_a(i) = \tilde{\mathbf{x}}_a(i) + \mathbf{K}_a(i)[\mathbf{z}(i) - \tilde{\mathbf{y}}(i)] \tag{7.2.65}$$

$$\hat{\mathbf{P}}_a(i) = [\mathbf{I} - \mathbf{K}_a(i)\mathbf{C}_a(i)]\tilde{\mathbf{P}}_a(i)[\mathbf{I} - \mathbf{K}_a(i)\mathbf{C}_a(i)]^T + \mathbf{K}_a(i)\mathbf{G}_v\mathbf{G}_v^T\mathbf{K}_a^T(i) \tag{7.2.66}$$

where $\mathbf{K}_a$ is the augmented Kalman gain matrix and the augmented system matrix $\mathbf{C}_a$ is defined to be,

$$\mathbf{C}_a(i) = \left.\frac{\partial g_a[\mathbf{x}_a(t), \mathbf{u}(t)]}{\partial \mathbf{x}_a}\right|_{\mathbf{x}_a=\tilde{\mathbf{x}}_a(i)} = \begin{bmatrix} \dfrac{\partial g}{\partial\mathbf{x}} & \dfrac{\partial g}{\partial\boldsymbol{\theta}} \end{bmatrix}_{\mathbf{x}_a=\tilde{\mathbf{x}}_a(i)} \tag{7.2.67}$$

Approximations of the augmented system matrices $\mathbf{A}_a$ and $\mathbf{C}_a$ are obtained in a similar manner to those in Equations (7.2.46) and (7.2.47) using the central-difference method.

It is necessary to specify the initial conditions $\mathbf{x}_{a0}$ and $\mathbf{P}_{a0}$ to start the algorithm. The initial covariances within $\mathbf{P}_{a0}$ which correspond to the unknown parameters $\boldsymbol{\theta}$ reflect confidence in the

starting values for these parameters. If prior knowledge of the values of the stability and control derivatives is limited, then the covariances within $\mathbf{P}_{a0}$ should be set to relatively high values, indicating reduced confidence in the initial estimates [34]. This will improve the algorithm's ability to track changes in the parameter values. Standard deviations of the parameter estimates are also obtained by taking the square roots of the elements of $\mathbf{P}$.

Compared to the filter error method, the EKF is not as mathematically complex. Another advantage it has is that it can be used for real-time, or recursive, parameter estimation [34]. This may be particularly important for UAV applications because a reduced development time is often a driving factor in the design of unmanned aircraft. However, prior specification of values for the process and measurement noise covariance matrices, $\mathbf{F}_a\mathbf{F}_a^T$ and $\mathbf{G}_v\mathbf{G}_v^T$, is needed. The measurement noise covariance can be obtained from laboratory calibration of the instrumentation or from the smoothing procedure described in Section 4.3. Specifying the process noise covariance is more difficult. The elements corresponding to the aircraft states will reflect the levels of atmospheric turbulence within the data. For the augmented states, representing the elements of $\boldsymbol{\theta}$, the values in $\mathbf{F}_a\mathbf{F}_a^T$ are generally set to zero, as the parameters have been assumed to remain constant over the observation period. In practice, a certain amount of tuning of $\mathbf{P}_{a0}$, $\mathbf{F}_a\mathbf{F}_a^T$ and $\mathbf{G}_v\mathbf{G}_v^T$ may be required before the algorithm performs well and this is the method's main disadvantage. As well as the problem of specifying the noise statistics, the first-order approximation used in the propagation of the states and error covariances may not be accurate enough to represent system nonlinearities, resulting in biased estimates or divergence [150]. To overcome this, evolutions of the EKF, such as the unscented Kalman filter, have been developed [151]. However, comparative studies have found that these approaches offer no significant performance gains over the EKF for aircraft parameter estimation problems [34]. The performance of the EKF can also be improved by incorporating a smoother into the algorithm. However, this requires knowledge of future data points, hence can only be used post-flight. The EKF combined with a smoother is commonly used for the data compatibility check, which is an off-line process, and is outlined in Chapter 9.

7.2.5 DEMON Roll Mode Example

As an example of estimation in the presence of turbulence, analysis of the roll dynamics of the 1/3 scale DEMON UAV is presented next. During the wind tunnel experiments, it was observed that the aircraft model was prone to an uncommanded rolling motion, a phenomenon which had been encountered in previous research with the wind tunnel facility. This was caused by fluctuations in the local flow velocity at various points across the span of the working section [152], resulting in a differential in the lift produced by each aircraft wing.

The analysis presented here was carried out on a segment of data containing two aileron doublets. The time delay in the input was found, from inspection of the data, to be 0.30 sec so the aileron input was time shifted manually by this amount prior to estimation. To start with, it was assumed that the turbulence effects were negligible, in which case the equations of motion were,

$$\begin{bmatrix} \dot{p} \\ \dot{\phi} \end{bmatrix} = \begin{bmatrix} l_p & 0 \\ 1 & 0 \end{bmatrix} \begin{bmatrix} p \\ \phi \end{bmatrix} + \begin{bmatrix} l_\xi \\ 0 \end{bmatrix} \xi \tag{7.2.68}$$

and estimation was performed using the time domain output error approach to determine values for l_p and l_ξ. The starting values for the output error method were obtained from least squares regression as l_p = -10.9998 and l_ξ = -1.6932 and the final estimates, along with their standard

errors, are given in Table 7.1. Convergence was reached after 7 iterations and $t_{comp} = 2.99$ sec. The standard errors of l_p and l_ξ were acceptable but the correlation coefficient between the two parameters was relatively high at $\rho = 0.8699$.

Figure 7.2 shows the measured roll rate and roll attitude time histories along with those obtained using the identified model. It can be seen that the match between the two is relatively close around the points where the two aileron doublets were applied. However, during the period between the two inputs, there is clearly some unmodelled rolling motion, which is due to the turbulence caused by the local flow fluctuations. The results of Theil's inequality analysis were as follows,

$$p : U = 0.2016, \ U_B = 0.0019, \ U_V = 0.0306, \ U_C = 0.9675$$
$$\phi : U = 0.4159, \ U_B = 0.1154, \ U_V = 0.1332, \ U_C = 0.7514$$

The above numbers indicate an adequate match between the measured and identified responses for the roll rate. However, the agreement is not as close for the roll attitude, with the covariance portion being relatively low. From the discussion in Section 4.5, the low value of U_C suggests the presence of a nonsystematic error in the data, such as process noise.

	$\hat{\theta}$	$100[s/|\hat{\theta}|]$
l_p	-18.0436	13.72
l_ξ	-2.3761	9.21

Table 7.1: Estimates of DEMON roll derivatives from output error method
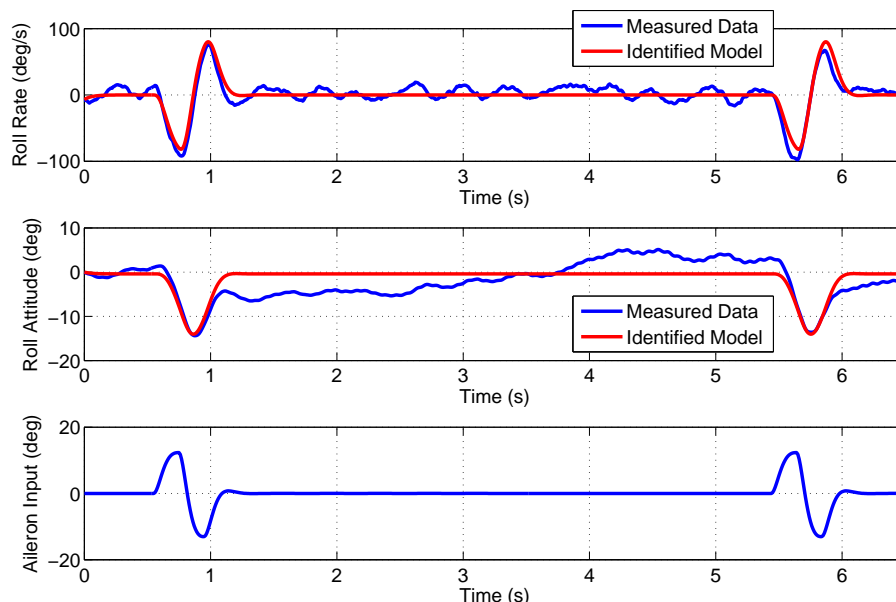
Figure 7.2: Measured and identified responses for aileron doublets: output error method

Estimation was then performed using the maximum likelihood filter error method, with the

equations of motion in (7.2.68) extended to,

$$\begin{bmatrix} \dot{p} \\ \dot{\phi} \end{bmatrix} = \begin{bmatrix} l_p & 0 \\ 1 & 0 \end{bmatrix} \begin{bmatrix} p \\ \phi \end{bmatrix} + \begin{bmatrix} l_\xi \\ 0 \end{bmatrix} \xi + \begin{bmatrix} f_p & 0 \\ 0 & f_\phi \end{bmatrix} \begin{bmatrix} w_p \\ w_\phi \end{bmatrix} \tag{7.2.69}$$

where f_p and f_ϕ are the elements of the process noise distribution matrix to be determined, while w_p and w_ϕ represent the process noise in each equation. As for the output error method, the initial estimates of l_p and l_ξ for the filter error method came from least squares regression, while f_p and f_ϕ were both given a starting value of 0.01. Convergence was achieved in 10.02 sec and took 9 iterations. Table 7.2 shows the final estimates and standard errors. In comparison to the output error estimates, the values of l_p and l_ξ obtained using the filter error method are around 20 to 25 % lower. The standard errors are slightly higher but remain acceptable and there is also less correlation between the stability and control derivatives (see Table 7.3).

	$\hat{\theta}$	$100[s/|\hat{\theta}|]$
l_p	-13.3797	15.86
l_ξ	-1.9348	12.30
f_p	0.4189	4.09
f_ϕ	0.0821	3.97

Table 7.2: Estimates of DEMON roll derivatives from filter error method

	l_p	l_ξ	f_p	f_ϕ
l_p	1	0.7946	0.1938	0.0008
l_ξ	-	1	0.1260	0.0003
f_p	-	-	1	0.0051
f_ϕ	-	-	-	1

Table 7.3: Correlation coefficients for DEMON roll derivatives - filter error method

Figure 7.3 shows the measured and identified roll responses obtained using the filter error method. Visually, the match is much better than that for the output error method in Figure 7.2. The filter error method is able to account for the uncommanded rolling motion between the aileron doublets and, in fact, it is difficult to discern the difference between the measured and identified responses. The results of Theil's inequality analysis also indicated high confidence in the identified model,

$$p : U = 0.0436, \ U_B = 0.0009, \ U_V = 0.0019, \ U_C = 0.9971$$
$$\phi : U = 0.0217, \ U_B = 0.0005, \ U_V = 0.0014, \ U_C = 0.9981$$

A good visual match between the measured and identified response, however, does not imply that the identified model is adequate, especially when using the filter error method which, as describe previously, will tend to lump any unmodelled dynamics into the process noise term. This makes the validation process crucial for establishing the suitability of the model, hence the identified model was used to predict the response to another aileron input not used for the preceding parameter estimation process. Plots of the measured and predicted responses to this input are given in Figure 7.4. The fits between the measured and predicted data for roll rate and roll attitude are both very close. Theil's inequality analysis also suggested accurate matches,

$$p : U = 0.0761, \ U_B = 0.0742, \ U_V = 0.0966, \ U_C = 0.8292$$
$$\phi : U = 0.0297, \ U_B = 0.0006, \ U_V = 0.0819, \ U_C = 0.9175$$

Next, the EKF approach was used. Although the data was being analysed after the experiment had been performed, the analysis presented here used the EKF as it would have been implemented in real-time i.e. no smoothing was incorporated into the process. The elements of
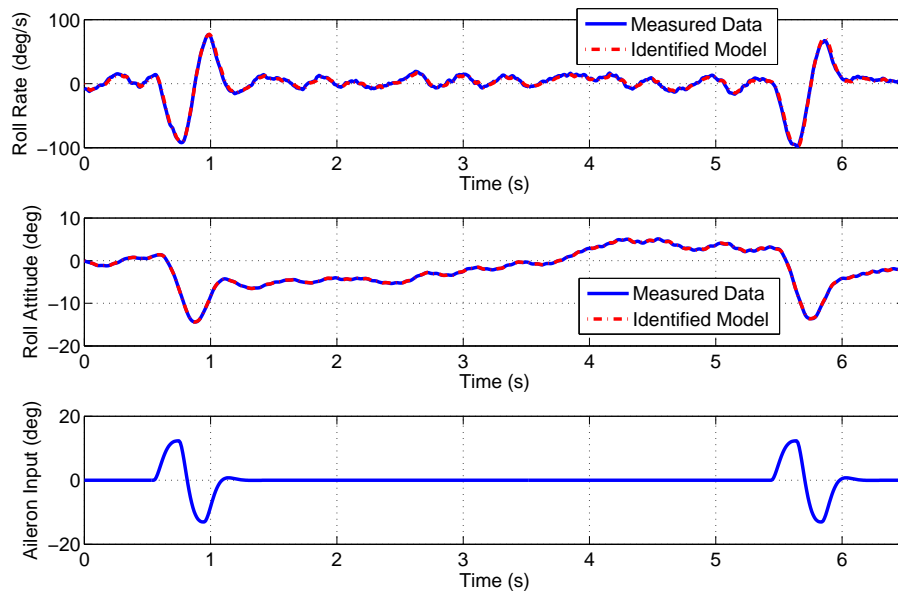
Figure 7.3: Measured and identified responses for aileron doublets: filter error method
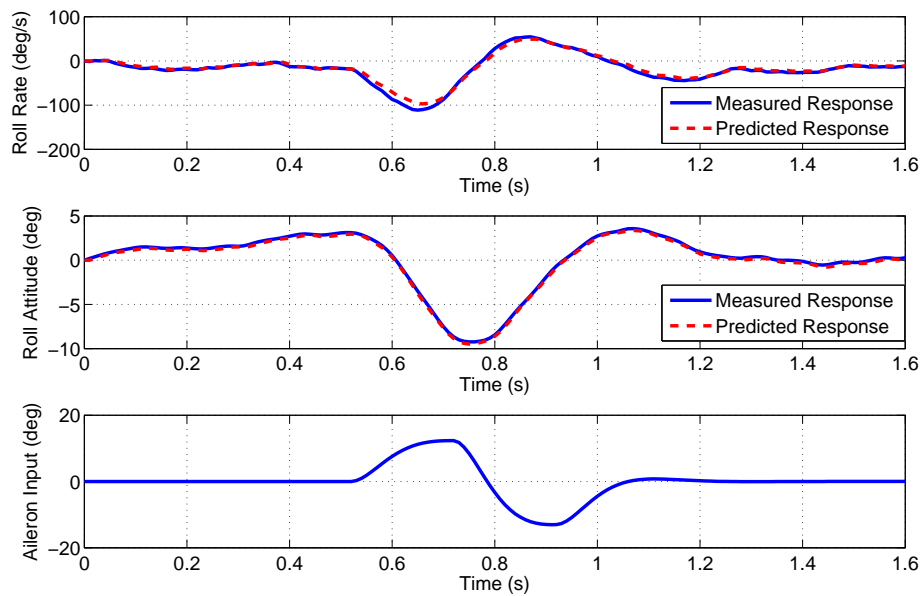
Figure 7.4: Measured and predicted responses for an aileron doublet validation manoeuvre: filter error method

the state covariance matrix $\mathbf{P}_a$ were all set to large initial values, to help the algorithm track large deviations in the states, and the measurement noise covariance matrix was estimated from Fourier smoothing analysis to be,

$$\mathbf{G}_v\mathbf{G}_v^T = \begin{bmatrix} 5.415 \times 10^{-4} & 0 \\ 0 & 3.8 \times 10^{-6} \end{bmatrix} \tag{7.2.70}$$

To start with, the algorithm was run assuming that there was little turbulence in the data and the diagonal elements of the process noise covariance matrix $\mathbf{FF}^T$ were set to 1×10^{-10}. It took the algorithm 1.24 sec to analysis the data and the resulting identified responses for p and ϕ are plotted in Figure 7.5 against the measured time histories. In this case, the EKF behaved very like the output error method, with the identified model matching closely to the measured response in the regions where the aileron doublets were applied but is unable to account for the changes in roll that occur in the time between the two inputs. This could have been expected, as it was assumed that the majority of the noise corrupting the data was measurement noise, while the process noise was negligible. The results of Theil's inequality analysis pointed to a good match between the measured and identified responses for roll rate but less agreement for the roll attitude responses,

$$p : U = 0.2147, \ U_B = 0.0022, \ U_V = 0.0055, \ U_C = 0.9923$$
$$\phi : U = 0.1376, \ U_B = 0.0246, \ U_V = 0.1811, \ U_C = 0.7943$$
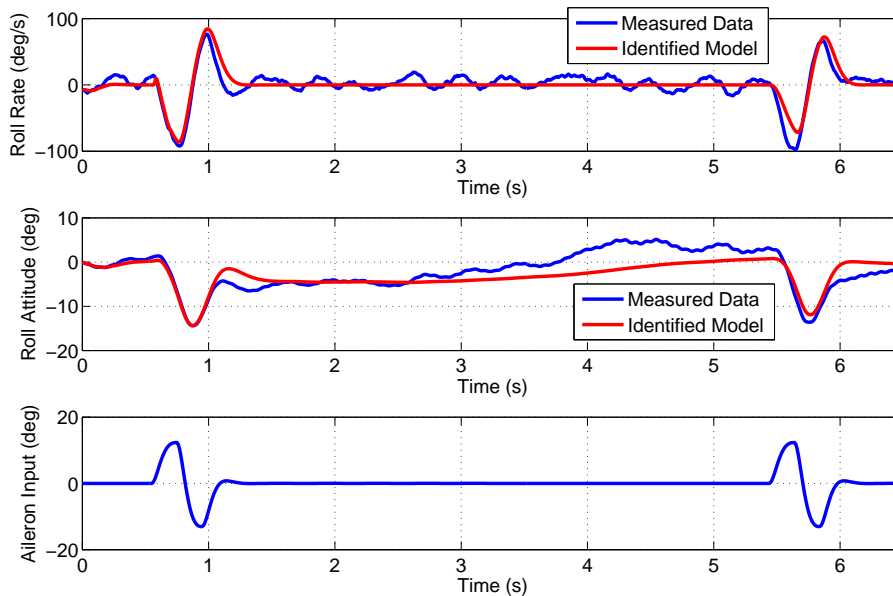
Figure 7.5: Measured and identified responses for aileron doublets: run 1 of the EKF

Next, the time histories of the estimated derivatives l_p and l_ξ were examined. These are shown in Figure 7.6 along with the corresponding estimates from the output error and filter error methods. Note that both the middle and bottom subplots show the results for l_ξ but the bottom plot focuses on the last 1.5 seconds of the data, which cannot be discerned clearly from the middle plot. The initial estimates of l_p and l_ξ for the EKF were, again, those from least squares

regression. Focusing on l_p, from its initial value the derivative rapidly decreases in magnitude, changes sign after just 0.1 sec and reaching a peak of around 5. Its value then rapidly decreases and becomes negative again. At a time of around 1 sec, the value oscillates around -14 before becoming more constant over the rest of the time period. For the last 10 data points, the average value of l_p is -13.81, which is closer to the filter error estimate that the output error estimate, despite the initial assumption of the process noise covariance being very small. The evolution of the estimate for l_ξ is much more settled than for l_p. However, there is a sharp increase in the estimated value around 0.6 sec where it peaks at a value of over 20. The estimated value then quickly returns back to the region around -2. Again, the estimate of l_ξ from the EKF matches more closely to the filter error values in comparison to those from the output error method (as can be seen in the bottom plot), with the average value over the last 10 data points being -1.96.
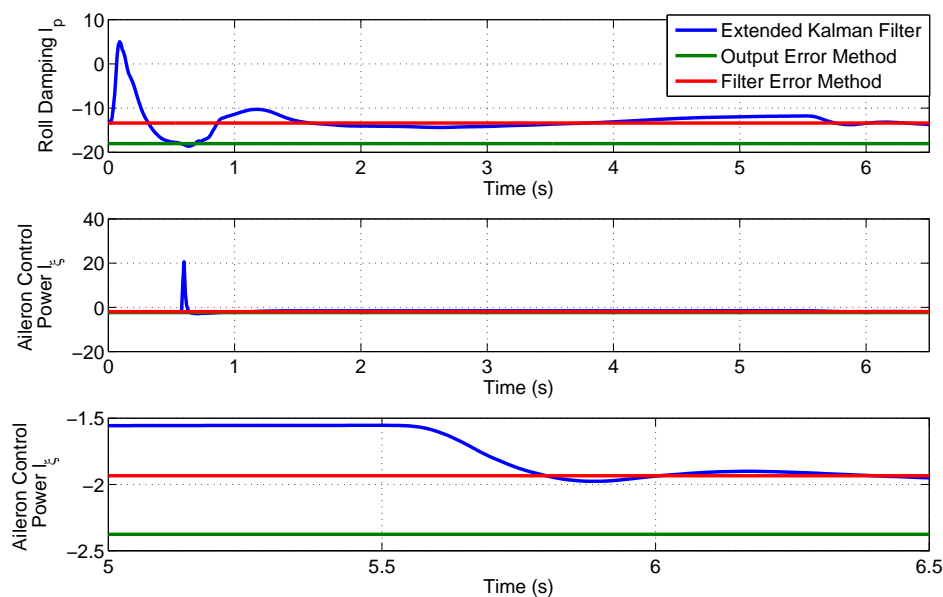
Figure 7.6: Comparison of parameter estimates from run 1 of the EKF, output error method and filter error method

The standard deviations of l_p and l_ξ expressed as percentages of the estimated magnitudes are plotted in Figure 7.7. For both derivatives, the initial standard deviations are high, which is a result of the initial state covariance $\mathbf{P}_{a0}$ being large, and remain so during the first second of data. This corresponds to the regions in which the estimated parameter values fluctuated most (see Figure 7.6). As more data points were analysed, the confidence in the parameter estimates grew, with the final standard deviations being less than 1 % of the estimated derivative values.

The EKF was then run for a second time with the same initial conditions except that the process noise covariance was chosen to match that estimated from the filter error method. The measured and identified responses for p and ϕ are plotted in Figure 7.8. This time, the visual match between the measured response and the identified model is much closer and is comparable to that obtained with the filter error method (Figure 7.3). Theil's analysis also indicated an improved match, particularly for the roll attitude response,

$$p : U = 0.0159, \ U_B = 0.0051, \ U_V = 0.0190, \ U_C = 0.9759$$
$$\phi : U = 0.0001, \ U_B = 0.0093, \ U_V = 0.0002, \ U_C = 0.9905$$
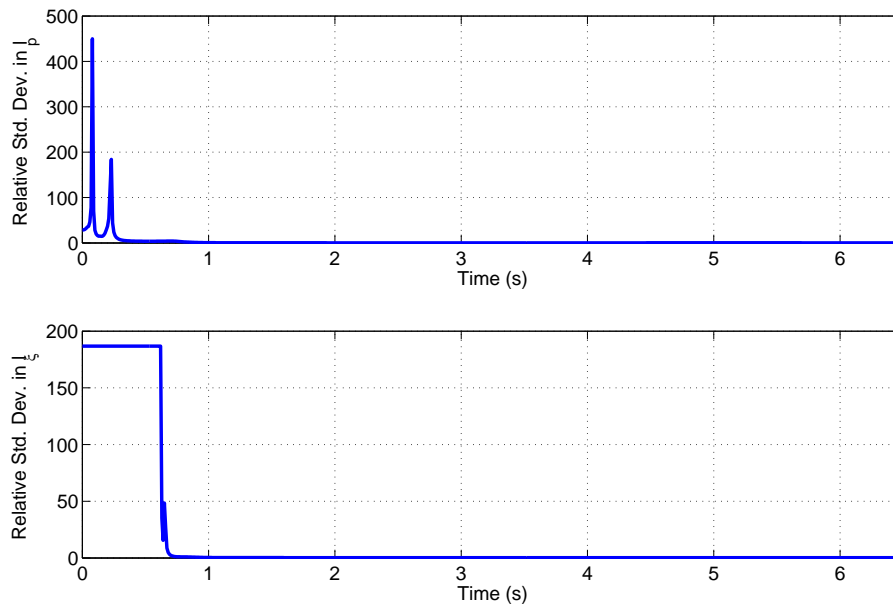
Figure 7.7: Relative standard deviations of parameter
estimates from run 1 of the EKF
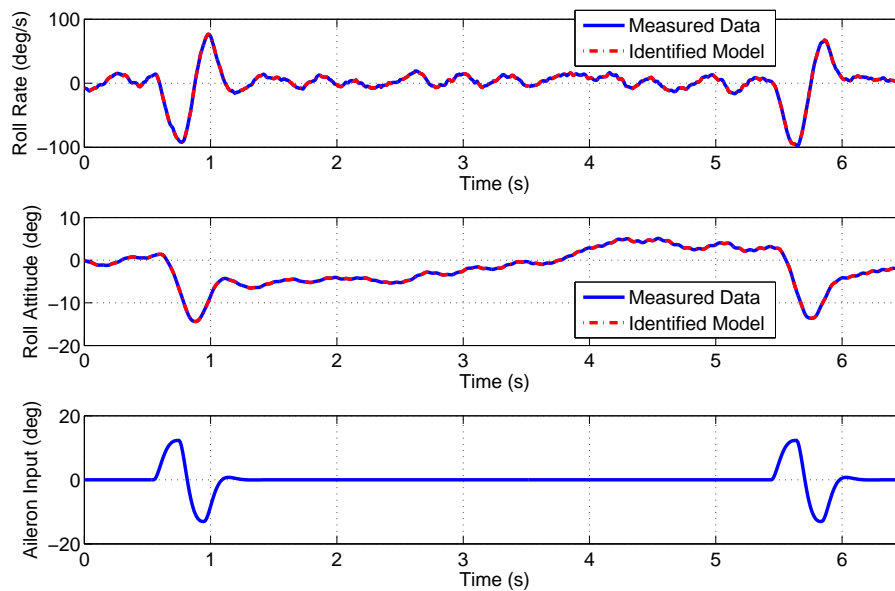
Figure 7.8: Measured and identified responses for aileron
doublets: run 2 of the EKF

Figure 7.9 shows time histories of the estimates of l_p and l_ξ. Again, the estimates obtained with the output error and filter error methods are also shown. In comparison to the time histories from the first run (Figure 7.6), the parameter estimates are much more constant and the oscillations in the derivative values within the first second are not as large. Based on the last 10 data points, the average estimates of l_p and l_ξ are -12.45 and -1.81 respectively. As with the first EKF analysis, these values are closer to the filter error estimates than the output error estimates.

The relative standard deviations of the estimates are given in Figure 7.10. The confidence in the estimated values is, again, at it lowest near the start of the data segment. However the relative standard deviations are not as high as they were in the first run, particularly for l_p. After 1 sec, the confidence in the estimated values increases, with the standard deviation in each parameter dropping to around 3 % and remaining relatively constant for the remainder of the data segment.
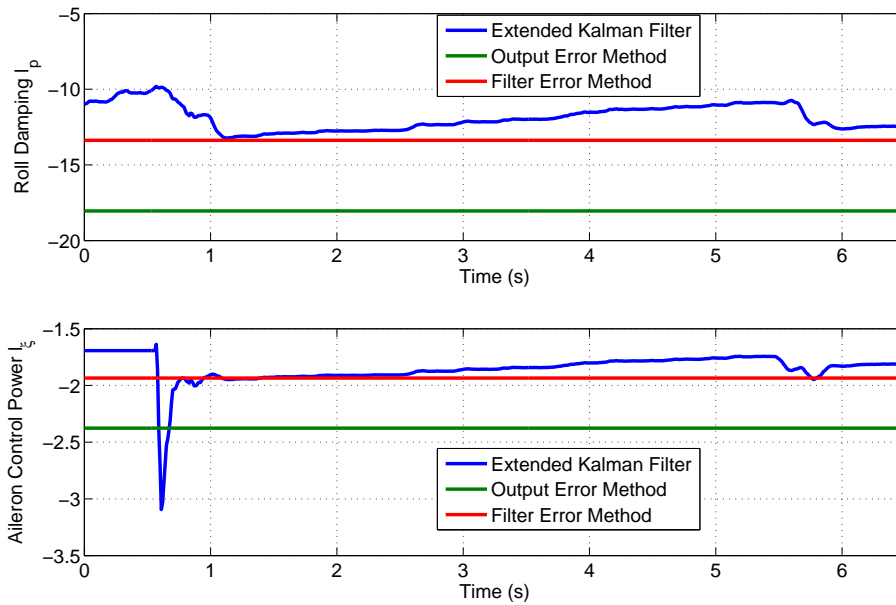
Figure 7.9: Comparison of parameter estimates from run 2 of the EKF, output error method and filter error method

The same aileron input used to validate the model identified from the filter error method was then used to validate the EKF estimates obtained on the second run. This is illustrated in Figure 7.11, in which the roll rate and roll attitude measurements are plotted against the predicted responses generated using the EKF results. As with the filter error method, there was good agreement between the measured and predicted responses. This was also confirmed by the results of Theil's analysis,

$$p : U = 0.0914, \ U_B = 0.0669, \ U_V = 0.1111, \ U_C = 0.8220$$
$$\phi : U = 0.0233, \ U_B = 0.0023, \ U_V = 0.0896, \ U_C = 0.9081$$

As already pointed out, a major difficulty with the EKF approach is specifying suitable values for the elements of the process noise covariance matrix and some tuning of these parameters is usually required. However, the estimates of l_p and l_ξ (calculated as an average of the final 10 data point values) obtained from the two runs did not differ from each other significantly. This was despite the elements of $\mathbf{FF}^T$ in the first run being 8 to 9 orders of magnitude smaller
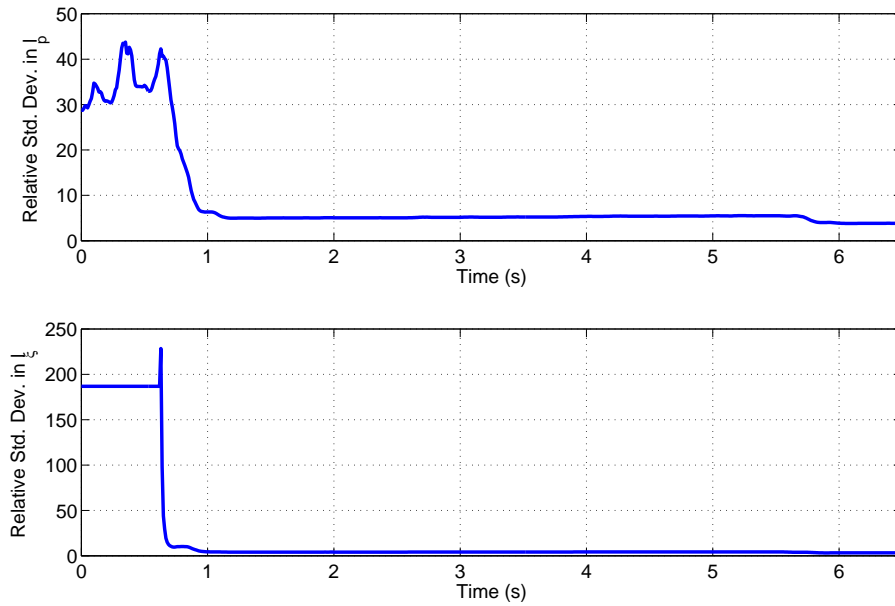
Figure 7.10: Relative standard deviations of parameter estimates from run 2 of the EKF
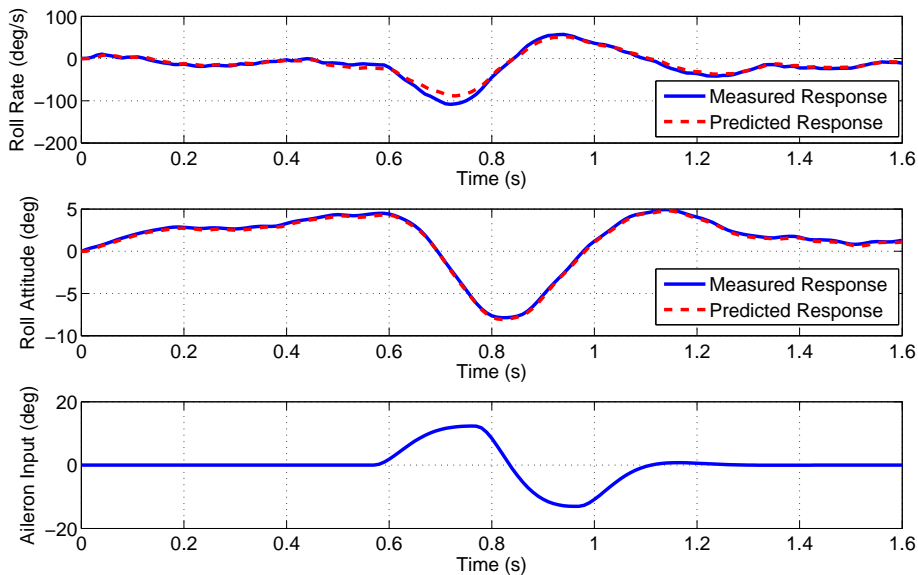
Figure 7.11: Measured and predicted responses for an aileron validation manoeuvre: EKF method

than those for the second run. Hence, this finding suggests that the values of the parameter estimates are relatively insensitive to changes in $\mathbf{FF}^T$. A final observation was that, once again, the derivative values obtained from the experiments were markedly different from the *a priori* estimates. For both l_p and l_ξ, the parameter estimates were almost five times smaller than the empirical estimates.

7.3 Parameter Estimation from Closed-Loop Data

There are two approaches to the problem, as depicted in Figure 7.12. The first is termed open-loop identification in which estimation is carried out as normal using knowledge of the inputs to the control surfaces and the measurements of the aircraft's resultant response. However, motion variables are fedback to augment the input to the aircraft's control surfaces. Hence, there is a potential for the derivatives with respect to the control surface deflections to be highly correlated with the derivatives due to the particular motion variables being fedback. Also, measurement noise introduced by the sensors is fedback along with the motion variables, leading to process noise corrupting the system. This could be of concern when using noisy MEMS sensors. Further, the objective of the controller is often to suppress oscillations and transient motion. This is to the detriment of system identification, which requires sufficient excitation of the aircraft dynamics, and is likely to lead to there being reduced information content in the data. A fourth issue of open-loop identification, particular to unstable aircraft, is that some estimation methods, such as the time domain output error method, incorporate integration of the equations of motion into their algorithms. Any attempt to integrate the equations of motion for an unstable system will lead to divergence and numerical problems. This is, interestingly, is not true for the filter error or EKF techniques. In these methods, the incorporation of the measured data during the correction step of the Kalman filter stabilises the estimate of the states [153, 34]. Estimation in the frequency domain also avoids the numerical integration problem.

The second approach is to identify an equivalent system, incorporating the airframe, the controller and any subsystems which have significant dynamics, for example the actuators. This approach is termed closed-loop identification. The commanded input δ, rather than the control surface deflection u, is treated at the input variable. Models of the controller and subsystem dynamics are assumed to be known and incorporated into the estimation process meaning that the only unknowns to be determined are still the airframe derivatives. Even for inherently unstable airframes, the equivalent system itself is stable so there is no restrictions on which estimation techniques can be used. However, the procedure relies on accurate knowledge of the control laws and subsystem dynamics. It also becomes complex if a range of flight conditions are being analysed, in which case any gain scheduling of the controller and variations in the subsystem dynamics will have to be accounted for. Therefore, the rest of this chapter will focus on the open-loop approach and discuss methods of overcoming the problems of correlated variables and poor identifiability.

7.3.1 Data Collinearity

As described in Chapter 4, it is assumed in estimation problems that the motion variables are independent of each other. However, if a regressor in a linear regression model is equal to a linear combination of one or more of the other regressors, then all involved regressors are said
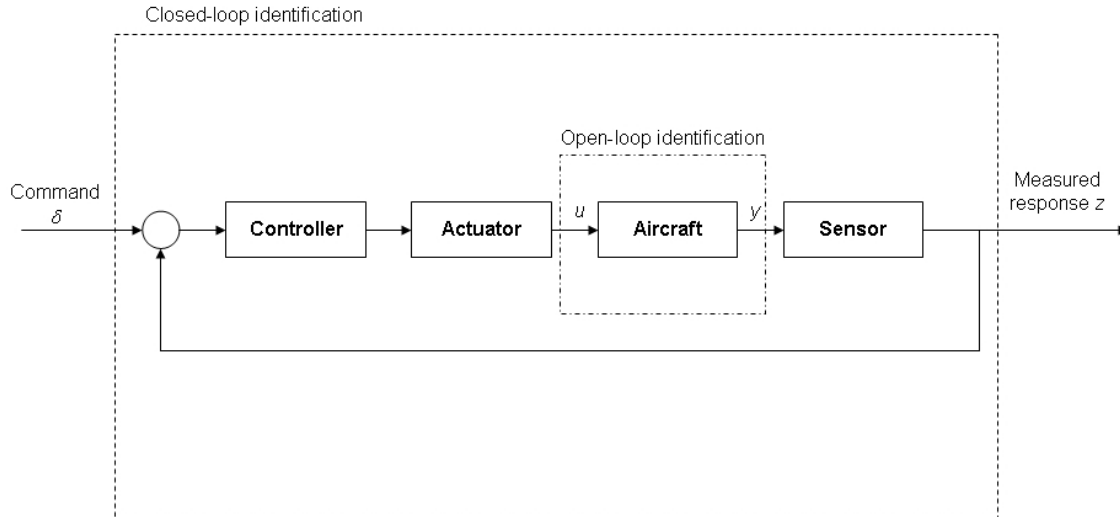
Figure 7.12: Closed-loop and open-loop parameter estimation

to be linearly dependent [31]. This means that the estimation algorithm may struggle to find a solution as, in theory, any weighted combination of the correlated parameters, associated with the linearly dependent regressors, could be used to match the measured aircraft response. This problem is often termed data collinearity and can lead to the parameters having large absolute values and large variances [154, 31]. This is true regardless of which parameter estimation method is used because collinearity is a data problem. However, it is most convenient to examine the issue using least squares regression [128, 31, 34].

In Section 4.5 the detection of linear dependencies between parameters by examination of the parameter covariance matrix $\mathbf{P}$ was introduced (see Equation (4.5.11)). However, the correlation coefficients obtained from $\mathbf{P}$ are pair-wise and only indicate correlation between two regressors. Equation (4.5.11) could show that the pair-wise correlation coefficients are acceptable (< 0.9) but it is still entirely possible for three or more regressors to be highly correlated. Therefore, two metrics which can be used to carry out a complete collinearity diagnostic are described next. Note that when assessing collinearity, it is usual to use a scaled version of the regressors, the derivation of which is given in Appendix C. These are termed the standardised regressors and have the same notation as that given in Chapter 4 but with the additional superscript *.

The first metric is based on singular value decomposition of the standardised regressor matrix $\mathbf{X}^*$, which can be expressed as,

$$\mathbf{X}^* = \mathbf{VST}^T \tag{7.3.1}$$

where $\mathbf{V}$ and $\mathbf{T}$ are matrices of size $N \times n$ and $n \times n$ respectively, n being the number of regressors, and $\mathbf{S}$ is a diagonal matrix of size $n \times n$. The diagonal elements of $\mathbf{S}$ are known as the singular values of $\mathbf{X}^*$ and $\mathbf{V}$ and $\mathbf{T}$ are mutually orthonormal i.e. $\mathbf{T}^T\mathbf{T} = \mathbf{V}^T\mathbf{V} = \mathbf{I}$. Singular value decomposition is closely related to the principle of eigenvalues and eigenvectors with,

$$\mathbf{X}^{*T}\mathbf{X}^* = \mathbf{TS}^2\mathbf{T}^T = \mathbf{T\Lambda T}^T \tag{7.3.2}$$

The matrix $\mathbf{\Lambda}$ denotes the eigenvalues of $\mathbf{X}^{*T}\mathbf{X}^*$, which are therefore equivalent to the squares of the singular values in $\mathbf{S}$. The columns of $\mathbf{T}$ are the associated eigenvectors.

Correlation amongst the regressors in $\mathbf{X}^*$ leads to the matrix $\mathbf{X}^{*T}\mathbf{X}^*$ being ill-conditioned, the severity of which is indicated by the relative sizes of the singular values. If one or more of the singular values is small in comparison to the largest singular value then this suggests linear dependencies amongst the regressors. This concept can be expressed as a condition index in terms of either the singular values or eigenvalues,

$$C_j = \frac{S_{max}}{S_j} = \sqrt{\frac{\lambda_{max}}{\lambda_j}}, \ \ j = 1, 2, \ldots, n \tag{7.3.3}$$

No consensus exists as to the value of $C_{max} = S_{max}/S_{min}$ which indicates the presence of collinearity. Belsley et al [155] suggest values over 100 require investigation. However, researchers in aircraft parameter estimation have found that significant collinearity can exist even if C_{max} is less than this figure [31, 34].

A second method for detecting collinearity is parameter variance decomposition. Combining Equations (4.5.1) and (7.3.2), the covariance of least squares parameter estimates can be expressed as,

$$\mathbf{P} = \sigma^2 \left(\mathbf{X}^{*T}\mathbf{X}^*\right)^{-1} = \sigma^2 \mathbf{T}\mathbf{\Lambda}^{-1}\mathbf{T}^T \tag{7.3.4}$$

thus the variance of the kth parameter is,

$$\mathrm{Var}(\hat{\theta}_k^*) = \sigma^2 \sum_{j=1}^{n} \frac{t_{kj}^2}{\lambda_j} = \sigma^2 \sum_{j=1}^{n} \frac{t_{kj}^2}{S_j^2}, \ \ k, j = 1, 2, \ldots, n \tag{7.3.5}$$

where t_{kj} is the kth element of the jth column of eigenvector matrix $\mathbf{T}$. In other words, the variance of each parameter can be decomposed into a sum of components corresponding to the n eigenvalues. Because, the summation of eigenvalues appears on the denominator, the small eigenvalues (associated with collinearity) will result in large variance for $\hat{\theta}_k^*$. If a high proportion of the variance in any number of the parameters is associated with the same small eigenvalue, then this suggests the presence of collinearity. The variance proportion for the kth parameter corresponding to the jth eigenvalue can be written as,

$$\pi_{kj} = \frac{\phi_{kj}}{\phi_k} \tag{7.3.6}$$

where,

$$\phi_{kj} = \frac{t_{kj}}{\lambda_j} \ \text{ and } \ \phi_k = \sum_{j=1}^{n} \frac{t_{kj}}{\lambda_j} = \sum_{j=1}^{n} \phi_{kj} \tag{7.3.7}$$

The advantage of parameter variance decomposition is that it will indicate correlation between more than two regressors. Klein and Morelli [31] suggest that possible collinearity problems are indicated by $\phi_{kj} > 0.5$.

In summary, the collinearity diagnostic is based on the calculation of condition indices to assess the severity of the collinearity and variance proportion decomposition to investigate which regressors are correlated [31].

Having detected collinearity, there are a number of methods of dealing with the problem [34, 31],

- Fix one or more of the correlated parameters at its *a priori* value.

- Include *a priori* information in the estimation process.

- Include more data/manoeuvres in the analysis.

The first option is probably the simplest and was used earlier in the dynamic wind tunnel example presented in Section 5.10, in which the derivatives y_r and n_v were found to be highly correlated. However, the disadvantage of this approach is that it relies on the *a priori* values, at which the correlated variables are held fixed, being known with a reasonable degree of confidence. This could be a problem for unconventional UAVs if the prior values are based on empirical analysis, which could be unreliable. The second method of incorporating *a priori* values into the estimation process is an extension of the first option and is termed biased estimation. This is discussed further below. On the third option, it may be difficult at first to see how the availability of more data will provide a solution, as all manoeuvres will have been carried out with the flight control system engaged and, therefore, the cause of the correlation persists. However, in reality, the flight control hardware introduces, albeit small, time delays into the system and the sensors will introduce noise. Therefore, the motion variables and the control surface inputs will never be completely correlated and the process of concatenating multiple manoeuvre segments together can lead to there being enough information content in the data to reliably estimate the derivatives.

7.3.2 Biased Estimation

Data collinearity in linear regression problems can result in least squares parameter estimates having large absolute values in comparison to the true parameter values and parameters estimates with large variances [31]. Consider the case in which the value of a parameter θ has been determined using two parameter estimation techniques, one estimate $\hat{\theta}$ being unbiased and the other $\tilde{\theta}$ containing a bias error $\mathrm{E}[\tilde{\theta}] - \theta$, where E again denotes the expected value. The variance of $\hat{\theta}$ is large, while the variance of $\tilde{\theta}$ is smaller, despite the presence of the bias error. This is illustrated in Figure 7.13 [154] which depicts the probability distribution for both estimates. The mean square error of $\tilde{\theta}$ is given by,

$$\mathrm{MSE}(\tilde{\theta}) = \mathrm{E}[\tilde{\theta} - \theta]^2 = \mathrm{Var}(\tilde{\theta}) + \{\mathrm{E}[\tilde{\theta} - \theta]\}^2 \qquad (7.3.8)$$

It is possible that for a small bias error, $\mathrm{MSE}(\tilde{\theta})$ could be smaller than the variance of $\hat{\theta}$. For the above scenario, the unbiased estimate $\hat{\theta}$ could have come from least squares estimation, which from the Gauss-Markov theorem has minimum variance in the class of unbiased estimators [154]. However, there is no guarantee that the variance will be small, particularly if collinearity is present in the data. This has lead to the development of a number of biased estimation techniques, many of which incorporate *a priori* information to improve the confidence of the parameter estimates.

One biased estimation technique that has been widely applied for aircraft parameter estimation is principal components regression [156, 154, 47, 53]. The problem of correlated variables is dealt with by transforming the regressors to form a new set of orthogonal variables, known as the principal components. This is performed with the matrix of eigenvectors $\mathbf{T}$,

$$\bar{\mathbf{X}}^* = \mathbf{X}^*\mathbf{T} \qquad (7.3.9)$$

where $^-$ denotes a variable in principal components form. A similar transformation is applied to the vector of unknown parameters,

$$\bar{\boldsymbol{\theta}}^* = \mathbf{T}^T\boldsymbol{\theta}^* \qquad (7.3.10)$$
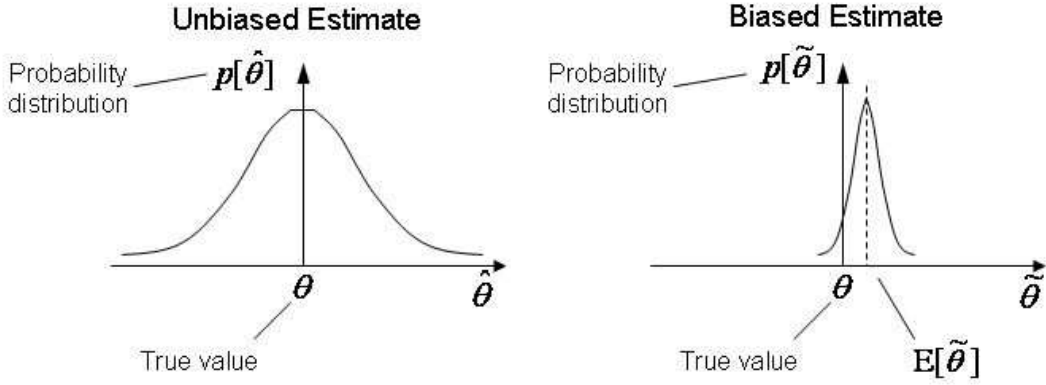
Figure 7.13: Probability distributions of unbiased and
biased estimates of θ

The least squares estimate of $\bar{\theta}^*$ is then obtained from,

$$\hat{\bar{\theta}}^* = (\bar{\mathbf{X}}^{*T}\bar{\mathbf{X}}^*)^{-1}\bar{\mathbf{X}}^{*T}\mathbf{z}^* \tag{7.3.11}$$

Utilising Equation (7.3.2), the estimate of the kth unknown parameter can be written in terms of the singular values of $\mathbf{X}^*$,

$$\hat{\bar{\theta}}_k^* = \frac{\bar{\mathbf{X}}_k^{*T}\mathbf{z}^*}{S_k^2}, \quad k = 1, 2, \ldots, n \tag{7.3.12}$$

where $\bar{\mathbf{X}}_k^*$ denotes the kth column of data from $\bar{\mathbf{X}}^*$. The principal components regression algorithm analyses the singular values of $\mathbf{X}^*$ for each of the n parameters and if the singular value is greater than a given threshold S_0 then the estimate of $\bar{\theta}_k^*$ is obtained from Equation (7.3.12). Otherwise, $\bar{\theta}_k^*$ is set to its *a priori* value $(\bar{\theta}_0^*)_k$. This is expressed mathematically as,

$$\hat{\bar{\theta}}_k^* = \begin{cases} \bar{\mathbf{X}}_k^{*T}\mathbf{z}^*/S_k^2 & S_k > S_0 \\ (\bar{\theta}_0^*)_k & S_k \leq S_0 \end{cases} \tag{7.3.13}$$

The vector of parameter estimates is then transformed back to its original basis,

$$\hat{\boldsymbol{\theta}}^* = \mathbf{T}\hat{\bar{\boldsymbol{\theta}}}^* \tag{7.3.14}$$

The mean square error of the principal components estimate is given by [156],

$$\text{MSE}(\hat{\boldsymbol{\theta}}^*) = \sigma^2 \sum_{k=1}^{r} \frac{1}{S_k}\mathbf{t}_k\mathbf{t}_k^T + \sigma_0^2 \sum_{k=r+1}^{n_\theta} \mathbf{t}_k\mathbf{t}_k^T \tag{7.3.15}$$

where r is the number of singular values S_k greater than the threshold S_0 and σ_0^2 is the variance in the *a priori* estimates $\boldsymbol{\theta}_0^*$.

A second approach is mixed estimation, in which the least squares cost function is augmented to include constraints based on the *a priori* estimates of the unknown parameters. It is assumed that these prior constraints are available for m of the n_θ and this knowledge is formulated as,

$$\mathbf{d} = \mathbf{B}\boldsymbol{\theta}^* + \varsigma \tag{7.3.16}$$

where $\mathbf{B}$ denotes an $(m \times n_\theta)$ matrix of constants based on the *a priori* information, $\mathbf{d}$ is an $(m \times 1)$ vector, while ς is a vector of random variables with the following properties,

$$\mathrm{E}[\varsigma] = \mathbf{0} \text{ and } \mathrm{E}[\varsigma\varsigma^T] = \sigma^2\mathbf{V}$$

where σ^2 is once again the constant variance of the equation errors defined in Chapter 4 and $\mathbf{V}$ is a known matrix reflecting the level of confidence in the *a priori* information. Combining Equation (7.3.16) with the linear regression model in Equation (4.2.3) gives,

$$\begin{bmatrix} \mathbf{z}^* \\ \mathbf{d} \end{bmatrix} = \begin{bmatrix} \mathbf{X}^* \\ \mathbf{B} \end{bmatrix} \boldsymbol{\theta}^* + \begin{bmatrix} \boldsymbol{\epsilon} \\ \varsigma \end{bmatrix} \tag{7.3.17}$$

where,

$$\mathrm{E}\left\{ \begin{bmatrix} \boldsymbol{\epsilon} \\ \varsigma \end{bmatrix} \right\} = \mathbf{0} \text{ and } \mathrm{E}\left\{ \begin{bmatrix} \boldsymbol{\epsilon} \\ \varsigma \end{bmatrix} \begin{bmatrix} \boldsymbol{\epsilon}^T & \varsigma^T \end{bmatrix} \right\} = \sigma^2 \begin{bmatrix} \mathbf{I} & \mathbf{0} \\ \mathbf{0} & \mathbf{V} \end{bmatrix}$$

The cost function to be minimised is then,

$$\begin{aligned} J(\boldsymbol{\theta}^*) &= \frac{1}{2} \begin{bmatrix} (\mathbf{z}^* - \mathbf{X}^*\boldsymbol{\theta}^*)^T \\ (\mathbf{d} - \mathbf{B}\boldsymbol{\theta}^*)^T \end{bmatrix} \begin{bmatrix} \mathbf{I} & \mathbf{0} \\ \mathbf{0} & \mathbf{V} \end{bmatrix}^{-1} \begin{bmatrix} (\mathbf{z}^* - \mathbf{X}^*\boldsymbol{\theta}^*) \\ (\mathbf{d} - \mathbf{B}\boldsymbol{\theta}^*) \end{bmatrix} \tag{7.3.18} \\ &= \frac{1}{2}(\mathbf{z}^* - \mathbf{X}^*\boldsymbol{\theta}^*)^T(\mathbf{z}^* - \mathbf{X}^*\boldsymbol{\theta}^*) + \frac{1}{2}(\boldsymbol{\theta}^* - \mathbf{B}^{-1}\mathbf{d})^T\mathbf{B}^T\mathbf{V}^{-1}\mathbf{B}(\boldsymbol{\theta}^* - \mathbf{B}^{-1}\mathbf{d}) \tag{7.3.19} \end{aligned}$$

and the mixed estimate of $\boldsymbol{\theta}^*$ is found from,

$$\hat{\boldsymbol{\theta}}^* = (\mathbf{X}^{*T}\mathbf{X}^* + \mathbf{B}^T\mathbf{V}^{-1}\mathbf{B})^{-1}(\mathbf{X}^{*T}\mathbf{z}^* + \mathbf{B}^T\mathbf{V}^{-1}\mathbf{d}) \tag{7.3.20}$$

Prior information about the parameters can also be included in the modified Newton-Raphson algorithm. In this case, the cost function to be minimised is based on that given in Equation (5.3.4) but modified to the following,

$$J(\boldsymbol{\theta}) = \frac{1}{2}\sum_{i=1}^{N} \boldsymbol{v}^T(i)\hat{\mathbf{R}}^{-1}\boldsymbol{v}(i) + \frac{1}{2}(\boldsymbol{\theta} - \boldsymbol{\theta}_0)^T\mathbf{R}_0^{-1}(\boldsymbol{\theta} - \boldsymbol{\theta}_0) \tag{7.3.21}$$

where $\boldsymbol{\theta}_0$ is the vector of *a priori* values of $\boldsymbol{\theta}$ and $\mathbf{R}_0$ is a diagonal covariance matrix, the elements of which define the confidence of each value in $\boldsymbol{\theta}_0$. The update of the parameter vector at each iteration of the modified Newton-Raphson algorithm is then computed from,

$$\Delta\boldsymbol{\theta} = -[\mathbf{M} + \mathbf{R}_0^{-1}]^{-1}[\mathbf{G} + \mathbf{R}_0^{-1}(\boldsymbol{\theta} - \boldsymbol{\theta}_0)] \tag{7.3.22}$$

where $\mathbf{G}$ and $\mathbf{M}$ are the gradient and information matrices of the standard modified Newton-Raphson algorithm, defined in Equations (5.3.9) and (5.3.11) respectively.

The disadvantage in using principal components regression, mixed estimation or the modified Newton-Raphson algorithm incorporating prior information is the requirement to specify variables which define the confidence in the *a priori* estimates (σ_0^2, $\mathbf{V}$ and $\mathbf{R}_0$ respectively). If the *a priori* estimates come from wind tunnel experiments or previous flight test results, these variables may be known. However, if the only source of information is empirical analysis, it is more difficult to specify appropriate confidence levels in $\boldsymbol{\theta}_0$, particularly for unconventional UAV configurations.

A biased estimation technique which avoids this problem is ridge regression. The estimate of $\boldsymbol{\theta}$ is found from,

$$\hat{\boldsymbol{\theta}}^* = (\mathbf{X}^{*T}\mathbf{X}^* + k_R\mathbf{I})^{-1}\mathbf{X}^{*T}\mathbf{z}^* \qquad (7.3.23)$$

where k_R is a scalar biasing parameter. When k_R is zero, the ridge estimator is the least squares estimator. The mean square error of the ridge estimate is [123],

$$\begin{aligned}
\mathrm{MSE}(\hat{\boldsymbol{\theta}}^*) &= \mathrm{Var}(\hat{\boldsymbol{\theta}}^*) + \{\mathrm{E}[\hat{\boldsymbol{\theta}}^* - \boldsymbol{\theta}^*]\}^2 \\
&= \hat{\sigma}^2 \sum_{i=1}^{n_\theta} \frac{S_i^2}{(S_i^2 + k_R)^2} + k_R^2 \hat{\boldsymbol{\theta}}^{*T}(\mathbf{X}^{*T}\mathbf{X}^* + k_R\mathbf{I})^{-2}\hat{\boldsymbol{\theta}}^*
\end{aligned} \qquad (7.3.24)$$

The first term on the right hand side of Equation (7.3.24) is the sum of the variances of the parameters in $\hat{\boldsymbol{\theta}}^*$ and the second term is the square of the bias. Inspection of Equation (7.3.24) reveals that an increase in the value of k_R will lead to a decrease in the variance of the estimates. At the same time, however, the bias in the estimates will increase. The objective when choosing the value of k_R therefore is to select a value which results in a reduction in the variance which is greater than the increase in the square of the bias. If such a value can be found for k_R, the mean square error of the ridge estimates will be less than the variance of the corresponding least squares estimates.

A number of methods for selecting k_R, both analytical and graphical, have been proposed [123]. Hoerl et al [157] suggested that the following equation for the biasing parameter,

$$k_R = \frac{n_\theta \hat{\sigma}^2}{\hat{\boldsymbol{\theta}}_{LS}^{*T}\hat{\boldsymbol{\theta}}_{LS}^*} \qquad (7.3.25)$$

where $\hat{\boldsymbol{\theta}}_{LS}^*$ contains the estimates of the parameters from least squares and $\hat{\sigma}^2$ is again the variance of the residuals found from Equation (4.5.12). It was shown by Hoerl et al through simulation that the resulting ridge estimates can have a significantly reduced mean square error in comparison to least squares estimates.

7.3.3 UAV Rolling Moment Example

To demonstrate the collinearity diagnostic and biased estimation, analysis was performed on three segments of UAV flight test data containing aileron doublets to determine the rolling moment derivatives in the following equation,

$$C_l = C_{l_0} + C_{l_\beta}\beta + C_{l_p}\hat{p} + C_{l_r}\hat{r} + C_{l_\xi}\xi + C_{l_\zeta}\zeta \qquad (7.3.26)$$

The rolling moment coefficient C_l was derived from the measured data using the expression,

$$C_n = \frac{1}{\bar{q}S\frac{b}{2}}\left[I_{xx}\dot{p} - I_{xz}(\dot{r} + pq) + (I_{zz} - I_{yy})qr\right] \qquad (7.3.27)$$

The aileron inputs are shown in Figure 7.14, along with the rudder position. As can be seen, rudder inputs are being applied as well as those to the ailerons. These rudder inputs are generated automatically to counteract adverse yawing motion caused by drag associated with the deflection of the ailerons. Comparing the shape of the two input time histories in Figure 7.14, it is clear that the rudder input is related to the aileron deflection. Thus, it is highly likely that

collinearity will exist between ξ and ζ. This automatic rudder deflection was highlighted earlier in Section 4.7. For that example, the correlation problem was avoided by combining aileron and rudder doublet data in the analysis, resulting in greater information content regarding the separate effects of each control surface. However, for the purposes of demonstrating collinearity, it will be assumed in the current example that the only data available are these three manoeuvres.
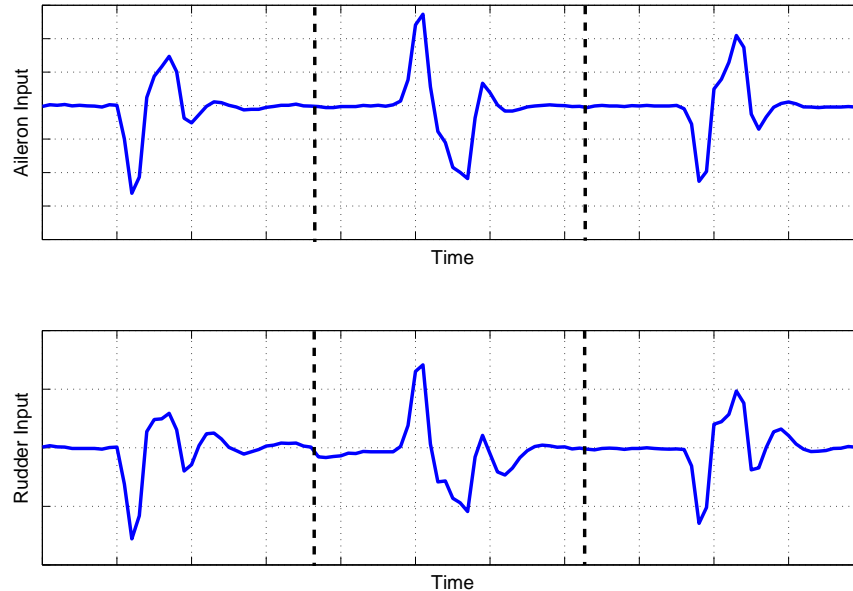
Figure 7.14: Time histories of aileron and rudder
deflections

Table 7.4 gives the parameter estimates and corresponding standard error obtained using ordinary least squares regression and Table 7.5 displays the pair-wise correlation coefficients between the parameters. Note that the offset term C_{l_0} was found to be negligibly small and, hence, removed from the model. The standard errors indicate that there is a high level of uncertainty in the estimates, particularly for C_{l_ζ}. Examination of Table 7.5 reveals that this parameter, as expected, is highly correlated with C_{l_ξ}. Figure 7.15 shows the rolling moment coefficient derived from the measured data plotted against the response reconstructed using the least squares estimates. Despite the uncertainty in the parameter estimates, the match between the two is close. However, this observation simply illustrates the point that a close visual match between the measured and identified responses is no guarantee of the parameter estimates being acceptable.

A collinearity diagnostic using eigenvalue analysis, condition indices and variance proportion decomposition was then carried out. The results of this are summarised in Table 7.6. The first column shows that one eigenvalue was found to be much smaller than the others and, as a result, the corresponding condition index was an order of magnitude greater than the other condition indices, with $C_{max} = 18.27$. The variance proportions associated with C_{max} showed large values for the aileron and rudder, 0.9963 and 0.9777 respectively, and therefore strong collinearity between these variables. The analysis also suggested that the correlation was not restricted to just ξ and ζ but also included roll rate $\hat{p}$ and yaw rate $\hat{r}$, as their proportions both exceeded the guideline value of 0.5. Note that the value of C_{max} was much less than the figure

	$\hat{\theta}$	$100[s/|\hat{\theta}|]$
C_{l_β}	1.616	46.32
C_{l_p}	1.044	8.46
C_{l_r}	0.921	51.28
C_{l_ξ}	1.074	21.83
C_{l_ζ}	2.884	140.04

Table 7.4: Estimates of roll derivatives from ordinary least squares regression

	C_{l_β}	C_{l_p}	C_{l_r}	C_{l_ξ}	C_{l_ζ}
C_{l_β}	1	0.4013	0.0676	0.2485	0.2271
C_{l_p}	-	1	0.3917	0.6963	0.5927
C_{l_r}	-	-	1	0.6611	0.6340
C_{l_ξ}	-	-	-	1	0.9790
C_{l_ζ}	-	-	-	-	1

Table 7.5: Correlation coefficients for roll derivatives from ordinary least squares regression
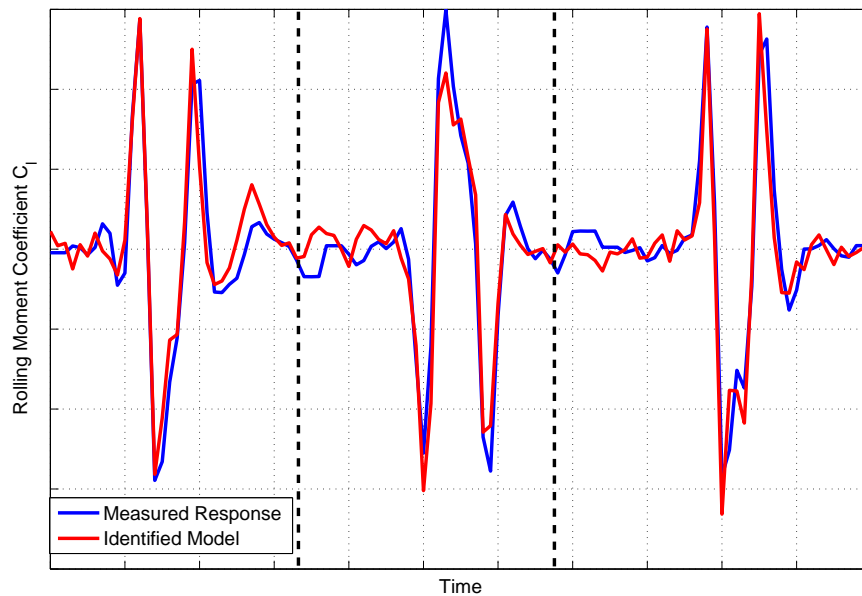
Figure 7.15: Measured and identified rolling moment responses: ordinary least squares regression

of 100 often quoted in the literature as an indication of the presence of collinearity. This seems to follow the observations of other practitioners, described in Section 7.3.1, that collinearity can still exist despite the largest condition index being less than 100.

Eigenvalues λ	Condition Index C	Variance Proportions π				
		β	$\hat{p}$	$\hat{r}$	ξ	ζ
2.8257	1	0.0013	0.0142	0.0123	0.0017	0.0025
1.3772	1.43	0.2874	0.0068	0.0729	0.0000	0.0001
0.4082	2.64	0.1164	0.1187	0.1985	0.0020	0.0186
0.3827	2.72	0.5389	0.1795	0.2075	0.0000	0.0012
0.0085	18.27	0.0560	0.6808	0.5088	0.9963	0.9777

Table 7.6: Collinearity diagnostics for aileron doublet data

Estimation was then performed, first using principal components regression and then with ridge regression. For principal components regression, the singular values were calculated by taking the square roots of the eigenvalues in Table 7.6. The singular value corresponding to C_{max} was $S_{min} = 0.09$, therefore the threshold S_0 for the algorithm defined in Equation (7.3.13) was set to 0.1. This meant that the estimate of the transformed parameter $\bar{\theta}_k^*$ corresponding to the smallest singular value was set to an estimate based on *a priori* information, rather than from least squares regression. The *a priori* estimates in this case were from empirical analysis. The parameter estimates were then transformed back to their original basis using Equation (7.3.14) and the results are shown in the second column of Table 7.7. In comparison to the estimates obtained from least squares regression, the principal components regression results are very similar. The exception to this is the estimate of C_{l_ζ}, which is around half the size of the least squares estimate. The standard errors of the principal components regression estimates are also given in Table 7.7. These were calculated as the square roots of the diagonal elements of the mean square error defined in Equation (7.3.15) and the computation required specification of the variance in the empirical estimates σ_0^2. Without any knowledge of this parameter, it was decided to set its value for each derivative to a figure corresponding to 50% of the *a priori* estimate value, thus reflecting a relatively high uncertainty in the *a priori* estimates. Despite this, the standard errors from principal components regression are much lower in comparison to the least squares results, especially for C_{l_ζ}, and indicate an improved confidence in the estimated values.

Ridge regression was performed next. Based on the least squares analysis, the value of the biasing parameter k_R was set to 0.0014 and the resulting estimates are displayed in the fourth column of Table 7.7. The derivative values obtained were very similar to those from principal components regression, with the value of C_{l_ζ} again being around half the size of the least squares estimate. The standard errors for the ridge estimates were determined as the square roots of the diagonal elements of the mean square error in Equation (7.3.24). These are shown in the last column of Table 7.7. Relative to the least squares result, the standard error of C_{l_ζ} has decreased by around a third but remains high. The standard errors of C_{l_β} and C_{l_r} are also high and, in fact, the uncertainty in these derivatives has actually increased.

A fourth segment of data containing an aileron input was used to validate the parameter estimates from least squares regression, principal components regression and ridge regression. The measured data from this manoeuvre is shown in Figure 7.16 along with the predicted responses from the three methods. As can be seen, the three methods provide very similar responses and

	Prin. Comp. Reg.		Ridge Reg.	
	$\hat{\theta}$	$100[s/|\hat{\theta}|]$	$\hat{\theta}$	$100[s/|\hat{\theta}|]$
C_{l_β}	1.678	31.36	1.663	74.83
C_{l_p}	1.009	4.03	1.005	9.09
C_{l_r}	1.012	24.84	1.003	61.15
C_{l_ξ}	0.984	2.12	0.980	6.78
C_{l_ζ}	1.500	37.91	1.471	98.50

Table 7.7: Estimates of roll derivatives from principal
components regression and ridge regression

this is also reflected by the results from Theil's analysis,

$$Least\ Squares : U = 0.2108,\ U_B = 0.0432,\ U_V = 0.0021,\ U_C = 0.9546$$
$$Principal\ Components : U = 0.2105,\ U_B = 0.0299,\ U_V = 0.0063,\ U_C = 0.9638$$
$$Ridge : U = 0.2093,\ U_B = 0.0654,\ U_V = 0.0227,\ U_C = 0.9119$$
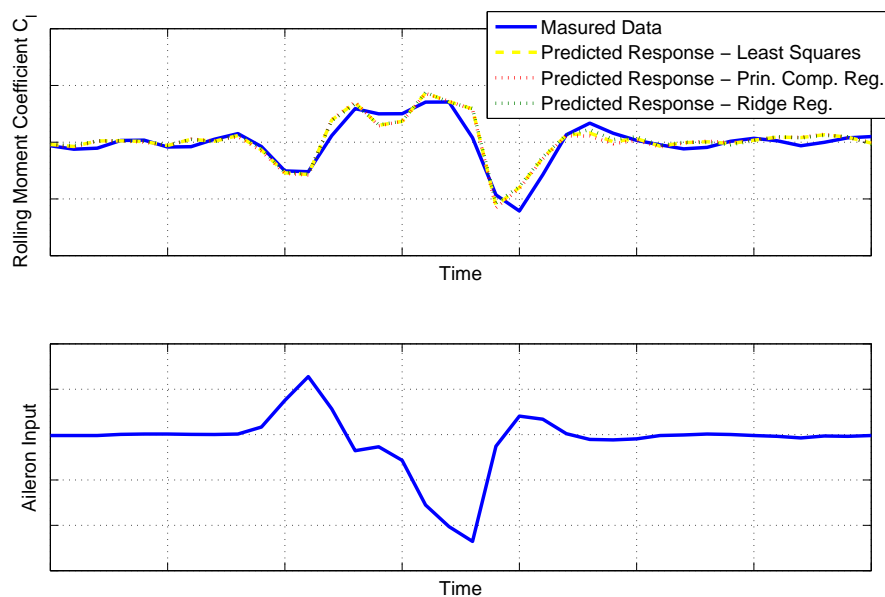
Figure 7.16: Measured and predicted rolling moment
responses for aileron validation manoeuvre

The analysis presented above found that, while very similar values for derivatives were obtained from the three method, principal components regression provided estimates with the lowest standard errors. However, the problem of specifying the confidence level for the *a priori* information remains. The next logical step was to include data in which the rudder was excited independently. When this was done, the investigation found that there was still insufficient information in the data to reliably identify C_{l_ζ} and, therefore, it was removed from the model. The process of determining the most appropriate model structure for a given response is described in Chapter 8, therefore the presentation of this analysis is deferred until then.

7.3.4 UAV Pitching Moment Example

As a second example of possible data collinearity, the analysis carried out on UAV pitching moment data is presented next. The pitching moment equation in this case is,

$$C_m = C_{m_0} + C_{m_\alpha}\alpha + C_{m_V}\hat{V} + C_{m_q}\hat{q} + C_{m_\eta}\eta \tag{7.3.28}$$

As for the pitching moment example presented in Section 6.6, Equation 7.3.28 contains the derivative C_{m_V} to model slight drifts in the airspeed during the manoeuvres.

The data contained two pitch doublets. However, pitch rate feedback was engaged for the flight test meaning that changes in q, rather than changes in elevator position η, were being demanded during the manoeuvres. This introduced a relationship between the pitch rate and the elevator deflection, as illustrated in Figure 7.17, which shows time histories of the two variables. It can be seen that the shape of the two plots look very similar (note the sign of the elevator time history has been changed to highlight the match).
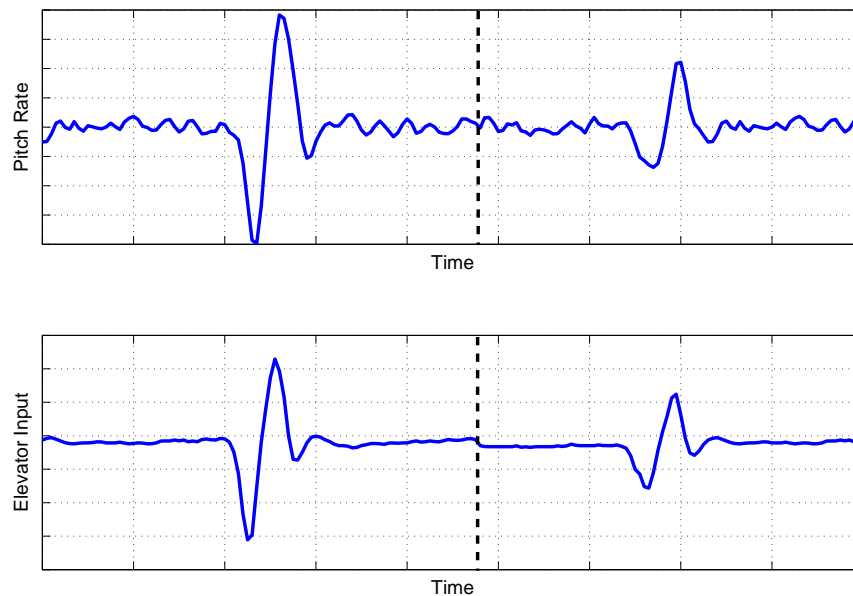
Figure 7.17: Time histories of pitch rate and elevator inputs

Least squares regression was performed first, with the estimates and standard errors given in Table 7.8. Despite the potential collinearity problems, the results suggested that the parameters were estimated with an acceptable degree of confidence, with all standard errors falling below 20% of the estimate magnitudes. The pair-wise correlation coefficients are displayed in Table 7.9 and show that some correlation did exist between the pitch rate and elevator deflection. However, the value of $\rho = 0.9004$ was right at the threshold of what is considered significant and indicated that the collinearity may not have been as severe as first thought. Figure 7.18 shows the pitching moment coefficient derived from the data plotted against the response reconstructed from the least squares estimates. The match between the two responses is close but, as pointed out for the previous example, this is no guarantee that the estimates are reliable.

	$\hat{\theta}$	$100[s/|\hat{\theta}|]$
C_{m_0}	0.956	0.24
C_{m_α}	1.178	8.17
C_{m_V}	0.933	13.31
C_{m_q}	1.099	17.37
C_{m_η}	0.934	8.57

Table 7.8: Estimates of pitch derivatives from ordinary least squares regression

	C_{m_0}	C_{m_α}	C_{m_V}	C_{m_q}	C_{m_η}
C_{m_0}	1	0.4418	0.5758	0.4398	0.5071
C_{m_α}	-	1	0.1854	0.7229	0.7007
C_{m_V}	-	-	1	0.1504	0.1192
C_{m_q}	-	-	-	1	0.9004
C_{m_η}	-	-	-	-	1

Table 7.9: Correlation coefficients for pitch derivatives from ordinary least squares regression
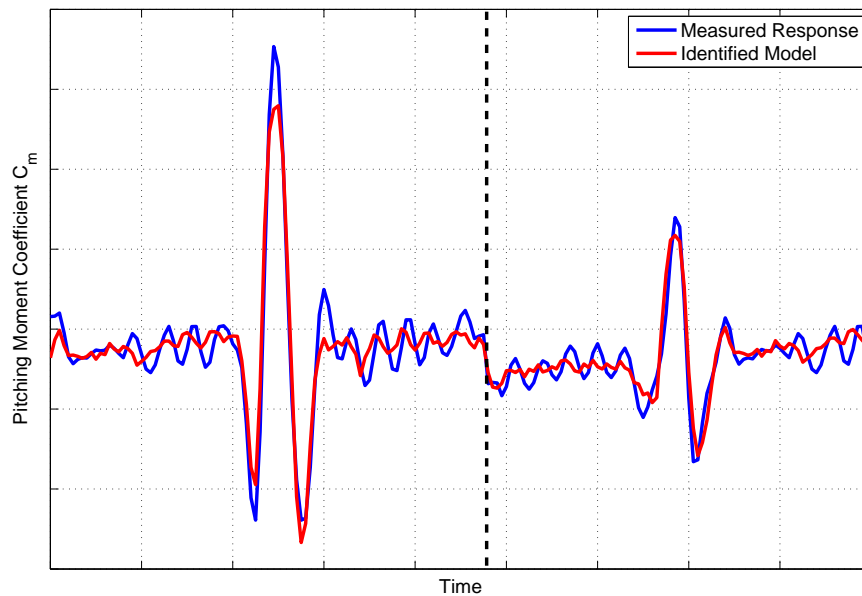
Figure 7.18: Measured and identified pitching moment responses: ordinary least squares regression

To investigate further, the eigenvalues, condition indices and variance proportions were calculated. These are shown in Table 7.10. The maximum condition index value was found to be very low at $C_{max} = 3.44$, further supporting the theory that there were no strong collinearity effects in the data. However, the variance proportions for $\hat{q}$ and η associated with the smallest eigenvalue were large so the analysis proceeded and biased estimation was performed. Principal components regression was carried out first. The lowest singular value was $S_{min} = 0.39$, therefore the singular value threshold S_0 was set to 0.4. The *a priori* estimates used in the calculations were again from empirical analysis. The principal component estimates and standard errors are shown in the second and third columns, respectively, of Table 7.11. To calculate the standard errors, the variance in the *a priori* estimates was again assumed to be 50% of the magnitude of empirical values. In comparison to the least squares estimates, the values obtained from principal components regression were very similar. However, the standard errors of the least squares estimates were all smaller. Ridge regression was then used to analyse the data, with the value of k_R calculated from Equation (7.3.25) to be 0.0027. The resulting estimates and standard errors are also shown in Table 7.11. Again, the derivative values matched very closely those found from least squares and principal components regression. There was also a slight improvement in the standard errors for C_{m_q} and C_{m_η} in comparison to the least squares estimates. However, there was reduced confidence in the remaining parameters, particularly for C_{m_V}.

Eigenvalues λ	Condition Index C	Variance Proportions π				
		1	α	$\hat{V}$	$\hat{q}$	η
1.7826	1	0.0201	0.0124	0.0004	0.0815	0.0773
1.3764	1.14	0.2289	0.0591	0.2823	0.0037	0.0078
1.0349	1.31	0.0740	0.4318	0.0472	0.0093	0.0328
0.6558	1.65	0.6415	0.0010	0.6425	0.0037	0.0049
0.1502	3.44	0.0355	0.4957	0.0276	0.9019	0.8772

Table 7.10: Collinearity diagnostics for elevator doublet data

	Prin. Comp. Reg.		Ridge Reg.	
	$\hat{\theta}$	$100[s/|\hat{\theta}|]$	$\hat{\theta}$	$100[s/|\hat{\theta}|]$
C_{m_0}	0.957	0.50	0.956	0.96
C_{m_α}	1.150	13.55	1.182	11.34
C_{m_V}	0.937	15.82	0.933	29.02
C_{m_q}	1.158	26.16	1.081	13.07
C_{m_η}	0.959	13.55	0.925	6.92

Table 7.11: Estimates of pitch derivatives from principal components regression and ridge regression

To validate the parameter estimates from least squares regression, principal components regression and ridge regression, the identified models were used to predict the pitching moment response to an elevator input not used in the estimation process. The measured data from this manoeuvre is shown in Figure 7.19 along with the predicted responses from the three methods. As with the example presented in Section 7.3.3, the three methods provided very similar

responses. The results from Theil's analysis were,

$$Least\ Squares: U = 0.0251,\ U_B = 0.1531,\ U_V = 0.1111,\ U_C = 0.7357$$
$$Principal\ Components: U = 0.0243,\ U_B = 0.1487,\ U_V = 0.0528,\ U_C = 0.7984$$
$$Ridge: U = 0.0256,\ U_B = 0.1508,\ U_V = 0.1409,\ U_C = 0.7083$$

From Figure 7.19, the predicted responses can be seen to match the measured data closely. Theil's inequality coefficient for the three methods were also low, suggesting a satisfactory fit to the measurements. However, the bias portions for the three methods, as well as the variance portions for least squares and ridge regression, could all be considered high.
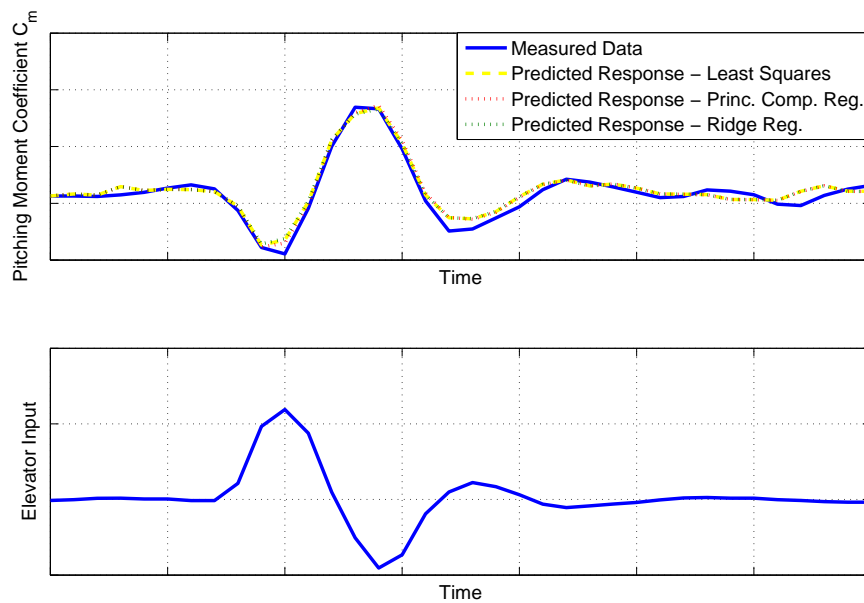
Figure 7.19: Measured and predicted pitching moment responses for elevator validation manoeuvre

The conclusion from the above analysis was that, in practice, the collinearity caused by the pitch rate feedback was minimal. It is likely that time delays introduced by the flight control hardware and noise in the pitch gyro measurements meant that there was enough information about the separate effects of q and η to reliably estimate C_{m_q} and C_{m_η}. In this case, the least squares estimation was adequate and had relatively low standard errors, indicating an acceptable level of confidence in the estimates. No significant improvement was found in using either of the biased parameter estimation techniques and, in fact, the majority of the standard errors obtained with principal components regression and ridge regression were greater than those from least squares.

Chapter 8

Model Structure Determination

8.1 Introduction

In the previous chapters on parameter estimation, it was largely assumed that the equations of motion used were the most appropriate given the aircraft's measured response. However, it may not always be clear what terms should be included in the model structure. This is especially true if the aircraft is operating at high angles of attack or undergoing large amplitude manoeuvres, in which case its dynamics are likely to be nonlinear. The process of determining the most appropriate model structure could be crucial even for UAVs flying in linear flight regimes due to their unconventional configurations. Using a typical UCAV configuration as an example, the lack of a conventional fin and rudder means that yaw control must be achieved through alternative means. One such method is to generate a drag differential between the wings using split flap trailing edge devices [4]. However, depending on the location of the split flaps relative to the aircraft's centre of gravity, this will produce adverse rolling, and possibly pitching moments, resulting in greater cross-coupling between each axis. Therefore, the focus of this chapter is on methods of model structure determination.

8.2 Regression Analysis

The first part of this chapter is concerned with linear regression models given by Equation (4.2.3),

$$\mathbf{z} = \mathbf{X}\boldsymbol{\theta} + \boldsymbol{\epsilon} \tag{8.2.1}$$

where $\boldsymbol{\epsilon}$ is again assumed to be a Gaussian random variable, with zero mean and variance σ^2, i.e.,

$$\boldsymbol{\epsilon} \sim \mathbb{N}[\mathbf{0}, \sigma^2\mathbf{I}]$$

Determining the correct model structure for Equation (8.2.1) is based on hypothesis testing in which decisions for adding or deleting terms from the model are made based on statistics calculated using the measured data.

The first hypothesis test is the test for overall regression, which aims to find if a linear relationship exists between the measured dependent variable $\mathbf{z}$ and a set of n candidate regressors X_j,

$j = 1,2,\ldots,n$. The offset parameter θ_0 is included in the model by default. Two hypotheses are formed as follows,

$$H_0 \quad : \quad \theta_1 = \theta_2 = \ldots = \theta_n = 0 \tag{8.2.2}$$

$$H_1 \quad : \quad \theta_j \neq 0 \text{ for at least one } j \tag{8.2.3}$$

where H_0 is known as the null hypothesis and H_1 is the alternative hypothesis. To assess which hypothesis is true, F-statistics are used and the following quantities are required in the calculation of these statistics,

$$SS_T \;\; = \;\; \sum_{i=1}^{N}[z(i) - \bar{z}]^2 = \mathbf{z}^T\mathbf{z} - N\bar{z}^2 \tag{8.2.4}$$

$$SS_R \;\; = \;\; \sum_{i=1}^{N}[\hat{y}(i) - \bar{z}]^2 \tag{8.2.5}$$

$$SS_E \;\; = \;\; \sum_{i=1}^{N}[z(i) - \hat{y}(i)]^2 = \mathbf{z}^T\mathbf{z} - \hat{\boldsymbol{\theta}}^T\mathbf{X}^T\mathbf{z} \tag{8.2.6}$$

where N is again the number of data points and $\bar{z}$ is the mean of the dependent variable,

$$\bar{z} = \frac{1}{N}\sum_{i=1}^{N} z(i) \tag{8.2.7}$$

The variable SS_T represents the sum of the squared variations of z about its mean value and is termed the total sum of squares, SS_R is the sum of the squared variations of the predicted dependent variable $\hat{y}$ about $\bar{z}$ and is known as regression sum of squares, while SS_E is the sum of the squared variations between measured dependent variable z and predicted dependent variable $\hat{y}$ and is called the residual sum of squares. The three quantities are related to each other by the following equation,

$$SS_T = SS_R + SS_E \tag{8.2.8}$$

Combining Equations (8.2.4), (8.2.6) and (8.2.8), the regression sum of squares can also be expressed as,

$$SS_R = \hat{\boldsymbol{\theta}}\mathbf{X}^T\mathbf{z} - N\bar{z}^2 \tag{8.2.9}$$

The F-statistic for the null hypothesis is then calculated from [31],

$$F_0 = \frac{SS_R/n}{SS_E/(N - n_\theta)} = \frac{\hat{\boldsymbol{\theta}}\mathbf{X}^T\mathbf{z} - N\bar{z}^2}{n\hat{\sigma}^2} \tag{8.2.10}$$

where $\hat{\sigma}^2$ is the estimate of the variance calculated earlier in Chapter 4 using Equation (4.5.12). The statistic F_0 is a random variable that follows the F-distribution, the values for which can be found from look up tables (for example Reference [130]). In the above expression, the numerator is said to have n degrees of freedom, while the denominator has $(N - n_\theta)$ degrees of freedom. The null hypothesis is rejected if,

$$F_0 > F(\alpha, n, N - n_\theta) \tag{8.2.11}$$

where α is a selected significance level, similar to that described for t-distributions in Section 4.5, with a value between 0 and 1. If the null hypothesis is rejected for a chosen value of α, this

is equivalent to saying that there is a 100(1-α) percent confidence that not all of the parameters are zero. A typical value for α in aircraft system identification is 0.05, corresponding to a 95% confidence level [31].

A second hypothesis test is the test for significance of individual regressor or partial F-test. In this case, the null and alternative hypotheses can be expressed as,

$$H_0 \;:\; \theta_j = 0 \tag{8.2.12}$$

$$H_1 \;:\; \theta_j \neq 0 \tag{8.2.13}$$

and the partial F-statistic for the null hypothesis is given by,

$$F_0 = \frac{\hat{\theta}_j^2}{s^2(\hat{\theta}_j)} \tag{8.2.14}$$

where $s^2(\hat{\theta}_j)$ is the estimate of the variance of $\hat{\theta}_j$ i.e. square of the standard error $s(\hat{\theta}_j)$. The numerator now has one degree of freedom and the denominator has $(N-n_\theta)$ degrees of freedom as before. The null hypothesis is rejected if,

$$F_0 > F(\alpha, 1, N - n_\theta) \tag{8.2.15}$$

In general, there are three procedures for adding or removing terms from the model structure. The first is termed forward selection, in which the initial model simply contains the offset parameter θ_0. One regressor is added at a time until all candidate regressors are in the model or until some criterion for an adequate model structure is met. The first regressor added to the model is the one that has the highest correlation with the dependent variable $\mathbf{z}$. This is determined from,

$$r_{jz} = \sum_{i=1}^{N} \frac{[X_j(i) - \bar{X}_j][z(i) - \bar{z}]}{\sqrt{S_{jj}S_{zz}}}, \;\; j = 1, 2, \ldots, n \tag{8.2.16}$$

where,

$$\bar{X}_j \;=\; \frac{1}{N} \sum_{i=1}^{N} X_j(i) \tag{8.2.17}$$

$$S_{jj} \;=\; \sum_{i=1}^{N} [X_j(i) - \bar{X}_j]^2 \tag{8.2.18}$$

$$S_{zz} \;=\; \sum_{i=1}^{N} [z(i) - \bar{z}]^2 \tag{8.2.19}$$

The regressor with the highest correlation with the dependent variable, denoted $\mathbf{X}_1$, will also be the regressor with the highest partial F-statistic. The second regressor added to the model is then the one with the highest correlation with the dependent variable adjusted for the effects of the offset parameter and first regressor i.e. $\mathbf{z} - \theta_0 - \theta_1\mathbf{X}_1$. The process continues until all candidate regressors are in the model or the partial F-statistics of the remaining regressors fall below a given threshold F_{in}. In general, the jth regressor is added to a model already containing m terms if,

$$F_0 = \frac{SS_R(\hat{\boldsymbol{\theta}}_{m+j}) - SS_R(\hat{\boldsymbol{\theta}}_m)}{\hat{\sigma}^2} > F_{\text{in}} \tag{8.2.20}$$

where $SS_R(\hat{\boldsymbol{\theta}}_m)$ is the regression sum of squares based on the m regressors currently in the model and $SS_R(\hat{\boldsymbol{\theta}}_{m+j})$ is the regression sum of squares when the jth term is added.

The second approach is essentially the reverse of forward selection and is known as backward elimination. To start with, all candidate regressors are included in the model and, at each step, the term with the smallest partial F-statistic is removed,

$$F_0 = \min_j \frac{SS_R(\hat{\boldsymbol{\theta}}_m) - SS_R(\hat{\boldsymbol{\theta}}_{m-j})}{\hat{\sigma}^2} < F_{\text{out}} \tag{8.2.21}$$

where $SS_R(\hat{\boldsymbol{\theta}}_{m-j})$ is the regression sum of squares when the jth regressor removed from the model.

The third approach is termed stepwise regression and can be considered a combination of forward selection and backward elimination. When a new term is added to the model, the regressors included previously are reassessed. It is entirely possible that a term which was significant at an early stage of the analysis may be become unnecessary once subsequent regressors are added to the model. This is the most widely-used of the three approaches and the following section looks at the procedure in more detail.

8.3 Stepwise Regression

The process begins in a similar manner to forward selection, with just the offset term θ_0 in the model. The first regressor to be added is the one with the highest correlation with $\mathbf{z}$, computed from (8.2.16). Letting this regressor be denoted $\mathbf{X}_1$, the model at this stage is,

$$\mathbf{z} = \hat{\theta}_0 + \hat{\theta}_1 \mathbf{X}_1 + \boldsymbol{v} \tag{8.3.1}$$

where $\boldsymbol{v}$ is again used to denote the vector of residuals. Least squares regression is then used to find estimates $\hat{\theta}_0$ and $\hat{\theta}_1$ which provide the best fit to $\mathbf{z}$ and the partial F-statistic is found from,

$$F_0 = \frac{SS_R(\hat{\boldsymbol{\theta}}_1)}{\hat{\sigma}^2} \tag{8.3.2}$$

A check is then made that $F_0 > F_{\text{in}}$ and the analysis proceeds.

Next, the regressor with the second highest correlation with $\mathbf{z}$ is added to the model. However, for this correlation calculation, the remaining candidate regressors are orthogonalised with respect to the terms already in the model to remove any variations that are already included. This is done by modelling each remaining regressor with $\mathbf{X}_1$ and the offset term and treating the resulting residual as a new candidate term. For example, the regressor $\mathbf{X}_2$ is modelled as,

$$\mathbf{X}_2 = \hat{a}_0 + \hat{a}_1 \mathbf{X}_1 + \boldsymbol{v}_2 \tag{8.3.3}$$

so that the new candidate regressor is the residual term $\boldsymbol{v}_2$,

$$\boldsymbol{v}_2 = \mathbf{X}_2 - \hat{a}_0 - \hat{a}_1 \mathbf{X}_1 \tag{8.3.4}$$

and the coefficients $\hat{a}_0$ and $\hat{a}_1$ are estimated using least squares. Similarly, the new dependent variable is the vector of residuals in Equation (8.3.1),

$$\boldsymbol{v} = \mathbf{z} - \hat{\theta}_0 - \hat{\theta}_1 \mathbf{X}_1 \tag{8.3.5}$$

The process of orthogonalising the candidate regressors with respect to the terms already in the model means that the model structure determination is always focused on terms necessary to characterise unmodelled variations in $\mathbf{z}$. It can also help when the contribution of regressors added early on dwarf those required later to model smaller variations in the dependent variable. Note that the orthogonalised terms are only required for the correlation calculation and the original candidate regressors and dependent variable are used for the other computations.

Every time a regressor is added to the model, the partial F-statistic for all terms is calculated and each F_0 is compared to a given value of F_{out}. As for backward elimination, any regressor with an F_0 value less than F_{out} is removed from the model. The point is made again that it is possible that a regressors added at an early stage could become insignificant as more terms are added to the model. The process continues until no more regressors are included or omitted from the model. The values for F_{in} and F_{out} are usually the same, although some analysts prefer $F_{\text{in}} > F_{\text{out}}$ making it more difficult to admit a term to the model than to remove one from it. The F-distribution value depends on the number of data points N and the number of regressors m currently in the model. For typical aircraft problems, $N >> 100 >> m$, therefore the 95% confidence $F(0.05, 1, N - m) \approx 4$. It has been suggested, however, that more suitable values of F_{in} and F_{out} are around four to five times the figure indicated by the F-distribution table [158].

The sole use of the partial F-statistics to determine the most appropriate model structure has been found to be too restrictive and can result in the model having too many parameters. Therefore, it is recommended that a number of metrics be used in assessing the suitability of the model [158, 31]. Various metrics have been proposed and the most common are summarised below.

A *Coefficient of Determination*

The coefficient of determination is denoted R^2 and represents the proportion of the variation in the dependent variable explained by the terms in the model. It is computed from,

$$R^2 = \frac{SS_R}{SS_T} = 1 - \frac{SS_E}{SS_T} = \frac{\hat{\boldsymbol{\theta}}^T \mathbf{X}^T \mathbf{z} - N \bar{z}^2}{\mathbf{z}^T \mathbf{z} - N \bar{z}^2} \tag{8.3.6}$$

The value of R^2 falls between 0 and 1 but is usually expressed as a percentage, 100% representing a perfect fit to the measured data. Adding a regressor to the model will always lead to an increase in R^2. However, the increase will be greater early on in the process when more influential terms are added. After all significant terms have been included in the model, the change in R^2 due to the inclusion of additional terms will be small and, therefore, the appropriate model structure is considered to have been found when the increase in R^2 falls below a given threshold. Typically, a term is considered significant if the resulting increase in R^2 is greater than 0.5 %.

The coefficient of determination is closely related to the test for overall regression introduced earlier. The F-statistic for the null hypothesis given in Equation (8.2.10) can be rewritten as,

$$F_0 = \frac{(N - m)R^2}{(m - 1)(1 - R^2)} \tag{8.3.7}$$

When influential regressors are added to the model early in the analysis, the value of F_0 will increase. However, when less significant terms are included, the increase in $R^2/(1 - R^2)$ could be smaller than the decrease in $(N - m)/(m - 1)$, leading to the

value of F_0 to decrease. Therefore, the maximum value of F_0 can also be used as the basis for finding the best model to fit the data.

B *Predicted Sum of Squares*

The predicted sum of squares (PRESS) is defined as the sum of the squares of the N residuals, which can be found from,

$$\text{PRESS} = \sum_{i=1}^{N} \left[\frac{\upsilon(i)}{(1 - k_{ii})} \right]^2 \tag{8.3.8}$$

where the residual $\upsilon(i)$ has been normalised with respect to the diagonal elements of the prediction matrix,

$$k_{ii} = \mathbf{x}^T(i)(\mathbf{X}^T\mathbf{X})^{-1}\mathbf{x}(i) \tag{8.3.9}$$

where $\mathbf{x}^T(i)$ is the ith row of $\mathbf{X}$. The correct model structure is then in theory the one with the minimum corresponding PRESS. However, in practice, it has been found that for cases where the number of data points N is much larger in comparison to the number of model terms m (which is true for typical aircraft applications) then PRESS can continue to decrease even when insignificant regressors are added to the model. Therefore, care must be taken when using PRESS to assess the adequacy of the model structure.

C *Predicted Square Error*

The predicted square error (PSE) is given by,

$$\text{PSE} = \frac{1}{N}(\mathbf{z} - \hat{\mathbf{y}})^T(\mathbf{z} - \hat{\mathbf{y}}) + \sigma_{max}^2 \frac{m}{N} \tag{8.3.10}$$

The first term on the right hand side of Equation (8.3.10) is known as the mean squared fit error (MSFE),

$$\text{MSFE} = \frac{1}{N}(\mathbf{z} - \hat{\mathbf{y}})^T(\mathbf{z} - \hat{\mathbf{y}}) \tag{8.3.11}$$

which will decrease each time a new regressor is added to the model. Hence, this term on its own cannot be used to indicate the most appropriate model structure. To compensate, the PSE includes a second term $\sigma_{max}^2 m/N$, known as the overfit penalty term, which increases as more regressors are included in the model. The minimum value of PSE is taken as an indicator of the most appropriate model structure given the measured response.

The parameter σ_{max}^2 is the *a priori* upper-bound estimate of the squared error between future data and the model. It is used to account for the fact that the PSE is calculated when the model structure is not correct. An estimate of σ_{max}^2 can be obtained from [31],

$$\sigma_{max}^2 = \frac{1}{N} \sum_{i=1}^{N} [z(i) - \bar{z}]^2 \tag{8.3.12}$$

D *Analysis of Residuals*

Examination of the residuals can also provide an indication of the adequacy of the model structure. If the model structure is correct then the residuals should be a sequence of uncorrelated random variables with a Gaussian distribution. On the other hand, if they

are found to contain a deterministic component, this could suggest that an important regressor has been omitted from the model.

The variance of the residuals is estimated using,

$$\hat{\sigma}^2 = \frac{\boldsymbol{v}^T \boldsymbol{v}}{N - m} \tag{8.3.13}$$

The square root of Equation (8.3.13) is referred to as the estimated fit error. The residual variance obtained from the expression above can be compared to an estimate obtained directly from the experimental data. For example, the Fourier smoothing algorithm described in Section 4.3 can be used to separate the deterministic component of the dependent variable from random measurement noise. If the model structure is correct then the estimate from Equation (8.3.13) should match the variance of the measurement noise component obtained from Fourier smoothing.

In many cases, it is unlikely that all of the criteria described in this section will be satisfied at any one time. Often, the choice of when to halt the process of adding and removing terms from the model is made based on a consensus of the metrics. The process of model structure determination is also one that cannot be used blindly but instead works best when utilised in conjunction with a physical understanding of the aircraft dynamics. Another useful rule when making a borderline decision as to whether a regressor is included or not is the principle of parsimony [34, 31], which says that given two models which have similar levels of fidelity, the better model is that which has the fewer number of parameters. The process of stepwise regression as applied to aircraft problems was pioneered by Klein et al [158, 134], who proposed a modification when selecting which terms should enter the model. If a borderline decision has to be made regarding which regressors to add, linear terms should always be included before nonlinear ones. This helps when dealing with more complex model structures such as those represented by spline functions. This procedure became known as modified stepwise regression.

8.4 UAV Rolling Moment Example

For an example of the application of stepwise regression, attention returns to the estimation of the UAV rolling moment derivatives presented in Section 7.3.3. The analysis presented previously was based on three aileron doublets but it was found that there was a high level of correlation between the aileron and rudder inputs. Therefore, the analysis was repeated, incorporating three extra manoeuvres in which the rudder was excited separately, and the model structure determination process is described here. Figure 8.1 shows the aileron and rudder inputs applied during the six manoeuvres.

For the first step of the analysis, the correlation r_{jz} between each of the regressors and the rolling moment coefficient C_l were calculated and are shown in the last column of Table 8.1. Also displayed are the initial values for the fit error $\hat{\sigma}$, the coefficient of determination R^2, PRESS and PSE. The regressor with the largest correlation with the dependent variable was the aileron input ξ, therefore the control derivative C_{l_ξ} was the first term added to the model.

In step 2 of the analysis, least squares estimation was then used to find the value of C_{l_ξ}. This is given in the first column of Table 8.2. The partial F-statistic for the derivative was calculated
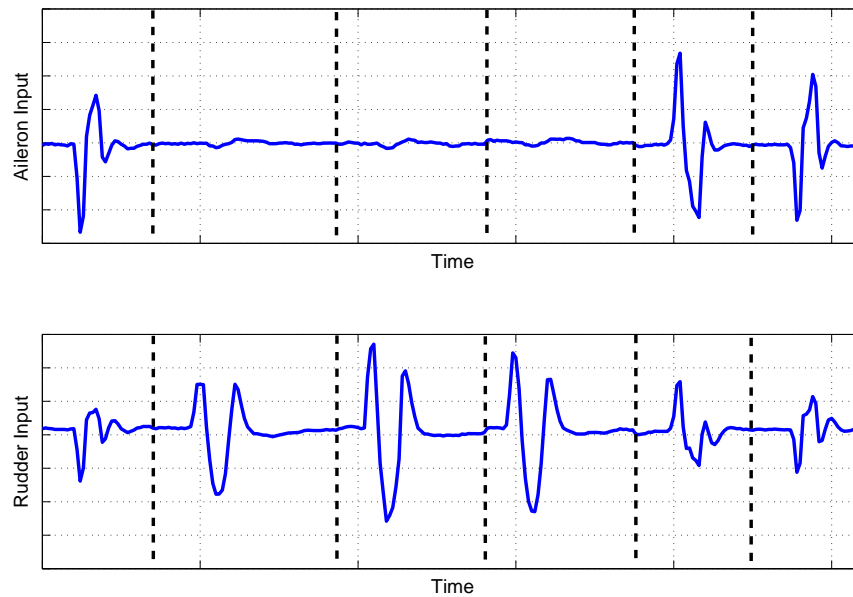
Figure 8.1: Time histories of aileron and rudder inputs

to be 160.94, as shown in the second column of the table. For the analysis presented here, parameters were considered to be significant if their partial F-statistic exceeded a value of $F_{in} = F_{out} = 20$. With the inclusion of C_{l_ξ} in the model, the values of $\hat{\sigma}$, PRESS and PSE all decreased in comparison to step 1 and R^2 increased to 38.23%. The values of r for the remaining candidate regressors were calculated and the next most significant term was found to be C_{l_p}.

Table 8.3 shows the results of adding the roll damping derivative to the model. Its F_0 value was found to be 310.90, while the same statistic for C_{l_ξ} increased to 663.64. Again, the inclusion of C_{l_p} led to decreases in the fit error, PRESS and PSE, while the coefficient of determination rose to 71.93%. Of the remaining terms, the yaw rate $\hat{r}$ was found to have the highest correlation to the as yet unmodelled effects in C_l, therefore C_{l_r} was the next derivative added to the model.

The results of step 4 of the analysis are displayed in Table 8.4. The new derivative C_{l_r} had a partial F-statistic of 74.754 and its addition to the model resulted in R^2 increasing to 78.24%. The other metrics $\hat{\sigma}$, PRESS and PSE also continued to decrease. The correlation values with the dependent variable for the two remaining candidate regressors, β and ζ, suggested that sideslip angle was the more significant term, hence it was included in the model next.

The addition of C_{l_β} to the model resulted in further reductions in the fit error, PRESS and PSE metrics and the coefficient of determination increased to 83.58%, as shown in Table 8.5. The value of F_0 for C_{l_β} was calculated to be 83.729 and the partial F-statistics for the other model parameters also increased with the addition of C_{l_β}.

In the sixth step of the process, the final candidate regressor ζ was added to the model and the results are displayed in Table 8.6. This time, the partial F-statistic of the new parameter C_{l_ζ} was found to be 5.414 - below the F_{in} value of 20. As well as this, the PSE value increased slightly from 2.3714×10^{-6} to 2.3769×10^{-6}. The addition of C_{l_ζ} to the model resulted in R^2 increasing to 83.92%, however this rise in comparison to the value in Table 8.5 was only 0.34%, which

fell below the guideline of a minimum increase of 0.5% in the coefficient of determination for a new regressor to be considered significant. On the other hand, the estimated fit error $\hat{\sigma}$ decreased, as did the PRESS metric. However, as explained above, for typical aircraft problems the value of PRESS can continue to decrease even when an insignificant regressor is added to the model. Taking all the metrics into account, as well as knowledge of aircraft dynamics and the principle of parsimony, it was decided that the derivative C_{l_ζ} should be removed from the model. The final rolling moment equation was then,

$$C_l = C_{l_\beta}\beta + C_{l_p}\hat{p} + C_{l_r}\hat{r} + C_{l_\xi}\xi \tag{8.4.1}$$

with least squares estimates of the derivatives given in the first column of Table 8.5. Note that the offset term C_{l_0} was again found to be negligibly small. The rolling moment coefficient derived from the data and response identified from the final model structure are shown in Figure 8.2.

	$\hat{\theta}$	F_0	r
C_{l_β}	-	-	0.0053
C_{l_p}	-	-	0.0000
C_{l_r}	-	-	0.0458
C_{l_ξ}	-	-	0.3823
C_{l_ζ}	-	-	0.1062
$\hat{\sigma}$		3.603×10^{-3}	
R^2		0.0%	
PRESS		3.415×10^{-3}	
PSE		1.299×10^{-5}	

Table 8.1: Stepwise regression results - step 1

	$\hat{\theta}$	F_0	r
C_{l_β}	-	-	0.0025
C_{l_p}	-	-	0.5455
C_{l_r}	-	-	0.0320
C_{l_ξ}	0.4345	160.94	-
C_{l_ζ}	-	-	0.0119
$\hat{\sigma}$		2.838×10^{-3}	
R^2		38.23%	
PRESS		2.174×10^{-3}	
PSE		8.089×10^{-6}	

Table 8.2: Stepwise regression results - step 2

	$\hat{\theta}$	F_0	r
C_{l_β}	-	-	0.1706
C_{l_p}	0.7469	310.90	-
C_{l_r}	-	-	0.2247
C_{l_ξ}	0.8215	663.64	-
C_{l_ζ}	-	-	0.0100
$\hat{\sigma}$		1.917×10^{-3}	
R^2		71.93%	
PRESS		9.963×10^{-4}	
PSE		3.780×10^{-6}	

Table 8.3: Stepwise regression results - step 3

	$\hat{\theta}$	F_0	r
C_{l_β}	-	-	0.2457
C_{l_p}	0.8071	450.76	-
C_{l_r}	1.9342	74.754	-
C_{l_ξ}	0.8305	871.04	-
C_{l_ζ}	-	-	0.0504
$\hat{\sigma}$		1.691×10^{-3}	
R^2		78.24%	
PRESS		7.775×10^{-4}	
PSE		3.014×10^{-6}	

Table 8.4: Stepwise regression results - step 4

The estimated fit error between the measured response and dependent variable predicted from the final model structure was calculated to be $\hat{\sigma} = 1.471 \times 10^{-3}$. As described previously, for a perfect model fit to the data, this value should match the square root of the variance of the random component of the measured dependent variable. Using Fourier smoothing to separate the deterministic and random components of C_l, the square root of the variance of the noise

	$\hat{\theta}$	F_0	r
C_{l_β}	1.3198	83.729	-
C_{l_p}	0.9440	676.07	-
C_{l_r}	2.0200	107.50	-
C_{l_ξ}	0.9105	1226.6	-
C_{l_ζ}	-	-	0.0207
$\hat{\sigma}$	1.471×10^{-3}		
R^2	83.58%		
PRESS	5.921×10^{-4}		
PSE	2.371×10^{-6}		

Table 8.5: Stepwise regression results - step 5

	$\hat{\theta}$	F_0	r
C_{l_β}	1.2506	73.114	-
C_{l_p}	0.9585	688.15	-
C_{l_r}	2.1083	114.68	-
C_{l_ξ}	0.9355	1119.3	-
C_{l_ζ}	0.3895	5.414	-
$\hat{\sigma}$	1.459×10^{-3}		
R^2	83.92%		
PRESS	5.827×10^{-4}		
PSE	2.377×10^{-6}		

Table 8.6: Stepwise regression results - step 6
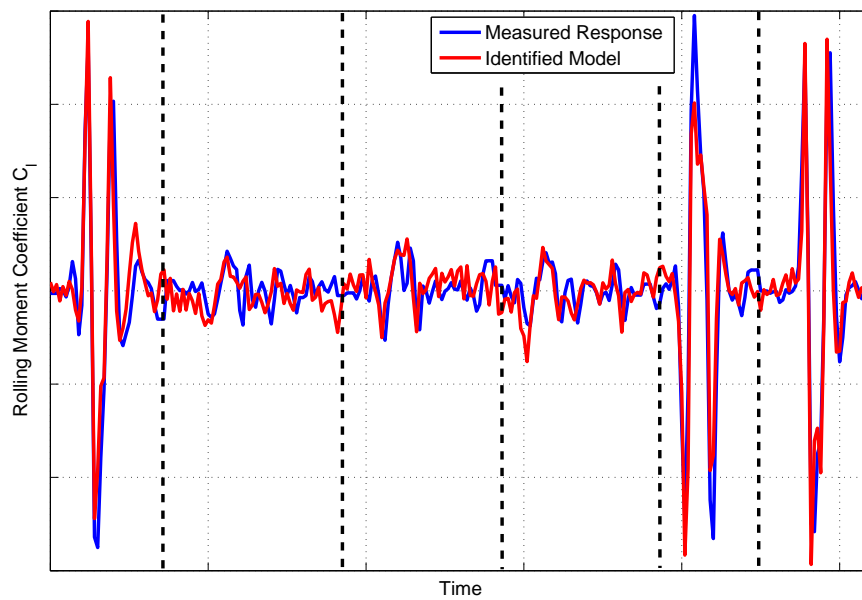
Figure 8.2: Comparison of measured and identified rolling moment time histories for final model structure

was estimated to be 1.990×10^{-4}. This is approximately an order of magnitude less than the estimated fit error obtained with the final model, indicating that the rolling moment residual may still contain a small deterministic component, most likely due to the unmodelled rudder contributions. A time history of the residual is shown in Figure 8.3, along with its associated power spectrum. The residual appears to be mostly random, however, for the segments corresponding to the rudder doublets, some deterministic content can be discerned. The power spectrum for the residual also shows some power concentrated at low frequencies, which corresponds to unmodelled rigid body dynamics. Despite these unmodelled dynamics, the final model structure can be considered a suitable representation of the aircraft roll dynamics, as indicated by the results of Theil's inequality analysis,

$$U = 0.2271, \ U_B = 0.0000, \ U_V = 0.0516, \ U_C = 0.9484$$
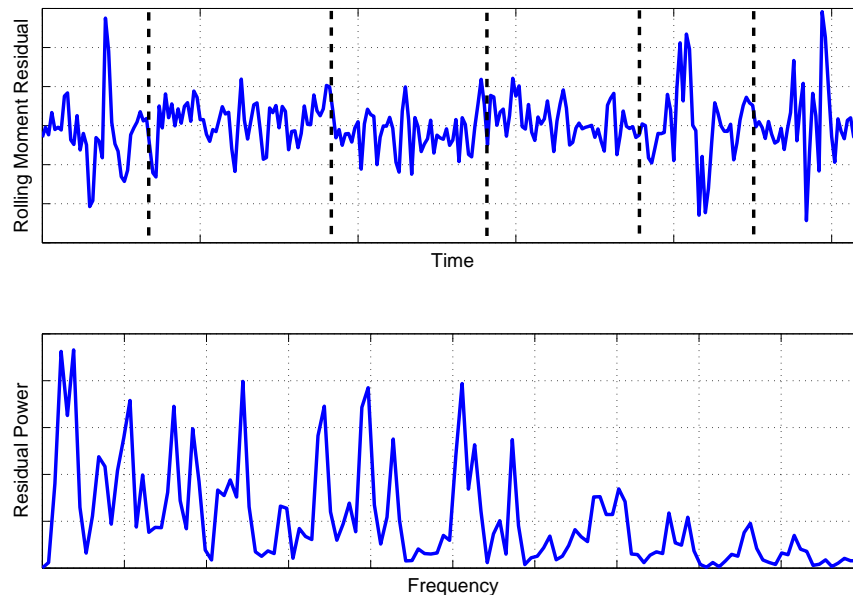
Figure 8.3: Time history of residual and corresponding
power spectrum

8.5 Hawk Short Period Example

Stepwise regression was also used to investigate the equations of motion for models tested in the dynamic wind tunnel facility. An example analysis of longitudinal data from the Hawk model is presented here and a lateral/directional example for the DEMON model is given in the section that follows. From theory, the longitudinal dynamics for a model restricted to 3 DoF motion can be expressed as,

$$\begin{bmatrix} \dot{w} \\ \dot{q} \end{bmatrix} = \begin{bmatrix} 0 & V_T \\ m_w & m_q \end{bmatrix} \begin{bmatrix} w \\ q \end{bmatrix} + \begin{bmatrix} 0 \\ m_\eta \end{bmatrix} \eta \tag{8.5.1}$$

The Hawk data contained a 1-1-2 input to the elevator and the candidate regressors for both the normal velocity and pitch equations were w, q and η. The time delay in the elevator input was found from inspection to be 0.27 sec and removed manually from the measurement.

The normal velocity equation was examined first and the results are shown in Tables 8.7 to 8.9. From the initial analysis, the regressor with the highest correlation with $\dot{w}$ was, by far, the pitch rate, therefore z_q was the first parameter added to the model. This resulted in an almost perfect fit to the measured data, with the coefficient of determination being 99.44%, and an estimate of z_q of 29.6915 (Table 8.8. When the next most significant regressor, normal velocity, was added to the model, Table 8.9 shows that the partial F-statistic of z_w was found to be well below the threshold F_{in}, which was again taken to be 20. As well as this, the increase in R^2 was negligible, while both the PRESS and PSE statistics increased. Therefore, z_w was dropped from the normal velocity equation, leaving only z_q in the equation. Note that, as described in Appendix A, for the 4 DoF equations of motion, the value of z_q corresponds to the wind tunnel speed V_T.

	$\hat{\theta}$	F_0	r
z_w	-	-	0.0000
z_q	-	-	0.9944
z_η	-	-	0.4838
$\hat{\sigma}$	7.2522		
R^2	0.0%		
PRESS	2.2563×10^4		
PSE	52.595		

Table 8.7: Stepwise regression results for the normal velocity equation - step 1

	$\hat{\theta}$	F_0	r
z_w	-	-	0.0026
z_q	28.6915	7.6163×10^4	-
z_η	-	-	0.0008
$\hat{\sigma}$	0.5415		
R^2	99.44%		
PRESS	126.51		
PSE	0.5376		

Table 8.8: Stepwise regression results for the normal velocity equation - step 2

	$\hat{\theta}$	F_0	r
z_w	0.0250	1.1247	-
z_q	28.6915	7.6185×10^4	-
z_η	-	-	0.0003
$\hat{\sigma}$	0.5414		
R^2	99.45%		
PRESS	127.37		
PSE	0.6597		

Table 8.9: Stepwise regression results for the normal velocity equation - step 3

Next, the pitching moment equation was analysed, with the results given in Tables 8.10 to 8.13. The first parameter added to the model was m_w. This was followed by m_η and then m_q. In each case, the inclusion of the new regressor in the model structure resulted in significant increases in the coefficient of determination and reductions in PRESS and PSE. The final value of R^2 was 93.37%, indicating a close match to the measured data, and the F_0 values for each term were comfortably above the F_{in} threshold.

The analysis of the Hawk data, therefore, indicated that the model structure determined from the experimental data matched that derived from theory. The response identified from the final

	$\hat{\theta}$	F_0	r
m_w	-	-	0.7180
m_q	-	-	0.0000
m_η	-	-	0.0415
$\hat{\sigma}$		1.9333	
R^2		0.0%	
PRESS		1603.5	
PSE		3.7378	

Table 8.10: Stepwise regression results for the pitch equation - step 1

	$\hat{\theta}$	F_0	r
m_w	-1.4761	1.0847×10^3	-
m_q	-	-	0.0002
m_η	-	-	0.3732
$\hat{\sigma}$		1.0279	
R^2		71.80%	
PRESS		455.26	
PSE		1.0690	

Table 8.11: Stepwise regression results for the pitch equation - step 2

	$\hat{\theta}$	F_0	r
m_w	-1.5553	1879.8	-
m_q	-	-	0.6249
m_η	-0.9358	253.07	-
$\hat{\sigma}$		0.8147	
R^2		82.33%	
PRESS		286.76	
PSE		0.6853	

Table 8.12: Stepwise regression results for the pitch equation - step 3

	$\hat{\theta}$	F_0	r
m_w	-1.6428	5456.5	-
m_q	-3.5897	706.50	-
m_η	-1.8861	1379.3	-
$\hat{\sigma}$		0.4995	
R^2		93.37%	
PRESS		109.12	
PSE		0.2813	

Table 8.13: Stepwise regression results for the pitch equation - step 4

model structure is shown in Figure 8.4 along with the measured data.

8.6 DEMON Dutch Roll Example

In the second wind tunnel example, the model structure for the DEMON due to a rudder input was investigated using data containing a doublet input. For this case, the theoretical equations of motion were,

$$\begin{bmatrix} \dot{v} \\ \dot{r} \end{bmatrix} = \begin{bmatrix} 0 & -V_T \\ n_v & n_r \end{bmatrix} \begin{bmatrix} v \\ r \end{bmatrix} + \begin{bmatrix} 0 \\ n_\zeta \end{bmatrix} \zeta \tag{8.6.1}$$

However, during the experiments, the model experienced some rolling motion when the rudder input was applied. Hence, as well as v, r and ζ, roll rate p was also included in the group of candidate regressors. As for the longitudinal example, the input time delay was removed manually from the data prior to the analysis.

Concentrating first on the sideslip velocity equation, the stepwise regression results are displayed in Tables 8.14 to 8.16. To start with, yaw rate r was found to be the regressor most significantly correlated with $\dot{v}$, hence was the first term added to the model. When this was done, a very close match to the measured data was achieved, with the coefficient of determination rising to 99.86%. The next most significant regressor was the rudder input so y_ζ was also added to the model. However, the increase in R^2 as a result was only 0.03%. There was also a rise in the PSE statistic. The partial F-statistic of y_ζ did exceed the F_{in} threshold of 20
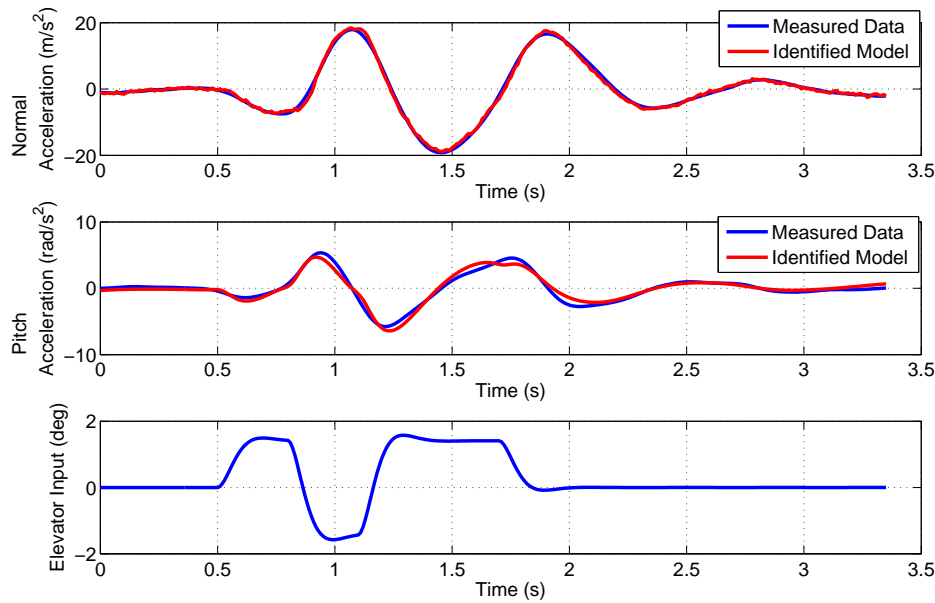
Figure 8.4: Measured and identified Hawk responses for a
1-1-2 input to the elevator - final model structure

(79.974 from Table 8.16) but was significantly smaller than the F_0 figure for y_r. Therefore, y_ζ was removed from the equations of motion.

	$\hat{\theta}$	F_0	r
y_v	-	-	0.0000
y_p	-	-	0.0854
y_r	-	-	0.9986
y_ζ	-	-	0.3272
$\hat{\sigma}$		10.3625	
R^2		0.0%	
PRESS		3.7584×10^4	
PSE		107.38	

Table 8.14: Stepwise regression results
for sideslip velocity equation - step 1

	$\hat{\theta}$	F_0	r
y_v	-	-	0.0000
y_p	-	-	0.1372
y_r	-29.0526	2.5248×10^5	-
y_ζ	-	-	0.1877
$\hat{\sigma}$		0.3845	
R^2		99.86%	
PRESS		52.343	
PSE		0.7623	

Table 8.15: Stepwise regression results
for sideslip velocity equation - step 2

Tables 8.17 to 8.21 present the results from the analysis of the yawing moment equation. The regressor with the highest correlation to yaw acceleration $\dot{r}$ was the sideslip velocity v, therefore n_v was the first derivative added to the model. The next term included was n_ζ and this was followed by n_r, leaving roll rate p as the only remaining candidate regressor. When n_p was added to the model, the improvement in the coefficient of determination was marginal, with R^2 increasing by 0.83%. However, this is greater than the 0.5% guideline suggested in Section 8.3. Also, the partial F-statistic for n_p was greater than F_{in} and its inclusion in the model structure led to decreases in PRESS and PSE. Therefore, it was a borderline decision as to whether n_p should be included in the equations of motion. Figure 8.5 displays the measured time history of $\dot{r}$ plotted against those from the identified model with and without n_p in the model structure. As can be seen, the inclusion of the derivative makes little difference to the reconstructed response

	$\hat{\theta}$	F_0	r
y_v	-	-	0.0004
y_p	-	-	0.0399
y_r	-28.7380	2.0847×10^5	-
y_ζ	0.6465	79.974	-
$\hat{\sigma}$		0.3470	
R^2		99.89%	
PRESS		42.810	
PSE		1.0424	

Table 8.16: Stepwise regression results for normal velocity
equation - step 3

so, using the principle of parsimony, it was felt that the most appropriate model structure was one without n_p and, as with the longitudinal example, the model form found from experiment matched the theoretical model structure. Figure 8.6 shows the identified response from the final model structure plotted against the measured data.

	$\hat{\theta}$	F_0	r
n_v	-	-	0.8477
n_p	-	-	0.2840
n_r	-	-	0.0000
n_ζ	-	-	0.0545
$\hat{\sigma}$		4.0250	
R^2		0.0%	
PRESS		5670.4	
PSE		16.201	

Table 8.17: Stepwise regression results for yawing moment equation - step 1

	$\hat{\theta}$	F_0	r
n_v	3.7214	1931.9	-
n_p	-	-	0.1149
n_r	-	-	0.0000
n_ζ	-	-	0.4636
$\hat{\sigma}$		1.5729	
R^2		84.77%	
PRESS		869.87	
PSE		2.5526	

Table 8.18: Stepwise regression results for yawing moment equation - step 2

8.7   Maximum Likelihood Model Structure Determination

As mentioned previously, regression analysis is limited to cases in which the equations of motion are linear in the unknown parameters. Therefore, it is convenient to have a method of model structure determination which can be applied to general, nonlinear cases. Such an approach, advocated by Tischler [6], is outlined here.

The most appropriate model structure is found based on three metrics derived from the Cramer-Rao bound. The first is the standard errors of the parameter estimates $s(\hat{\theta})$. As described in Section 5.8, these are calculated as the square root of the diagonal elements of the covariance matrix $\mathbf{P}$, which approximates the inverse of the Fisher information matrix $\mathbf{M}$,

$$s(\hat{\theta}_j) = \sqrt{\mathbf{P}_{jj}} \approx \sqrt{(\mathbf{M}^{-1})_{jj}}, \;\; j = 1, 2, \ldots, n_\theta \tag{8.7.1}$$

	$\hat{\theta}$	F_0	r
n_v	3.7589	3659.4	-
n_p	-	-	0.0495
n_r	-	-	0.3949
n_ζ	-3.4481	299.01	-
$\hat{\sigma}$		1.1537	
R^2		91.83%	
PRESS		476.81	
PSE		1.4588	

Table 8.19: Stepwise regression results for yawing moment equation - step 3

	$\hat{\theta}$	F_0	r
n_v	3.7762	6082.3	-
n_p	-	-	0.1682
n_r	-2.4468	225.15	-
n_ζ	-5.0213	717.87	-
$\hat{\sigma}$		0.8987	
R^2		95.06%	
PRESS		290.33	
PSE		0.9841	

Table 8.20: Stepwise regression results for yawing moment equation - step 4

	$\hat{\theta}$	F_0	r
n_v	3.2809	1963.0	-
n_p	1.9669	69.551	-
n_r	-3.7023	305.64	-
n_ζ	-6.2952	752.95	-
$\hat{\sigma}$		0.8209	
R^2		95.89%	
PRESS		240.96	
PSE		0.8963	

Table 8.21: Stepwise regression results for yawing moment equation - step 5
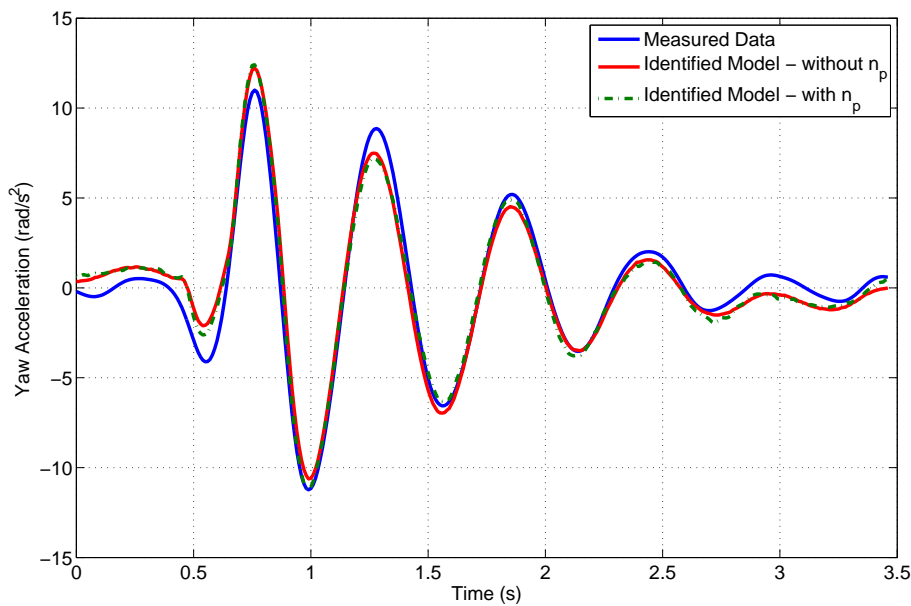
Figure 8.5: Comparison of identified DEMON yaw responses with and without n_p in model structure
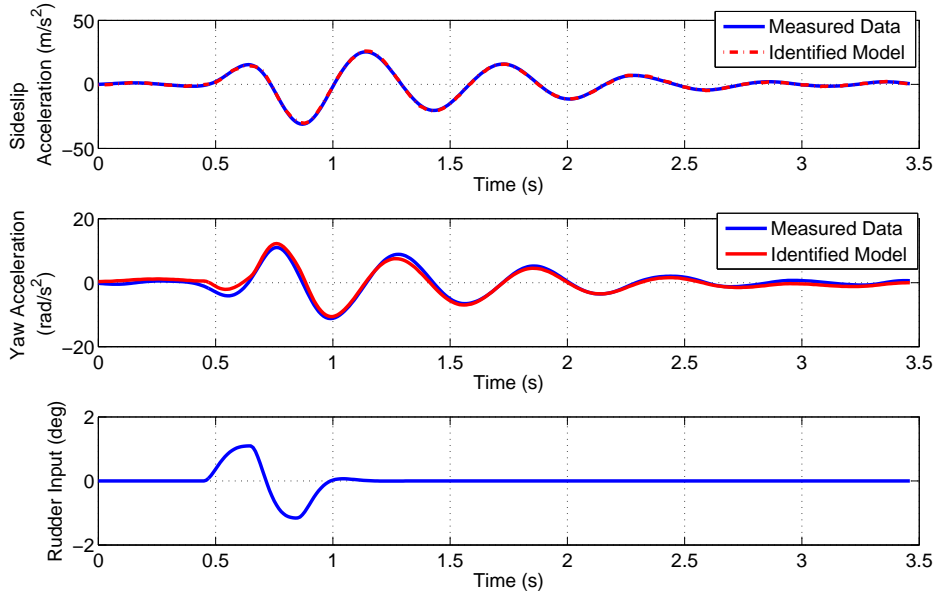
Figure 8.6: Measured and identified DEMON responses
for a doublet input to the rudder - final model structure

The second statistic is parameter insensitivity, which for the jth parameter is given by,

$$\mathbf{I}_j = \frac{1}{\sqrt{\mathbf{M}_{jj}}} \tag{8.7.2}$$

The insensitivity is a measure of how much a parameter value can be changed without causing an increase in cost function. It therefore provides a measure of the significance of each parameter. At first glance, it may appear from Equations (8.7.1) and (8.7.2) that the standard error and insensitivity are the same. However, there is a subtle difference between the two. The insensitivity is approximately the conditional standard deviation of the parameter estimate, given that all other parameters are known i.e. have fixed values. The standard error is an approximation of the unconditional standard deviation [132].

The third metric is correlation between the parameters. The pair-wise correlation has been calculated previously using the parameter covariance matrix $\mathbf{P}$ as,

$$\rho_{ij} = \frac{\mathbf{P}_{ij}}{\sqrt{\mathbf{P}_{ii}\mathbf{P}_{jj}}}, \quad i, j = 1, 2, \ldots, n_\theta \tag{8.7.3}$$

However, it has already been noted that the pair-wise coefficients only indicate correlation between two parameters and are unable to account for correlation between three or more terms. A method of detecting correlation between multiple parameters is the uncertainty or confidence ellipsoid [6, 132]. For the jth parameter, this can be expressed as [6],

$$\bar{\mathbf{\Theta}}_j = \frac{\mathbf{T}^{-1}\mathbf{M}_j^{-1}}{s(\hat{\theta}_j)} \tag{8.7.4}$$

where $\mathbf{T}$ is a diagonal matrix containing the insensitivities from Equation (8.7.2) and $\mathbf{M}_j^{-1}$ denotes the jth column of the inverse of the information matrix. For each of the parameters,

$\bar{\Theta}$ is a vector of length n_θ, the elements of which are usually scaled to unity. For $\bar{\Theta}_j$, the jth element is equal to 1 and correlation is indicated if any of the remaining elements are large ($>$ 0.6) in comparison to the jth element [6].

The model structure determination procedure based on the above statistics is described as follows. The standard errors and insensitivities are both assigned given thresholds. The aim of the process is to obtain a set of equations for which all the derivatives meet these limits and therefore have roughly the same degree of confidence. Initially, parameter estimation is carried out with all possible parameters included in the model structure, in a similar manner to the backward elimination approach described in Section 8.2. The insensitivities are checked against the threshold and the derivative with the highest insensitivity exceeding the limit is removed from the analysis i.e. it is held fixed at zero or another appropriate *a priori* value. Parameter estimation is then repeated and this process continues until all derivatives remaining in the model structure have insensitivities within the threshold. At this stage, it may be that all derivatives have acceptable insensitivities but the standard errors of some parameters are large. This is most likely due to correlation between parameters, so the correlation coefficients or confidence ellipsoid for the parameter with the largest standard error are analysed. If correlation between parameters is indicated then the choice of which parameter to drop must be made. This decision can be a difficult one and it may be useful to rely on an understanding of the physics of the aircraft to choose which term to remove.

Suggested guidelines for satisfactory parameter estimates are [6],

$$\frac{s(\hat{\theta}_j)}{|\hat{\theta}_j|} \times 100 \le 20\% \text{ and } \frac{\mathbf{I}_j}{|\hat{\theta}_j|} \times 100 \le 10\% \tag{8.7.5}$$

However, it should be noted that these thresholds are suggested for the case where the cost function is expressed in terms of frequency response curves (see Equation (6.5.16)). The difference in the formulation of the cost function for the frequency response case and that for other parameter estimation methods means that the definition of the information matrix also differs. Therefore, the thresholds in Equation (8.7.5) may not be reliable guidelines for all estimation techniques. However, the standard errors, insensitivities, pair-wise correlation and confidence ellipsoid make no assumptions about which estimation method is used, so an investigation into using the above approach with maximum likelihood estimation was attempted. Some example results, using the same three test cases outlined for stepwise regression, are presented next.

8.8 UAV Rolling Moment Example

The first example is based on the UAV rolling moment data used to demonstrate stepwise regression in Section 8.4. The initial equation for the rolling moment was,

$$C_l = C_{l_\beta}\beta + C_{l_p}\hat{p} + C_{l_r}\hat{r} + C_{l_\xi}\xi + C_{l_\zeta}\zeta + C_{l_0} \tag{8.8.1}$$

and the time domain, modified Newton-Raphson algorithm was used to estimate the aerodynamic derivatives at each step of the analysis. The initial results are given in Table 8.22, which shows the estimated derivative values, the standard errors (corrected for coloured residuals) and the insensitivities. Of the six parameters, the offset term C_{l_0} had by far the largest insensitivity at 140.21% so was removed from the model structure. Parameter estimation was repeated and

the results are displayed in Table 8.23. This time, C_{l_ζ} was found to have the highest insensitivity at 22.69% so this parameter was also removed from the model. On the third run, the standard errors were all found to be below 20% and all insensitivities were under 10%. Therefore, the procedure was halted. The final model structure matched that found from the stepwise regression analysis in Section 8.4 so, for this particular example, the respective thresholds for the standard errors and insensitivities worked well in determining the appropriate model structure. Figure 8.7 shows plots of the rolling moment coefficient and roll rate along with the responses predicted using the parameter estimates in Table 8.24.

	$\hat{\theta}$	$100[s/|\hat{\theta}|]$	$100[\mathbf{I}/|\hat{\theta}|]$
C_{l_β}	1.6444	12.40	6.02
C_{l_p}	1.2200	6.05	1.70
C_{l_r}	1.9693	8.41	6.69
C_{l_ξ}	1.0605	4.65	1.33
C_{l_ζ}	0.5640	36.00	21.94
C_{l_0}	1.2100	212.71	140.21

Table 8.22: Results for rolling moment equation - step 1

	$\hat{\theta}$	$100[s/|\hat{\theta}|]$	$100[\mathbf{I}/|\hat{\theta}|]$
C_{l_β}	1.6874	7.52	5.87
C_{l_p}	1.2211	6.00	1.69
C_{l_r}	1.9620	8.52	6.72
C_{l_ξ}	1.0600	4.68	1.34
C_{l_ζ}	0.5465	35.28	22.69
C_{l_0}	0	-	-

Table 8.23: Results for rolling moment equation - step 2

	$\hat{\theta}$	$100[s/|\hat{\theta}|]$	$100[\mathbf{I}/|\hat{\theta}|]$
C_{l_β}	1.7470	8.58	5.67
C_{l_p}	1.2013	5.88	1.72
C_{l_r}	1.8740	9.61	7.04
C_{l_ξ}	1.0275	4.50	1.38
C_{l_ζ}	0	-	-
C_{l_0}	0	-	-

Table 8.24: Results for rolling moment equation - step 3

8.9 Hawk Short Period Example

The maximum likelihood model structure determination process was also applied to the Hawk 1-1-2 elevator input data used in Section 8.5. The starting model structure for the process was equivalent to a short period model for a free-flying aircraft,

$$\begin{bmatrix} \dot{w} \\ \dot{q} \end{bmatrix} = \begin{bmatrix} z_w & z_q \\ m_w & m_q \end{bmatrix} \begin{bmatrix} w \\ q \end{bmatrix} + \begin{bmatrix} z_\eta \\ m_\eta \end{bmatrix} \eta \tag{8.9.1}$$

Again, the time domain modified Newton-Raphson algorithm was used to estimate the derivatives and the results of the analysis are presented in Tables 8.25 to 8.27. On the first run, z_η was found to have the highest insensitivity of 14.70%, so was held fixed at zero for the remaining steps. The next parameter to be removed from the model was z_w, whose insensitivity jumped to 44.10% on the second run of the algorithm. At the third step, all derivatives had standard errors below 20% and insensitivities under 10% so the process was stopped. Again, the final model structure matched that found from stepwise regression in Section 8.5. Also, the 20% standard
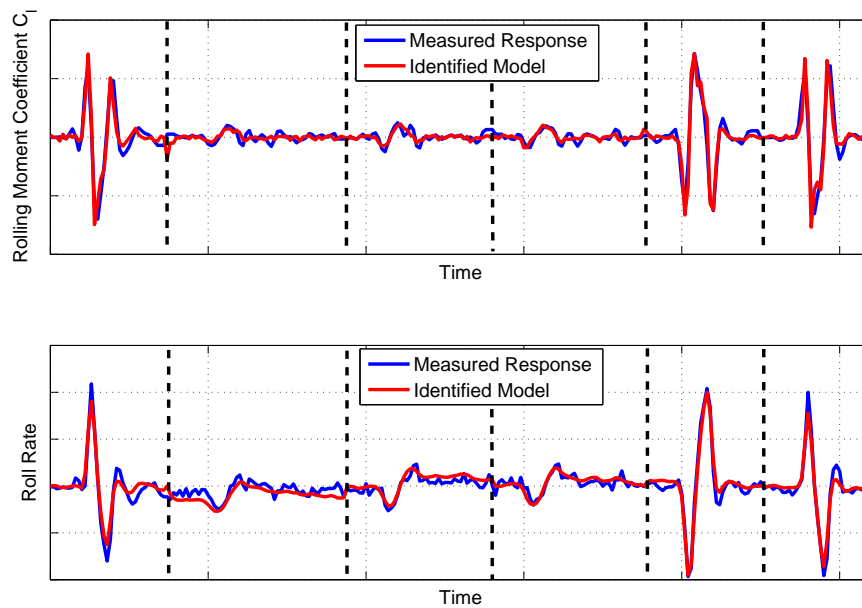
Figure 8.7: Comparison of measured and identified roll
responses for final model structure

error and 10% insensitivity guidelines appeared to be reliable metrics for finding the final form of the equations of motion. The measured and identified response for the final model are shown in Figure 8.8.

	$\hat{\theta}$	$100[s/|\hat{\theta}|]$	$100[\mathbf{I}/|\hat{\theta}|]$
z_w	0.2370	85.82	10.95
z_q	29.9630	3.72	0.38
z_η	0.3404	88.06	14.70
m_w	-1.7079	4.03	0.39
m_q	4.0020	7.08	0.73
m_η	-2.0453	4.54	0.63

Table 8.25: Results for Hawk
longitudinal dynamics - step 1

	$\hat{\theta}$	$100[s/|\hat{\theta}|]$	$100[\mathbf{I}/|\hat{\theta}|]$
z_w	0.0591	438.43	44.10
z_q	29.1787	3.69	0.40
z_η	0	-	-
m_w	-1.7065	4.04	0.40
m_q	3.8161	8.48	0.78
m_η	-2.0397	4.65	0.64

Table 8.26: Results for Hawk
longitudinal dynamics - step 2

8.10 DEMON Dutch Roll Example

The third example utilises the DEMON rudder doublet data, used previously in Section 8.6. The modified Newton-Raphson algorithm was again used but, this time, estimation was performed in the frequency domain using the equation error formulation. The time delay in the rudder input was also treated as an additional unknown parameter to be determined. The initial model structure was assumed to be,

$$\begin{bmatrix} \dot{v}(t) \\ \dot{r}(t) \end{bmatrix} = \begin{bmatrix} y_v & y_r \\ n_v & n_r \end{bmatrix} \begin{bmatrix} v(t) \\ r(t) \end{bmatrix} + \begin{bmatrix} y_p & y_\zeta \\ n_p & n_\zeta \end{bmatrix} \begin{bmatrix} p(t) \\ \zeta(t - \tau_\zeta) \end{bmatrix} \qquad (8.10.1)$$

	$\hat{\theta}$	$100[s/|\hat{\theta}|]$	$100[\mathbf{I}/|\hat{\theta}|]$
z_w	0	-	-
z_q	29.2019	3.67	0.39
z_η	0	-	-
m_w	-1.7018	3.94	0.40
m_q	3.7581	4.83	0.79
m_η	-2.0407	4.51	0.64

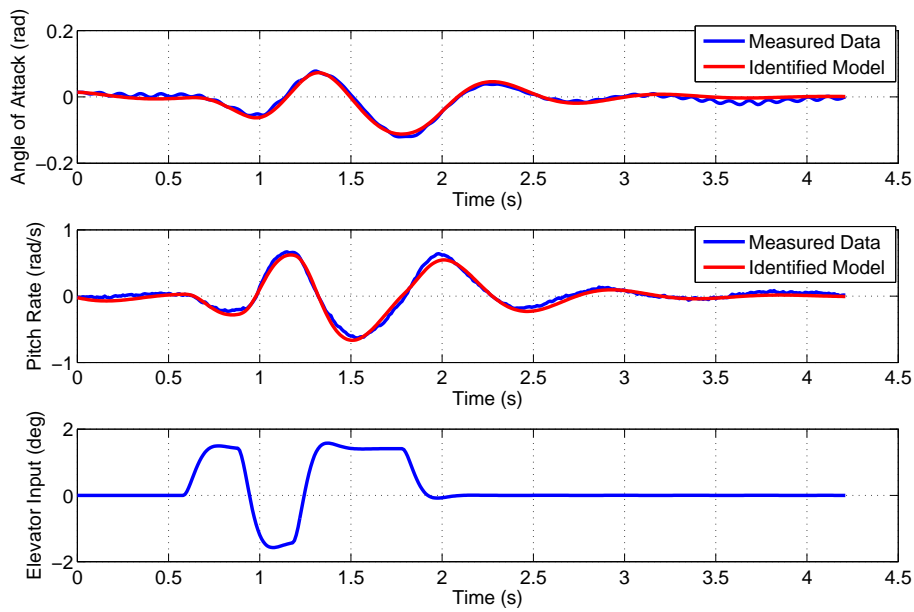**Table 8.27:** Results for Hawk
longitudinal dynamics - step 3

Figure 8.8: Comparison of measured and identified Hawk
longitudinal response for final model structure

Note that the roll rate p has been included in Equation (8.10.1) not as a state variable but as, what is termed, a pseudo-control input [34]. This approach allows the effects of additional motion variables to be incorporated into the equations of motion without increasing the model complexity. For this example, the intention of the experiment was to simply excite the DEMON's dutch roll dynamics, in which rolling motion is largely assumed to be negligible. However, because the DEMON experienced some rolling motion when the rudder input was applied, the effects of p can be investigated without incorporating an additional state equation for roll.

The results of the first parameter estimation step are displayed in Table 8.28. The control derivative y_ζ was found to have the highest insensitivity at 21.62% so was the first parameter removed from the model. When the estimation process was repeated, all the parameters were found to have insensitivities below the 10% guideline, as shown in Table 8.30. However y_v, y_p, n_p and n_r had standard errors greater than 20%. The derivative with the lowest confidence was n_p, which had a standard error of 76.88%, therefore the correlation coefficients and confidence ellipsoid for this parameter were analysed. These are shown in the left and right hand columns of Table 8.30 respectively. None of the correlation coefficients exceeded 0.9 but the values of ρ were still relatively high (≈ 0.8) between n_p and the other yawing moment derivatives n_v, n_r and n_ζ. The elements of the confidence ellipsoid also suggested that some correlation existed between n_p and other parameters, particularly n_r and n_v, for which the absolute values of Θ were greater than 0.6. A choice then had to be made regarding which derivative to remove from the model. Based on knowledge of the model dynamics, it would be expected that, for a rudder input, the derivatives n_v, n_r and n_ζ would be more significant than the cross-coupling term n_p, hence n_p was dropped from the model structure.

	$\hat{\theta}$	$100[s/|\hat{\theta}|]$	$100[\mathbf{I}/|\hat{\theta}|]$
y_v	-0.1775	69.12	8.13
y_p	0.6833	59.01	5.62
y_r	-29.2864	1.15	0.13
y_ζ	0.2117	170.34	21.62
n_v	3.6444	7.66	0.90
n_p	1.2484	79.76	6.99
n_r	-3.2726	26.48	2.73
n_ζ	-5.8163	15.50	1.79
τ_ζ	0.2820	1.28	0.48

Table 8.28: Results for DEMON yaw dynamics - step 1

	$\hat{\theta}$	$100[s/|\hat{\theta}|]$	$100[\mathbf{I}/|\hat{\theta}|]$
y_v	-0.2453	38.67	5.96
y_p	0.9495	28.13	4.10
y_r	-29.4711	0.64	0.14
y_ζ	0	-	-
n_v	3.6359	7.49	0.90
n_p	1.2628	76.88	6.91
n_r	-3.2624	25.80	2.74
n_ζ	-5.8058	14.74	1.79
τ_ζ	0.2814	2.66	0.50

Table 8.29: Results for DEMON yaw dynamics - step 2

Table 8.31 gives the results from step 3 of the process. Again, all parameters had sensitivities below the 10% threshold but the standard errors for y_v, y_p and n_r remained greater than 20%. The derivative with the largest standard error was y_v so the correlation between this parameter and the other derivatives was examined, with the correlation coefficients and confidence ellipsoid elements given in Table 8.32. Both metrics indicated that some correlation existed between y_v and y_p and it was decided that y_v would be removed from the equations of motion. When this was carried out, the next run of the parameter estimation algorithm (Table 8.33) revealed y_p to have an insensitivity of 11.95%, therefore this parameter was also dropped from the model.

When y_p was removed from the equations of motion and parameter estimation was repeated, all

	ρ	Θ
y_v	0.1509	-0.0880
y_p	0.2019	0.1246
y_r	0.0943	-0.0407
n_v	0.8099	-0.6040
n_p	1.0000	1.0000
n_r	0.8237	-0.6979
n_ζ	0.7823	-0.5789
τ_ζ	0.4223	0.2017

Table 8.30: Correlation between n_p and other parameters

	$\hat{\theta}$	$100[s/|\hat{\theta}|]$	$100[\mathbf{I}/|\hat{\theta}|]$
y_v	-0.2151	43.83	6.93
y_p	0.8313	31.72	4.77
y_r	-29.4372	0.64	0.14
y_ζ	0	-	-
n_v	3.9179	4.21	0.89
n_p	0	-	-
n_r	-2.3718	20.87	3.98
n_ζ	-4.9724	11.07	2.21
τ_ζ	0.2762	3.03	0.63

Table 8.31: Results for DEMON yaw dynamics - step 3

	ρ	Θ
y_v	1.0000	1.0000
y_p	0.7528	-0.7916
y_r	0.3487	0.2591
n_v	0.1761	0.1324
n_r	0.1318	-0.1093
n_ζ	0.1638	-0.1296
τ_ζ	0.0457	0.0348

Table 8.32: Correlation between y_v and other parameters

	$\hat{\theta}$	$100[s/|\hat{\theta}|]$	$100[\mathbf{I}/|\hat{\theta}|]$
y_v	0	-	-
y_p	0.3740	55.01	11.95
y_r	-29.2826	0.67	0.16
y_ζ	0	-	-
n_v	4.0080	3.98	0.83
n_p	0	-	-
n_r	-2.5206	19.98	3.61
n_ζ	-5.2338	11.07	2.03
τ_ζ	0.2781	1.78	0.57

Table 8.33: Results for DEMON yaw dynamics - step 4

insensitivities and standard errors fell within the thresholds, as shown in Table 8.34. Therefore, the process was halted at this point. Figure 8.9 compares the identified response from the final model with the measured data in the frequency domain, while Figure 8.10 shows the match between the measured and identified responses for sideslip angle and yaw rate transformed back into the time domain. As with the previous two examples, the final model structure matched that determined using stepwise regression, further indicating that the standard error and insensitivity thresholds of 20% and 10% are reliable, not just for the frequency response method but also for maximum likelihood approach as well.

	$\hat{\theta}$	$100[s/|\hat{\theta}|]$	$100[\mathbf{I}/|\hat{\theta}|]$
y_v	0	-	-
y_p	0	-	-
y_r	-29.1316	0.78	0.17
y_ζ	0	-	-
n_v	3.9808	3.92	0.82
n_p	0	-	-
n_r	-2.6302	18.89	3.37
n_ζ	-5.3959	9.53	1.91
τ_ζ	0.2835	2.55	0.53

Table 8.34: Results for DEMON yaw dynamics - step 4
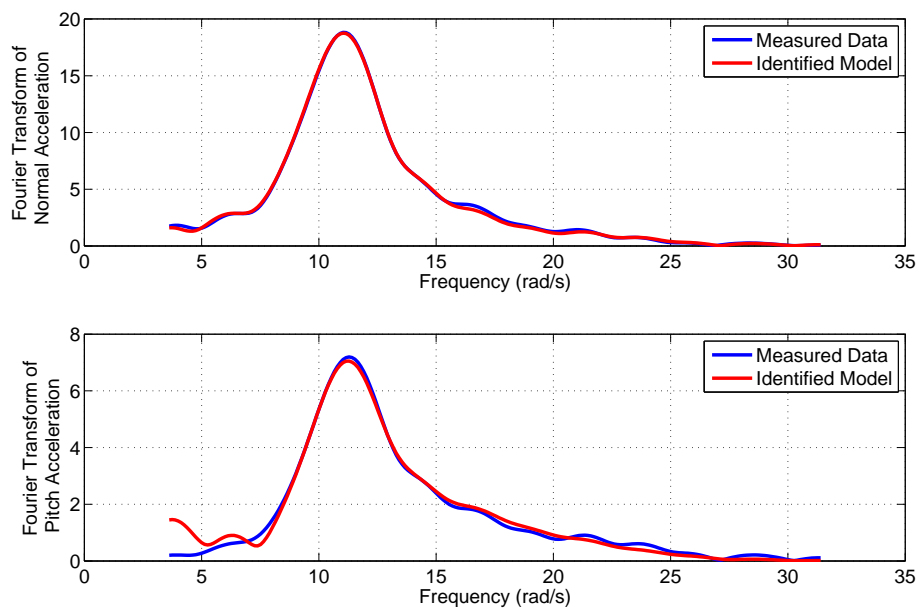

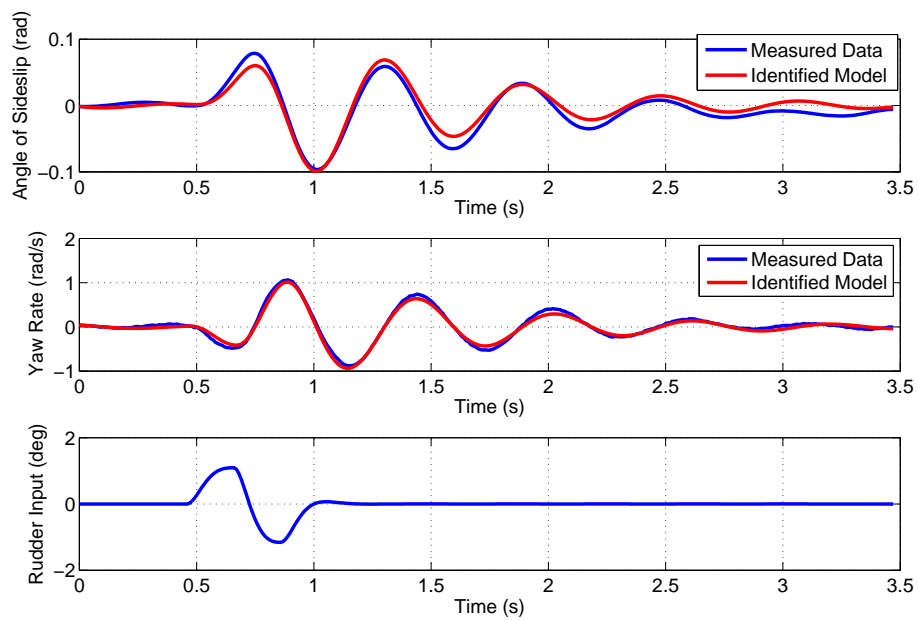**Figure 8.9:** Comparison of measured and identified yaw responses in the frequency domain

Figure 8.10: Measured and identified time histories for
angle of sideslip angle and yaw rate

Chapter 9

Data Compatibility Check

9.1 Introduction

This chapter returns to the data compatibility check, or flight path reconstruction, performed prior to parameter estimation and model structure determination. The aim of the process is to verify the accuracy and consistency of the data before it is used in the later stages of the analysis. This includes inspection of the measurements to remove obvious errors, such as dropouts in the signals or variables measured with the incorrect signs. The data is then checked for kinematic consistency. The time histories of certain motion variables can be reconstructed analytically using information from other variables and compared against the measured values. Another function of the data compatibility check is to generate data for aircraft states that are typically not measured directly during flight tests but are often required for parameter estimation, such as velocity components u, v and w. The kinematic relationships which facilitate the data compatibility check are outlined next.

9.2 Kinematic Relationships

The kinematic relationships can be expressed as a set of nine differential equations grouped into three categories: translational, rotational and position equations. To start with, from the translational equations of motion, the following differential equations for the velocity components u, v and w are obtained,

$$\dot{u} = -qw + rv - g\sin\theta + a_x \tag{9.2.1}$$
$$\dot{v} = -ru + pw + g\cos\theta\sin\phi + a_y \tag{9.2.2}$$
$$\dot{w} = -pv + qu + g\cos\theta\cos\phi + a_z \tag{9.2.3}$$

Next, the rotational equations define the relationship between the attitude angles and the angular rates. These were given previously in Section 3.3 and repeated here,

$$\dot{\phi} = p + q\sin\phi\tan\theta + r\cos\phi\tan\theta \tag{9.2.4}$$
$$\dot{\theta} = q\cos\phi - r\sin\phi \tag{9.2.5}$$
$$\dot{\psi} = q\sin\phi\sec\theta + r\cos\phi\sec\theta \tag{9.2.6}$$

Thirdly, the aircraft's position relative to the earth can be found from,

$$
\begin{aligned}
\dot{x}_E =\,& u \cos \psi \cos \theta + v(\cos \psi \sin \theta \sin \phi - \sin \psi \cos \phi) \\
& + w(\cos \psi \sin \theta \cos \phi + \sin \psi \sin \phi) \quad (9.2.7) \\
\dot{y}_E =\,& u \sin \psi \cos \theta + v(\sin \psi \sin \theta \sin \phi + \cos \psi \cos \phi) \\
& + w(\sin \psi \sin \theta \cos \phi - \cos \psi \sin \phi) \quad (9.2.8) \\
\dot{h} =\,& u \sin \theta - v \cos \theta \sin \phi - w \cos \theta \cos \phi \quad (9.2.9)
\end{aligned}
$$

where x_E and y_E are geodetic coordinates of the aircraft relative to some Earth-fixed origin and h is the vehicle's altitude.

Another useful set of equations for the data compatibility check are the air data relationships,

$$
\begin{aligned}
V &= \sqrt{u^2 + v^2 + w^2} & (9.2.10) \\
\alpha &= \tan^{-1}\left(\frac{w}{u}\right) & (9.2.11) \\
\beta &= \sin^{-1}\left(\frac{v}{V}\right) & (9.2.12) \\
& & (9.2.13)
\end{aligned}
$$

where V is the aircraft's true airspeed. Equations (9.2.1) to (9.2.9) assume that the aircraft is a rigid body and that the earth is flat and non-rotating, which is a valid approximation for typically short data segments. It is also assumed that the values of the motion variables are those that would be measured at the aircraft's centre of gravity (CG). However, it is not always practical to mount instrumentation at this point in the aircraft. This is particularly true for small UAVs in which space within the airframe is limited, therefore restricting the choice of where the sensors are housed. Hence, the measured values of the motion variables must be transformed from a reference frame defined by the sensor measurement axes to a reference frame with origin fixed at the CG. For example, the accelerations at the CG are obtained from the measured values as follows,

$$
\begin{aligned}
a_x^{cg} &= a_x^{m} + x_{acc}(q^2 + r^2) - y_{acc}(pq - \dot{r}) - z_{acc}(pr + \dot{q}) & (9.2.14) \\
a_y^{cg} &= a_y^{m} - x_{acc}(pq + \dot{r}) + y_{acc}(p^2 + r^2) - z_{acc}(qr - \dot{p}) & (9.2.15) \\
a_z^{cg} &= a_z^{m} - x_{acc}(pr + \dot{q}) - y_{acc}(qr + \dot{p}) + z_{acc}(p^2 + q^2) & (9.2.16)
\end{aligned}
$$

where superscript m denotes the acceleration values measured at the sensor location, while x_{acc}, y_{acc} and z_{acc} are the coordinates of the accelerometers relative to the CG. The air data will also be measured at a position away from the CG (see Section 3.4), where the local velocity components will be different from u, v and w. The relationship between the velocity components at each location is given by,

$$
\begin{aligned}
u &= u_m + r y_{air} - q z_{air} & (9.2.17) \\
v &= v_m + p z_{air} - r x_{air} & (9.2.18) \\
w &= w_m + q x_{air} - p y_{air} & (9.2.19)
\end{aligned}
$$

where m again denotes the value at the measurement location and x_{air}, y_{air} and z_{air} are coordinates of the air data sensors relative to the CG. If a nose boom is used to measure the air data, then Equations (9.2.17) to (9.2.19) assume it to be rigid. Utilising Equations (9.2.10) to

(9.2.12), the above expressions can be written in terms of airspeed, angle of attack and angle of sideslip measured at the sensor location,

$$u = V_m \sqrt{\frac{1 - \sin^2 \beta_m}{1 + \tan^2 \alpha_m}} + r y_{air} - q z_{air} \tag{9.2.20}$$

$$v = V_m \sin \beta_m + p z_{air} - r x_{air} \tag{9.2.21}$$

$$w = V_m \tan \alpha_m \sqrt{\frac{1 - \sin^2 \beta_m}{1 + \tan^2 \alpha_m}} + q x_{air} - p y_{air} \tag{9.2.22}$$

Note that the measurements of attitude and angular rate do not required transformations if the sensor are located away from the CG. The same values should be measured regardless of the sensor positions within the airframe. However, the angular measurements will require a correction if the measurement axes of the sensors are not aligned with the axes of the reference frame at the CG. This misalignment is illustrated in Figure 9.1. Using the rate gyro measurements as an example, the misalignment is accounted for using the following expression,

$$\begin{bmatrix} p_{cg} \\ q_{cg} \\ r_{cg} \end{bmatrix} = \mathbf{C}_m^T \begin{bmatrix} p_m \\ q_m \\ r_m \end{bmatrix} \tag{9.2.23}$$

where,

$$\mathbf{C}_m = \begin{bmatrix} \cos \epsilon_y \cos \epsilon_z & -\cos \epsilon_x \sin \epsilon_z + \sin \epsilon_x \sin \epsilon_y \cos \epsilon_z & \sin \epsilon_x \sin \epsilon_z + \cos \epsilon_x \sin \epsilon_y \cos \epsilon_z \\ \cos \epsilon_y \sin \epsilon_z & \cos \epsilon_x \cos \epsilon_z + \sin \epsilon_x \sin \epsilon_y \sin \epsilon_z & -\sin \epsilon_x \cos \epsilon_z + \cos \epsilon_x \sin \epsilon_y \sin \epsilon_z \\ -\sin \epsilon_y & \sin \epsilon_x \sin \epsilon_y & \cos \epsilon_x \sin \epsilon_y \end{bmatrix} \tag{9.2.24}$$

and ϵ_x, ϵ_y and ϵ_z are the angular offsets between each axis, as shown in Figure 9.1. Similar transformations can be applied to other measurements if necessary.

9.3   Sensor Error Models

In any practical situation, the data will contain measurement errors. If a variable was to be reconstructed using the expressions given in the previous section, the errors would lead to a mismatch between the measured and analytical time histories, thus making the two kinematically inconsistent. However, the sensor and its associated errors can, in general, be modelled using the following equation,

$$y_m(t) = (1 + k_y)y(t - \tau) + b_y + v_y(t) \tag{9.3.1}$$

where y_m is the measured value of the true variable y, k_y is the scale factor error, b_y is a bias error, τ is a time delay and v_y is random measurement noise. For the short lengths of data typically analysed for system identification, the scale factor error, bias error and time delay can be treated as constants. This allows an error model for each sensors to be proposed and the kinematic relationships provide a framework for estimating the values of the systematic errors in a similar way to the aerodynamic derivatives. Therefore, the data compatibility check becomes a parameter estimation problem.
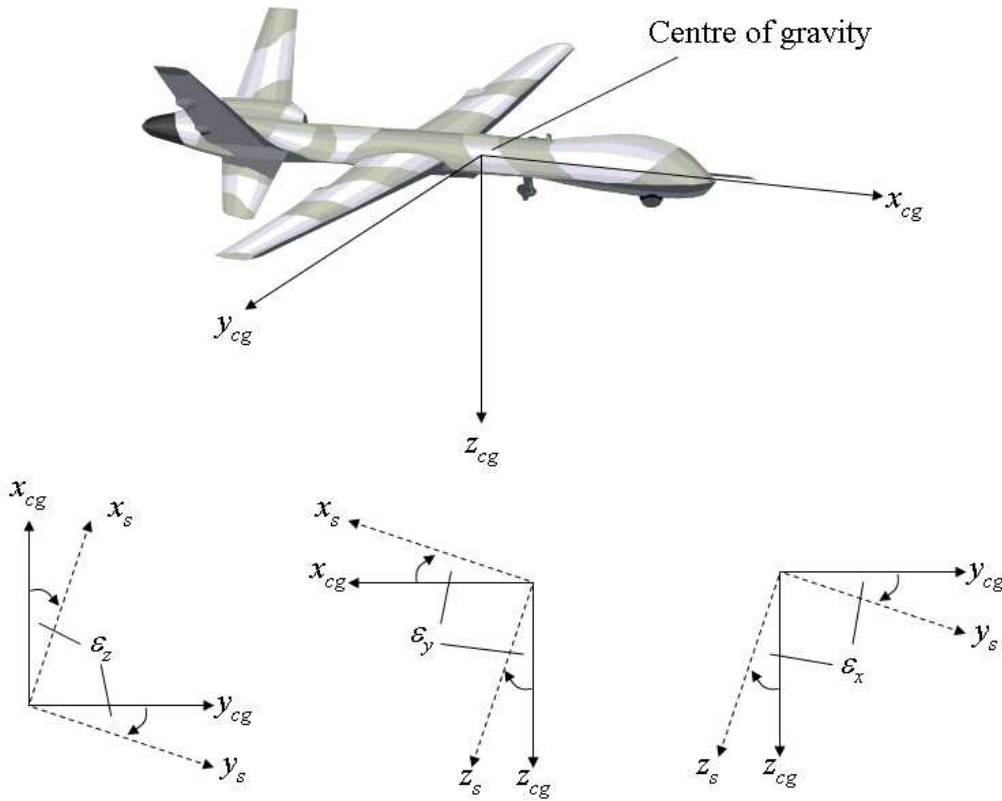
Figure 9.1: Illustration of sensor misalignment relative to
the centre of gravity

As has been described throughout, to reliably estimate a derivatives, there has to be enough information content in the data about that particular parameter and the same holds true for the data compatibility check. For example, it is unlikely that the systematic errors in sideslip data can be obtained from a measurement recorded during an elevator excitation. Therefore, the estimation of errors for both longitudinal and lateral/directional sensors requires a manoeuvre containing an excitation in each axis. Alternatively, multiple manoeuvre segments can be concatenated together. If the focus of the analysis is on small perturbation manoeuvres or excitation in one axis then the relationships in Section 9.2 can be linearised and the longitudinal and lateral/directional expressions can be decoupled. It is usually not necessary to account for a bias, scale factor and time delay error in every sensor and, in any case, this would likely lead to identifiability problems. Which systematic errors to include in the models varies from sensor to sensor and is often based on experience. The model structure determination described in the previous chapter can also be used to help determine which parameters to include in the error model.

9.4 Estimation Techniques

The estimation problem can be formulated as follows,

$$\dot{\mathbf{x}}(t) = f[\mathbf{x}(t), \mathbf{u}(t), \boldsymbol{\theta}], \ \mathbf{x}(0) = \mathbf{x}_0 \tag{9.4.1}$$

$$\mathbf{y}(t) = g[\mathbf{x}(t), \boldsymbol{\theta}] \tag{9.4.2}$$

$$\mathbf{z}(i) = \mathbf{y}(i) + \mathbf{v}(i), \ i = 1, 2, \ldots, N \tag{9.4.3}$$

where $\mathbf{v}$ is a vector of noise corrupting the measured outputs. For a general data compatibility check involving the equations outlined in Section 9.2, the elements of the state vector are the velocity components, the attitude angles and the altitude,

$$\mathbf{x} = \begin{bmatrix} u & v & w & \phi & \theta & \psi & h \end{bmatrix}^T \tag{9.4.4}$$

Note that the geodetic coordinates x_E and y_E have not been included in the state vector. This is because the aircraft dynamics are independent of its position relative to the earth (altitude h is included because aerodynamic characteristics are influenced by atmospheric density). As x_E and y_E do not appear on the right hand side of any of the expressions in Section 9.2, Equations (9.2.7) and (9.2.8) can easily be omitted from the analysis. The same argument could be used to remove the yaw attitude ψ from the state vector. The dynamic characteristics of an aircraft do not change depending on its heading and ψ is also absent from the right hand side of the kinematic relationships. However, it is retained as it aids in the estimation of the yaw gyro errors [34].

For the data compatibility check, the accelerations and angular rates are treated as inputs variables so,

$$\mathbf{u} = \begin{bmatrix} a_x & a_y & a_z & p & q & r \end{bmatrix}^T \tag{9.4.5}$$

The output vector comprises air data, attitudes and altitude,

$$\mathbf{y} = \begin{bmatrix} V & \alpha & \beta & \phi & \theta & \psi & h \end{bmatrix}^T \tag{9.4.6}$$

and the unknown parameter vector $\boldsymbol{\theta}$ contains the systematic errors to be estimated.

The simplest approach to the estimation problem is to use the maximum likelihood output error method, presented in Chapter 5. However, there are two disadvantages in using this algorithm for the data compatibility check. Firstly, the output error method assumes the equations of motion to be deterministic, but because the accelerations and angular rates are treated as input variables rather than output variables, measurement noise in the accelerometers and gyros becomes process noise, thus making the system stochastic. This could be particularly an issue for MEMS inertial sensors. Secondly, the systematic sensor errors can change depending on flight conditions and manoeuvre types [31]. Therefore, in the case where multiple manoeuvres are being analysed, the values of the unknown parameters can vary but the output error method will try to find one value to fit the whole data set. This could lead to convergence problems or an inaccurate match between the measured and reconstructed variables.

A more widely used method for the data compatibility check is the extended Kalman filter (EKF). As described in Chapter 7, this algorithm accounts for process noise and treats the unknown parameters as artificial state variables, therefore it does not suffer from the two issues highlighted above. The algorithm used for flight path reconstruction usually incorporates a smoother to reduce the inherent bias in the basic EKF, discussed in Chapter 7. Such a technique is the Rauch-Tung-Striebel method [159, 35, 160], which is a fixed-interval smoother. Essentially, the EKF is run as normal and, once the N data points have been analysed, the filter is run again but in reverse from the Nth data point to the first. The smoothed estimate at each data point is then a weighted combination of the two Kalman filter estimates.

Using information from the forward run of the EKF defined in Equations (7.2.59) to (7.2.67), the smoothed states are found from the following equation,

$$\hat{\mathbf{x}}_{aS}(i) = \hat{\mathbf{x}}_a(i) + \mathbf{K}_{aS}(i) \left[\mathbf{x}_{aS}(i+1) - \tilde{\mathbf{x}}_a(i+1) \right], \quad i = N, N-1, \ldots, 1 \tag{9.4.7}$$

where subscript S denotes a smoothed variable. The smoothed Kalman gain $\mathbf{K}_{aS}$ is found from,

$$\mathbf{K}_{aS}(i) = \hat{\mathbf{P}}_a(i)\mathbf{\Phi}_a^T(i+1)\tilde{\mathbf{P}}_a^{-1}(i+1) \tag{9.4.8}$$

and error covariance matrix for the smoothed states is given by,

$$\mathbf{P}_{aS}(i) = \hat{\mathbf{P}}_a(i) + \mathbf{K}_{aS}(i)\left[\mathbf{P}_{aS}(i+1) - \tilde{\mathbf{P}}(i+1)\right]\mathbf{K}_{aS}^T(i) \tag{9.4.9}$$

Fixed-point smoothers have also been used for data compatibility checking [161, 162].

9.5 Gust Estimation

As described in Chapter 7, UAVs are more susceptible to the effects of atmospheric turbulence due to their small masses and inertias in comparison with manned aircraft. For data significantly corrupted with turbulence, the parameter estimation can be complex. However, the data compatibility check provides an alternative means of dealing with turbulence by allowing the estimation of gust velocities. These components can then be subtracted from the motion variables, thus simplifying the subsequent parameter estimation process.

There are two approaches to this. The first is to incorporate a model of the gust components into the state equations. Such a model is that proposed by Dryden [148], which was introduced briefly in Chapter 7. Assuming that the turbulence field is steady and homogeneous (i.e. having the same statistical properties at each point in the field) then the power spectral densities of the gust components can be written as,

$$S_{ug}(\omega) = \sigma_{ug}^2 \frac{2L_u}{\pi} \frac{1}{1 + \left(L_u\frac{\omega}{V}\right)^2} \tag{9.5.1}$$

$$S_{vg}(\omega) = \sigma_{vg}^2 \frac{L_v}{\pi} \frac{1 + 3\left(L_v\frac{\omega}{V}\right)^2}{\left[1 + \left(L_v\frac{\omega}{V}\right)^2\right]^2} \tag{9.5.2}$$

$$S_{wg}(\omega) = \sigma_{wg}^2 \frac{L_w}{\pi} \frac{1 + 3\left(L_w\frac{\omega}{V}\right)^2}{\left[1 + \left(L_w\frac{\omega}{V}\right)^2\right]^2} \tag{9.5.3}$$

where the subscripts u, v and w denote components of the gust along the x, y and z axes respectively, σ_g^2 is the variance of the gust components and L is the scale length of the turbulence. Further simplification can be made if the turbulence field is assumed to be isotropic (i.e. statistical properties of the gusts are independent of the orientation of the coordinate system), in which case,

$$L_u = L_v = L_w = L \tag{9.5.4}$$
$$\sigma_{ug}^2 = \sigma_{vg}^2 = \sigma_{wg}^2 = \sigma_g^2 \tag{9.5.5}$$

The expressions for power spectral densities of the lateral and vertical gusts can also be simplified to,

$$S_{vg}(\omega) = S_{wg}(\omega) = \sigma_g^2 \frac{3L}{2\pi} \frac{1}{1 + \left(\frac{L}{\sqrt{2}}\frac{\omega}{V}\right)^2} \tag{9.5.6}$$

The gust velocity components are modelled using a first-order Gauss-Markov process, which is given by,

$$\dot{x}_g = -ax_g + b\mu_g \tag{9.5.7}$$

where x_g is the gust component (u_g, v_g or w_g) and μ_g is the driving process noise, assumed to be Gaussian white noise with zero mean and variance σ_g^2. For the horizontal gust, the constants a and b are,

$$a = \frac{V}{L} \ \text{ and } \ b = V\sqrt{\frac{2}{\pi L}} \tag{9.5.8}$$

while for lateral and vertical gusts,

$$a = \sqrt{2\frac{V}{L}} \ \text{ and } \ b = V\sqrt{\frac{3}{\pi L}} \tag{9.5.9}$$

For the scale length of turbulence, a value of around L = 300m is often used [161, 163] and an estimate of σ_g^2 can be obtained from analysis of the random component of the airspeed measurements.

Now, it is assumed that only the air data measurements of airspeed, angle of attack and angle of sideslip are directly affected by the gusts. The perturbations in these variables as a result of the gusts can be expressed as,

$$V_g \approx u_g, \ \ \alpha_g \approx \frac{w_g}{u}, \ \ \beta_g = \frac{v_g}{u} \tag{9.5.10}$$

so the air data variables can be found from,

$$V = \sqrt{u^2 + v^2 + w^2} - u_g \tag{9.5.11}$$

$$\alpha = \tan^{-1}\left(\frac{w}{u}\right) - \frac{w_g}{u} \tag{9.5.12}$$

$$\beta = \sin^{-1}\left(\frac{v}{V}\right) - \frac{v_g}{u} \tag{9.5.13}$$

The second approach estimates the gust components as the difference between the velocity components of the aircraft relative to the earth and those derived from the air data measurements. This is achieved using the equation,

$$\begin{bmatrix} u_g \\ v_g \\ w_g \end{bmatrix} = \mathbf{C}_E \begin{bmatrix} \dot{x}_E \\ \dot{y}_E \\ \dot{h} \end{bmatrix} - \begin{bmatrix} u \\ v \\ w \end{bmatrix} \tag{9.5.14}$$

where the matrix $\mathbf{C}_E$ is a direction cosine matrix to transform $\dot{x}_E$, $\dot{y}_E$ and $\dot{h}$ from the earth axes to body axes. It is identical to that given in Equation (9.2.24) but with ϵ_x, ϵ_y and ϵ_z replaced by the attitude angles ϕ, θ and ψ. Measurements of $\dot{x}_E$ and $\dot{y}_E$ can be provided by the inertial navigation system or GPS. If these are unavailable, then accelerometer data can be transformed to earth axes and integrated to obtain $\dot{x}_E$ and $\dot{y}_E$[164].

9.6 Dynamic Wind Tunnel Examples

For the first set of examples in this chapter, data from the dynamic wind tunnel is used. In this case, all measurements were provided by the IMU, therefore the only compatibility check

that could be made was on the angular rates and the attitudes. No check could be made on the accelerometer data. However, for the 3 DoF case, this was not considered to be critical as only the angular rate and attitude measurements were used for the subsequent parameter estimation step. From Section 9.2, the kinematic equations of interest were,

$$\dot{\phi} = p + q \sin\phi \tan\theta + r \cos\phi \tan\theta \qquad (9.6.1)$$

$$\dot{\theta} = q \cos\phi - r \sin\phi \qquad (9.6.2)$$

$$\dot{\psi} = q \sin\phi \sec\theta + r \cos\phi \sec\theta \qquad (9.6.3)$$

The manoeuvres performed in the wind tunnel experiments were small perturbations about trim, in which case Equations (9.6.1) to (9.6.3) can be linearised and the motion about each axis can be decoupled,

$$\dot{\phi} = p \qquad (9.6.4)$$

$$\dot{\theta} = q \qquad (9.6.5)$$

$$\dot{\psi} = r \qquad (9.6.6)$$

To start with, analysis performed on pitch measurements from the Hawk is presented. The data analysed contained a 1-1-2 input to the elevator. The IMU was positioned in the model 0.18m ahead of the gimbal, which was the point at which the origin of body axes was located. There were also small misalignments in roll and pitch between the measurement and body axes of ϵ_x = -3.7 deg and ϵ_y = -2.4 deg. Note, however, that only angular data was being examined therefore only the angular misalignment needed to be corrected for.

The error model for the pitch gyro was,

$$q_m = (1 + k_q)q + b_q \qquad (9.6.7)$$

An attempt was made initially to estimate a bias and a scale factor error for the pitch attitude measurements as well. However, these errors were found to have large standard errors and were highly correlated with the gyro errors. The removal of the attitude errors from the analysis also had little effect on the resulting match between the measured and reconstructed pitch attitudes. Hence, θ was treated as being error free and the data compatibility check focused on the estimation of the pitch gyro parameters. Substituting Equation (9.6.7) into (9.6.5), the state equation became,

$$\dot{\theta} = (q_m - b_q)/(1 + k_q) \qquad (9.6.8)$$

and the unknown parameters to be determined were the bias and scale factor errors b_q and k_q.

Figure 9.2 shows the pitch rate time history. It can be seen that a small amount of noise is present in the measurement. Initially, the output error method was applied to the estimation problem, assuming that the pitch gyro data was free of noise. The bias and scale factor errors obtained are shown in the first column of Table 9.1, with the associated standard errors given in the second column. Figure 9.3 shows the measured pitch attitude data plotted against reconstructed response and, despite the presence of noise in the gyro, a very close match between the two was achieved. The output error method was then run again but with the pitch rate data smoothed prior to estimation. The results are also given in Table 9.1 and, as can be seen, they were almost identical to the estimates and standard errors obtained in the first run. This suggests that, despite the gyros being of the MEMS variety which are traditionally regarded as having noisier output in comparison with more conventional instrumentation, the noise in the data is not large enough to adversely affect the estimation process.

The EKF was then used to find b_q and k_q. To implement the algorithm, estimates of the measurement noise and process noise covariance matrices were obtained from Fourier smoothing analysis of the pitch attitude and pitch rate data respectively. Figure 9.4 shows the time histories for b_q and k_q from the forward run of the algorithm, while Figure 9.5 shows plots of the estimates when the Rauch-Tung-Striebel smoothing step was subsequently applied. On the forward run, there is some variation in the estimates to begin with, as the algorithm attempts to converge on an appropriate value. As time increases, the estimated values settle down to their constant converged values. When the reverse smoothing algorithm was then run, Figure 9.5 shows that the same constant values were estimated for b_q and k_q at each point in time. The final estimates are displayed in Table 9.1 along with their standard errors. There was good agreement between the results obtained using the EKF and the output error method. Figure 9.6 shows a comparison of the measured and reconstructed pitch attitude responses for the EKF. Again, there is a close match between the measured and reconstructed time histories.
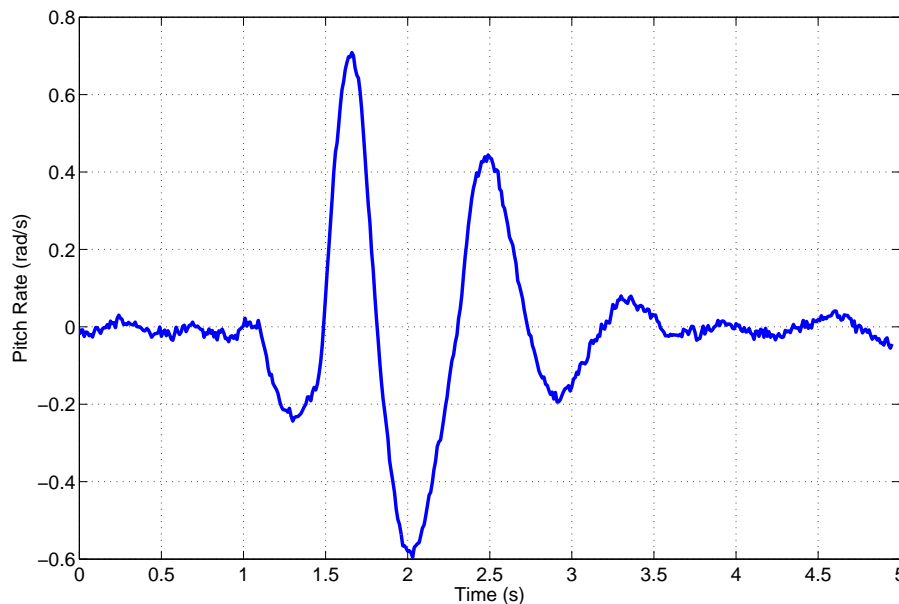

Figure 9.2: Pitch rate gyro data time history

	OE		OE - smoothed		EKF	
	$\hat{\theta}$	$100[s/|\hat{\theta}|]$	$\hat{\theta}$	$100[s/|\hat{\theta}|]$	$\hat{\theta}$	$100[s/|\hat{\theta}|]$
b_q	-0.0048	5.10	-0.0048	5.30	-0.0037	12.15
k_q	0.0475	0.75	0.0470	0.76	0.0479	0.58

Table 9.1: Results of data compatibility check on Hawk
pitch data

A similar piece of analysis to that presented above was applied to measurements from the DEMON model. This time, two data segments were concatenated together. The first contained a 1-1-2 input to the elevator, while the second comprised a doublet to the rudder followed by an aileron doublet. Because motion was excited about all three axes, the nonlinear state equations (9.6.1) to (9.6.3) were used. As with the Hawk example, the IMU in the DEMON had slight
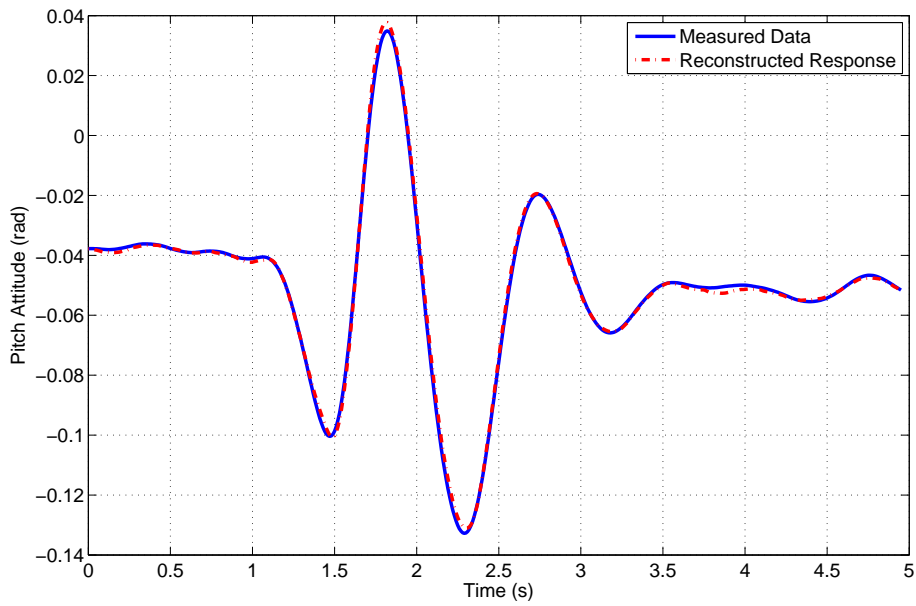
Figure 9.3: Measured and reconstructed pitch attitudes -
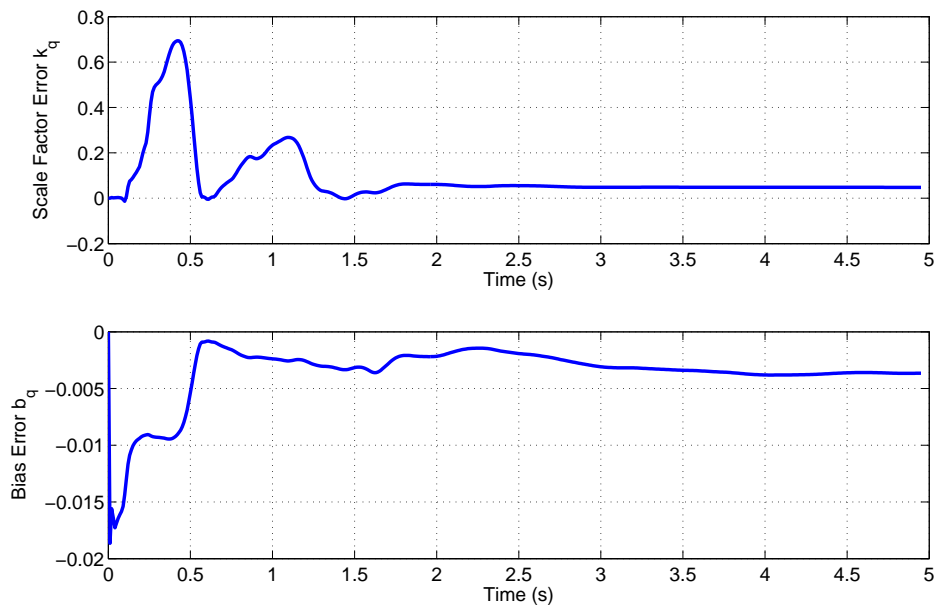output error method

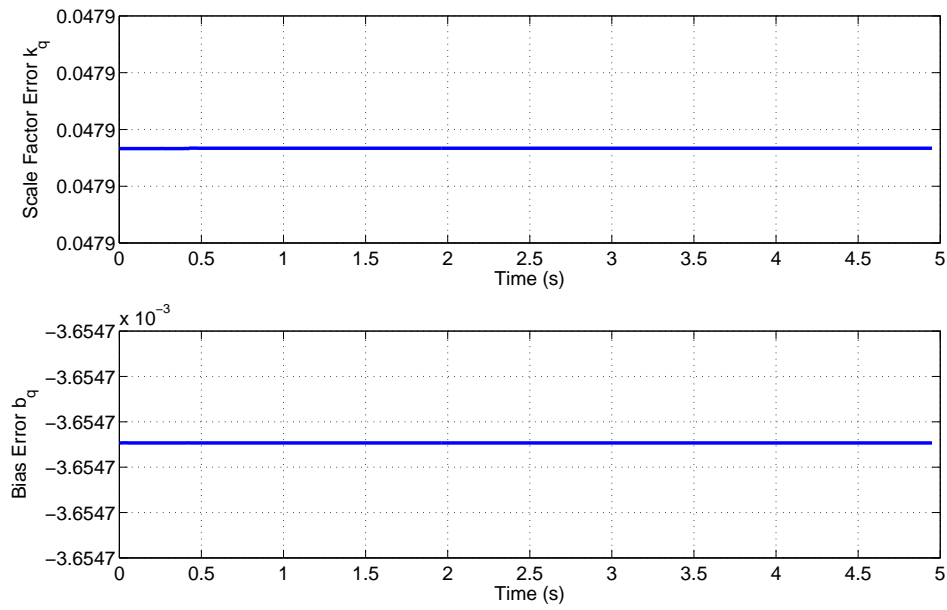**Figure 9.4:** Time histories of pitch gyro sensor errors for
forward run of EKF

Figure 9.5: Time histories of pitch gyro sensor errors
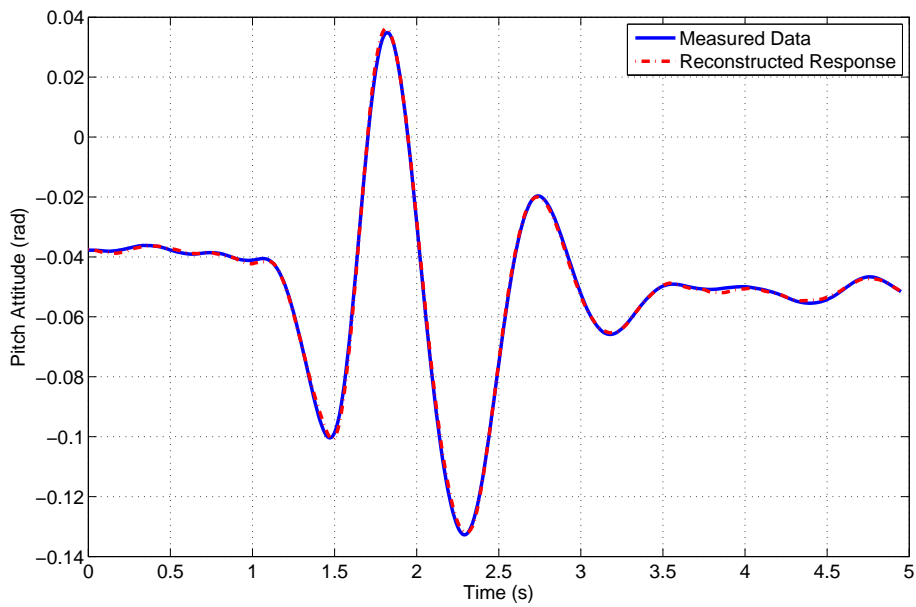from EKF plus smoother

Figure 9.6: Measured and reconstructed pitch attitudes -
EKF

misalignment errors relative to the body axes in roll and pitch. These were $\epsilon_x = 1.3$ deg and ϵ_y = -1.3 deg and were accounted for prior to estimation.

The gyros were initially modelled using the same form as that given in Equation (9.6.7), however a model structure determination analysis indicated that, in this case, the scale factor errors k_p and k_q were insignificant. For the same reasons given previously, the systematic errors in the attitude measurements were also removed from the analysis. The output error method was again carried out first assuming that the measurements of p, q and r (shown in Figure 9.7) were free of noise. The first column of Table 9.2 contains the estimated values and the second column displays the corresponding standard errors. The match between the measured and reconstructed attitude angles is illustrated in Figure 9.8. The plots clearly show some mismatch between the measured and reconstructed responses, particularly for pitch and yaw. The output error method was then run for a second time with the rates smoothed prior to the analysis. As with the Hawk example, the results matched very closely those obtained when no smoothing was done on the gyro data beforehand, as displayed in the third and fourth columns of Table 9.2. This observation again indicates that the low noise levels on the gyros have little effect on the estimation results. However, the discrepancies between the measured and reconstructed attitudes, depicted in Figure 9.8, remained.

The EKF incorporating the Rauch-Tung-Striebel smoother was then used to find the bias and scale factor errors. The plots in Figure 9.9 show the time histories of b_p, b_q, b_r and k_r determined from the forward run of the Kalman filter. For each parameter, there were large fluctuations in the estimates, especially in the first data segment. For the second piece of data, the estimates again experienced some fluctuations to begin with but quickly settled and remained at relative constant values. Figure 9.10 shows the same plots but with the Rauch-Tung-Striebel smoother applied to the data. This time, the value of each parameter was constant for each piece of data but the magnitudes of these estimates differed between the two segments. The reason for this was that different dynamics were being excited in the two data segments. In the first piece of data, an elevator doublet was applied, meaning that the signals were likely to contain sufficient information about b_q but less information about b_p, b_r and k_r. In the second segment, the opposite was true, with doublets being applied to the aileron and rudder, leading to better information about the lateral/directional parameters. The EKF estimates are also given in Table 9.2. The fifth column shows the smoothed estimates determined from the first data segment and the sixth column gives the values obtained from the second data segment. The standard errors, based on the entire time history, are displayed in the last column of the table. Interestingly, the values for b_p and b_r from the output error method match closely those determined from the second piece of data. The output error estimate of k_r on the other hand was closer to the EKF estimate from the first segment. However, it would be expected that the EKF estimate of k_r from the second piece of data would be more reliable, as it was in this segment that the yaw dynamics were excited. Figure 9.11 shows the measured and reconstructed attitudes from the EKF. In comparison to the output error method, the match between the two is improved. However, this is to be expected because the EKF allows the estimates of the parameters to vary with time, whereas the output error method is trying to find one set of values to fit the entire time history. The above analysis indicates that the EKF approach is better suited when carrying out a data compatibility check on multiple segments of data.
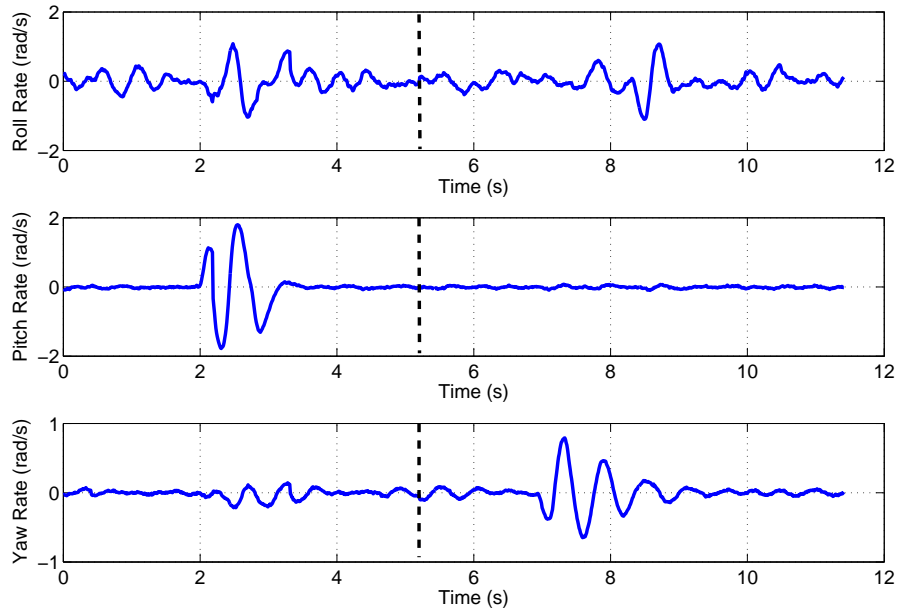
Figure 9.7: Rate gyro time histories

	OE		OE - smoothed		EKF		
	$\hat{\theta}$	$100[s/|\hat{\theta}|]$	$\hat{\theta}$	$100[s/|\hat{\theta}|]$	$\hat{\theta}_1$	$\hat{\theta}_2$	$100[s/|\hat{\theta}|]$
b_p	0.0062	4.42	0.0058	4.90	0.0043	0.0057	22.89
b_q	-0.0115	2.45	-0.0116	2.44	-0.0170	-0.0075	12.93
b_r	0.0022	23.89	0.0023	21.87	0.0013	0.0019	25.36
k_r	-0.3089	12.07	-0.3051	11.64	-0.3021	0.0179	3.69

Table 9.2: Results of data compatibility check on DEMON
data

Figure 9.8: Measured and reconstructed attitude angles - output error method

Figure 9.9: Time histories of gyro sensor errors for forward run of EKF
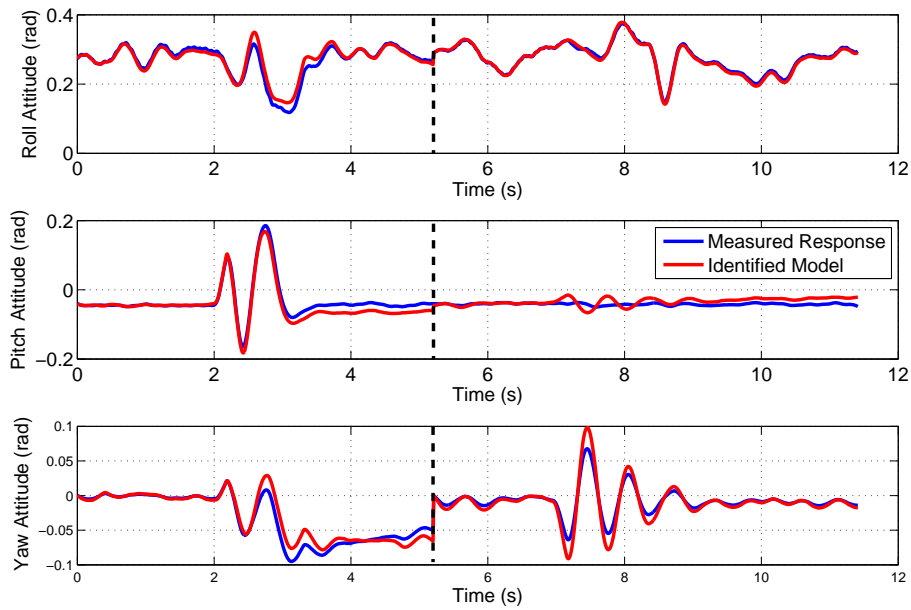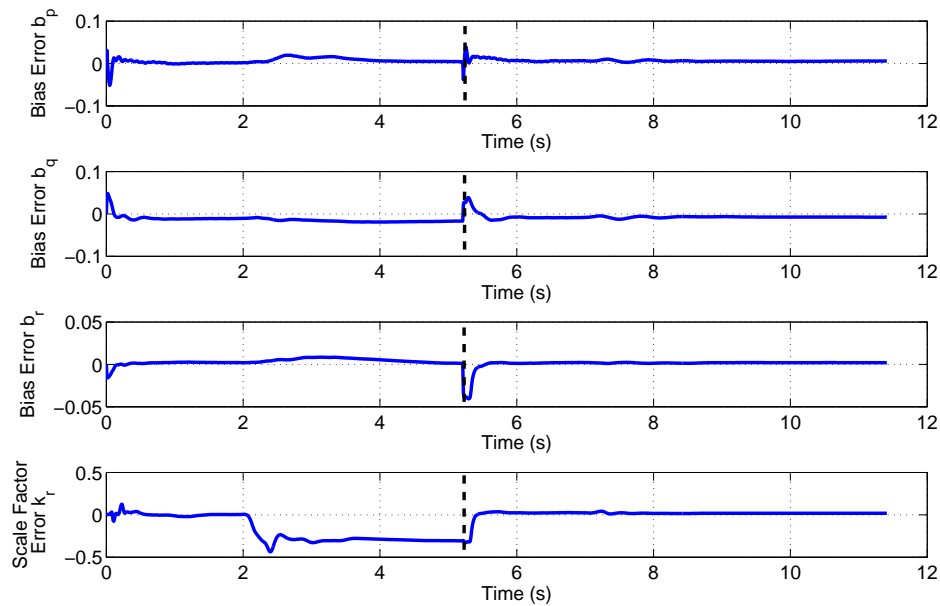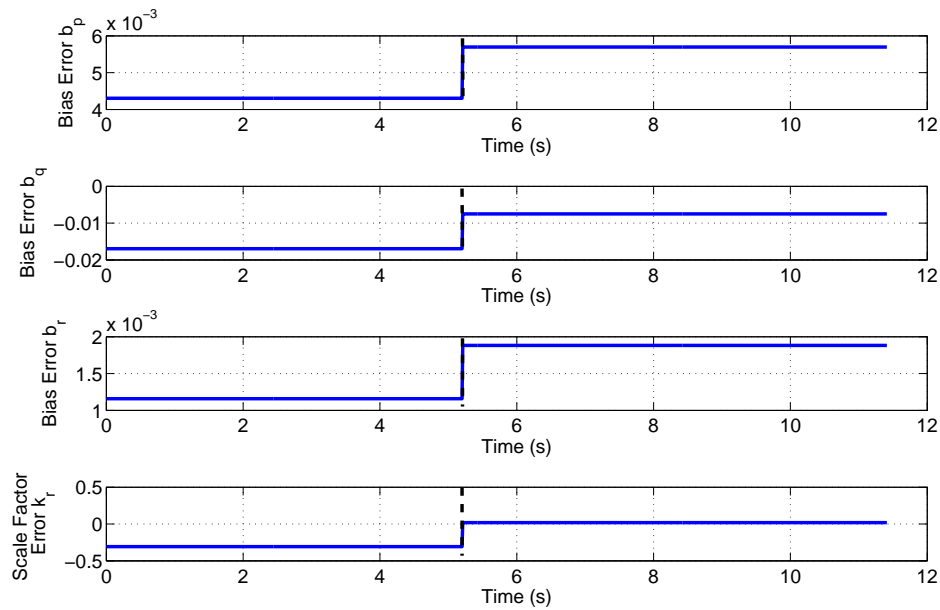
Figure 9.10: Time histories of gyro sensor errors from EKF plus smoother
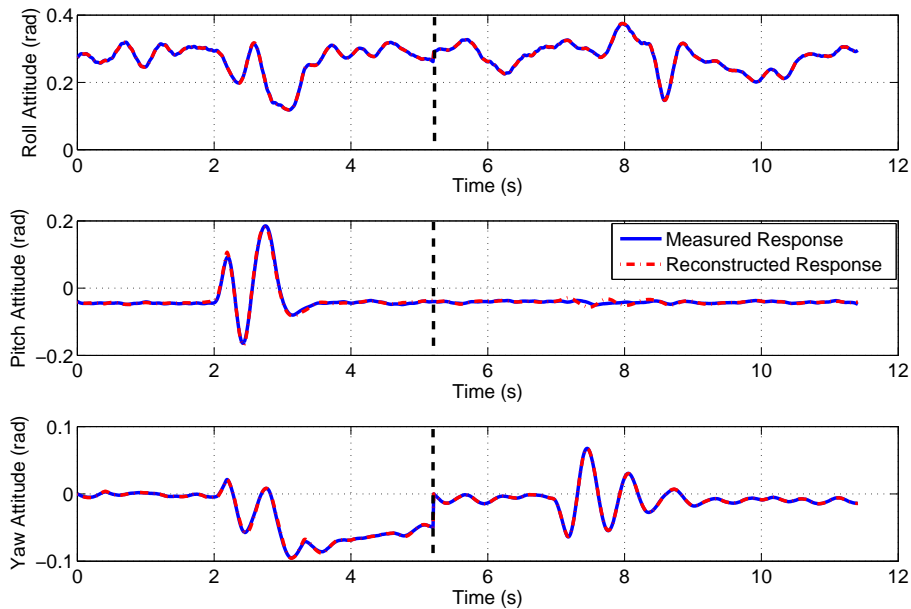

Figure 9.11: Measured and reconstructed attitudes angles - EKF

9.7   UAV Gust Estimation Example

In this section, a data compatibility check on the UAV data is presented. This time, the analysis used the full nonlinear expressions given in Section 9.2. The state vector **x**, input vector **u** and output vector **y** were those defined in Equations (9.4.4), (9.4.5) and (9.4.6) respectively. The data examined was three manoeuvre segments concatenated together, which contained an aileron doublet, a rudder doublet and an elevator doublet as shown in Figure 9.12.
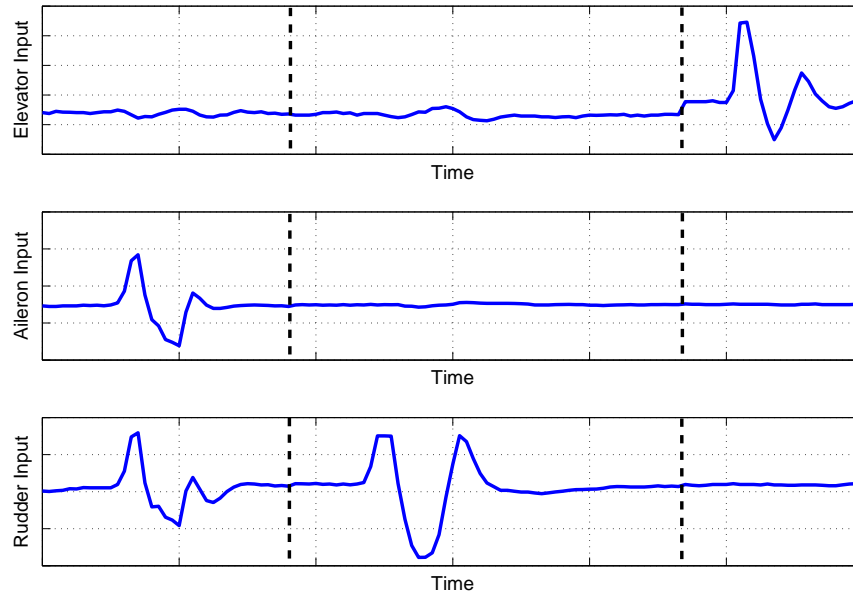
Figure 9.12: Control surface inputs in data segments used
for data compatibility check

Examination of the data revealed that the data supplied by BAE Systems was already kinematically consistent, with no significant systematic errors in any of the measurements. The plots in Figure 9.13 show the measured and reconstructed responses and, as can be seen, a very close match was achieved for each motion variable. It was assumed the atmospheric conditions were calm when the data was recorded. However, an attempt was also made to estimate the gust components experienced by the aircraft during the flight test. Therefore, the analysis was repeated but the EKF was used to estimate the states, which incorporated the Dryden model of turbulence outlined in Section 9.5. Figure 9.14 shows the estimated time histories of u_g, v_g and w_g. All three were found to be very small, with no component exceeding a speed greater than around 2 m/s at any point. This confirms the observation that the tests were conducted in calm atmospheric conditions.

Figure 9.13: Time histories of the measured and reconstructed motion variables

Figure 9.14: Time histories of gust component estimates

Chapter 10

Discussion and Conclusions

10.1 Conclusions

The aim of this research was to examine aspects of system identification for UAVs. Each of the steps involved in the process for aircraft in general was reviewed and potenti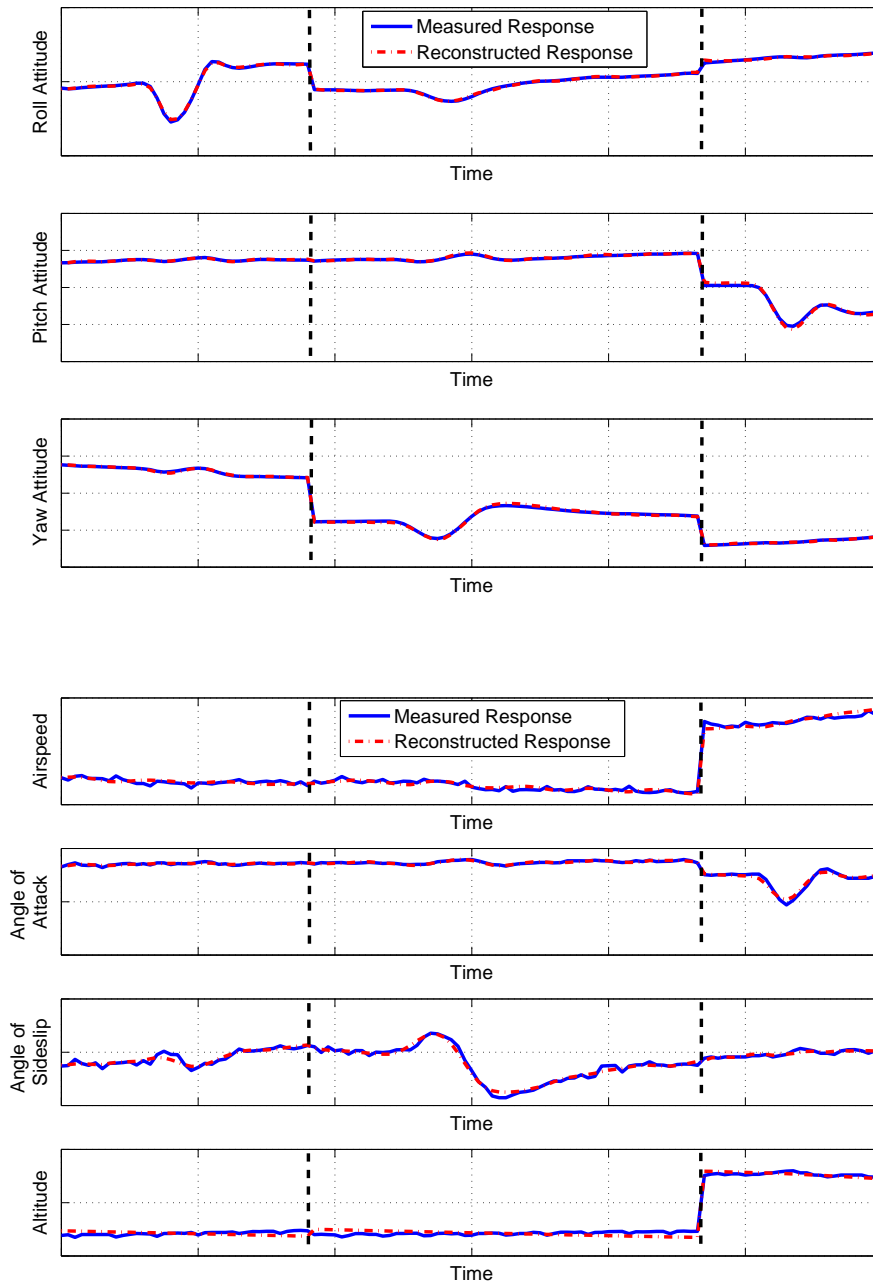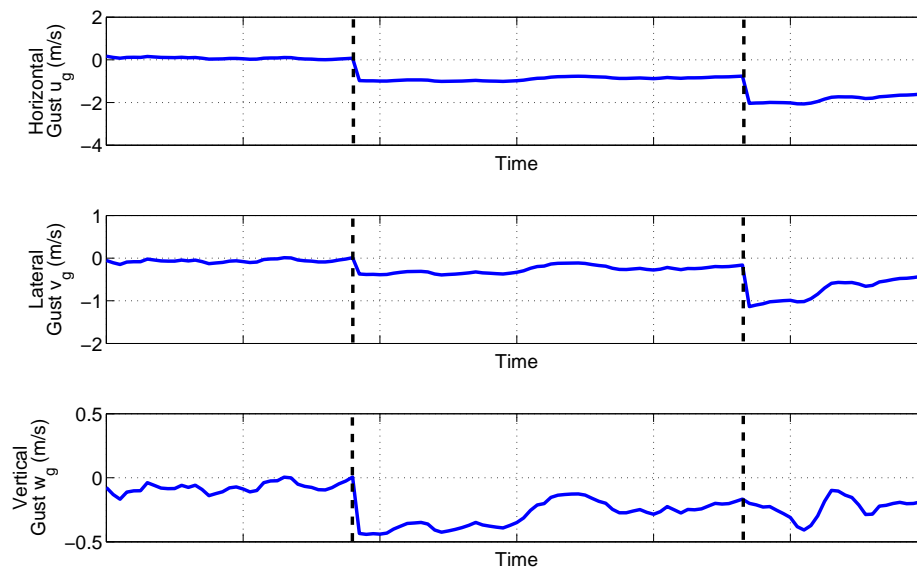al issues that could be encountered when analysing UAV data were identified. These issues were then investigated using measurements from two experimental sources. Firstly, Cranfield University's dynamic wind tunnel facility was utilised, in which scale models are flown in semi-free flight. The control surfaces are actuated so that inputs, similar to those used when flight testing full-sized aircraft, can be applied and the resultant response of the model is recorded. During the course of the research, a 1/12 scale BAe Hawk and a 1/3 scale DEMON UAV were tested. An added benefit of the facility to this work was that the wind tunnel models were comparable in size to the miniature class of UAVs. Therefore, practical issues, similar to those faced for these aircraft, were encountered with the wind tunnel experiments. The second source of experimental data was UAV flight test data supplied by BAE Systems. The conclusions reached for each stage of the system identification process are presented in the subsections below, followed by a brief outline of general findings relevant to the procedure as a whole.

10.1.1 Manoeuvre Design

The goal of the manoeuvre design step is to ensure that there is sufficient information in the data regarding the aircraft dynamics of interest. Three commonly used methods for aircraft were reviewed: frequency sweeps, design by statistical analysis and multistep inputs. Their use for exciting the dynamics of the wind tunnel models was then examined. The advantage of frequency sweeps is that they excite a wide band of frequencies and are useful when *a priori* information of the vehicle dynamics is limited or poor, a problem commonly faced for UAVs. However, they take a relatively long time to apply and, when frequency sweeps were attempted with the Hawk, it was difficult to keep the model close to the trim condition. This has also been observed when flight testing small UAVs [48]. Design by statistical analysis leads to input signals with a sound theoretical basis. However, the method can be complex and involved. Further, *a priori* estimates of the aircraft dynamics are required for the process. This is also true of the multistep approach. However, compared to the statistical design method, the multisteps are much simpler to implement. They also have a much shorter duration in

comparison to frequency sweeps and, therefore, were the preferred inputs for the dynamic wind tunnel experiments.

A number of different input shapes were tried during the research. These were the doublet, 3-2-1-1, 1-1-2-3 and 1-1-2. Based on *a priori* estimates, the time steps required to optimally excite the model dynamics were very small, so computer generated inputs, rather than manual inputs, were applied. In this situation, the upper limit on the frequencies that can be excited are governed by the performance of the control surface actuators. The electrical actuation devices which are small enough to be housed in miniature UAVs or wind tunnel models typically have a much lower natural frequency than the larger hydraulic actuators used on manned aircraft. At the same time, however, the natural frequency of the vehicle increases as its mass and inertias reduce. If the aircraft and actuator dynamics are located at similar frequencies, it may be difficult to properly excite the airframe dynamics without the actuator reaching its operating limits. Hence, there is a potential for system identification to be hampered by the performance of the actuators, leading to less reliable estimates of the stability and control derivatives.

10.1.2   Sensors and Instrumentation

Another aspect of the experimental design process is the selection of an appropriate instrumentation system. Due to the lack of space within the airframe, particularly for small UAVs, the size and number of sensors that can be accommodated in the aircraft may be limited. An attractive option for the measurements of accelerations and angular rates, when space is limited, are inertial sensors developed using MEMS technology. Their main advantages are their small size, light weight and low cost, although in comparison to more mature sensor technologies they have traditionally been less accurate, exhibiting noisier outputs and more significant systematic errors. However, their performance has improved dramatically over the last two decades and this is predicted to continue in the future. MEMS inertial measurement units are also available which use sensor fusion techniques to determine attitude, avoiding the need for bulky sensors to measure these variables directly. Miniaturised air data systems, relying on MEMS pressure transducers, have also been reported. The process of data acquisition is also affected by the size of the aircraft. As the mass and inertias of a vehicle decrease, its natural frequency increases. Hence, the data sampling rate required to adequately capture the aircraft dynamics increases.

For the wind tunnel tests, the motion of the models was recorded using an off-the-shelf MEMS IMU. This allowed the suitability of such units for the dynamic wind tunnel experiments to be assessed. In the past, the emulation of flight test-like experiments in the wind tunnel environment had relied on potentiometers to measure the model's attitude, then kinematic relationships were used to generate data for other motion variables. This lack of redundancy meant that any errors in the output of the potentiometers would directly affect the stability and control derivatives. However, with the MEMS IMU, it was possible to perform a kinematic consistency check on the angular rates and attitudes.

One practical problem encountered with the models was that it was not possible to measure the control surface deflections directly due to lack of space to mount devices such as a potentiometer at the control surface hinges. Instead, the control surface deflections were inferred through knowledge of the commanded inputs, the dynamics of the actuators and the dynamics of the control linkages. To determine its characteristics, frequency sweeps were applied to the actuators in isolation and, using the input/output information, a second-order transfer function was found to match its response. The accuracy of the control surface deflections determined

using this approach are dependent on the fidelity of the actuator and control linkage models. There can be significant nonlinearities in the actuator behaviour, particularly for small low-cost electrical devices, and their performance will vary under different loading conditions. The control linkages can also introduce nonlinear effects due to hysteresis and dead bands. While the approach worked well for this research, direct measurement of the control surface positions, if possible, is preferred.

10.1.3   Parameter Estimation

Chapters 4 to 7 have outlined a number of parameter estimation algorithms commonly used for aircraft. Their respective merits and drawbacks have been presented and practical examples of their use in estimating unknown parameters from experimental data have been provided. The first of these to be examined was the equation error formulation solved using ordinary least squares regression. The appeal of this approach is its simplicity, with the parameter estimates determined in one step using matrix algebra. The major disadvantage with the algorithm is that measurement errors in the regressors result in the least squares estimates being asymptotically biased, inconsistent and inefficient. When high-precision sensors are used, this is less of an issue and it was shown that, for the UAV flight test data, the results obtained from smoothed and unsmoothed regressors were virtually identical. Errors in the regressors is potentially more of a problem when utilising MEMS sensors, which have traditionally suffered from more significant errors in comparison to conventional instrumentation. However, analysis of data from both wind tunnel models revealed that the noise levels on the signals provided by the MEMS IMU were not large enough to adversely affect the least squares estimates, indicating that the unit's performance was adequate for this application. Despite the quality of the wind tunnel measurements, it was in some instances best to smooth the regressors because of the presence of a high frequency component in the signals. This was due to an undesirable structural vibration in the test rig. A Fourier smoothing technique developed by Morelli [127] was found to work well in this case. An added advantage of this method was that it allowed properties of the noise in the signals to be estimated. It could also be easily used to numerically differentiate the smoothed data, which is typically required when deriving the dependent variable from the measurements.

The second technique to be studied was the maximum likelihood output error approach. Its advantages over the least squares equation error method are that it explicitly accounts for measurement noise and that it can be used to solve estimation problems which are nonlinear in the parameters. However, it is a more complex, iterative method and therefore requires initial estimates of the unknown parameters to start the algorithm. Often, these initial estimates come from the least squares equation error method but if the estimation problem is nonlinear then the starting values will have to come from other sources. The most widely used method of minimising the output error cost function is the modified Newton-Raphson algorithm. It has been found, however, that this technique can struggle to converge if the initial parameter estimates are far from the optimum values. This may present a problem if the *a priori* information is limited or poor. When analysing the DEMON model, for which the sources of *a priori* information were minimal, it was found, however, that the modified Newton-Raphson algorithm converged. Further, in runs of the output error method to estimate the UAV short period derivatives, it was only when all parameters were set to starting values of 1 that the algorithm failed. In this case, Levenberg-Marquardt method was still able to arrive at the same stability and control derivative values.

The least squares and maximum likelihood techniques can also be formulated in the frequency domain. An advantage of this approach is that the analysis can be restricted to a given band of frequencies. For the wind tunnel data, this meant that the effects of the rig vibration could be removed and estimation could concentrate on the frequency region corresponding to the rigid-body dynamics. Another practical issue faced with the wind tunnel data was the presence of a time delay in the input information caused by the wireless network. Two approaches for accounting for this delay were used, with both found to be viable in practice. First, the input data was time shifted manually through inspection of the data. In the second approach, the time delay was included in the vector of unknowns to estimated. This made the estimation problem nonlinear so an iterative algorithm, such as the modified Newton-Raphson technique, was required. In the time domain, the estimation of time delays required that some additional subroutines be added to the algorithm. Also, without interpolating the data, the time delay had to be a multiple of the data sampling time Δt. In the frequency domain, time delay estimation is more straightforward. No additional subroutines were required and there was no constraint that the time delay be a multiple of Δt.

In the final chapter focusing on parameter estimation, two issues of particular concern for UAVs were explored. Firstly, estimation from data recorded in the presence of atmospheric turbulence was described. In comparison to manned aircraft, UAVs are more susceptible to the effects of turbulence due to their smaller size. Atmospheric disturbance can be dealt with in two ways. The turbulence can be modelled and its properties can estimated along with the stability and control derivatives. Alternatively, gust velocity components can be estimated during the data compatibility check and removed prior to parameter estimation. The equation error and output error methods are not well suited to estimation when the measurements are corrupted by turbulence. Process noise leads to an increased variance in the least squares parameter estimates, while the output error approach only accounts for measurement noise and may struggle to converge if the process noise is significant. Two parameter estimation techniques, which explicitly model the effects of turbulence, were therefore investigated. These were the filter error method and the extended Kalman filter (EKF). Both were used successfully to find estimates of the DEMON's roll characteristics from data in which flow disturbances existed. The main disadvantage of the filter error method is its complexity. It must also be ensured that the model structure is correct as the algorithm will always yield a good match to the measured response, even if important terms have been omitted. The EKF has the advantage that it is a recursive technique so can be used for real-time parameter estimation. However, to initialise the algorithm the measurement and process noise covariance matrices must be specified. While the covariance of the measurement noise can be estimated from bench tests of the instrumentation or from Fourier smoothing, the process noise matrix is much harder to specify and may require some tuning. When analysing the DEMON data, however, it was found that the values of the parameter estimates were largely insensitive to changes in the process noise covariance.

A second issue for UAVs which was investigated was estimation of the aircraft's open-loop dynamics from closed-loop data. With the drive towards autonomy, the level of control system technology employed on UAVs is high. Ideally, any feedback systems should be disengaged during the flight tests as they will tend to augment the properties of the basic airframe. However, this may be impractical, particularly if the basic airframe is unstable. The presence of feedback can lead to variables being highly correlated, requiring a process for detecting data collinearity. The resulting parameter estimates can then be obtained through biased estimation techniques, such as principal components regression and ridge regression. Two examples using UAV flight

test data were presented. In the first, the aileron and rudder inputs were highly correlated. The standard errors of the parameter estimates were lower in comparison to the least squares estimates when biased estimation was used. In the second example, the correlation between pitch rate and elevator deflection, due to pitch rate feedback, was analysed. This time, the correlation was less significant and standard errors in the least squares estimates were similar to those of principal components and ridge regression. A possible explanation for this was that the time delays introduced by the flight control system led to there being enough information about the separate effects q and η had on the pitching moment.

When estimation was carried out on data from the wind tunnel models, the resulting values for the parameters were, in some cases, significantly different from the *a priori* estimates used to design the multistep inputs. This was particularly true for the DEMON model. However, the estimates obtained were statistically reliable, with few instances of high standard errors or correlation coefficients, and the estimated values were confirmed when validating the identified model using separate pieces of data. Therefore, it can be concluded that, despite the inaccuracy of *a priori* information, there was still sufficient information in the data regarding the model dynamics. Most likely, this is due to the ability of the multistep inputs to excite a wideband of frequencies.

10.1.4   Model Structure Determination

The process of determining the most appropriate model structure could be crucial for UAVs of unusual configuration. For example, greater cross coupling between the dynamic in each axis may exist for these vehicles. Two approaches to model structure determination were presented and applied to both UAV flight test data and wind tunnel measurements. The first was stepwise regression, while the second was a more general approach which could be applied to nonlinear maximum likelihood estimations problems. It was based on the analysis of parameter standard errors, insensitivities and correlation outlined by Tischler [6] for the frequency response method. Guidelines for removing insignificant terms from the model structure had been suggested by Tischler so an investigation of the suitability of the guidelines for other estimation techniques was investigated. Three test cases were described: one for the UAV, one for the Hawk and one for the DEMON. In each case, both stepwise regression and the maximum likelihood approach arrived at the same final model structure. The maximum likelihood approach was applied in both the time and frequency domain and the guidelines suggested by Tischler for the frequency response method appear to also work well for the other estimation methods. It is clear, however, that the model structure determination process is one that cannot be used blindly but works best when combined with a physical understanding of the aircraft dynamics.

10.1.5   Data Compatibility Check

The final chapter focused on the data compatibility check, also sometimes referred to as flight path reconstruction, the aim of which is to check the accuracy and kinematic consistency of the measurements before they are used for parameter estimation. The procedure can also be used to determine gust velocity components and remove the effects of atmospheric turbulence prior to the estimation of the stability and control derivatives. Two estimation methods were investigated for the data compatibility check on the angular rates and attitude information from the wind tunnel tests. These were the maximum likelihood output error method and the EKF

incorporating a Rauch-Tung-Striebel smoother. The output error approach is the simpler of the two. However, the angular rates are treated as input variables for the estimation problem. Therefore, any noise in the gyro data will enter the system as process noise, in which case the output error method may give poor estimates or struggle to converge. The systematic errors to be estimated can also vary depending on flight conditions and manoeuvre types. Therefore, when multiple manoeuvres are being analysed, the values of the unknown parameters can fluctuate but the output error method will try to find one value to fit the whole data set. This can lead to convergence problems or an inaccurate match between the measured and reconstructed responses. The EKF approach, on the other hand, accounts for process noise and treats the unknown parameters as artificial state variables which can vary with time. Hence it does not suffer from the two issues highlighted above. When analysing single manoeuvres from the dynamic wind tunnel tests, the output error method was found to give similar results to the EKF even though noise in the angular rate information was not accounted for. Smoothing the rates prior to applying the output error method also had little effect on the resulting estimates. This again indicated that the noise in the measurements provided by the MEMS IMU is not large enough to adversely affect the estimation process. It also further confirms the conclusion from Chapter 4 that MEMS technology has matured to a level where the performance of such devices is sufficient for the applications explored in this research. As expected, when analysing multiple segments of data, the output error did not provide as close a match to the measured data as the EKF. This was due to some variability in the gyro errors between the manoeuvres.

10.1.6   General Conclusions

From the discussion in this thesis, it can be concluded that no one technique is particularly well suited for the analysis of UAV data. Because of the wide range of sizes and configurations of unmanned aircraft, practical issues will be encountered in the analysis of one aircraft that will not be faced with another. In particular, more problems are likely to be met the smaller the vehicle is. Based on experience with the wind tunnel models, these include the impracticality of measuring control surface deflections directly, the dynamics of the subsystems (such as the actuators) being located in the same frequency region as the airframe itself and a greater susceptibility to the effects of atmospheric turbulence. Therefore, the best approach is to have a number of techniques for each step in the system identification process which can be readily applied to a given UAV. The comparison of results from more than one algorithm is also recommended to ensure confidence in the derivative estimates.

10.2   Summary of Contributions to Knowledge

While researching system identification for UAVs, a number of contributions to knowledge have been made, particularly regarding the practical side of the subject. Firstly, the use of MEMS sensor technology for dynamic wind tunnel experiments had not been investigated previously and it was shown that the performance of a MEMS IMU, purchased off-the-shelf, was satisfactory for the wind tunnel application. This was despite these devices traditionally exhibiting noisier outputs in comparison to more mature sensor technologies. Further, it was shown that the noise levels on the measurements provided by the MEMS IMU were not high enough to adversely affect the estimation process, even for estimation methods in which the

motion variables are assumed to be noise-free. Secondly, the analysis performed on the DE-MON UAV wind tunnel model was the first time system identification had been applied to this particular aircraft configuration and therefore this research has increased the information about the dynamic characteristics of this particular airframe. With regards to the BAE Systems UAV, while system identification had been performed on this aircraft prior to this work, the analysis presented throughout this thesis was the first time that a range of parameter estimation methods had been used to study this aircraft and some advanced techniques, such as the filter error method and extended Kalman filter approach, had not be previously used to analyse this UAV. Finally, it was shown that, because of the wide range of sizes and configurations of UAVs, the practical issues encountered with one aircraft can be very different from those faced with another vehicle and, therefore, it is best to have a number of analytical tools which can be applied to a given problem. In particular, more problems will be met the smaller the aircraft is.

10.3   Recommendations for Future Work

A number of interesting possibilities exist for building on the research outlined in this thesis. An obvious one is further development of the wind tunnel facility. To start with, the data used for the analysis was from wind tunnel models restricted to 3 DoF motion only. As mentioned, the models tend to be very responsive in heave and will quickly hit the end stops on the vertical rod. This precludes safe testing in 4 DoF without some form of closed-loop height control system. Although such a system had been successfully implemented in previous work [84], it has yet to be reproduced with the updated sensors and instrumentation due to difficulties in obtaining an accurate value of height.

Future work could also explore different approaches to determining the control surface deflections of the models. While the approach adopted in this research worked well, knowledge of control surface positions are crucial for system identification and any inaccuracies in the models of the actuator and control linkage dynamics will directly affect the parameter estimates. Therefore, characterisation of nonlinearities in small, low-cost actuators and the control linkages could be investigated. The motion of the model itself could be also be ascertained using novel techniques, such as vision-based or remote-sensing methods. This would avoid the need to mount sensors and the associated electronics in the model and make the process of scaling the model's masses and inertias to correspond to the full-sized aircraft easier.

Another aspect which may be of interest is real-time parameter estimation for UAVs. The current work has focused on estimation post-flight and, while the extended Kalman filter was discussed in Chapter 7, a study of other real-time estimation algorithms and their application (for both the wind tunnel or flight tests) could be conducted. Other issues for aircraft system identification in general in which there is scope for future research are in the area of nonlinear and unsteady aerodynamics. The flight conditions in which these phenomena occur tend to be at high angles of attack and sideslip. These conditions can be dangerous to fly in, especially for prolonged periods of time. Therefore, the wind tunnel facility may provide a safe means for investigating more complex flight regimes.

References

[1] Anon. "UAS Unmanned Aircraft Systems: The Global Perspective". UVS International Yearbook 2007/2008, Blyenburgh & Co., Paris, 2007.

[2] ESDU. "Aerodynamics Series". Engineering Sciences Data Unit, ESDU International, London.

[3] "USAF Stability and Control DATCOM". Flight Control Division, U.S. Air Force Flight Dynamics Laboratory, Wright-Patterson Air Force Base, Fairborn, OH.

[4] Flux, P. "Some Stability and Control Aspects of UCAV Configurations". *CEAS Aerospace Aerodynamics Research Conference*, London, June 2003.

[5] Cook, M. V. *Flight Dynamics Principles*. Edward Arnold, London, 1997.

[6] Tischler, M. B., and Remple, R. K. *Aircraft and Rotorcraft System Identification: Engineering Methods with Flight Test Examples*. American Institute of Aeronautics and Astronautics, Reston, Virginia, 2006.

[7] Babcock, D. A. and Arena, A. S. "Estimating Aircraft Stability Derivatives Through Finite Element Analysis". *AIAA Atmospheric Flight Mechanics Conference and Exhibit*, Providence, Rhode Island, 2004.

[8] Klausmeyer, S. M. "Drag, Lift, and Pitching Moment Estimates of Transonic Aircraft Using the Navier-Stokes Equations". *42nd AIAA Aerospace Sciences Meeting and Exhibit*, Reno, Nevada, 2004.

[9] Husmeier, D., Dybowski, R. and Roberts, S. *Probabilistic Modeling in Bioinformatics and Medical Informatics*. Springer, London, 2005.

[10] Massart, D. L., Vandeginste, B. G. M., Deming, S.N., Michotte, Y. and Kaufman, L. *Chemometrics : A Textbook*. Elsevier, Amsterdam, 1988.

[11] Berndt, E. R. *The Practice of Econometrics: Classic and Contemporary*. Addison-Wesley, Reading, Massachusetts, 1991.

[12] Bryan, G. H. *Stability in Aviation*. Macmillan, London, 1911.

[13] Glauert, H. "Analysis of Phugoids Obtained by a Recording Airspeed Indicator". Aeronautical Research Council R&M 576, 1919.

[14] Norton, F. H. "The Measurement of the Damping in Roll on a JN4h in Flight". NACA Report 167, 1923.

[15] Norton, F. H. "A Study of Longitudinal Dynamic Stability in Flight". NACA Report 170, 1923.

[16] Greenberg, H. "A Survey of Methods for Determining Stability Parameters of an Airplane from Dynamic Flight Measurements". NACA TN-2340, April 1951.

[17] Hamel, P. G. and Jategaonkar, R. V. "Evolution of Flight Vehicle System Identification". *Journal of Aircraft*. Vol. 33, No. 1, 1996, pp 9-28.

[18] Milliken, W. F. "Progress in Dynamic Stability and Control Research". *Journal of Aeronautical Sciences*. Vol. 14, No. 9, 1947, pp 493-519.

[19] Seamans, R. C., Blasingame, B. P. and Clementson, G. C. "The Pulse Method for the Determination of Aircraft Dynamic Performance". *Journal of Aeronautical Sciences*. Vol. 17, No. 1, 1950, pp 22-38.

[20] Shinbrot, M. "A Least-Squares Curve Fitting Method with Applications to the Calculation of Stability Coefficients from Transient Response Data". NACA TN-2341, April 1951.

[21] Doetsch, K. H. "The Time Vector Method for Stability Investigations". RAE Report Aero 2495, August 1953.

[22] Sternfield, L. "A Vector Method Approach to Dynamic Lateral Stability of Aircraft". *Journal of Aeronautical Sciences*. Vol. 21, No. 4, 1954, pp 251-256.

[23] Wolowicz, C. H. and Holleman, E. C. "Stability-derivative Determination from Flight Data". AGARD Report 224, October 1958.

[24] Burrows, D. A. B. "Development of a Method for Measuring Dynamic Stability Derivatives Using an Analogue Matching Technique". PhD thesis, Cranfield Institute of Technology, 1965.

[25] Wolowicz, C. H. "Considerations in the Determination of Stability and Control Derivatives and Dynamic Characteristics from Flight Data". AGARD AR-549, Part 1, 1966.

[26] Iliff, K.W. *Aircraft Identification Experience*. Paper 6, AGARD Lecture Series No. 104: Parameter Identification, 1979.

[27] Iliff, K. W. and Maine, R. E. "NASA Dryden's Experience in Parameter Estimation and Its Use in Flight Test". *AIAA Atmospheric Flight Mechanics Conference*, San Diego, California, 1982.

[28] Maine, R. E. and Iliff, K. W. "Identification of Dynamic Systems: Theory and Formulation". NASA Reference Publication 1138, 1985.

[29] Wang, K. C. and Iliff, K. W. "Retrospective and Recent Examples of Aircraft Parameter Identification at NASA Dryden Flight Research Center". *Journal of Aircraft*. Vol. 41, No. 4, 2004, pp 752-764.

[30] Morelli, E. A. and Klein, V. "Application of System Identification to Aircraft at NASA Langley Research Center". *Journal of Aircraft*. Vol. 42, No. 1, 2005, pp 12-25.

[31] Klein, V., and Morelli, E. A. *Aircraft System Identification: Theory and Practice*. American Institute of Aeronautics and Astronautics, Reston, Virginia, 2006.

[32] Tischler, M. B. and Cauffman, M. G. "Frequency-Response Method for Rotorcraft System Identification: Flight Applications to BO 105 Coupled Rotor/Fuselage Dynamics". *Journal of the American Helicopter Society*. Vol. 37, No. 3, 1992, pp 3-17.

[33] Jategaonkar, R. V., Fischenberg, D. and von Gruenhagen, W. "Aerodynamic Modelling and System Identification from Flight Data - Recent Applications at DLR". *Journal of Aircraft*. Vol. 41, No. 4, 2004, pp 681-691.

[34] Jategaonkar, Ravindra V. *Flight Vehicle System Identification: A Time Domain Methodology*. American Institute of Aeronautics and Astronautics, Reston, Virginia, 2006.

[35] Mulder, J. A., Sridhar, J. K., and Breeman, J. H. "Identification of Dynamic Systems - Application to Aircraft". AGARD AG-300 Vol.3 Part 2, 1994.

[36] Laban, M. "On-line Aircraft Aerodynamic Model Identification". PhD thesis, Technical University of Delft, 1994.

[37] Ross, A. J. and Foster, G. W. "Fortran Programs for the Determination of Aerodynamic Derivatives from Transient Longitudinal or Lateral Responses of Aircraft". RAE Technical Report 75090, 1975.

[38] Ross, A. J. "Application of Parameter Identification Techniques to Analysis of Flight Data". *Progress in Aerospace Sciences*. Vol. 18, No. 4, 1979, pp 325-350.

[39] Klein, V. "Parameter Identification Applied to Aircraft". PhD thesis, Cranfield Institute of Technology, 1973.

[40] Hui, K., Leach, B., Swail, C., Collins, D. and Srinivasan, R. "Advances in flight test for aerodynamic model identification". *Canadian Aeronautics and Space Journal*. Vol. 47, No. 3, September, 2001, pp 197-205.

[41] Mulder, J. A. "Design and Evaluation of Dynamic Flight Test Manoeuvres". PhD thesis, Delft University of Technology, 1986.

[42] Morelli, E. A. "Practical Input Optimization for Aircraft Parameter Estimation Experiments". PhD thesis, George Washington University, 1990.

[43] Breeman, J. H., van Woerkom, K., Jonkers, H. L. and Mulder, J. A. "Aspects of Flight Test Instrumentation". AGARD LS-104, Novermber 1979, Paper 4.

[44] Mace, W. D. and Pool, A. (eds.). "Basic Principles of Flight Test Instrumentation Engineering". AGARD AG-160, Vol. 1, March 1994.

[45] Crounse, D. R. "Flight Test Instrumentation". AGARD AG-300, Vol. 14, September 1995, Paper 6.

[46] Hodgkinson, J., Boland, J. R., Brandt, M. Q., Lavretsky, E., Rossito, K. F., Stephens, A. T., Stevenson, S. W. and Thompson, T. L. "An Aircraft Manufacturer's View of Parameter Identification". *Proceedings of the Nato/Research and Technology Organisation Symposium on System Identification for Integrated Aircraft Development and Flight Testing*. Madrid, Spain, May, 1998.

[47] Bava, R., Hoare, G. T., Garcia-Mesuro, G. and Oelker, H. "Recent Experiences on Aerodynamic Parameter Identification for EUROFIGHTER at Alenia, British Aerospace, CASA and Daimler-Benz Aerospace". *Proceedings of the Nato/Research and Technology Organisation Symposium on System Identification for Integrated Aircraft Development and Flight Testing*. Madrid, Spain, May, 1998.

[48] Theodore, C. R., Tischler, M. B., and Colbourne, J. D. "Rapid Frequency Domain Modeling Methods for UAV Flight Control Applications". *Journal of Aircraft*. Vol. 41, No. 4, 2004, pp 735-743.

[49] Klein, V. , Ratvasky, T. R. and Cobleigh, B. R. "Aerodynamic Parameters of High-Angle-of-Attack-Research-Vehicle (HARV) Estimated from Flight Data". NASA TM-102692, 1990.

[50] Klein, V. and Murphy, P. C. "Aerodynamic Parameters of High Performance Aircraft Estimated from Wind Tunnel and Flight Test". *Proceedings of the Nato/Research and Technology Organisation Symposium on System Identification for Integrated Aircraft Development and Flight Testing*. Madrid, Spain, May, 1998.

[51] Weiss, S., Friehmelt, H., Plaetschke, E. and Rohlf, D. "X-31A System Identification Using Single-Surface Excitation at High Angles of Attack". *Journal of Aircraft*. Vol. 33, No. 3, 1996, pp 485-490.

[52] Drobik, J. S. and Brian, G. J. "Application of System Identification Techniques to the F-111C and P/C 9/A Aircraft". *Journal of Aircraft*, Vol. 41, N0. 4, 2004, pp 744-751.

[53] Paris, A. C. and Bonner, M. "Nonlinear Model Development from Flight Test Data for F/A-18E Super Hornet". *Journal of Aircraft*. Vol. 41, No. 4, 2004, pp 692-702.

[54] Paris, A. C. and Alaverdi, O.. "Nonlinear Aerodynamic Model Extraction from Flight-Test Data for the S-3B Viking". *Journal of Aircraft*, Vol. 42, N0. 1, 2005, pp 26-32.

[55] Trankle, T. L. and Bachner, S. D. "Identification of a Nonlinear Aerodynamic Model of the F-14 Aircraft". *Journal of Guidance, Control and Dynamics*. Vol. 18, No. 6, pp 1292-1297, 2004.

[56] Morelli, E. A. "Low-Order Equivalent System Identification for Tu-144LL Supersonic Transport Aircraft". *Journal of Guidance, Control and Dynamics*, Vol. 26, No. 2, 2003, pp 354-362.

[57] Napolitano, M. R., Paris, A. C., Seanor, B. A. and Bowers, A. H. "Parameter Estimation for a Cessna U-206 Aircraft Using the Maximum Likelihood Method". *AIAA Atmospheric Flight Mechanics Conference and Exhibit*, Scottsdale, Arizona, 1994.

[58] Kim, E., Kim, Y. and Seong, K. "A Study on the Parameter Estimation for a General Aviation Canard Aircraft ". *AIAA Atmospheric Flight Mechanics Conference and Exhibit*,Austin, Texas, 2003.

[59] Oliveira, J., Chu, Q., Mulder, J., Balini, H. and Vos, W. "Output Error Method and Two Step Method for Aerodynamic Model Identification ". *AIAA Atmospheric Flight Mechanics Conference and Exhibit*, San Francisco, California, 2005.

[60] Milne, G. W., Mulder, J. A., Soijer, M. W., Juliana, S. and Hermansyah, M. R. "Maximum Likelihood Stability and Control Derivative Identification of a Cessna Citation II ". *AIAA Atmospheric Flight Mechanics Conference and Exhibit*, Montreal, Canada, 2001.

[61] Waelkens, S. J. W., Chu, Q. P. and Mulder, J. A. "Aerodynamic Model Identification from Flight Data for the Eclipse 500 Very Light Jet ". *AIAA Atmospheric Flight Mechanics Conference and Exhibit*,San Francisco, California, 2005.

[62] Hui, K.,Ricciardi, J., Ellis, K. and Tuomey, D. "Beechjet Flight Test Data Gathering and Level-D Simulator Aerodynamic Mathematical Model Development ". *AIAA Atmospheric Flight Mechanics Conference and Exhibit*, Montreal, Canada, 2001.

[63] Ham, J. A., Gardner, C. K. and Tischler, M. B. "Flight Testing and Frequency Domain Analysis for Rotorcraft Handling Qualities". *Journal of the American Helicopter Society*,Vol. 40, No. 2, 1995, pp 28-38.

[64] Tischler, M. B., Colbourne, J. D., Jenkins, J. L., Cicolani, L. S., Cheung, K. K., Wright, S. C., Acunzo, A. C., Yakzan, N. S. and Sahasrabudhe, V. "Integrated System Identification and Flight Control Optimization in S-92 Handling Qualities Development". *American Helicopter Society Annual Forum*, May 2001.

[65] Tischler, M. B. and Tomashofski, C. "Flight Test Identification of SH-2G Flapped-Rotor Helicopter Flight Mechanics Models". *Journal of the American Helicopter Society*,Vol. 47, No. 1, 2002, pp 18-32.

[66] Thomson, D. G. and Houston, S. S. "Application of Parameter Estimation to Improved Autogyro Simulation Model Fidelity". *Journal of Aircraft*,Vol. 42, No. 1, 2005, pp 33-40.

[67] Morelli, E. A., Derry, S. D. and Smith, M. S. "Aerodynamic Parameter Estimation for the X-43A (Hyper-X) from Flight Data". AIAA Paper 2005-5921, 2005.

[68] Chowdhary, G. and Lorenz, S. "Control of a VTOL UAV via Online Parameter Estimation". *AIAA Guidance, Navigation and Control Conference and Exhibit*, San Francisco, California, 2005.

[69] Chowdhary, G. and Jategaonkar, R. "Aerodynamic Parameter Estimation from Flight Data Applying Extended and Unscented Kalman Filter". *AIAA Atmospheric Flight Mechanics Conference and Exhibit*, Keystone, Colorado, 2006.

[70] Lisoski, D. L. and Tischler, M. B. "Solar Powered Stratospheric Research Aircraft - Flight Test and System Identification". *Proceedings of the Nato/Research and Technology Organisation Symposium on System Identification for Integrated Aircraft Development and Flight Testing*. Madrid, Spain, May, 1998.

[71] Lucas, J., Martin, B., Ericsson, L., Catterall, C. and Cole, M. "Combining Static Analyses and Frequency Domain System Identification to Enhance the Accuracy of a Fixed-Wing UAV Simulation". *44th AIAA Aerospace Sciences Meeting and Exhibit*, Reno, Nevada, 2006.

[72] Jang, J. S. and Tomlin, C. J. "Longitudinal Stability Augmentation System Design for the DragonFly UAV Using a Single GPS Receiver". *AIAA Guidance, Navigation and Control Conference and Exhibit*, Austin, Texas, 2003.

[73] Kowalchuk, S., Holly, L., Lederbogen, P. and Colgren, R. "UAV Dynamic Modeling and Flight Testing using a Raptor 50 V2 Helicopter". *AIAA Atmospheric Flight Mechanics Conference and Exhibit*, Providence, Rhode Island, 2004.

[74] Holly, L., Kowalchuk, S., Lederbogen, P. and Colgren, R. "University of Kansas UAV Dynamic Modeling and Flight Testing Development Program". *AIAA 3rd "Unmanned Unlimited" Technical Conference, Workshop and Exhibit*, Chicago, Illinois, 2004.

[75] Bhandari, S., Colgren, R., Lederbogen, P. and Kowalchuk, S. "Six-DoF Dynamic Modeling and Flight Testing of a UAV Helicopter". *AIAA Modeling and Simulation Technologies Conference and Exhibit*, San Francisco, California, 2005.

[76] Bhandari, S. and Colgren, R. "6-DoF Dynamic Model for a Raptor 50 UAV Helicopter Including Stabilizer Bar Dynamics". *AIAA Modeling and Simulation Technologies Conference and Exhibit*, Keystone, Colorado, 2006.

[77] Hsiao, F., Chan, W., Lai, Y., Tseng, L., Hsieh, S. and Tenn, H. "Landing Longitudinal Control System Design for a Fixed Wing UAV". *45th AIAA Aerospace Sciences Meeting and Exhibit*, Reno, Nevada, 2007.

[78] Ippolito, C., Yeh, Y., and Kaneshige, J. "Neural Adaptive Flight Control Testing on an Unmanned Experimental Aerial Vehicle". *AIAA Infotech@Aerospace 2007 Conference and Exhibit*, Rohnert Park, California, 2007.

[79] Spaulding, C. M., Mansur, M. H., Tischler, M. B., Hess, R. A. and Franklin, J. A. "Nonlinear Inversion Control for a Ducted Fan UAV". *AIAA Atmospheric Flight Mechanics Conference and Exhibit*, San Francisco, California, 2005.

[80] Malik, I. A. "The design, development and evaluation of an active control aircraft model wind tunnel facility". PhD thesis, College of Aeronautics, Cranfield Institute of Technology, 1982.

[81] Kumar, H. "A preliminary study into the design of a free flight wind tunnel model for demonstrating the dynamic characteristics of aircraft". Master's thesis, College of Aeronautics, Cranfield Institute of Technology, 1980.

[82] Heydari, F. "On the estimation of stability and control characteristics of a generalised forward swept wing aircraft". PhD thesis, College of Aeronautics, Cranfield Institute of Technology, 1986.

[83] Hinds, H. A. "The application of a modified stepwise regression (MSR) method to the estimation of aircraft stability and control derivatives". PhD thesis, College of Aeronautics, Cranfield Institute of Technology, 1996.

[84] S. W. Filmer. "Artificial G control system for the dynamic wind tunnel facility". Master's thesis, College of Aeronautics, Cranfield Institute of Technology, 1989.

[85] Orlik-Ruckemann, K. "Review of Techniques for Determination of Dynamic Stability Parameters in Wind Tunnels". AGARD LS-114, 1981, Paper 3.

[86] Bennett, R. M., Farmer, M. G., Mohr, R. L., and Hall, E. W. "Wind Tunnel Technique for Determination of Dynamic Stability Derivatives from Cable-Mounted Models". *Journal of Aircraft*. Vol. 15, No. 5, 1978, pp 304-309.

[87] Subke, H. "Test Installations To Investigate The Dynamic Behaviour Of Aircraft With Scaled Models In Wind Tunnels". *Transactions of the Institute of Measurement and Control*. Vol. 1, No. 3, 1979, pp 135-140.

[88] Krag, B. "The Wind Tunnel Behaviour Of A Scaled Model With A Gust Alleviation System In A Deterministic Gust Field". *Transactions of the Institute of Measurement and Control*. Vol. 1, No. 3, 1979, pp 141-153.

[89] Cook, M. V. "On the use of small scale aircraft models for dynamic wind tunnel investigation of stability and control". *Transactions of the Institute of Measurement and Control*. Vol. 9, No. 4, 1987, pp 190-197.

[90] Rajamurthy, M. S. "Generation Of Comprehensive Longitudinal Aerodynamic Data Using Dynamic Wind-Tunnel Simulation". *Journal of Aircraft*. Vol. 34, No.1, 1997, pp 29-33.

[91] "Airplane Simulator Qualification". FAA Advisory Cicular, AC 120-40C, Draft Version, July 1995.

[92] "Joint Aviation Requirements - Aeroplane Flight Simulators". JAR-STD 1A, Westward Digital, Cheltenham, April 1997.

[93] Lee, R. E. "Handling Qualities". AGARD-AR-300 Vol. 14, Paper No. 15, September 1995.

[94] "Flying Qualities of Piloted Vehicles". MIL-HDBK-1797A, Department of Defense, December 1997.

[95] "Airworthiness Standards: Normal, Utility, and Acrobatic Category Airplanes". Federal Aviation Regulations, Part 23.

[96] "Airworthiness Standards: Transport Category Airplanes". Federal Aviation Regulations, Part 25.

[97] Plaetschke, E. and Schulz, G. "Practical Input Signal Design". AGARD LS-104, November 1979, Paper 3.

[98] Cooke, A. K. "Simulation Model of the NFLC Jetstream 31". College of Aeronautics Report 0402, Cranfield Uinversity, May 2006.

[99] Buonanno, A. "Flight Dynamics Model of the Flying Demonstrator UAV". FLAVIIR Project Internal Report, FLAV-A01-003, 2005.

[100] Buonanno, A. "Modified Configuration (2) of the Flying Demonstrator UAV". FLAVIIR Project Internal Report, FLAV-A01-005, 2005.

[101] Titterton, D. H. and Weston, J. L. *Strapdown Inertial Navigation Technology*. Institution of Engineering and Technology, Stevenage, 2nd edition, 2004.

[102] Merhav, S. *Aerospace Sensor Systems and Applications*. Springer-Verlag, New York, 1996.

[103] Kayton, M. and Fried, W. R. (eds.). *Avionics Navigation Systems*. John Wiley & Sons, New York, 2nd edition, 1997.

[104] Barbour, N. M. "Inertial Navigation Sensors". RTO SET Educational Notes, RTO-EN-SET-064, February 2004.

[105] Barbour, N., Anderson, R., Connelly, J., Hanson, D., Kourepenis, A., Sitomer, J., Ward, P. "Inertial MEMS System Applications". RTO SET Educational Notes, RTO-EN-SET-064, February 2004.

[106] Yadzi, N., Ayazi, F. and Najafi, K. "Micromachined Inertial Sensors". *Proceedings of the IEEE*. Vol. 86, No. 8, 1998, pp 1640-1659.

[107] Gebre-Egziabher, D., Hayward, R. C. and Powell, J. D. "Design of Multi-Sensor Attitude Determination Systems". *IEEE Transactions on Aerospace and Electronic Systems*. Vol. 40, No. 2, 2004, pp 627-649.

[108] Gebre-Egziabher, D., Hayward, R. C. and Powell, J. D. "A Low-cost GPS/Inertial Attitude Heading Reference System (AHRS) for General Aviation". *IEEE Position, Location and Navigation Symposium 1998*. pp 518-525.

[109] Caruso, M. J. "Application of Magnetoresistive Sensors in Navigation Systems". Honeywell Inc., February 1997.

[110] Lam, Q. M., Stamatakos, N., Woodruff, C. and Ashton, S. "Gyro Modeling and Estimation of Its Random Noise". *AIAA Guidance, Navigation and Control Conference and Exhibit*, Austin, Texas, 2003.

[111] Ng, L. C. and Pines, D. J. "Characterization of Ring Laser Gyro Performance Using the Allan Varianc Method". *Journal of Guidance, Control and Dynamics*. Vol. 20, No. 1, 1997, pp 211-214.

[112] IEEE Std 647-2006. "IEEE Standard Specification Format Guide and Test Procedures for Single Axis Laser Gyros". IEEE Aerospace and Electronic System Society, September 2006.

[113] Markley, F. L., Crassidis, J. L. and Cheng, Y. "Nonlinear Attitude Filtering Methods". *AIAA Guidance, Navigation and Control Conference and Exhibit*, San Francisco, California, 2005.

[114] Rogers, R. M. *Applied Mathematics in Integrated Navigation Systems*. American Institute of Aeronautics and Astronautics, Reston, Virginia, 2nd edition, 2003.

[115] Haering, E. A. "Airdata Measurement and Calibration". AGARD AG-300, Vol. 14, September 1995, Paper 11.

[116] Whitmore, S. A., Moes, T. R. and Larson, T. J. "High Angle-of-Attack Flush Airdata Sensing System". *Journal of Aircraft*. Vol. 29, No. 5, 1992, pp 915-919.

[117] Parameswaran, V., Jategaonkar, R. V. and Press, M. "Calibration of Five-Hole Probe for Flow Angles from Dynamic and Tower Flyby Maneuvers". *Journal of Aircraft*. Vol. 42, No. 1, 2005, pp 80-86.

[118] Zeiger, M. and Rediniotis, O. "Embedded-Sensor Air-Dat Systems for UAVs". *AIAA's 1st Technical Conference and Workshop on Unmanned Aerospace Vehicles*, Portsmouth, Virginia, 2002.

[119] Rediniotis, O. K., Johansen, E. S., Tsao, T., Seifert, A. and Pack, L. G. MEMS-Based Probes for Velocity and Pressure Measurements in Unsteady and Turbulent Flowfields". *37th AIAA Aerospace Sciences Meeting and Exhibit*, Reno, Nevada, 1999.

[120] Allen, R., Traub, L., Johansen, E. S., Rediniotis, O. K. and Tsao, T. A MEMS-Based 5-Sensor Probe". *38th AIAA Aerospace Sciences Meeting and Exhibit*, Reno, Nevada, 2000.

[121] Shannon, C. E. "Communication in the Presence of Noise". *Proceedings of the IRE*, Vol. 37, No.1, 1949, pp 10-21.

[122] Fielding, C. and Flux, P. K. "Non-linearities in Flight Control Systems". *The Aeronautical Journal*. Vol. 107, No. 1077, 2003, pp 673-696.

[123] Montgomery, D. C., Peck, E. A. and Vining, G. G. *Introduction to Linear Regression Analysis*. Wiley, New York, 2001.

[124] Mendel, J. M. *Discrete Techniques of Parameter Estimation: The Equation Error Formulation*. Marcel Dekker, New York, 1973.

[125] Laban, M. and Masui, K. "Total Least Squares Estimation of Aerodynamic Model Parameters from Flight Data". *Journal of Aircraft*. Vol. 30, No. 1,1993, pp 150-152.

[126] Klein, V. "Identification Evaluation Methods". AGARD LS-104, November 1979, Paper 2.

[127] Morelli, E. A. "Estimating Noise Characteristics from Flight Test Data using Optimal Fourier Smoothing". *Journal of Aircraft*, Vol. 32, No. 4, 1995, pp 689-695.

[128] Morelli, E. A. "Practical Aspects of the Equation-Error Method for Aircraft Parameter Estimation". *AIAA Atmospheric Flight Mechanics Conference and Exhibit*, Keystone, Colorado, 2006.

[129] Upton, G. and Cook, I. *A Dictionary of Statistics*. Oxford University Press, Oxford, 2nd edition, 2006.

[130] Kreyszig, E. *Advanced Engineering Mathematics*. John Wiley, New York, 8th edition, 1999.

[131] Maine, R. E. and Iliff, K. W. "Application of Parameter Estimation to Aircraft Stability and Control: The Output-Error Approach". NASA Reference Publication 1168, 1986.

[132] Maine, R. E. and Iliff, K. W. "The Theory and Practice of Estimating the Accuracy of Dynamic Flight-Determined Coefficients". NASA Reference Publication 1077, 1981.

[133] Morelli, E. A. and Klein, V. "Accuracy of Aerodynamic Model Parameters Estimated from Flight Test Data". *Journal of Guidance, Control, and Dynamics*. Vol. 20, No. 1, 1997, pp 74-80.

[134] Klein, V. and Batterson, J. G. "Determination of Airplane Model Structure from Flight Data Using Splines and Stepwise Regression". NASA TP-2126, March 1983.

[135] Steers, S. T., and Iliff, K. W. "Effects of Time-shifted Data on Flight-Determined Stability and Control Derivatives". NASA-TN-D-7830, March 1975.

[136] Eykhoff, P. *System Identification: Parameter and State Estimation*. John Wiley & Sons, London, 1977.

[137] Iliff, K. W. and Taylor, L. W. "Determination of Stability Derivatives from Flight Data Using a Newton-Raphson Minimization Technique". NASA TN D-6579, 1972.

[138] Chapra, S. C. and Canale, R. P. *Numerical Methods for Engineers: with Programming and Software Applications*. McGraw-Hill, Boston, 4th edition, 2002.

[139] Maine, R. E. and Iliff, K. W. "Formulation and Implementation of a Practical Algorithm for Parameter Estimation with Process and Measurement Noise". *SIAM Journal of Applied Mathematics*, Vol. 41, No. 3, 1981, pp. 558-579.

[140] Foster, G. W. "The Identification of Aircraft Stability and Control Parameters in Turbulence ". PhD thesis, Cranfield Institute of Technology, 1982.

[141] Purcell, A. G. "The Development of Quasi-Newton Methods for Unconstrainted Minimisation". RAE Technical Report 77132, 1977.

[142] Jategaonkar, R. V. and Plaetschke, E. "Maximum Likelihood Estimation of Parameters in Nonlinear Flight Mechanics Systems". *Proceedings of the IFAC Symposium on "Identification and System Parameter Estimation"*, York, 1985, pp 665-668.

[143] Murphy, P. C. "A Methodology for Airplane Parameter Estimation and Confidence Interval Determination in Nonlinear Estimation Problems". NASA RP 1153, April 1986.

[144] Blackwell, J. and Feik, R. A. "Identification of Time Delays in Flight Measurement". *Journal of Guidance, Control, and Dynamics*. Vol. 14, No. 1, 1991, pp 132-139.

[145] Morelli, E. A. "High Accuracy Evaluation of the Finite Fourier Transform Using Sampled Data". NASA TM 110340, 1997.

[146] Klein, V. "Aircraft Parameter Estimation in Frequency Domain". *AIAA Atmospheric Flight Mechanics Conference*, Palo Alto, California, 1978.

[147] Bendat, J. S. and Piersol, A. G. *Random Data Analysis and Measurement Procedures*. Wiley, New York, 2nd edition, 1986.

[148] Dryden, H. L. "A Review of the Statistical Theory of Turbulence". *Turbulence: Classic Papers on Statistical Theory*, edited by S. K. Friedlander and L. Topper, Interscience, New York, 1961, pp 115-150.

[149] Schulz, G. "Influence of Gust Modelling on the Identification of the Derivatives of the Longitudinal Motion of an Aircraft". RAE Library Translation 1944, 1977.

[150] Ljung, L. "Asymptotic Behavior of the Extended Kalman Filter as a Parameter Estimator for Linear Systems". *IEEE Transactions on Automatic Control*. Vol. AC-24, No. 1, 1979, pp 36-50.

[151] Julier, S. and Uhlmann, J. K. "Unscented Filtering and Nonlinear Estimation". *Proceedings of the IEEE*. Vol. 92, 2004, pp 401-422.

[152] Malik, I. A. "Preliminary Calibration of the 42 inches Diameter 'Weybridge' Tunnel". College of Aeronautics Memo 8008, October 1980.

[153] Jategaonkar, R. V. and Thielecke, F. "Evaluation of Parameter Estimation Methods for Unstable Aircraft". *Journal of Aircraft*. Vol. 33, No. 1,1996, pp 9-28.

[154] Klein, V. "Estimation of Aircraft Aerodynamic Parameters from Flight Data". *ProgRess in Aerospace Sciences*. Vol. 26, No. 1,1989, pp 1-77.

[155] Belsley, D. A., Kuh, E. and Welsh, R. E. *Regression Diagnostics: Identifying Influential Data and Sources of Collinearity*. John Wiley, New York, 1980.

[156] Anderson, L. C. "Robust Parameter Identification for Nonlinear Systems Using a Principal Components Regression Algorithm". AIAA Paper 85-1766, August 1985.

[157] Hoerl, A. E., Kannard, R. W. and Baldwin, K. F. "Ridge Regression: Some Simulations". *Communications in Statistics - Theory and Methods*. Vol. 4, No. 2, 1975, pp 105-123.

[158] Klein, V., Batterson, J. G. and Murphy, P. C. "Determination of Airplane Model Structure from Flight Data Using Modified Stepwise Regression". NASA TP-1916, October 1981.

[159] Rauch, H. E., Tung, F. and Striebel, C. T. "Maximum Likelihood Estimation of Linear Dynamic Systems". *AIAA Journal*, Vol. 3, No. 8, 1965, pp 1445-1450.

[160] Brown, R. G. and Hwang, P. Y. C. *Introduction to Random Signals and Applied Kalman Filtering*. John Wiley & Sons, New York, 3rd edition, 1997.

[161] Klein, V. and Schiess, J. R. "Compatibility Check of Measured Aircraft Responses Using Kinematic Equations and Extended Kalman Filter". NASA TN D-8514, August 1977.

[162] Mulder, J. A., Chu, Q. P., Sridhar, J. K., Breeman, J. H. and Laban, M. "Non-linear Aircraft Flight Path Reconstruction Review and New Advances". *Progress in Aerospace Sciences*, Vol. 35, No. 6, 1999, pp 673-726.

[163] Etkin, B. *Dynamics of Flight: Stability and Control*. John Wiley & Sons, New York, 1959.

[164] Bach, R. E. "State Estimation Applications in Aircraft Flight Data Analysis". NASA RP 1252, March 1991.

[165] Carnduff, S. D. and Cooke, A. K. "Formulation and System Identification of the Equations of Motion for a Dynamic Wind Tunnel Facility". College of Aeronautic Report 0801, Cranfield University, March 2008.

Appendix A

4 DoF Equations of Motion

A.1   Description of Equations of Motion

The equations of motion for a model on the rig can be developed from first principles in a similar manner to those for a 6 DoF free-flying aircraft. This was been done by Carnduff and Cooke [165], with a summary of the equations given in this section.

For the current discussion, it is assumed that motion of the model on the rig can be approximated by small perturbations from an initial equilibrium or trim condition and that longitudinal and lateral/directional motion can be suitably decoupled. Equations describing the model's dynamics are referenced to a Cartesian axis system with origin fixed at a given point within the model. The most convenient choice for the axes origin is the location of the gimbal, as this is the point about which the model manoeuvres relative to the rig. It is also noted that, when the wind tunnel tests were conducted, the gimbal and the model centre of gravity were coincident. The wind tunnel velocity vector is assumed to act parallel to the ground, so the model's pitch attitude θ and angle of attack α are the same. Also, when the model is wings level, a positive yaw angle ψ (nose to starboard) equates to a negative sideslip angle β. For the case where the model is experiencing zero roll, pitch and yaw angles, motion is restricted along the x and y axes.

In comparison to the longitudinal motion of an equivalent free-flying aircraft, axial velocity perturbations experienced by the model will be suppressed by the rig. It is, therefore, not possible to simulate the aircraft's phugoid, as axial velocity is a dominant variable in this particular mode of motion. However, it is possible to use the rig to simulate the aircraft's short period. This mode of motion is characterised by oscillations in heave and pitch, which are variables unconstrained by the rig (although heaving motion is restricted by the length of the rig's vertical rod). The inability to simulate the phugoid is not considered a great disadvantage in the use of the rig for predicting the dynamics of the full-sized aircraft. This is because it is usually the short period dynamics that are of particular interest when, for example, designing stability augmentation and flight control systems and performing handling qualities analysis [5].

The longitudinal equations of motion of the model can be expressed in state-space form as

$$\begin{bmatrix} \dot{w} \\ \dot{q} \end{bmatrix} = \begin{bmatrix} z_w & z_q \\ m_w & m_q \end{bmatrix} \begin{bmatrix} w \\ q \end{bmatrix} + \begin{bmatrix} z_\eta \\ m_\eta \end{bmatrix} \eta \qquad\qquad (A.1.1)$$

where w is the model's normal velocity, q its pitch rate and η denotes elevator deflection. These variables represent perturbations from initial values needed to trim the model. The stability and control derivatives z_w, z_q, z_η, m_w, m_q and m_η are given in concise form, the definitions of which can be found, for example, in Cook [5]. As expected from the description of the constrained longitudinal motion above, Equation (A.1.1) is identical to the short period approximation of a free-flying aircraft.

In this case where the model is permitted to manoeuvre in 3 DoF only, the longitudinal equations of motion become,

$$\begin{bmatrix} \dot{w} \\ \dot{q} \end{bmatrix} = \begin{bmatrix} 0 & V_T \\ m_w & m_q \end{bmatrix} \begin{bmatrix} w \\ q \end{bmatrix} + \begin{bmatrix} 0 \\ m_\eta \end{bmatrix} \eta \tag{A.1.2}$$

where V_T is the wind tunnel velocity.

For motion in the lateral/directional plane, the principal difference between motion of the model and the aircraft is that the rig suppresses lateral translation. This means that the spiral mode is not simulated in the wind tunnel, but roll-subsidence and dutch roll motion are observed. As with the longitudinal case, this is not viewed as a major drawback as it is generally the short term roll-subsidence and dutch roll modes, rather than the long term spiral mode, that are of interest.

The roll mode of the wind tunnel model can be approximated by the single degree of freedom equation

$$\dot{p} = l_p p + l_\xi \xi \tag{A.1.3}$$

where p is the model's roll rate, ξ represents the input to the ailerons and l_p and l_ξ are the stability and control derivatives. The dutch roll dynamics can be described by the expression,

$$\begin{bmatrix} \dot{v} \\ \dot{r} \end{bmatrix} = \begin{bmatrix} 0 & -V_T \\ n_v & n_r \end{bmatrix} \begin{bmatrix} v \\ r \end{bmatrix} + \begin{bmatrix} 0 \\ n_\zeta \end{bmatrix} \zeta \tag{A.1.4}$$

where v denotes sideslip velocity, r is yaw rate and ζ represents the rudder input. Due to the suppression of any lateral motion, the sideforce derivatives with respect to v and ζ are zero. The suppression of the model's lateral translation means that the dutch roll mode simulated in the wind tunnel is only an approximation of the free-flight case.

Appendix B

Properties of Least Squares Estimates

B.1 Ideal Case

The properties of least squares estimates can be examined in terms of bias, covariance of the parameter estimation error and consistency [34, 31]. First, the case in which the equation errors are uncorrelated with the regressors, are characterised by white noise with zero mean and variance σ^2 and the regressors are known without error is investigated.

Bias is found by examining the expected value of the least squares estimates $\mathrm{E}[\hat{\boldsymbol{\theta}}]$. From Equation (4.2.7),

$$\mathrm{E}[\hat{\boldsymbol{\theta}}] = \mathrm{E}[(\mathbf{X}^T\mathbf{X})^{-1}\mathbf{X}^T\mathbf{z}] \tag{B.1.1}$$

Replacing $\mathbf{z}$ with the expression in Equation (4.2.3) leads to,

$$\begin{aligned}
\mathrm{E}[\hat{\boldsymbol{\theta}}] &= \mathrm{E}[(\mathbf{X}^T\mathbf{X})^{-1}\mathbf{X}^T(\mathbf{X}\boldsymbol{\theta} + \boldsymbol{\epsilon})] \\
&= \mathrm{E}[(\mathbf{X}^T\mathbf{X})^{-1}\mathbf{X}^T\mathbf{X}\boldsymbol{\theta}] + \mathrm{E}[(\mathbf{X}^T\mathbf{X})^{-1}\mathbf{X}^T\boldsymbol{\epsilon}] \\
&= \mathrm{E}[\boldsymbol{\theta}] + \mathrm{E}[(\mathbf{X}^T\mathbf{X})^{-1}\mathbf{X}^T\boldsymbol{\epsilon}]
\end{aligned} \tag{B.1.2}$$

Now, for two independent variables A and B, the expected value of their product is equal to the product of their individual expected values [34] i.e.,

$$\mathrm{E}[AB] = \mathrm{E}[A]\mathrm{E}[B] \tag{B.1.3}$$

Therefore, as the equation errors are uncorrelated with the regressors,

$$\mathrm{E}[(\mathbf{X}^T\mathbf{X})^{-1}\mathbf{X}^T\boldsymbol{\epsilon}] = \mathrm{E}[(\mathbf{X}^T\mathbf{X})^{-1}\mathbf{X}^T]\mathrm{E}[\boldsymbol{\epsilon}] \tag{B.1.4}$$

Also, $\mathrm{E}[\boldsymbol{\theta}]$ is simply the true value of the unknown parameter vector $\boldsymbol{\theta}$ and, under the outlined assumptions, the regressors are known without error, therefore their expected values are the same as their actual values, thus Equation (B.1.2) reduces to,

$$\mathrm{E}[\hat{\boldsymbol{\theta}}] = \boldsymbol{\theta} + (\mathbf{X}^T\mathbf{X})^{-1}\mathbf{X}^T\mathrm{E}[\boldsymbol{\epsilon}] \tag{B.1.5}$$

However, the expected value of the equation errors is zero so,

$$\mathrm{E}[\hat{\boldsymbol{\theta}}] = \boldsymbol{\theta} \tag{B.1.6}$$

In other words, for the given assumptions, the least squares estimates are unbiased.

The parameter error covariance matrix, often referred to simply as the parameter covariance matrix, is defined as,

$$\mathbf{P} = \mathrm{E}[(\hat{\boldsymbol{\theta}} - \boldsymbol{\theta})(\hat{\boldsymbol{\theta}} - \boldsymbol{\theta})^T] \tag{B.1.7}$$

Expanding the terms in Equation (B.1.7) and using the result from Equation (B.1.6), it can be shown that,

$$\mathbf{P} = \mathrm{E}[\hat{\boldsymbol{\theta}}\hat{\boldsymbol{\theta}}^T] - \boldsymbol{\theta}\boldsymbol{\theta}^T \tag{B.1.8}$$

Substituting (4.2.7) into (B.1.8) and noting that in matrix algebra $(\mathbf{AB})^T = \mathbf{B}^T\mathbf{A}^T$,

$$
\begin{aligned}
\mathbf{P} &= \mathrm{E}\left[\left((\mathbf{X}^T\mathbf{X})^{-1}\mathbf{X}^T\mathbf{z}\right)\left((\mathbf{X}^T\mathbf{X})^{-1}\mathbf{X}^T\mathbf{z}\right)^T\right] - \boldsymbol{\theta}\boldsymbol{\theta}^T \\
&= \mathrm{E}\left[(\mathbf{X}^T\mathbf{X})^{-1}\mathbf{X}^T\mathbf{z}\mathbf{z}^T\mathbf{X}(\mathbf{X}^T\mathbf{X})^{-1}\right] - \boldsymbol{\theta}\boldsymbol{\theta}^T \\
&= (\mathbf{X}^T\mathbf{X})^{-1}\mathbf{X}^T\mathrm{E}[\mathbf{z}\mathbf{z}^T]\mathbf{X}(\mathbf{X}^T\mathbf{X})^{-1} - \boldsymbol{\theta}\boldsymbol{\theta}^T
\end{aligned}
\tag{B.1.9}
$$

The term $\mathrm{E}[\mathbf{z}\mathbf{z}^T]$ can be expanded using Equation (4.2.3),

$$
\begin{aligned}
\mathrm{E}[\mathbf{z}\mathbf{z}^T] &= \mathrm{E}[(\mathbf{X}\boldsymbol{\theta} + \boldsymbol{\epsilon})(\mathbf{X}\boldsymbol{\theta} + \boldsymbol{\epsilon})^T] \\
&= \mathrm{E}[\mathbf{X}\boldsymbol{\theta}\boldsymbol{\theta}^T\mathbf{X}^T + \boldsymbol{\epsilon}\boldsymbol{\theta}^T\mathbf{X}^T + \mathbf{X}\boldsymbol{\theta}\boldsymbol{\epsilon}^T + \boldsymbol{\epsilon}\boldsymbol{\epsilon}^T] \\
&= \mathbf{X}\boldsymbol{\theta}\boldsymbol{\theta}^T\mathbf{X}^T + \mathrm{E}[\boldsymbol{\epsilon}]\boldsymbol{\theta}^T\mathbf{X}^T + \mathbf{X}\boldsymbol{\theta}\mathrm{E}[\boldsymbol{\epsilon}^T] + \mathrm{E}[\boldsymbol{\epsilon}\boldsymbol{\epsilon}^T]
\end{aligned}
\tag{B.1.10}
$$

Assuming, again, that the equation errors have zero mean and a covariance of $\mathrm{E}\left[\boldsymbol{\epsilon}\boldsymbol{\epsilon}^T\right] = \sigma^2\mathbf{I}$, then Equation (B.1.10) becomes,

$$\mathrm{E}[\mathbf{z}\mathbf{z}^T] = \mathbf{X}\boldsymbol{\theta}\boldsymbol{\theta}^T\mathbf{X}^T + \sigma^2\mathbf{I} \tag{B.1.11}$$

Substituting Equation (B.1.11) into (B.1.9) gives,

$$
\begin{aligned}
\mathbf{P} &= (\mathbf{X}^T\mathbf{X})^{-1}\mathbf{X}^T(\mathbf{X}\boldsymbol{\theta}\boldsymbol{\theta}^T\mathbf{X}^T + \sigma^2\mathbf{I})\mathbf{X}(\mathbf{X}^T\mathbf{X})^{-1} - \boldsymbol{\theta}\boldsymbol{\theta}^T \\
&= \boldsymbol{\theta}\boldsymbol{\theta}^T + \sigma^2(\mathbf{X}^T\mathbf{X})^{-1} - \boldsymbol{\theta}\boldsymbol{\theta}^T \\
&= \sigma^2(\mathbf{X}^T\mathbf{X})^{-1}
\end{aligned}
\tag{B.1.12}
$$

It can be shown that the least squares estimate $\hat{\boldsymbol{\theta}}$, with covariance given by Equation (B.1.12) above, is a minimum variance, or efficient, estimate [123]. This, along with the result of the estimate being unbiased, is known as the Gauss-Markov theorem.

An estimator is said to be consistent if, as the number of data point used in the analysis increases, the parameter estimates converge on their true values. To investigate the consistency of the least squares estimator, the expression for the parameter covariance matrix in Equation (B.1.12) is rewritten as [126, 34],

$$\mathbf{P} = \frac{1}{N}\sigma^2\left(\frac{1}{N}\mathbf{X}^T\mathbf{X}\right)^{-1} \tag{B.1.13}$$

Taking the limit as $N \to \infty$,

$$\lim_{N\to\infty}\mathbf{P} = \lim_{N\to\infty}\left\{\frac{1}{N}\sigma^2\left(\frac{1}{N}\mathbf{X}^T\mathbf{X}\right)^{-1}\right\} = 0 \tag{B.1.14}$$

where it is assumed that the inverse term exists. Equation (B.1.14) implies that there is no error in the estimate $\hat{\boldsymbol{\theta}}$, so the least squares estimate is equal to the true parameter vector $\boldsymbol{\theta}$.

To summarise, under the assumption that the equation errors are uncorrelated with the regressors, are characterised by white noise with zero mean and variance σ^2 and that the regressors are known without error, the least squares estimator is an unbiased, efficient and consistent estimator.

B.2 Practical Case

In practice, measured variables will always contain errors, hence the assumption that the regressors are known without error is likely to be invalid. Errors in measured signals tend to be either systematic, such as bias or scale factor errors, or random measurement noise. Another source of error is the effects of atmospheric turbulence, which is modelled as process noise. Therefore, the properties of the least squares estimator, when these errors sources are present, are investigated next.

Consider the case where measurements of the regressors $\mathbf{X}$ are corrupted by a constant bias error $\Delta\mathbf{X}$ and random measurement noise $\mathbf{v_x}$ having zero mean. The true value of the regressor matrix is,

$$\mathbf{X}_T = \mathbf{X} - \Delta\mathbf{X} - \mathbf{v_x} \tag{B.2.1}$$

The dependent variable $\mathbf{y}$ is then modelled as,

$$\begin{aligned} \mathbf{y} &= \mathbf{X}_T\boldsymbol{\theta} + \mathbf{w} \\ &= (\mathbf{X} - \Delta\mathbf{X} - \mathbf{v_x})\boldsymbol{\theta} + \mathbf{w} \end{aligned} \tag{B.2.2}$$

where $\mathbf{w}$ is a vector of white noise with zero mean representing the effects of atmospheric turbulence. The measurements of the dependent variable are also corrupted by noise,

$$\mathbf{z} = \mathbf{y} + \mathbf{v_y} \tag{B.2.3}$$

where $\mathbf{v_y}$ is a white noise process with zero mean. To investigate the bias and covariance of the estimates under the above conditions, Equation (B.2.2) is first premultiplied by the term $(\mathbf{X}^T\mathbf{X})^{-1}\mathbf{X}^T$ [126, 34],

$$\left(\mathbf{X}^T\mathbf{X}\right)^{-1}\mathbf{X}^T\mathbf{y} = \left(\mathbf{X}^T\mathbf{X}\right)^{-1}\mathbf{X}^T(\mathbf{X} - \Delta\mathbf{X} - \mathbf{v_x})\boldsymbol{\theta} + \left(\mathbf{X}^T\mathbf{X}\right)^{-1}\mathbf{X}^T\mathbf{w} \tag{B.2.4}$$

Using Equation (B.2.3), Equation (B.2.4) can be rewritten as,

$$\left(\mathbf{X}^T\mathbf{X}\right)^{-1}\mathbf{X}^T(\mathbf{z} - \mathbf{v_y}) = \left(\mathbf{X}^T\mathbf{X}\right)^{-1}\mathbf{X}^T(\mathbf{X} - \Delta\mathbf{X} - \mathbf{v_x})\boldsymbol{\theta} + \left(\mathbf{X}^T\mathbf{X}\right)^{-1}\mathbf{X}^T\mathbf{w} \tag{B.2.5}$$

Next, after substituting (4.2.7) into (B.2.5) and rearranging the resultant expression, the least squares estimate is given by,

$$\hat{\boldsymbol{\theta}} = \boldsymbol{\theta} + \left(\mathbf{X}^T\mathbf{X}\right)^{-1}\mathbf{X}^T[\mathbf{w} + \mathbf{v_y} - (\Delta\mathbf{X} + \mathbf{v_x})\boldsymbol{\theta}] \tag{B.2.6}$$

The expected value of the estimator is then,

$$\mathrm{E}[\hat{\boldsymbol{\theta}}] = \boldsymbol{\theta} + \mathrm{E}\left[\left(\mathbf{X}^T\mathbf{X}\right)^{-1}\mathbf{X}^T[\mathbf{w} + \mathbf{v_y} - (\Delta\mathbf{X} + \mathbf{v_x})\boldsymbol{\theta}]\right] \tag{B.2.7}$$

Remembering, from Equation (B.1.3), that the expectation of the product of two independent variables is equal to the product of each variable's expected value, and that $\mathbf{w}$ and $\mathbf{v_y}$ are assume to have zero mean then the expected value of the least squares estimate becomes,

$$\mathrm{E}[\hat{\boldsymbol{\theta}}] = \boldsymbol{\theta} - \mathrm{E}[(\mathbf{X}^T\mathbf{X})^{-1}\mathbf{X}^T(\Delta\mathbf{X} + \mathbf{v_x})]\boldsymbol{\theta} \qquad (\text{B.2.8})$$

Hence, for the more realistic case accounting for the effects of measurement errors and atmospheric turbulence, the least squares estimate is shown to be biased. It is also interesting to note that, under the assumption of $\mathbf{w}$ and $\mathbf{v_y}$ having zero mean, the bias is due entirely to errors in the knowledge of the regressors.

Focusing now on the parameter covariance matrix, from Equation (B.1.8),

$$\mathbf{P} = \mathrm{E}[\hat{\boldsymbol{\theta}}\hat{\boldsymbol{\theta}}^T] - \boldsymbol{\theta}\boldsymbol{\theta}^T \qquad (\text{B.2.9})$$

Inserting Equation (B.2.6) into (B.2.9) and again using the property of products of expected values from Equation (B.1.3), it can be shown that [126],

$$\begin{aligned}
\mathbf{P} = \ &\mathrm{E}\left[(\mathbf{X}^T\mathbf{X})^{-1}\mathbf{X}^T(\mathbf{w} + \mathbf{v_y})(\mathbf{w} + \mathbf{v_y})^T\mathbf{X}(\mathbf{X}^T\mathbf{X})^{-1}\right] \\
&+ \mathrm{E}\left[(\mathbf{X}^T\mathbf{X})^{-1}\mathbf{X}^T(\Delta\mathbf{X} + \mathbf{v_x})\boldsymbol{\theta}\boldsymbol{\theta}^T(\Delta\mathbf{X} + \mathbf{v_x})^T\mathbf{X}(\mathbf{X}^T\mathbf{X})^{-1}\right]
\end{aligned} \qquad (\text{B.2.10})$$

So, from Equation (B.2.10), it can be concluded that, while the bias of the least squares estimates is due solely to errors in the regressors, the variance is affected by measurement errors (in both the regressors and the dependent variable) and process noise.

Appendix C

Standardised Regressors

C.1 Formulation of Standardised Regressors

This section describes the formulation of the standardised regressors used when carrying out a collinearity diagnostic and biased estimation. Each of the regressors and the dependent variable can be scaled to unit length using the following expressions,

$$X_j^*(i) = \frac{X_j(i) - \bar{X}_j}{\sqrt{S_{jj}}}, \quad i = 1, 2, \ldots, N; \quad j = 1, 2, \ldots, n \tag{C.1.1}$$

$$z^*(i) = \frac{z(i) - \bar{z}}{\sqrt{S_{zz}}} \tag{C.1.2}$$

where,

$$S_{jj} = \sum_{i=1}^{N} [X_j(i) - \bar{X}_j]^2 \tag{C.1.3}$$

$$S_{zz} = \sum_{i=1}^{N} [z(i) - \bar{z}]^2 \tag{C.1.4}$$

The variables S_{jj} and S_{zz} are known, respectively, as the centred sum of squares for the regressors and the centred sum of squares for the dependent variable. When scaled, each of the standardised regressors has a mean value of zero and a length of one,

$$\bar{X}_j^* = 0 \tag{C.1.5}$$

$$\|\mathbf{X}_j^*\| = \sqrt{\sum_{i=1}^{N} [X_j^*(i)]^2} = 1 \tag{C.1.6}$$

The standardised dependent variable is then found from,

$$z^*(i) = \theta_1^* X_1^*(i) + \theta_2^* X_2^*(i) + \ldots + \theta_n^* X_n^*(i) + \epsilon(i) \tag{C.1.7}$$

where θ_1^*, θ_2^*, $\ldots$, θ_n^* are the standardised parameters. Note that in Equation (C.1.7) the offset term θ_0^* is absent as the regressors were centred during the scaling process. If θ_0^* is to be analysed in the collinearity diagnostic then the regressors must be scaled without centring.

The least squares estimates of the standardised parameters are obtained from,

$$\hat{\boldsymbol{\theta}}^* = (\mathbf{X}^{*T}\mathbf{X}^*)^{-1}\mathbf{X}^{*T}\mathbf{z}^* \tag{C.1.8}$$

The values of the original parameter estimates are then calculated as follows,

$$\hat{\theta}_j = \hat{\theta}_j^*\sqrt{\frac{S_{zz}}{S_{jj}}} \tag{C.1.9}$$

If the regressors were centred, the estimate of the original offset parameter is calculated with the expression,

$$\hat{\theta}_0 = \bar{z} - \sum_{i=1}^{n} \hat{\theta}_j \bar{X}_j \tag{C.1.10}$$

Appendix D

List of Publications

Conferences, reports and journals

- Carnduff, S. D., Erbsloeh, S. D., Cooke, A. K. and Cook, M. V.,"Experimental Investigation of UAV Flight Dynamics", *Proceedings of the 22nd International Bristol Unmanned Air Vehicle Systems Conference*, April 2007

- Carnduff, S. D., Erbsloeh, S. D., Cooke, A. K. and Cook, M. V.,"Development of a Low Cost Dynamic Wind Tunnel Facility Utilizing MEMS Inertial Sensors", AIAA Paper 2008-196, *46th AIAA Aerospace Sciences Meeting & Exhibit*, Reno, Nevada, January 2008

- Carnduff, S. D. and Cooke, A. K.,"Formulation and System Identification of the Equations of Motion for a Dynamic Wind Tunnel Facility", Cranfield College of Aeronautics Report 0801, March 2008

- Carnduff, S. D., Erbsloeh, S. D., Cooke, A. K. and Cook, M. V.,"Characterizing Stability and Control of Subscale Aircraft from Dynamic Motion in a Wind Tunnel", *Journal of Aircraft*, Vol. 49, No. 1, pp 137-147.